Dissertation zur Erlangung des Doktorgrades
der Fakultät für Chemie und Pharmazie
der Ludwig-Maximilians-Universität München

Shedding Light on PolyQ Aggregation

How chaperones, aggregate morphology, and cellular background influence biological effects of polyQ in *S. cerevisiae*

Michael Heinrich Manfred Gropp

aus

Mannheim, Deutschland

2022

Erklärung

Diese Dissertation wurde im Sinne von §7 der Promotionsordnung vom 28. November 2011 von Herrn Prof. Dr. F. Ulrich Hartl betreut.

Eidesstattliche Versicherung

Diese Dissertation wurde eigenständig und ohne unerlaubte Hilfe erarbeitet.

München, den 2. November 2022

Michael H. M. Gropp

Dissertation eingereicht am: 15. November 2022

1. Gutachter: Prof. Dr. F. Ulrich Hartl

2. Gutachter: Prof. Dr. Roland Beckmann

Mündliche Prüfung am: 15. Dezember 2022

Acknowledgments

Throughout my studies, I have been surrounded and supported by my family, friends, colleagues and mentors and this endeavor would not have been possible without them. Each and every one was vital for successfully completing this PhD and I am deeply grateful to have them in my life.

I would like to express my deepest appreciation to my PhD supervisor Prof. Dr. F. Ulrich Hartl for giving me the opportunity to perform my PhD studies in his group. Working with Ulrich was an honor. His insatiable curiosity, unparalleled knowledge as well as the constant flow of new ideas he produces on a daily basis were an inspiration and I have learned and grown a lot during my time under his tutelage – as a scientist and as a person. I am truly grateful for this experience. Even though I never had the pleasure of working with Dr. Manajit Hayer-Hartl directly, I thank her for constructive feedback and discussions about my project during our regular lab meetings.

This thesis would not have been written if it hadn't been for my mentor Dr. Courtney Klaips. By providing the right balance of close supervision and the freedom to pursue my own ideas, she has encouraged me to become an independent and critical mind. Despite many adversaries we faced along the way, Courtney always helped me to see the positive side of things, taught me to never give up and remain focused even in scientifically challenging times. Courtney was not only a great mentor, but she is also an incredibly talented scientist and I am grateful of having had the opportunity of working with and learning from her.

I thank the members of my thesis defense and advisory committees for their time and their constructive feedback leading to the successful completion of my PhD. In particular, I am beyond grateful for the constant support, guidance and close mentorship I have received from Prof. Dr. Roland Beckmann throughout the past 10 years. Similarly, I owe an immense amount of gratitude to Dr. Birgitta Beatrix. Under her demanding but caring tutelage, I was taught the essentials of biochemical experimentation, the importance of proper controls and how to plan a project thoroughly – skills that were essential for surviving my PhD. She has been a constant inspiration and her ongoing support even after my time in her lab has helped me to stay on track with my PhD.

Throughout my more than six years in the Hartl department, I have seen many people come and go but a few constants were always there. I thank the administrative and technical staff, Massimo Bossi, Emmanuel Burghardt, Silvia Gärtner, Romy Lange, Darija Pompino, Albert Ries and Nadine Wischnewski for their help throughout the years. Without their essential support, the lab would not be functional – and definitely less fun. Working in the Hartl department meant working with incredibly talented and intelligent colleagues that I have learned a great deal from. I thank them for critical discussions, helpful feedback and creating an atmosphere of productivity and comradeship that made even tough workdays enjoyable. Special thanks to Max Garhammer and Cole Sitron for our lunches and helping to escape the stressful days for at least an hour each day. Patricia Yuste-Checa and Martin Müller were companions since the first day and have not only been excellent colleagues but have also become great friends.

It all started with them: Rainer Kreusel and Dr. Jürgen Ries, my biology and chemistry teachers of the first hour. They raised my interest in the natural sciences and did everything to keep that curiosity alive during my years at high school.

This thesis would not have been possible without the support I have received from my friends. Without people to celebrate victories with or that help putting things in perspective when experiments are not going as planned, the PhD would be an impossible undertaking.

Sometimes the biggest support comes unexpectedly and from the other side of the world. Without the help of my partner Axel Ruiz, who provided stability and secureness in my private life when things were turbulent at work, I could not have completed this PhD. His love, patience, constant encouragement and belief in my abilities helped me through the scientific hardships a PhD comes with, and I would not be where I am today without him. I am deeply grateful.

Lastly, I want to thank my parents Martina and Thomas Gropp. Through their tireless and continuous effort to support me throughout my life, from providing a childhood home that allowed me to pursue my passions and grow up without worries to their ongoing assistance during my studies that allowed me to focus on my education, they have created an environment of safety and personal growth that I thrived in and am grateful for. Without them I would not only not be here, but I would also not be the person that I am today.

Table of Contents

Abbreviations & Important Definitions

A. thaliana	*Arabidopsis thaliana*
AAA+	ATPase associated with various cellular activities
ACN	Acetonitrile
AD	Alzheimer's disease
ADP	Adenosine diphosphate
AGC	Automatic gain control
ATP	Adenosine triphosphate
BCA	Bicinchoninic acid
β-Gal	β-Galactosidase
BSE	Bovine spongiform encephalopathy
C. elegans	*Caenorhabditis elegans*
CG*	Cytosolic carboxypeptidase Y* fused to GFP
CHX	Cycloheximide
CTD	C-terminal domain
CV	Column volume
DD	Dimerization domain
DNA	Deoxyribonucleic acid
DOX	Doxycycline
DTT	Dithiothreitol
E. coli	*Escherichia coli*
EDTA	Ethylenediaminetetraacetic acid
FACS	Fluorescence-activated cell sorting
FAD	Flavin adenine dinucleotide
FlucDM	Double mutant firefly luciferase
FRAP	Fluorescence recovery after photobleaching
G418	Geneticin
Gal	Galactose
GdnHCl	Guanidinium hydrochloride
GFP	Green fluorescent protein
GO Term	Gene ontology term
GST	Glutathione S-transferase
HCD	Higher energy collisional dissociation
HD	Huntington's disease
HRP	Horseradish peroxidase
HS	Heat shock
HSE	Heat shock element
Hsp	Heat shock protein
HSR	Heat stress response
HTT/Htt	Huntingtin

iBAQ	Intensity based absolute quantification
IP	Immunoprecipitation
IPTG	Isopropyl β-D-1-thiogalactopyranoside
LC-MS	Liquid chromatography-mass spectrometry
LCR	Low complexity region
LFQ	Label-free quantification
LiOAc	Lithium acetate
Da/kDa/MDa	Dalton (unit for protein size), kilodalton, megadalton
MS	Mass spectrometry
MU	Miller unit
n.s.	Not statistically significant
NBD	Nucleotide binding domain
NEF	Nucleotide exchange factor
OD/OD_{600}	Optical density/Optical density at 600 nm wavelength
OGP	n-Octyl-β-D-glucopyranoside
ONPG	ortho-Nitrophenyl-β-galactoside
OVA	Ovalbumin
PCR	Polymerase chain reaction
PD	Parkinson's disease
PEG	Polyethylene glycol
PHR	Photolyase homology region
[*PIN*]	Rnq1 prion status, '[*PSI*]-inducing'
[*pin*$^-$]	Rnq1 prion-free strain, Rnq1 is soluble
[*PIN*$^+$]	Rnq1 prion positive, Rnq1 forms amyloid prion aggregates
PMSF	Phenylmethylsulfonyl fluoride
polyQ	Poly glutamine
PP	Poly proline
[*PSI*]	Sup35 prion status
Raf	Raffinose
RNA	Ribonucleic acid
S. cerevisiae	*Saccharomyces cerevisiae*
SBD	Substrate binding domain
SDD-AGE	Semi-denaturating detergent agarose gel electrophoresis
SDS	Sodium dodecyl sulfate
SDS-PAGE	Sodium dodecyl sulfate polyacrylamide gel electrophoresis
smHsp	Small heat shock protein
TCA	Trichloroacetic acid
Tris	Tris(hydroxymethyl)aminomethane
UPR^{ER}/UPR^{mt}	Unfolded protein response in the endoplasmic reticulum/mitochondria
vCJD	Variant Creutzfeldt-Jakob disease
Wt	Wild type

List of Figures

List of Main Tables

List of Appendix Tables

Summary

Neurodegenerative diseases pose immense hardship for affected individuals and are becoming an increasing burden for the communal health system in ageing societies. Many of these diseases share protein misfolding and aggregation as a common hallmark contributing to toxicity. Intriguingly, while the disease-associated proteins are typically ubiquitously expressed throughout the nervous system and beyond, their aggregation often initiates only in a specific subset of neurons, characteristic for individual disorders, a phenomenon known as selective vulnerability. Cells are equipped with a versatile toolbox of cellular factors and stress-inducible transcription programs to ensure the integrity of the proteome and counteract aberrant protein misfolding and aggregation. Despite the existence of these defense mechanisms, many disease-associated protein aggregates avoid recognition by the quality control machinery and do not lead to robust induction of beneficial stress responses.

In Huntington's disease, the protein Huntingtin is found in aggregate inclusions in neurons of the brain. Aggregation of Huntingtin is driven by a heritable expansion of a poly glutamine (polyQ) stretch within the first exon of the protein. In this work, we use an expanded polyQ model protein on the basis of Huntingtin exon 1 to investigate disease-associated aggregation processes in the yeast *S. cerevisiae*. Just as in the mammalian system, polyQ aggregates fail to effectively induce the cytosolic heat stress response in yeast. We demonstrate that elevated levels of the Hsp40 chaperone Sis1, an essential co-chaperone of the Hsp70 Ssa1, allow polyQ aggregates to activate a heat shock transcription factor (Hsf1) dependent stress response. This stress response requires the interaction of Ssa1 with polyQ. Sis1 leads to a change in polyQ aggregate morphology, forming cloud-like condensate structures rather than dense inclusions, in turn allowing sequestration of Ssa1 and other cellular factors to activate the stress response. We demonstrate that Sis1 acts in a similar fashion to allow the recognition of heat-denatured protein aggregates, suggesting a more general role for Sis1 in eliciting a stress response to protein aggregation. The mammalian Sis1 homolog DNAJB6 performs an analogous role in the mammalian system, indicating conservation of this process.

In the second part of this work, we elucidate the role of the yeast prion protein Rnq1 in the aggregation process of polyQ. Similar to the selective vulnerability observed for the

aggregation of disease-associated proteins in the mammalian neuronal system, yeast also show an influence of the cellular background on the aggregation of proteins. Using a novel optogenetic approach, we identify Rnq1 prions as crucial interaction partners of soluble polyQ, catalyzing its aggregation through cross-seeding. By-products of this templating are soluble polyQ oligomers. We present evidence that these oligomers are not only responsible for mediating a Sis1-dependent stress response, but also cause cell-toxic effects. Prion-free yeast strains do not experience polyQ aggregation and are therefore spared from detrimental biological consequences. A complementary *in silico* analysis of previously published data on protein aggregation in higher organisms suggests a similar role for prion-like protein aggregates in the manifestation of neurodegenerative diseases. Thus, our work not only offers an intriguing synthesis of the previously postulated models of cross-seeding and proteostatic decline in facilitating disease-relevant aggregation, but also presents a possible explanation for the phenomenon of selective vulnerability.

In summary, work described in this thesis provides novel insight in the process of disease-relevant protein aggregation and associated cellular responses. Based on our findings, we offer suggestions for therapeutic strategies to combat neurodegeneration in the future.

Introduction

Protein folding, misfolding and aggregation

Proteins are of vital importance for all forms of life. Proteins are not only required as catalysts to enable basic cellular functions such as respiration, but they also form essential building blocks that sustain the structural integrity of every cell. Synthesized in the process of translation as a linear chain of amino acids, most proteins need to adopt complex folding topologies in order to be able to perform their cellular function (Dobson et al., 1998; Radford, 2000) (Figure 1). Early researchers postulated the ability of proteins to fold by themselves, following a building plan intrinsic to each protein (Anfinsen, 1973). While this was an appropriate estimation for many very small proteins, including the model proteins that were used for these early *in vitro* folding studies, it could not adequately explain the complex folding mechanisms large, multi-domain proteins have to undergo on their way to a functional fold in the challenging crowded environment of a living cell (Ellis and Minton, 2006; Levinthal, 1968; 1969).

It was not until the 1980s that more evidence emerged, suggesting that a specific class of helper proteins – termed chaperones – plays a role in preventing aggregation and perhaps in the folding process itself (Ellis, 1987; Hartl, 1996; Pelham, 1986). It became clear later that chaperones, as the historic origin of their name implies, accompany proteins from the time they emerge as amino acid chains from the ribosome throughout their lifetime: they are required to ensure the proper folding and maintenance of most of the cell's proteome and also contribute to eventual removal of proteins by degradation (Balchin et al., 2016; Hendrick and Hartl, 1993; Kim et al., 2013; Saibil, 2013). Functions that chaperones fulfil along the way are numerous and discussed in more detail in the following chapter. Problems during initial protein synthesis or a lack or malfunction of chaperones can lead to misfolding of proteins (Drummond and Wilke, 2008; Hipp et al., 2014; Tyedmers et al., 2010) (Figure 1). However, even when proteins have acquired their proper three-dimensional structure, they are metastable and their structural integrity is constantly challenged through multiple forms of stress (Chen et al., 2011; Hartl, 2017; Tyedmers et al., 2010). These stresses, external (e.g., thermal stress, reactive oxygen species) or internal (e.g., mutations in the amino acid sequence, decline in proteostasis capacity with age), can lead to the (partial) unfolding or

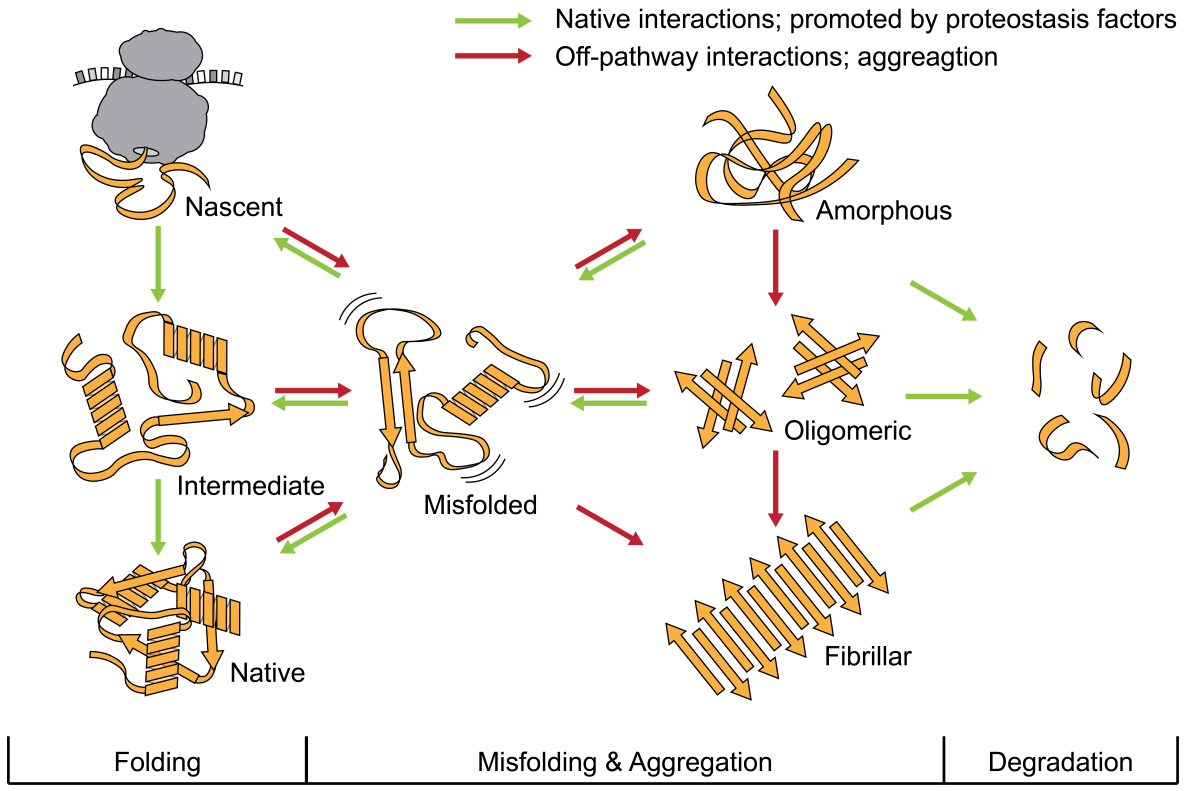

Figure 1: Protein folding, aggregation and the proteostasis network. Most proteins are only functional with a proper tertiary structure. Synthesized as linear chains of amino acids on the ribosome, proteins need to fold – via folding intermediates – into their native, functional three-dimensional conformation. Stress can lead to the accumulation of aberrant misfolded species that can associate into oligomers, amorphous aggregates, or large amyloid fibers. Proteostasis factors assist nascent polypeptides on their way to their native structure and deal with misfolded proteins and aggregates via refolding or degradation to minimize deleterious effects for the cell.

misfolding of a protein and a non-native folding conformation (Ben-Zvi et al., 2009; Chen et al., 2011; Gandhi et al., 2019; Grune et al., 2004; Sahni et al., 2015).

Regardless of the time when protein misfolding occurs, it poses a significant risk not only for the affected protein itself but for the cell as a whole. Due to the lack of their proper tertiary structure, non-native proteins can lose the ability to perform their endogenous function, show a non-physiological localization pattern or be degraded at a higher rate, all leading to classical loss-of-function phenotypes as observed in diseases such as cystic fibrosis or alpha-1 antitrypsin deficiency (Hartl, 2017; Valastyan and Lindquist, 2014). In addition, misfolded, non-native proteins can expose regions that are usually buried deep within the core of the protein. If these regions – often times highly interactive hydrophobic patches with the propensity to form β-sheet structures – are exposed, they may interact with other cellular factors and with other non-native proteins that expose regions with similar characteristics

(Chiti, 2006; Dobson, 2004). These aberrant (non-functional) interactions of two or more proteins eventually lead to the formation of protein aggregates (Fink, 1998; Roberts, 2007).

Protein aggregates can appear in different shapes, ranging from the assembly of only very few misfolded proteins in the form of oligomers, to large amorphous inclusions and fibrillar structures containing orders of magnitudes more misfolded protein molecules (Chiti and Dobson, 2017). Fibrillar structures are typically the end point of disease aggregates. They are present in the Aβ plaques of Alzheimer's disease, in Tau tangles and in Huntingtin inclusions. In these fibrils, referred to as amyloid or amyloid-like, the misfolded proteins are organized in a highly ordered cross-β structure, with strands of continuous β-sheets arranged perpendicular to the fiber axis (Figure 2). Such aggregates are thermodynamically extremely stable, reflected in their (partial) resistance to denaturing detergents such as SDS (Chiti and Dobson, 2006; 2017). Through their highly interactive nature, protein aggregates possess the ability to attract and sequester other cellular factors, increasingly depleting the functional proteome (gain-of-function) (Balch et al., 2008; Hartl, 2017; Valastyan and Lindquist, 2014). For these reasons, protein aggregation is often times associated with toxicity, cell death and disease, especially in the context of neurodegenerative disorders (Haass and Selkoe, 2007; Ross and Poirier, 2004; Stefani and Dobson, 2003).

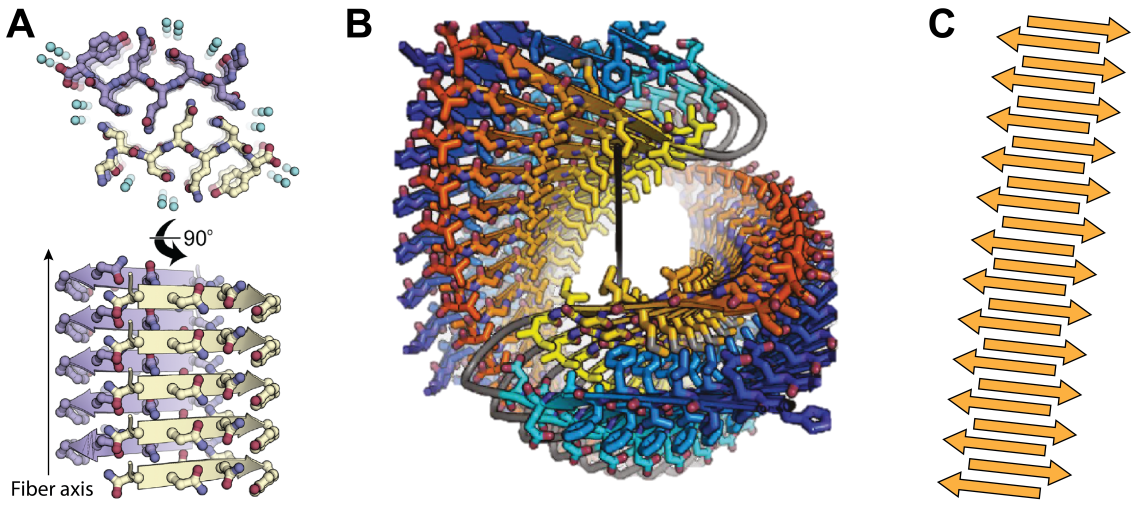

Figure 2: Examples of amyloid structures. (**A**) Atomic structure of amyloid fiber formed by the GNNQQNY peptide found in the low complexity region of the yeast prion protein Sup35. Single GNNQQNY peptides form β-strands (depicted as arrows) that are stacked onto each other via hydrogen bonds to form β-sheets. Two β-sheets (purple and yellow) are paired around a central axis, forming a protofilament. Top view (top), side view (bottom). The fiber axis is indicated with a black arrow. (**B**) High resolution structure of amyloid-beta (Aβ) fiber found in plaques in neurons of Alzheimer's disease patients. The superhelical axis of the protofilament is indicated with a black arrow. (**C**) Schematic representation of amyloid fiber used in this study. (A) and (B) are adapted from Landreh et al., 2016.

Proteostasis network

The integrity of the cellular proteome is constantly challenged. Starting from the process of proper protein folding itself, proteins require constant surveillance to prevent or reverse misfolding and aggregation, and to remove irreversibly misfolded species. A multitude of cellular factors ensures the protein homeostasis or proteostasis (Balch et al., 2008). Members of this proteostasis network include not only chaperones but also factors involved in post-translational modification, trafficking, signaling and protein degradation (Powers and Balch, 2013; Powers et al., 2009). Proteins interact with these machineries throughout their lifetime. Chaperones assist in the initial folding process of proteins with complex folding topologies but can also help refold proteins once they have misfolded, even in the context of an aggregate (Balchin et al., 2016; Hartl et al., 2011; Nillegoda et al., 2018). When proteins reach the end of their lifetime or if refolding attempts of aggregated proteins have failed, proteins involved in proteasomal degradation and autophagy clear these species to avoid further harm (Arndt et al., 2007; Bett, 2016; Jackson and Hewitt, 2016).

The proteostasis network is dynamic: it can adapt to the environment and augment its capacities in the face of stress or other challenges to proteome integrity (Jayaraj et al., 2020; Klaips et al., 2018; Taylor et al., 2014). Pathways like the cytoplasmic heat stress response (HSR) or the unfolded protein response in endoplasmic reticulum and mitochondria (UPR^{ER} and UPR^{mt} respectively) are temporarily activated upon protein conformation stress and increase the expression of proteostasis components to counteract this insult (Anckar and Sistonen, 2011; Shpilka and Haynes, 2018; Walter and Ron, 2011). For this reason chaperones were historically called 'heat shock proteins' (HSPs), as many of them have been found to be upregulated upon stress (e.g., heat stress) (Lindquist and Craig, 1988). However, when the capacity of the proteostasis network is overly challenged, through an accumulation of stress or naturally with increasing age of the organism, the integrity of the proteome is endangered, ultimately resulting in the accumulation of misfolded proteins and protein aggregates that cannot be dealt with efficiently (Douglas and Dillin, 2010; Hartl, 2016; Hipp et al., 2014; Labbadia and Morimoto, 2015).

Molecular chaperones

Chaperones are arguably the most prominent members of the proteostasis network. As their name implies (Ellis, 1987), chaperones are guardians of a protein's structural integrity and proper folding but also participate in disaggregation and protein degradation. Among the chaperone family, many different classes exist that are named according to the molecular weight of their members (Balchin et al., 2016; Kim et al., 2013). In the following, a brief overview of the most relevant chaperone classes showcases the enormous functional diversity of these proteins and serves to illustrate how small perturbations in this intricate system can lead to deleterious effects in disease.

Small heat shock proteins

Members of the small heat shock protein (smHsp) family have been found in all kingdoms of life. While most archaea, bacteria and lower eukaryotes possess only one or two smHsps, higher eukaryotes such as humans or *Arabidopsis thaliana* have a large number (10 and 19, respectively) of more specialized smHsps (Haslbeck et al., 2005a). smHsps are characterized by their relatively small size (12-43 kDa) and the presence of the characteristic, highly conserved alpha-crystallin domain, usually found in the center of the protein (Haslbeck et al., 2019). Flanking N- and C-terminal regions of smHsps are highly variable in sequence and length and play important roles in substrate recognition and binding, organellar targeting and modulation of oligomeric state (Haslbeck and Vierling, 2015; Haslbeck et al., 2019). smHsps can exist as simple monomers or in oligomeric forms, with complexes of up to 40 subunits having been observed, dependent on post-translational modifications and environmental changes (Carra et al., 2017). This regulation of oligomeric state is key in modulating the binding affinities of smHsps for their substrates (Ecroyd et al., 2007; Rajagopal et al., 2015).

smHsps represent the first line of defense of cells to maintain proteostasis upon protein conformation stress (Haslbeck and Vierling, 2015). smHsps can recognize and bind to misfolded proteins and in doing so prevent their irreversible aggregation (Haslbeck et al., 2005a). In contrast to many other chaperones, however, smHsps do not possess ATPase activity and are thus defined as 'holdases': They are able to bind to substrate proteins and buffer aggregation but the ultimate fate of a substrate – refolding or degradation – is

dependent on the activity of other chaperones (e.g., Hsp70 or Hsp100) (Haslbeck et al., 2005b; Ungelenk et al., 2016). Through their inherent ability to form large oligomeric complexes, smHsps can also act as 'sequestrases' driving the aggregation of bound near-native client proteins into designated quality control compartments, thereby facilitating the post-stress refolding or clearance of the client (Escusa-Toret et al., 2013; Specht et al., 2011; Ungelenk et al., 2016).

In line with their important function in counteracting irreversible protein aggregation, deregulation of smHsp expression has been implicated in a wide range of diseases (Haslbeck et al., 2019; Sun and MacRae, 2005). Reduced levels of smHsps increase proteotoxic stress and correlate with progression of neurological disorders, cancers, or multiple sclerosis, while elevated smHsp levels can support tumorigenesis and protect malignant cells from therapeutic intervention (Haslbeck et al., 2019). In addition, mutations in smHsps have been shown to directly cause neuropathies, myopathies, and cataract formation (Irobi et al., 2004; Kakkar et al., 2014; Litt et al., 1998; Vicart et al., 1998).

Hsp70s and their Hsp40 co-chaperones

Proteins of the Hsp70 family are ATP-dependent chaperones that bind to hydrophobic sequence motifs exposed in client proteins (Rüdiger et al., 1997). Through their reaction cycle of substrate binding and release (Figure 3), Hsp70s participate in a multitude of different cellular functions such as protein folding, refolding, disaggregation, trafficking, and transcriptional control (Balchin et al., 2016; Kim et al., 2013). Hsp70s consist of an N-terminal nucleotide binding domain (NBD) and a C-terminal substrate binding domain (SBD), which recognizes hydrophobic sequences of 5 to 7 amino acids exposed in non-native protein clients (Clerico et al., 2015; Mayer, 2013).

The Hsp70 family is one of the most ubiquitous classes of chaperones. Members show a high degree of sequence and structural conservation, but evolution has led to the diversification of the spectrum. While bacteria contain only a few Hsp70s (most prominently DnaK), eukaryotes have developed a diverse range of Hsp70s (Ghazaei, 2017; Mayer, 2021). In humans, a constitutive Hsp70 (HSPA8) is supported by a stress-inducible ortholog

(HSPA1A), and organelle-specific members act in ER (HSPA5) and mitochondria (HSPA9) (Ghazaei, 2017).

However, the real driver of Hsp70 multifunctionality is its co-chaperone Hsp40, responsible for loading substrate onto Hsp70 (Kampinga and Craig, 2010). Hsp40s possess substrate specificity, selectivity, and defined localization that most Hsp70s are lacking (Craig et al., 2006; Kampinga and Craig, 2010). This is underlined by the fact that humans express more than 40 different Hsp40s in contrast to only 13 Hsp70s (Kampinga and Craig, 2010; Qiu et al., 2006; Radons, 2016). While all Hsp40s have the characteristic J-domain in common, necessary for interaction with Hsp70, they share relatively little structural or sequence similarity beyond, allowing for a wide range of different clients and specialized functions (Cheetham and Caplan, 1998; Kampinga and Craig, 2010).

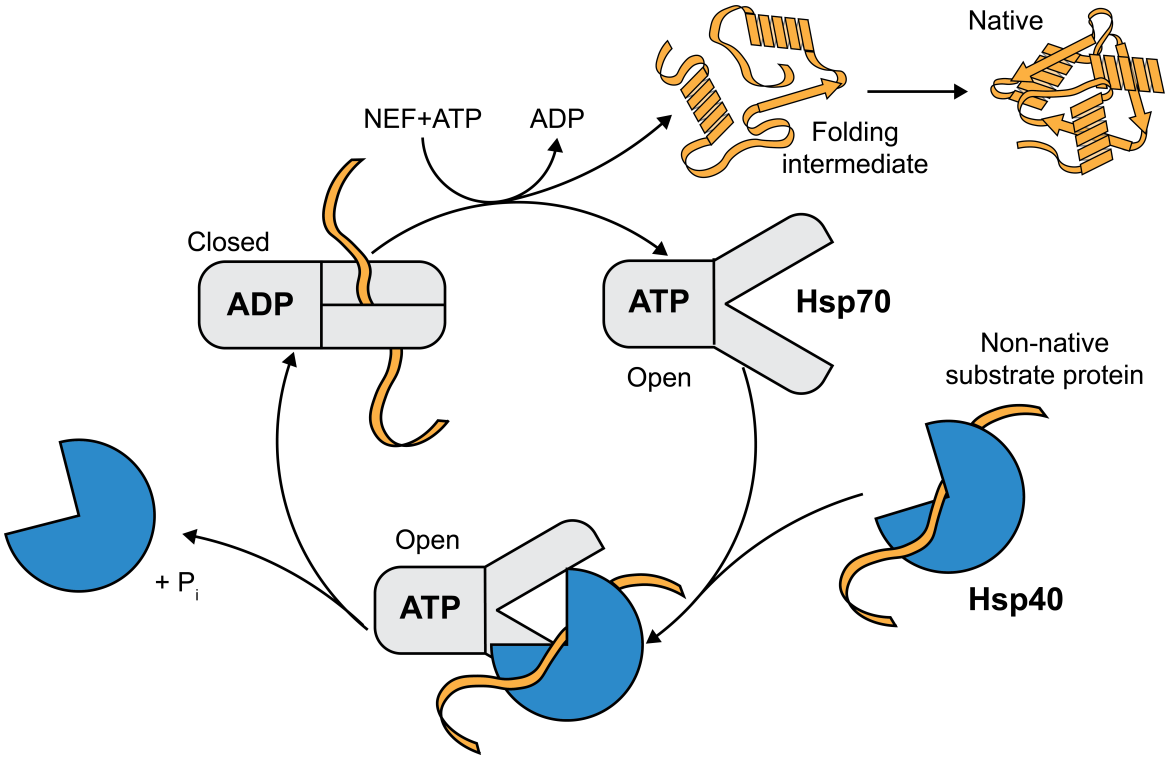

Figure 3: The Hsp70 reaction cycle. When ATP is bound, Hsp70 is in its 'open' conformation with a high on- and off-rate for substrate binding (low affinity). Non-native substrate proteins are recognized and bound by Hsp40 and delivered to ATP-bound Hsp70. Upon substrate handover, Hsp40 stimulates the ATPase activity of Hsp70 leading to the hydrolysis of ATP and the closure of the Hsp70 substrate binding domain. In the ADP-bound 'closed' state, the protein substrate is tightly bound by Hsp70 (low on-rate, low off-rate). Binding of multiple Hsp70 molecules can cause local expansion of the substrate protein. Replacement of ADP with ATP through the action of a nucleotide exchange factor (NEF) results in the opening of the substrate binding domain and the release of the client protein, which can continue to fold, be transferred to a downstream chaperone or enter another interaction cycle with Hsp70.

The Hsp70/Hsp40 reaction cycle has been a field of intense investigation over the past decades and significant insights have been gained about its mechanism (Figure 3) (Laufen et al., 1999; Mayer, 2013; Mayer and Bukau, 2005; Rosenzweig et al., 2019). Briefly, Hsp40 identifies and binds substrate proteins and loads them onto Hsp70 in its ATP-bound, 'open' conformation, characterized by a high on- and off-rate for substrate. Interaction of the J-domain of Hsp40 with Hsp70 not only facilitates this handover but also stimulates the ATPase activity of Hsp70. Hydrolysis of ATP to ADP converts the SBD of Hsp70 to the 'closed' conformation in which the substrate is tightly bound and partially unfolded. Interaction with a nucleotide exchange factor (NEF) and the replacement of ADP with ATP leads to the subsequent release of the client protein from Hsp70. Once released, clients can either continue their folding to a native, functional state or, if non-native interactions persist, be rebound by Hsp70 for another reaction cycle and potential transfer to other downstream chaperones (Hartl et al., 2011; Imamoglu et al., 2020; Langer et al., 1992; Sharma et al., 2008; Sharma et al., 2010; Wegele et al., 2006).

With the exception of the recently reported association of inflammatory bowel disease with a mutation in the human Hsp70 HSPA1L (Takahashi et al., 2017), no inherited genetic disorder has been described for members of the Hsp70 chaperone family to date, either due to functional redundancies or because disruptions of this central chaperone system is inevitably lethal (Kakkar et al., 2014). However, altered Hsp70 levels have been detected in many diseases such as cancer, diabetes, stroke, and atherosclerosis, making Hsp70 a promising biomarker for medical diagnostics and preventative therapy (Garg et al., 2018; Radons, 2016). In contrast, mutations in members of the Hsp40 chaperone class have been demonstrated to cause, among others, motor neuropathy, muscular dystrophy, juvenile parkinsonism and ataxia, due to defective client recognition, protein mistargeting or loss of interaction with their Hsp70 partners (Kakkar et al., 2014).

The yeast Hsp40 Sis1

The yeast protein Sis1 is an essential member of the type II family of Hsp40 chaperones (Kampinga and Craig, 2010; Luke et al., 1991). It has been found to be enriched in the nucleus while constantly shuttling between nucleus and cytoplasm (Luke et al., 1991; Park et al.,

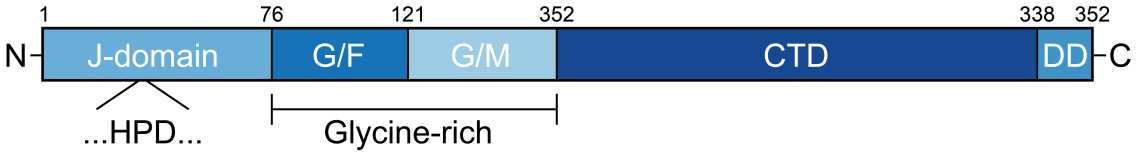

Figure 4: Domain architecture of Sis1. Sis1 consists of an N-terminal J-domain with a conserved HPD motif, important for interaction with Hsp70 and stimulation of its ATPase activity, an unstructured glycine-rich region comprised of the glycine/phenylalanine-rich (G/F) and the glycine/methionine-rich (G/M) domains, a C-terminal domain (CTD), involved in substrate recognition and binding, as well as a very C-terminal dimerization domain (DD). Amino acid residues are indicated above.

2013). Sis1 cooperates with the yeast Hsp70 Ssa1 in many distinct functions (Aron et al., 2005; Kampinga and Craig, 2010; Qian et al., 2002). Sis1 is not only involved in protein folding (Lu and Cyr, 1998), but also in the clearance of cytosolic misfolded proteins most likely by mediating their delivery to the nucleus for proteasomal degradation (Park et al., 2013; Summers et al., 2013). In the context of neurodegeneration, Sis1 has been shown to interact with and be sequestered by amyloid-like aggregates such as inclusions formed by extended polyQ (Park et al., 2013). Importantly, Sis1 is involved in loading Hsf1 on Ssa1, thereby contributing to a silencing of the cytosolic heat stress response (Feder et al., 2021).

As any other Hsp40, Sis1 contains an N-terminal J-domain, with its conserved His, Pro and Asp tripeptide (HPD), important for interaction with and stimulation of the ATPase activity of Hsp70 (Craig et al., 2006; Greene et al., 1998; Yan and Craig, 1999) (Figure 4). Adjacent to the J-domain is a largely intrinsically disordered glycine-rich region, consisting of a glycine- and phenylalanine-rich (G/F) and a glycine- and methionine-rich (G/M) domain. While found in all type I and II Hsp40s, the G/F region is especially critical for essential functions of Sis1 (Yan and Craig, 1999). Furthermore, the high degree of structural flexibility in the G/F and G/M domains is thought to be responsible for the substrate preference of Sis1 for similarly unstructured clients, as exemplified by the importance of these domains for prion maintenance (Fan et al., 2004; Lopez et al., 2003; Sondheimer et al., 2001; Yan and Craig, 1999). The defining feature of type II Hsp40s is the C-terminal domain (CTD) that – in contrast to members of type I Hsp40s – lacks a characteristic zinc-finger domain (Kampinga and Craig, 2010; Wu et al., 2005). The CTD is involved in substrate binding and delivery to Hsp70s (Sha et al., 2000). The dimerization domain (DD) at the very C-terminus of Sis1 allows dimer formation and thereby increases the affinity for substrates (Sha et al., 2000). Based on

sequence, the closest human Sis1 homolog is DNAJB1, while the G/F domain of DNAJB6 has an intrinsically disordered character, which closely resembles that of Sis1 (Kampinga and Craig, 2010).

The Hsp60s

Hsp60s – also called chaperonins – are multimeric cylindrical protein complexes with ATPase activity that allow folding to occur unimpaired by aggregation, while a substrate protein is enclosed in a cage-like structure (Balchin et al., 2016; 2020; Hartl et al., 2011). Type I chaperonins are present in prokaryotes and the matrix of mitochondria and chloroplasts while type II chaperonins are found in the cytoplasm of eukaryotes and archaea (Hayer-Hartl et al., 2016; Lopez et al., 2015).

The most prominent type I chaperonin is bacterial GroEL, required for the folding of about 10% of the proteome in *E. coli*, mostly proteins with complex fold topologies and aggregation-prone folding intermediates exposing hydrophobic regions (Kerner et al., 2005; Tartaglia et al., 2010). GroEL consists of two stacked heptameric rings of identical GroEL subunits, forming a large ~800 kDa complex, harboring two separate, hollow chambers, each large enough to accommodate a single substrate protein up to 60 kDa in size (Saibil et al., 2013). The reaction cycle of GroEL has been a field of intense investigation for decades (Figure 5). Initially, GroEL binds its non-native substrates via multivalent hydrophobic interactions (Farr et al., 2000). Binding of ATP in combination with the heptameric co-factor GroES, closes the GroEL cage and fully releases the substrate into the folding chamber (Cliff et al., 2006; Saibil et al., 2013). Closure of the chamber is accompanied by large structural rearrangements on its inside, switching its biophysical characteristics from hydrophobic to hydrophilic (Hartl et al., 2011; Xu et al., 1997). Substrate proteins can now fold inside the GroEL/ES chamber, shielded from aggregation, for the duration of ATP hydrolysis by GroEL, a few seconds dependent on temperature (Gupta et al., 2014). Eventually, binding of GroES and ATP to the opposite GroEL ring allosterically induces transient ring separation, dissociation of ADP and GroES and release of the folded substrate protein (Yan et al., 2018). If folding is incomplete or incorrect, substrates can rebind to GroEL and undergo multiple cycles of folding (Sharma et al., 2008; Singh et al., 2020).

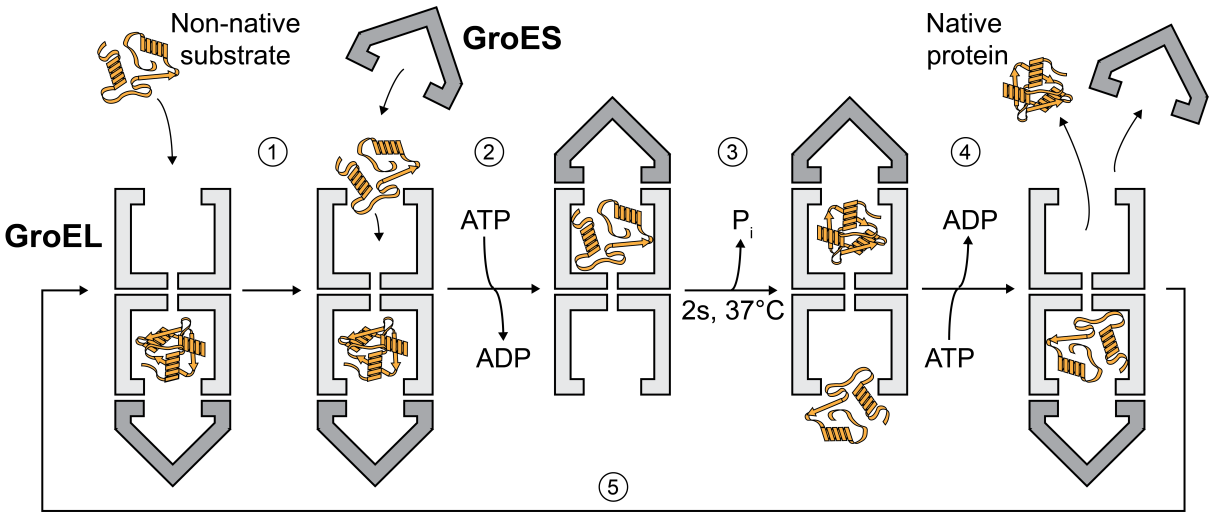

Figure 5: The GroEL/ES reaction cycle. (1) A non-native substrate protein binds to an empty GroEL ring via multivalent hydrophobic interactions. (2) Binding of GroES and ATP releases the substrate into and closes the GroEL folding chamber. (3) The substrate protein is allowed to fold inside the folding chamber for the duration of ATP hydrolysis (approx. 2 s at 37 °C). (4) Binding of ATP and GroES to the opposite ring allosterically leads to the dissociation of ADP and GroES and releases the native protein. (5) If folding is incomplete, the substrate can rebind to GroEL to undergo an additional round of folding.

The general principle of protein folding described above for GroEL is similar in type II chaperonins such as the eukaryotic TRiC, but structural differences exist. Type II chaperonins consist of two rings of eight (rarely nine) paralogous subunits with distinct characteristics (Balchin et al., 2016; Hartl et al., 2011; Lopez et al., 2015). In contrast to GroEL, TRiC does not need a co-factor to close the folding chamber but can do so on its own via an iris-like mechanism of structural subunit rearrangement (Douglas et al., 2011; Zhang et al., 2010). Once a substrate is encapsulated, ATP cycling does not proceed simultaneously as in type I chaperonins but sequentially. In conjunction with an asymmetric charge distribution inside the folding chamber, this mechanism is critical in promoting folding (Balchin et al., 2018; Rivenzon-Segal et al., 2005). TRiC supports the folding of about 10 % of the eukaryotic proteome, including obligate substrates such as actin and tubulin (Yam et al., 2008).

Given their crucial role in assisting the folding of many clients, mutations in Hsp60s come with deleterious effects and are implicated in disease. The neurodegenerative diseases MitCHAP-60 and hereditary spastic paraplegia 13 are caused by mutations in the mitochondrial Hsp60, a type I chaperonin, leading to reduced chaperonin activity, a destabilization of the Hsp60 complex and its premature disassembly (Kakkar et al., 2014; Macario et al., 2005). Similarly, mutations in CCT4 and CCT5, subunits of the cytosolic

eukaryotic type II chaperonin TRiC, have been identified to cause hereditary sensory neuropathies (Grantham, 2020; Kakkar et al., 2014). Here, reduced activity of TRiC and a failure to properly fold its obligate substrates actin and tubulin leads to cytoskeletal instability, primarily affecting long axons in the limbs (Kakkar et al., 2014).

Hsp90s

ATP-dependent chaperones of the Hsp90 family are highly conserved from prokaryotes to higher eukaryotes and, with the exception of archaea, can be found in organisms across all kingdoms of life. In higher eukaryotes, Hsp90s are essential and present in almost every cellular compartment, where they participate in the stabilization and folding of metastable clients. Their substrates include – among others – transcription factors as well as signal-transduction molecules like kinases and steroid hormone receptors (Balchin et al., 2016; Taipale et al., 2010).

Hsp90 monomers are modular: they contain an N-terminal nucleotide binding domain (NBD), a middle domain participating in substrate binding and ATP hydrolysis, and a C-terminal dimerization domain (Schopf et al., 2017). The functional Hsp90 unit is a dimeric complex (Ali et al., 2006; Wayne and Bolon, 2007). In its V-shaped 'open' conformation, the Hsp90 dimer is available for substrate binding, most likely through hydrophobic interactions with non-native but also near native client proteins (Shiau et al., 2006; Street et al., 2014). Binding of ATP leads to large conformational changes and the closure of the Hsp90 dimer, holding the substrate in a clamp-like fashion (Hessling et al., 2009; Mayer, 2010; Prodromou et al., 2000). Contact of the NBDs of the two Hsp90 monomers and stimulating influences of the middle domains lead to ATP hydrolysis and release of the substrate (Cunningham et al., 2008; Meyer et al., 2003). If and how Hsp90 binding and ATP hydrolysis induces conformational changes within substrate proteins remains elusive.

More than any other chaperone family, the function of Hsp90 is modulated by co-chaperones. These include HOP, Aha1 or p23, which regulate substrate handover, ATP hydrolysis or progression of the chaperone cycle (Li et al., 2012; Schopf et al., 2017). Given its role in the maturation of clients such as transcription factors and steroid hormone receptors, a role of Hsp90 in buffering destabilizing mutations during protein evolution has been

highlighted (Lindquist, 2009; Rutherford and Lindquist, 1998). Similar to members of the Hsp70 family, no genetically inherited diseases are associated with members of the Hsp90 class of chaperones (Kakkar et al., 2014). However, due to its involvement in stabilizing kinases important for tumor development or disease-associated proteins such as α-synuclein and tau, Hsp90 has been of interest as a potential therapeutic target in cancer therapy and treatment of neurodegenerative diseases (Barrott and Haystead, 2013; Luo et al., 2010; Schopf et al., 2017).

Hsp100s

In contrast to other chaperone families that promote *de-novo* protein folding and structural maintenance of metastable clients, members of the Hsp100 family engage in protein remodeling, unfolding, and disaggregation (Jayaraj et al., 2020; Saibil, 2013). Hsp100s are AAA+ (ATPase associated with various cellular activities) protein complexes found in bacteria, plants and fungi (Nillegoda et al., 2018).

Hsp104, the Hsp100 in fungi such as *S. cerevisiae*, is a prototypical member of this chaperone family (Doyle et al., 2013; Parsell et al., 1994). Like most members of the AAA+ family of proteins, Hsp104 functions as a hexameric complex (Hanson and Whiteheart, 2005; Lee et al., 2010). Each Hsp104 protomer consists of an N-terminal domain and two nucleotide-binding domains (NBD1 & NBD2). Together, six Hsp104 monomers form a cylindrical complex with three stacked hexameric rings: two large rings formed by each NBD and a smaller ring on top formed by the N-terminal domains (Lee et al., 2010; Lee et al., 2003). The resulting central channel is used to thread substrates in an ATP-dependent, ratchet-like manner, leading to their unfolding (Gates et al., 2017; Glover and Tkach, 2001). Hsp104 is thus not only able to completely unfold misfolded substrates but can also extract misfolded proteins from large aggregates – even amyloids – and mediate disaggregation (DeSantis et al., 2012; Glover and Lindquist, 1998; Shorter and Lindquist, 2004; Vashist et al., 2010). Once a substrate has been unfolded by Hsp104, it might be able to refold to its native conformation or be sent for degradation (Doyle et al., 2013). Hsp104 functionally cooperates with other chaperones, especially the Hsp70/Hsp40 system (Glover and Lindquist, 1998; Mogk et al., 2015).

Hsp104 also plays an essential role in the maintenance of yeast prions (see detailed description below) as it allows the fragmentation of large prion amyloids into smaller seeds that are then inherited by budding daughter cells (Chernoff et al., 1995; Kushnirov and Ter-Avenesyan, 1998; Liebman and Chernoff, 2012). In bacteria, some Hsp100s can directly interact with proteolytic enzymes to create a central hub for targeted protein unfolding and subsequent degradation (Sauer and Baker, 2011). A designated functional Hsp100 ortholog has not yet been identified in metazoa. Instead, in an intricate mechanism involving stepwise binding and complex formation, Hsp40s (in humans: DNAJA1/2 and DNAJB1/4), Hsp70 (HSPA8) and a nucleotide exchange factor (HSPA4) are able to generate a power stroke strong enough to disaggregate not only large amorphous aggregates but even amyloid fibrils (Gao et al., 2015; Nillegoda et al., 2015; Nillegoda et al., 2018). In addition, AAA+ proteins such as VCP and RUVBL1/2 have recently been shown to contribute to protein disaggregation, potentially performing the role of a metazoan Hsp100 (Darwich et al., 2020; Zaarur et al., 2015).

The cytosolic heat stress response

Throughout their lifetime, cells are constantly challenged by various forms of stress, endangering the integrity of their genome and proteome. In order to face these challenges and minimize long-term damage, cells have developed stress-inducible transcriptional programs that help counteract these detrimental influences. In the case of proteostasis stress – e.g., the accumulation of misfolded proteins, ubiquitin proteasome system intermediates, mistargeted organellar proteins or unassembled ribosomal proteins in the cytosol – cells react with the upregulation of proteostasis components, most prominently chaperones, in a process termed cytosolic heat stress response (HSR) (Pincus, 2020; Verghese et al., 2012). Despite its name, the HSR is not only triggered by thermal stress, which can upset the labile structural balance most proteins find themselves in, but also by the expression of mutant, aggregation-prone proteins, oxidative stress, nutrient starvation or chemical compounds that all lead to an accumulation of aberrant non-native protein species (Pincus, 2020). While the HSR is conserved throughout all kingdoms of life, subtle differences in its specific mechanism and regulation exist. Here, we showcase its general principle based on the mechanism in the yeast *S. cerevisiae* (Masser et al., 2020; Pincus, 2020) (Figure 6).

Upon accumulation of aberrant protein species, a cell's proteostasis capacity is quickly overwhelmed and the amount of chaperones present is not sufficient to deal with the substantial number of clients. In order to relieve this burden, cells need to upregulate chaperones and other proteostasis factors. The transcriptional master-regulator for the expression of such factors is heat shock factor 1 (Hsf1), active as a trimer (Anckar and Sistonen, 2011; Gomez-Pastor et al., 2018). Under non-stress conditions, Hsf1 monomers are bound by Hsp70 (Ssa1 in yeast) and thereby kept in an inactive state (Masser et al., 2020; Masser et al., 2019; Zheng et al., 2016) (Figure 6). When aberrant protein species accumulate, Hsp70s are recruited to these proteins, binding to exposed hydrophobic patches and shielding them from undesired interactions with other proteins (Clerico et al., 2015; Mayer, 2013; Rüdiger et al., 1997). Ultimately, if the number of aberrant proteins exceeds the cell's present proteostasis capacity, Hsp70 is titrated away from Hsf1 (Masser et al., 2019; Zheng et al.,

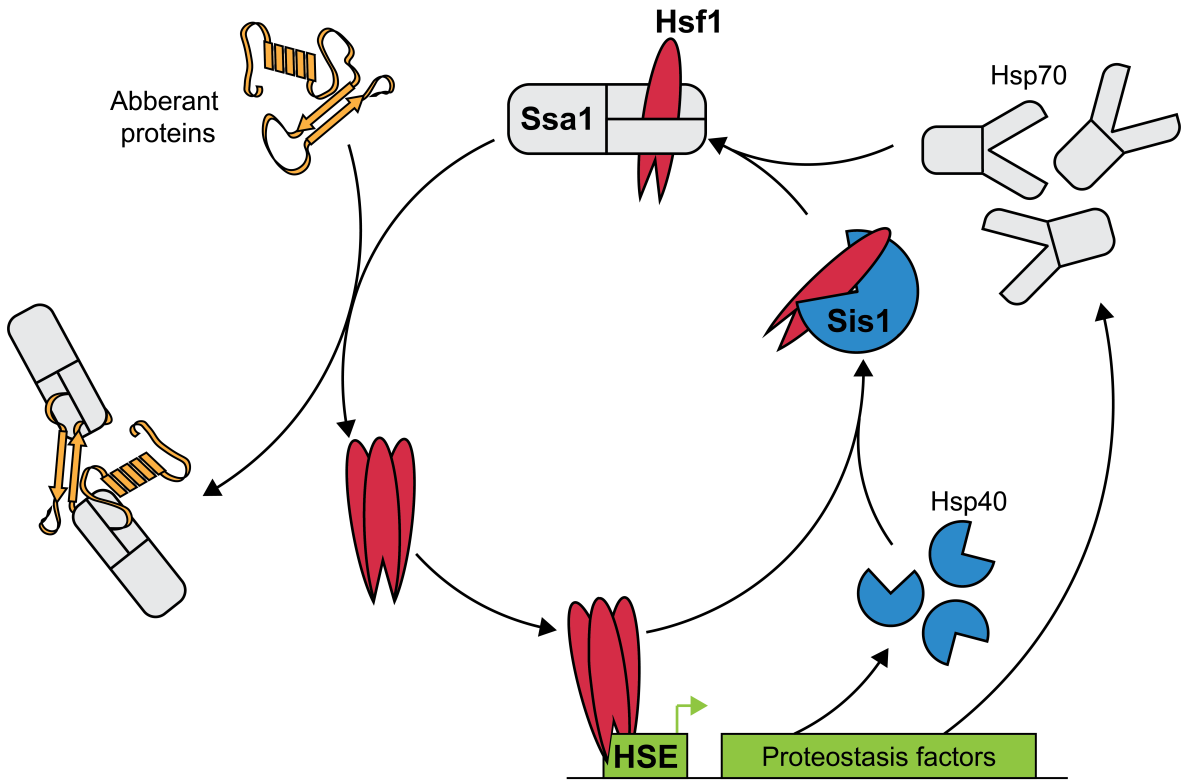

Figure 6: A feedback loop controls the regulation of the cytosolic heat stress response via Hsf1. Under non-stress conditions, Hsf1 monomers are bound by the Hsp70 Ssa1 and kept in an inactive state. If aberrant protein species accumulate during stress, Ssa1 is titrated away, releasing Hsf1. Hsf1 trimerizes and binds to heat shock elements in the promoter region of proteostasis factors to activates their expression. Production of chaperones such as Hsp40s and Hsp70s increases the cell's capacity to deal with aberrant proteins. Once stress relieves, the Hsp40 Sis1 starts loading Hsf1 onto Ssa1 again, shutting down the HSR and corresponding proteostasis factor expression, allowing the system to return to a ground state.

2016). Once released, Hsf1 can trimerize and activate the expression of proteostasis factors through binding to conserved DNA binding motifs, called heat shock elements (HSEs), in their promoters (Amin et al., 1988; Sorger and Nelson, 1989). The increased amount of proteostasis components can restore and maintain proteostasis until stress relieves. Once stress relieves and aberrant proteins are dealt with, either through refolding or degradation, more and more Hsp70 becomes available and its cochaperone Hsp40 (Sis1 in yeast) starts loading Hsp70 onto Hsf1 again, thereby shutting off heat stress response expression (Feder et al., 2021). This feedback loop guarantees that cells return to a proteostasis ground state and are ready for the next stress to arrive (Pincus, 2020). Regulation of Hsf1 activity by Hsp90 and posttranslational modifications such as phosphorylation have been described as well but are far less understood (Gomez-Pastor et al., 2018; Masser et al., 2020; Pincus, 2020).

Despite decades of intense investigation and recent major advances in understanding the Hsf1-mediated regulation of the HSR, many questions remain unanswered. It is still puzzling how cytosolic substrates efficiently titrate away nuclear Hsp70 from Hsf1 when their molar ratio exceeds 1000:1 and how a proper fine-tuning of the HSR can be achieved when ratios are so dramatically different (Feder et al., 2021; Klaips et al., 2020). Furthermore, while it has been appreciated that the activation of the HSR can occur through various types of aberrant protein species, the mechanism of how cells sense these species – either directly or via other changes to the cellular environment such as lowering of cytosolic pH – is still under controversial debate (Klaips et al., 2020; Triandafillou et al., 2020). Finally, given this broad spectrum of potential inducers of the HSR, it is surprising that the presence of disease-related protein aggregates rarely leads to an induction of the HSR (Olzscha et al., 2011; San Gil et al., 2020).

Neurodegenerative diseases

Many neurodegenerative diseases are characterized as gain-of-function protein misfolding diseases due to their underlying mechanism of toxicity, based on the misfolding of proteins and the distinctive appearance and accumulation of protein aggregates in the form of soluble oligomers, amorphous inclusions or amyloid fibrils in the brain of patients (Chiti and Dobson, 2017; Hartl, 2017; Ross and Poirier, 2004; Stefani and Dobson, 2003). Neurodegenerative

diseases pose a major challenge not only for affected individuals and their families but also the communal health care system in general, as their prevalence and impact increases in our ageing societies (AlzheimerAssociation, 2021; Arthur et al., 2016; Whetten-Goldstein et al., 2015; Yang et al., 2020). Many of these diseases such as Alzheimer's, Parkinson's and Huntington's disease (AD, PD and HD, respectively) are known to the public as widespread common diseases, while others such as amyotrophic lateral sclerosis or Pick's disease affect small numbers of patients but are equally devastating (Chiti and Dobson, 2017). Even though most neurological disorders differ quite substantially from each other in terms of age of onset, observable symptoms or affected tissues and brain region, they all share as a hallmark the presence of protein aggregates in affected neurons (Dugger and Dickson, 2017; Ross and Poirier, 2004; Soto and Pritzkow, 2018). The fact that these aggregates are formed by different proteins – e.g., Aβ and Tau in AD, α-synuclein in PD, or Huntingtin in HD – in cells of different brain regions, can account for their distinct clinical pathology, but the underlying principle of protein misfolding and accumulation of highly interactive aggregates is shared (Chiti and Dobson, 2017; Fu et al., 2018; Hipp et al., 2014; Olzscha et al., 2011). Understanding the biochemical basis of aggregate toxicity has been of key interest in the study of neurodegenerative diseases. Based on our knowledge to date, first therapeutic approaches are being developed that have the potential to improve the lives of patients (Chiti and Dobson, 2017; Gandhi et al., 2019).

Selective cellular vulnerability

One hallmark of most neurodegenerative diseases is the formation of protein aggregates in neurons of the brain (Chiti and Dobson, 2017; Ross and Poirier, 2004). Depending on the type of disease, different proteins are implicated in forming these aggregates and while at later stages of disease pathology protein aggregates can be found throughout most regions of the brain, initial aggregate appearance is disease-specific (Brettschneider et al., 2015; Fu et al., 2018) (Figure 7). In AD, aggregates of Aβ are first found in the neocortex while Tau inclusions form in the locus coeruleus and hippocampus first and only later reach the neocortex (Braak et al., 2006; Thal et al., 2002; Thal et al., 2000). In PD, α-Synuclein inclusions first appear in the olfactory bulb and brainstem, while Huntingtin aggregates are initially detected in the

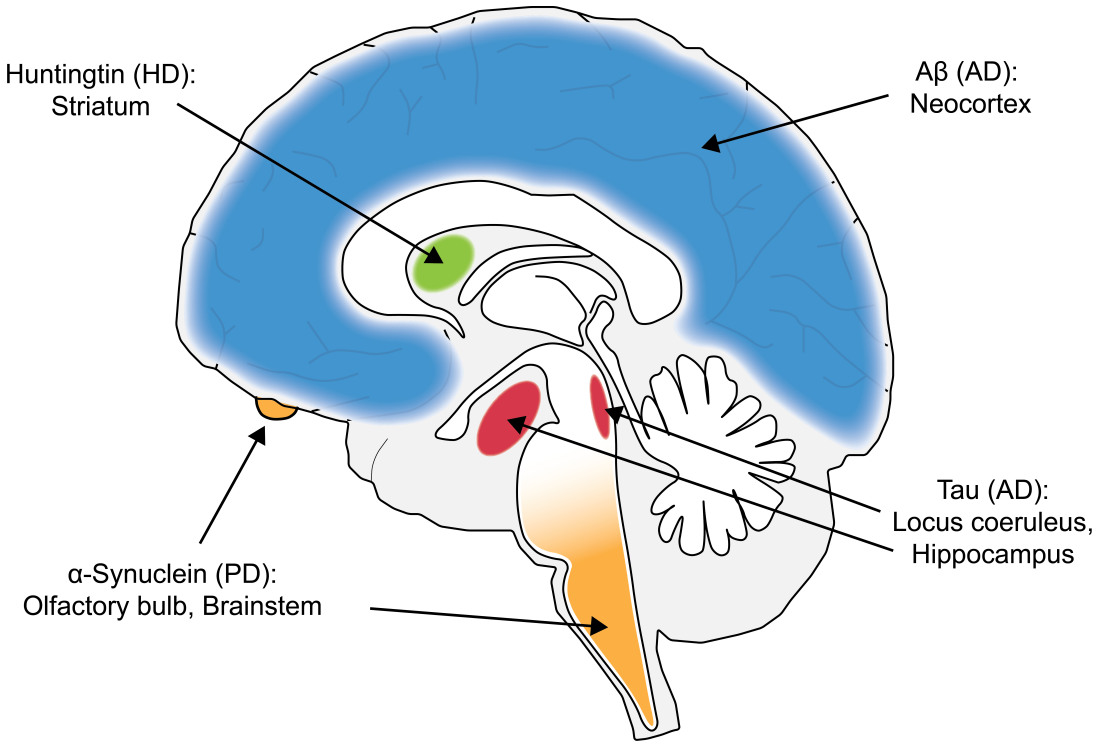

Figure 7: Selective vulnerability of different brain areas to pathological protein aggregation. Indicated are areas of the brain where protein aggregation of selected proteins in different neurodegenerative diseases is initially observed. HD, Huntington's disease; AD, Alzheimer's disease; PD, Parkinson's disease.

striatum in HD (Braak et al., 2003; Fu et al., 2018; Walker, 2007). This observation is striking, as most of these proteins implicated in forming disease-associated aggregates are ubiquitously expressed throughout the brain and in some cases even the entire human body (Uhlen et al., 2015). It seems that there is a selective influence of the cellular background on the aggregation process of different proteins. While this observation has been known for a while, researchers struggle to identify these influences due to the complex environment of the brain. Additionally, protein aggregation of one particular protein can be influenced by the presence of protein aggregates of another, as has been shown for Tau and α-Synuclein or Aβ (Guo et al., 2013; Morales et al., 2013; Vasconcelos et al., 2016). Interactions of α-Synuclein, Tau and Aβ have also been reported for the aggregation of the disease-related TAR DNA Binding Protein, TDP-43 (Dhakal et al., 2021; Montalbano et al., 2020; Shih et al., 2020). This mechanism of cross-seeding aggregation further complicates investigations as it adds another layer to the question of how the cellular background influences pathological protein aggregation.

Huntingtin, Huntington's disease and other polyQ diseases

The large, 3144 amino acid protein Huntingtin (HTT) is generally expressed in metazoans, showing a high degree of conservation among vertebrates (Schulte and Littleton, 2011; Tartari et al., 2008). While its exact function is still the focus of ongoing research, HTT seems to be a versatile protein, participating in numerous different biological processes such as vesicle and organelle trafficking, ciliagenesis, cell division, and regulation of transcription (Saudou and Humbert, 2016). HTT is ubiquitously expressed throughout the entire body, with the highest expression levels found in the brain (Marques Sousa and Humbert, 2013; Saudou and Humbert, 2016; Schulte and Littleton, 2011; Uhlen et al., 2015). Most prominently, HTT is found in large protein inclusions in the brain of patients with Huntington's Disease (HD).

HD is a complex neurodegenerative disorder with a mean age of onset of 40 years (Ross and Tabrizi, 2011). Patients suffering from this disease experience many classical symptoms of neurological disorders such as progressive motor dysfunction, cognitive decline, and psychiatric disturbance (Ross and Tabrizi, 2011; Walker, 2007). Unfortunately, HD, just as many other neurodegenerative diseases, cannot be cured and inevitably leads to death within 20 years of the appearance of first symptoms (Ross and Tabrizi, 2011). One characteristic hallmark of HD is the formation of large neuronal protein inclusions (Davies et al., 1997; DiFiglia et al., 1997). Pathology usually starts with the appearance of HTT aggregates in the medium spiny GABAergic neurons in the striatum, eventually affecting other areas across the brain such as the substantia nigra, motor cortex and hippocampus (Fu et al., 2018; Walker, 2007).

When these aggregates were analyzed with regard to their composition, predominantly N-terminal fragments of HTT, corresponding to HTT exon 1, were found (Becher et al., 1998; DiFiglia et al., 1997; Landles et al., 2010; Li et al., 2000). These short fragments can be generated through proteolytic cleavage of full-length HTT or translation of alternative splicing products (Sathasivam et al., 2013; Saudou and Humbert, 2016). The exon 1 of HTT contains a CAG trinucleotide repeat sequence that, when translated, produces multiple glutamine residues (Figure 8). In healthy individuals, this poly glutamine (polyQ) stretch is about 10 to 29 (median, 18) residues long, while HD patients show an abnormal expansion of this sequence of 36 to more than one hundred glutamine residues (Kremer et al., 1994). These disease-associated, expanded glutamine repeat regions are able to convert

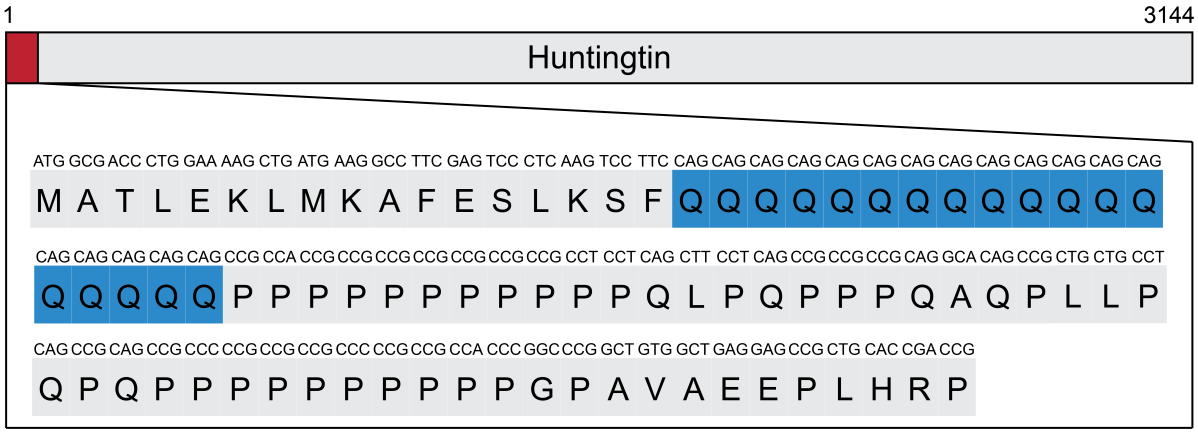

Figure 8: Huntingtin and its polyQ-containing exon 1. Schematic representation of the full-length Huntingtin protein with its exon 1 (aa 1-85) highlighted in red. Box shows nucleotide and corresponding amino acid sequence of exon 1, marked in blue is the poly glutamine (polyQ) tract of a healthy individual with 18 glutamine residues.

from a disordered state to stable intramolecular β-sheet stacks with the propensity to grow into amyloid-like aggregates (Chen et al., 2002; Yushchenko et al., 2018).

Aggregation of mutant HTT follows an association-conformational conversion mechanism: first, protein monomers accumulate locally, as suggested for example through oligomerization, micelle formation or liquid-liquid phase separation (Jayaraman et al., 2012; Peskett et al., 2018; Thakur et al., 2009). Within these local accumulations, an aberrant conformational transition takes place, stochastically generating a critical nucleus with partial β-sheet structure (Sinnige et al., 2021; Walters and Murphy, 2011). Due to the high local concentration of HTT in these local protein accumulations, this structural rearrangement can propagate to neighboring molecules invoking similar conformational changes to take place and trigger downstream aggregation of the whole protein population (Chen et al., 2002; Yushchenko et al., 2018). The length of the polyQ stretch and the protein concentration are crucial determinants for the aggregation and toxicity of Huntingtin *in vivo* (Arrasate et al., 2004; Martindale et al., 1998; Sinnige et al., 2021). In addition, the 17 aa N-terminal as well as the proline-rich C-terminal flanking region of the polyQ tract have also been implicated in modulating the aggregation propensity and toxicity of mutant Huntingtin as well as its interaction with proteostasis components (Dehay and Bertolotti, 2006; Duennwald et al., 2006b; Shen et al., 2016; Urbanek et al., 2020). As with neurodegenerative diseases in general, whether early soluble oligomers or late-stage amyloid deposits, or both, are causative for the toxic effects observed in HD, remains an open question. (Arrasate and

Finkbeiner, 2012; Chiti and Dobson, 2017; Ross and Poirier, 2005; Ross and Tabrizi, 2011). Despite toxic effects however, inclusions of polyQ-expanded Huntingtin, just like other pathological protein aggregates, fail to activate the HSR (Gomez-Pastor et al., 2017; Gomez-Pastor et al., 2018), even though its activity has been shown to ameliorate disease (Fujimoto et al., 2005; Maheshwari et al., 2014; Neef et al., 2011; Sittler et al., 2001).

The fact that exon 1 of HTT, containing the polyQ region, is the prevalent species found in disease-associated aggregates, has made exon 1 a widely used model protein to study the fundamental principles of pathological protein aggregation and toxicity not only in HD but also other neurodegenerative polyQ disorders, including spinal and bulbar muscular atrophy or various forms of spinocerebellar ataxia.

The model system *S. cerevisiae*

Intuitively, studies on neurodegenerative diseases should be performed in experimental systems as close to the physiological reality as possible, such as human cell culture or mouse models. However, the complexity of these systems may limit the ability to explore fundamental principles of cellular aggregate pathology. Therefore, researchers have been employing model organisms as simple as the yeast *S. cerevisiae* for decades (Botstein and Fink, 1988). While this unicellular organism lacks many features of higher eukaryotic cells, fundamental pathways and molecular machineries are conserved up to human cells, offering the possibility to gain valuable insights into complex biological processes, especially with regard to diseases (Botstein et al., 1997). *S. cerevisiae* has been used extensively in the past to not only advance our understanding of central cell biological processes such as transcription and translation, but also to deepen our knowledge about basic aspects of neurodegenerative diseases, including Huntington's disease (Duennwald, 2011; Khurana and Lindquist, 2010; Winderickx et al., 2008). Expressing variants of HTT exon 1 in yeast has revealed the polyQ-length dependence of HTT aggregation and the modulation of this process by molecular chaperones (Krobitsch and Lindquist, 2000; Muchowski et al., 2000). Equipped with specific information from experiments in yeast, many of these principles could later be recapitulated and validated in higher organisms (Gillis et al., 2013; Khurana and Lindquist, 2010; Kim et al., 2016).

Generally, *S. cerevisiae* offers a potent platform for biochemical and cell biological studies: generation times are sufficiently short to quickly progress with experimental procedures, its genome has been fully sequenced and annotated in detail and a versatile toolbox is available for genomic manipulation in order to generate gene knock outs and mutations (Goffeau et al., 1996; Xiao, 2014). Additionally, extensive data resources exist that enable the systematic analysis of cellular processes and phenotypes (Khurana and Lindquist, 2010).

Prions in yeast

The term *prion* is generally associated with the fatal neurodegenerative variant Creutzfeldt-Jakob Disease (vCJD) and bovine spongiform encephalopathy ('mad cow disease', BSE) that made the news in the 1980s and 1990s (Diack et al., 2014). vCJD patients developed signs of severe neurodegeneration, especially the formation of protein inclusions in the central nervous system, most likely after eating meat from cattle infected with BSE (Ward et al., 2006; Will et al., 1996). It was found that animals infected with BSE and related transmissible spongiform encephalopathies (e.g., scrapie in goats and sheep) equally showed extensive signs of neurodegeneration, characterized by the aggregation of a specific protein termed Prion Protein, PrP (Bolton et al., 1982; Jeffrey and Gonzales, 2004). Interestingly, when PrP aggregate-containing brain homogenates derived from cattle infected with BSE were injected into mice, previously soluble mouse PrP protein formed inclusions with similar aggregate signatures (Bruce et al., 1997; Hill et al., 1997).

Per definition, a prion is a proteinaceous infectious particle that – in contrast to other pathogens such as bacteria, fungi, parasites, viruses, and viroids – does not contain nucleic acid (Prusiner, 1982; 1997). One characteristic of a prion protein is its propensity to self-assemble into filamentous, amyloid prions with cross-β structure (Glynn et al., 2020; Serio, 2018; Sunde et al., 1997) (Figure 9). The initial conversion from the natively folded, soluble state to the aggregation-prone prion conformation is a stochastic process and for most prion proteins an extremely rare event (Cohen et al., 1994; Liebman and Chernoff, 2012). Once formed however, prions are able to impose this structure to any other soluble protein of its kind that it encounters, leading to amyloid fiber growth and triggering the rapid conversion

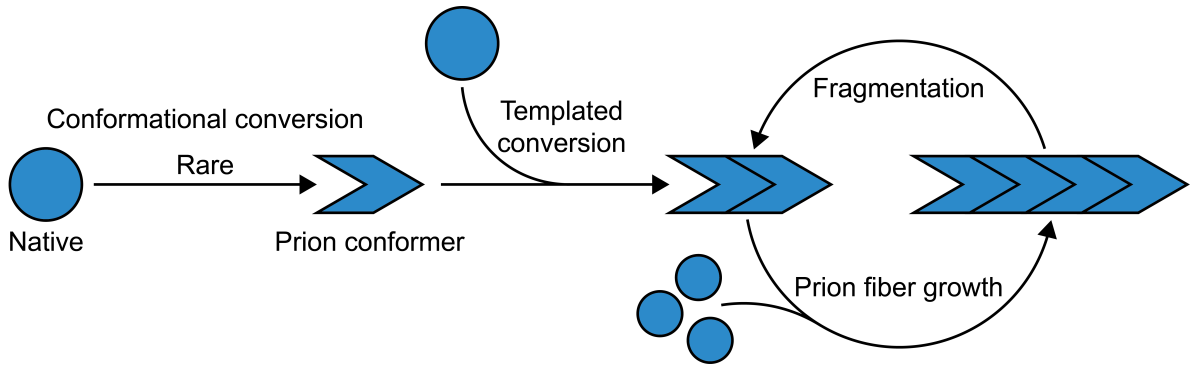

Figure 9: Formation and maintenance of prions. Prion proteins can exist in two distinct conformations, a native and an aggregation-prone prion conformation. Conformational conversion from the native to the prion conformer is a stochastic, rare event. Once a prion protein has adopted its prion conformation, it can impose this conformation on other native proteins of its kind and template their conversion. Association of aggregation-prone prion conformers and continuous conversion of native prion proteins leads to a growing prion fiber. These fibers can be fragmented by cellular chaperones leading to the generation of small prion seeds that exacerbate the prion phenotype and are important for prion inheritance.

of the whole protein population into prion aggregates (Satpute-Krishnan and Serio, 2005) (Figure 9). The second defining hallmark of prions is the fact that this prion state can be inherited by daughter cells during cell division or transferred to other cells in an organism in a non-mendelian fashion (Cox, 1994; Liebman and Chernoff, 2012; Tuite and Cox, 2003). In some cases – as described above for BSE and vCJD– the prion state can even be passed on across species.

In higher eukaryotes, such as humans, PrP is the only true prion protein identified to date. Many proteins have been designated as prion-like, based on the presence of specific aggregation-prone low complexity regions (LCRs), sequences with little diversity in amino acid composition and thus a lower propensity to form structured domains (Coletta et al., 2010; Kastano et al., 2021), or the ability to include soluble protein into preexisting aggregates, but these prion-like proteins most likely lack the ability to transmit these traits between individuals in a non-mendelian manner (Cascarina and Ross, 2014; Fraser, 2014; March et al., 2016). Interestingly, prions are a common phenomenon in yeast and many true prion proteins have been identified over the years (Liebman and Chernoff, 2012; Wickner et al., 2015). The most prominent example is the 43 kDa protein 'Rich in Arginine and Glutamine 1', Rnq1, whose function is – despite extensive research – still unknown (Sondheimer and Lindquist, 2000). Rnq1 prion formation is mediated by the protein's extensive prion domain, spanning almost 270 amino acids and containing three LCRs with a strong enrichment of glutamine,

asparagine, and glycine residues. Rnq1 has been identified as an important epigenetic factor in yeast: only in cells where Rnq1 forms amyloid prions (a state termed [*PIN*$^{+}$] for '[*PSI*] inducing'), not when it is in its soluble [*pin*$^{-}$] state, can other prions, such as the [*PSI*] prion formed by Sup35, spontaneously appear (Derkatch et al., 2000; Serio, 2018). How the presence of a preexisting prion favors the appearance of another is still under debate (Liebman and Chernoff, 2012; Osherovich and Weissman, 2002; Serio, 2018; Tuite and Cox, 2003) (Figure 10). It has been suggested that the presence of preexisting prions is necessary for cross-templating aggregation (Bradley et al., 2002; Derkatch et al., 2001; Derkatch et al., 2004; Vitrenko et al., 2007). Others propose that prions sequester the cell's proteostasis

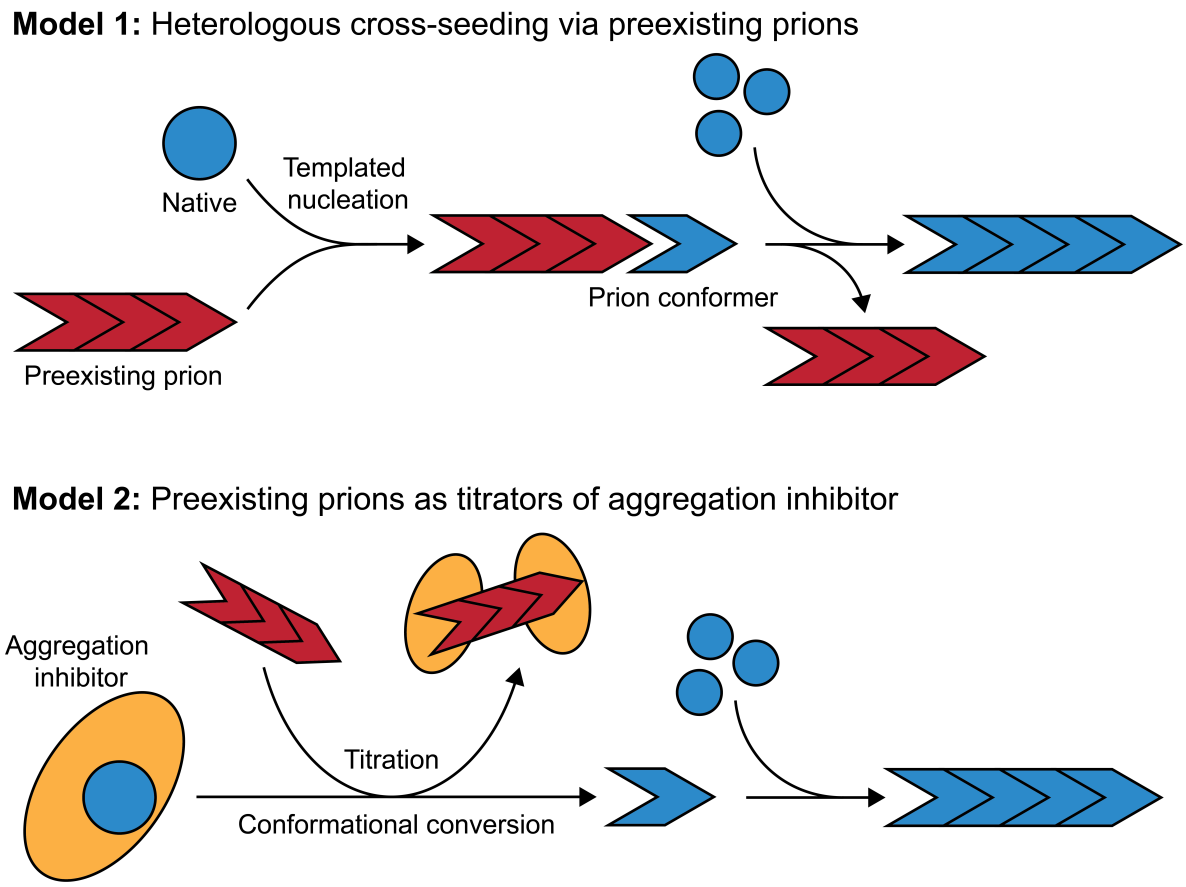

Figure 10: Proposed mechanisms of secondary prion appearance. Two proposed models explain the effect of preexisting prions on the *de novo* formation of other prions. In the heterologous cross-seeding model (model 1), preexisting prions act as heterologous nuclei that catalyze the conversion of another prion protein from its native to a prion conformation through direct templating. Once this prion protein has adopted a structure competent for prion formation, it can itself impose this structure onto other native proteins of its kind and allow the formation of new prion amyloids. The titration model (model 2) proposes that prion proteins are kept in a native conformation by binding to an aggregation inhibitor (e.g., chaperones). Sequestration of such factors by preexisting prion amyloids frees the prion proteins that can then undergo a conformational conversion from a native to a prion-competent conformer. Once such a nucleus has formed, it can convert other native proteins of its kind resulting in the formation of new prions.

capacity, thereby indirectly allowing aberrant misfolding events and downstream protein aggregation of proteins prone to misfolding (Douglas et al., 2008; Lopez et al., 2003; Osherovich and Weissman, 2001; Sondheimer et al., 2001).

In yeast, prions are dynamic structures despite their amyloid nature: while prions constantly grow through the conversion and addition of new proteins, the large amyloid fibrils are also continually sheared and broken down into smaller fragments by chaperones, most prominently the yeast disaggregase Hsp104 (Kushnirov and Ter-Avenesyan, 1998; Paushkin et al., 1996). In fact, this mechanism is crucial for the non-mendelian inheritance of prion phenotypes (Chernoff et al., 1995; Moriyama et al., 2000; Sondheimer and Lindquist, 2000). Small seeds generated by the fragmentation of large amyloid prion fibers are passed on to budding daughter cells and in turn lead to the conversion of soluble prion protein in this emerging cell (Liebman and Chernoff, 2012; Tuite and Cox, 2003). Consequently, transient inhibition or deletion of Hsp104 leads to the curing of many prions (Ferreira et al., 2001). A prion positive yeast strain can hereby be converted to a prion-free one within only a few generations as large amyloid fibrils are not broken down and cannot be passed on to the next generation (Wegrzyn et al., 2001).

The conversion of prion proteins from their soluble to the prion state can result in a loss of function (e.g., the [*PSI*] prion-forming protein Sup35 is a translation termination factor that cannot perform its function when assembled in prions, leading to increased stop codon read-through and nonsense mutation suppression) or gain of function (e.g., presence of the Rnq1 prion [*PIN*$^+$] enhances *de novo* formation of other prions) (Derkatch et al., 2000; Liebman and Chernoff, 2012; Paushkin et al., 1996; Serio, 2018). However, prion formation in yeast seems to be largely benign as no overt growth defect or toxicity has been observed for most prions under laboratory growth conditions. Hence, it has been hypothesized that the prion phenotype acts as evolutionary capacitator allowing cells to adapt to fluctuations in environmental conditions that they encounter much more frequently in nature than in a well-controlled laboratory (Halfmann et al., 2010; Shorter and Lindquist, 2005).

For our work, the prion phenomenon in yeast offers a great opportunity to investigate the influence of the cellular background on the aggregation of disease-relevant proteins such as polyQ-expanded Huntingtin exon 1. Interestingly, polyQ proteins form visible aggregates

only in the presence of Rnq1 prions in [*PIN*$^+$] but remain soluble in prion-free [*pin*$^-$] strains. (Duennwald et al., 2006a; Meriin et al., 2002; Osherovich and Weissman, 2001). Here, the influence of the conformation of one single protein seems to dictate the aggregation behavior of another, completely unrelated protein in otherwise isogenic cells.

Optogenetics

The ability to manipulate cellular processes such as gene expression, signaling, transport or migration is key in molecular biological research and a driver of new discoveries. Being able to tightly control expression of target genes can help inform about their cellular function and provide insight into the consequence of its absence. Targeted induction of signaling cascades enables the investigation of specific responses. Over recent decades, many tools have been invented to facilitate the researcher's ability to influence such processes. However, many of these tools also come with disadvantages. Some of these controllable systems require the use of chemical compounds that may have off-target effects.

In recent years, the emerging field of optogenetics has helped overcome many of these drawbacks while providing exquisite control over various cellular processes (Seong and Lin, 2021). In optogenetics, light responsive polypeptides such as photosensory domains from plants, algae or bacteria are coupled to effector proteins and utilized to allow the control of cellular process in other model organisms simply by the illumination with light (or the withdrawal thereof). The steadily growing toolbox of optogenetics includes dozens of photosensory proteins and domains that can be stimulated at discrete wavelengths ranging from infrared to ultraviolet light (Baumschlager and Khammash, 2021; Seong and Lin, 2021). The use of focused lasers and automated illumination periods allows for a high spatiotemporal accuracy of induction (Baumschlager and Khammash, 2021; Shin et al., 2017). The effects of light stimulation on these proteins varies. While for some of them light illumination simply leads to small conformational changes resulting in e.g., the opening or closing of a protein channel, others form defined protein-protein dimers or oligomers (Lu et al., 2020; Seong and Lin, 2021). Depending on the coupled effector protein, a diverse range of different cellular pathways can be regulated with light, ranging from transcriptional control to kinase signaling or targeted genome editing (Leopold et al., 2018; Nihongaki et al., 2017;

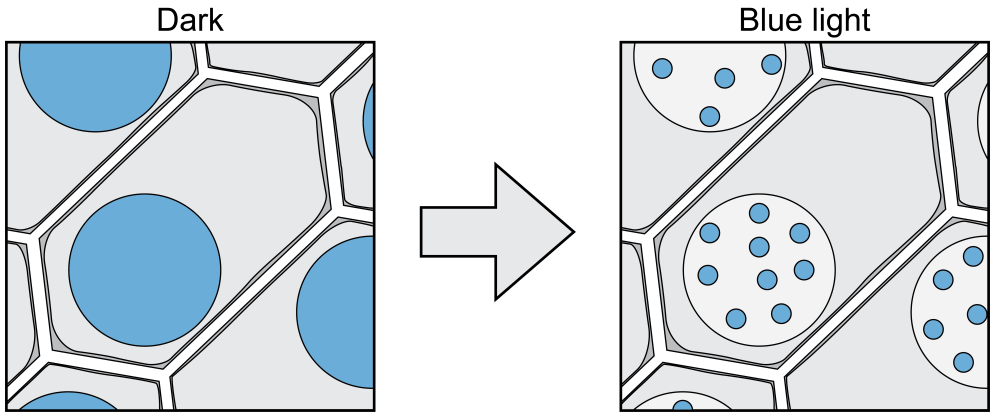

Figure 11: CRY2 forms homo-oligomers upon induction with blue light. CRY2 is soluble and diffusely distributed throughout the nucleus of *A. thaliana* cells when grown in the absence of light (left). Upon expose to blue light, CRY2 rapidly forms reversible homo-oligomeric protein clusters (right).

Polesskaya et al., 2018; Seong and Lin, 2021). Furthermore, light regulation does not only allow for a spatiotemporal regulation of these cellular processes, but – if used properly – does so without overt toxicity or harm for the respective model organism. As a result, optogenetics has become an important experimental means for exploratory research that can be applied in a wide range of different contexts and questions.

One prominent example that has found application in many different areas is the *Arabidopsis thaliana* photoreceptor protein Cryptochrome 2, CRY2 (Wang and Lin, 2020). CRY2 is a 70 kDa blue light-absorbing protein that forms transient homo-oligomeric protein clusters termed 'photobodies' in response to a blue light stimulus (wavelengths below 500 nm) (Ahmad, 2016; Mas et al., 2000) (Figure 11). In plants it is implicated in many cellular functions such as hypocotyl elongation, de-etiolation or entrainment of circadian rhythm via transcriptional regulation (Wang and Lin, 2020; Yu et al., 2010). Upon illumination with blue light, the flavine adenine dinucleotide (FAD) chromophore of CRY2 is reduced by electron transfer from a conserved triad of tryptophan residues, leading to conformational changes within the protein that result in homo-oligomer formation (Ma et al., 2020; Palayam et al., 2021). It is this unique characteristic that has been adopted for many optogenetic applications like endocytosis regulation, signaling, modulation of intracellular calcium levels or liquid-liquid phase separation in various different model organisms such as human cell culture, zebrafish or mice (Bugaj et al., 2013; Kyung et al., 2015; Shin et al., 2017; Taslimi et al., 2014).

Aims of This Study

Huntington's disease is a progressive neurological disorder, characterized by the presence of nuclear inclusions of polyQ-expanded Huntingtin protein in affected neurons in the brain of patients. Aggregation of mutant Huntingtin typically commences in neurons of the striatum and spreads throughout the brain as the disease progresses. In the yeast model *S. cerevisiae*, expression of a polyQ-expanded model protein on the basis of exon 1 of Huntingtin leads to the formation of insoluble inclusions only when the endogenous prion-forming protein Rnq1 is in its amyloid prion conformation. Just as in the mammalian system, these polyQ inclusions fail to robustly induce the cytosolic heat stress response even though they are highly interactive and sequester a broad range of cellular factors. In this work, we investigated how chaperones, aggregate morphology, and cellular background influence the aggregation and biological effects of polyQ in *S. cerevisiae* and how our findings translate to the disease condition in humans.

In the first chapter of this study, we aimed at obtaining insight into why inclusions of an expanded polyQ model protein do not lead to a robust induction of the cytosolic heat stress response (HSR) in yeast. Given the importance of proteostasis components – especially chaperones – in the process of HSR induction, we investigated whether the endogenous protein levels of any of these factors might be limiting for an efficient recognition of aberrant polyQ species and whether augmenting the expression levels of such a limiting factor would allow an efficient induction of the HSR by aggregated forms of polyQ. In the framework of this research question, we analyzed the importance of aggregate morphology and dynamics on the inducibility of the HSR and how they are modulated by cellular factors, such as chaperones.

In the second part of this study, we wanted to explore the influence of the cellular background, especially with regard to the presence or absence of the endogenous [*PIN*] yeast prion, on the aggregation of polyQ. In the context of this chapter, we also investigated the nature of the active polyQ species – whether it is soluble oligomers or large amyloid-like inclusion – responsible for biological effects such as heat stress response induction and toxicity, and how the cellular background modulates the formation of these active polyQ species.

Chapter I

The Hsp40 Sis1 Mediates the Stress Response to Protein Aggregation

Summary

The formation of protein aggregates in neurons in the brain is a hallmark of many neurodegenerative diseases, including Huntington's disease. Despite their toxic nature, sequestering many critical cellular proteins and proteostasis components, such as chaperones, disease-associated aggregates often times avoid recognition by the cell and fail to induce the HSR, although activation of the HSR could help reduce the burden of aberrant protein species and their detrimental impact. Similarly, expression and aggregation of a polyQ-expanded model protein on the basis of Huntingtin exon 1 does not elicit a productive HSR in the yeast *S. cerevisiae*.

Screening a library of proteostasis components, consisting of most of the yeast Hsp40s and Hsp70s, we found the Hsp40 chaperone Sis1 to be limiting for the activation of the HSR. Consistently, overexpression of *SIS1* but not other Hsp40s led to the induction of the HSR selectively by aggregated forms of expanded polyQ.

We demonstrated that overexpression of *SIS1* mediates changes in aggregate morphology, especially by enhanced formation of soluble polyQ oligomers that compose extended cloud-like condensates instead of typical dense polyQ inclusions. Analysis of the dynamic properties of these condensates revealed that while still static in nature, other cellular factors such as the Hsp70 Ssa1, were able to penetrate the condensates and interact with the polyQ oligomers. The changes in the physico-chemical properties of the polyQ aggregates thus led to an increased accumulation of Ssa1 in these condensates, possibly driving the release of Hsf1 from Ssa1 and consequently the activation of the HSR.

Using a mutationally destabilized variant of firefly luciferase, we further presented evidence that Sis1 also mediates the recognition of and HSR activation by heat-denatured protein aggregates. Therefore, our results demonstrate a more general role of Sis1 in promoting the ability of cells to recognize aberrant protein species and regulate the HSR in response to protein conformation stress. The human Sis1 homologue DNAJB6 similarly acts as a critical regulator of the HSR, highlighting the conservation of this mechanism even in higher eukaryotes.

Results

This work was part of a collaboration with Dr. Courtney Klaips and resulted in a publication in *Nature Communications* in 2020 (Klaips et al., 2020). In the following I will describe mainly the results of experiments I contributed to this study. Wherever necessary for coherence, other data are explained but not shown in detail. The reader may be referred to the original publication for the full scope of this work.

Length-dependent aggregation of polyQ in yeast

The polyQ length-dependent aggregation of model proteins has been demonstrated in yeast before (Krobitsch and Lindquist, 2000). In order to recapitulate these findings and lay the foundation for following experiments, we designed constructs containing Huntingtin exon 1 with either 20 glutamine residues (Htt20Q), a Q-length below the threshold for aggregation, or 97 glutamine residues (Htt97Q), shown to form inclusions when expressed in yeast (Gruber et al., 2018) (Figure 12A). These constructs also contained the polyQ-adjacent poly proline domain, allowing for expression without overt toxicity in yeast. The C-terminal fusion of the

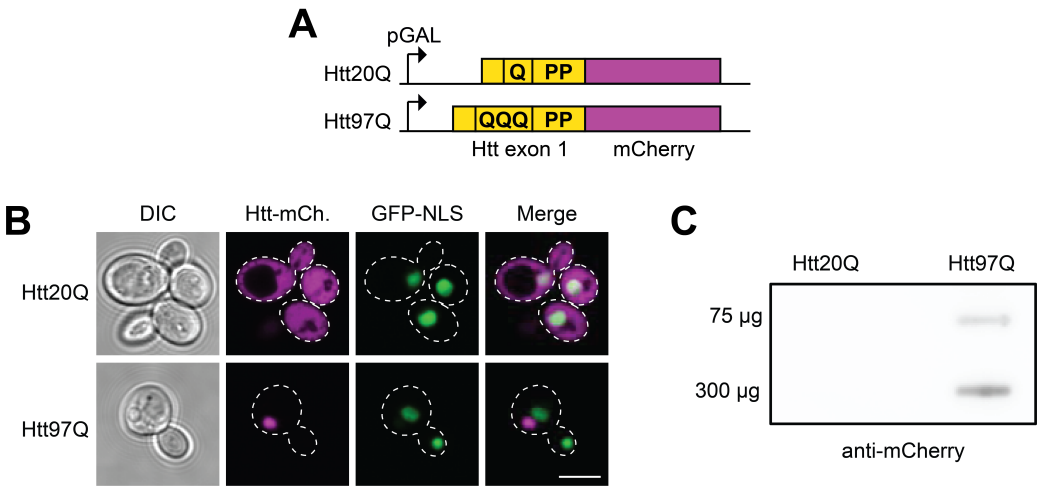

Figure 12: Aggregation of polyQ depends on Q-repeat length. (**A**) Schematic illustration of polyQ construct design. Huntingtin exon 1 with either 20Q (Htt20Q) or 97Q (Htt97Q), including the polyQ-adjacent proline-rich region (PP), was N-terminally fused to an mCherry fluorophore and expressed under the control of a galactose-inducible promoter (pGAL). (**B**) Htt97Q forms cytoplasmic inclusions. Representative confocal micrographs of [*PIN*$^+$] yeast cells expressing either Htt20Q or Htt97Q, grown in galactose-containing media for ~21 h. Cells were coexpressing *GFP-NLS* as nuclear marker. Experiments were performed in triplicate. Scale bar, 5 µm. (**C**) Htt97Q forms SDS-resistant inclusions. Cells expressing Htt20Q or Htt97Q were grown in galactose-containing media for ~21 h prior to harvest. Cell lysates were treated with SDS/DTT and subjected to filtration and subsequent immunodetection with anti-mCherry antibody. Representative result is shown from experiments performed in triplicate.

fluorescent protein mCherry allowed the detection and visualization of the proteins in cells via microscopy. When expressed from multicopy 2µ vectors under the control of the strong, galactose-inducible *GAL* promoter in Rnq1 prion containing [*PIN*$^{+}$] cells, Htt20Q remained diffusely distributed while Htt97Q formed single bright inclusions in cells (Figure 12B). These inclusions were partially SDS-resistant and could be retained on a filter membrane with a pore size of 0.2 µm (Figure 12C). Coexpression of the *GFP-NLS* nuclear marker indicated that while Htt20Q was located throughout the cytoplasm and nucleus, Htt97Q inclusions formed exclusively outside the nucleus (Figure 12B).

Sis1 enables stress response activation by polyQ aggregates

The presence of aberrant protein species is known to induce the HSR (Pincus, 2020). Thus, we investigated whether the inclusions formed by Htt97Q were able to trigger the HSR in affected cells. To test this, we employed a β-galactosidase (β-gal) reporter assay. Here, the enzyme β-galactosidase is expressed in cells under the control of a promoter containing stress-inducible heat shock elements (HSE). Any cellular stress that activates the HSR via the Hsf1 master regulator will also lead to an increase in the reporter activity and can be detected quantitatively through an enzymatic assay. Interestingly, the expression and aggregation of Htt97Q did not lead to a strong induction of the reporter, indicating no activated HSR in these cells compared to empty vector or Htt20Q controls (Figure 13A). The activation of the HSR through thermal stress (induced through growth at 37 °C) or overexpression of *HSF1* was not affected in cells expressing Htt97Q (Figure 13A). This argued that failure to induce the HSR by Htt97Q inclusions was not due to a general inability of these cells to induce such a response but suggested a lack of recognition of the Htt97Q aggregates by the cells themselves.

Molecular chaperones have been shown to modulate polyQ aggregation and toxicity and play a vital role in the regulation of the HSR (Kobayashi and Sobue, 2001; Muchowski et al., 2000; Pincus, 2020). Thus, we wondered whether the overexpression of individual chaperones could enable cells to detect and act upon Htt97Q inclusions. To test this, we overexpressed a library containing most of the known Hsp40 and Hsp70 chaperones in yeast, trying to identify potential candidates that showed an increased HSR upon coexpression of Htt97Q. Among the 50 tested candidates, only six (Sse1, Sis1, Xdj1, Ssz1, Sse2 and Ydj1) led

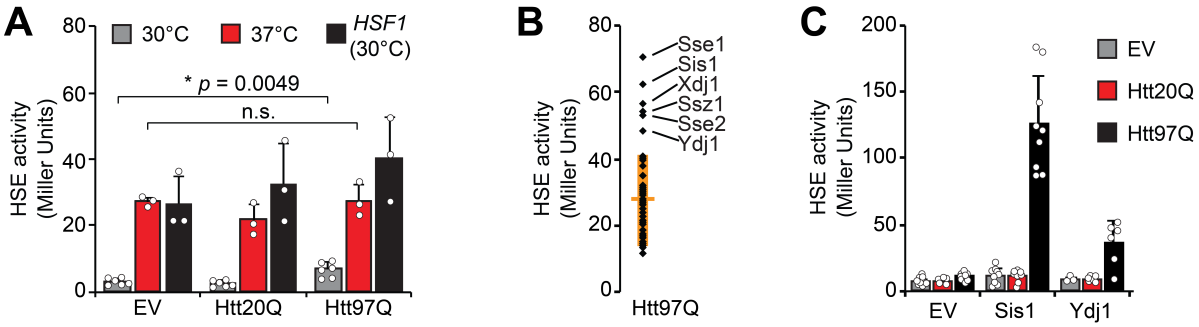

Figure 13: SIS1 overexpression enables heat stress response activation by aggregated polyQ. (**A**) Aggregated Htt97Q does not elicit a potent HSR. β-Galactosidase (β-Gal) activity was measured in cells expressing a LacZ reporter under the control of a minimal promoter containing a HSE from *SSA3* (pHSELacZ), coexpressing either an empty vector control, Htt20Q or Htt97Q. Cultures were grown in galactose-containing media at 30 °C for ~20 h. Cells were either maintained at 30 °C, shifted to 37 °C for 1 h or additionally expressed *HSF1*. HSE activity is reported in standard Miller Units. Data represent mean + SD from at least three independent experiments, *p*-values were calculated by unpaired, two-sided *t*-test. n.s., not statistically significant. (**B**) Screen for factors allowing HSR activation by Htt97Q. β-Gal activity is shown for pHSELacZ-containing cells expressing Htt97Q and coexpressing one of 50 yeast chaperones from 2µ plasmids under the control of a galactose-inducible promoter. Cultures were grown in galactose-containing media at 30 °C for ~21 h. Orange line is average HSE activity, orange bars are ± SD. Hits outside SD are annotated. (**C**) *SIS1* but not *YDJ1* overexpression allows HSR activation by Htt97Q. β-Gal activity is shown for pHSELacZ-containing cells overexpressing either an empty vector control, *SIS1* or *YDJ1* from the constitutive *GPD* promoter as well as an empty vector control, Htt20Q or Htt97Q. Cultures were grown in galactose-containing media at 30 °C for ~21 h. Data represent mean + SD from at least three independent experiments.

to a significant Htt97Q-dependent activation of the β-galactosidase reporter in this screen (Figure 13B). After validation of these hits in single, independent experiments, only the Hsp40 Sis1 remained as promising candidate. Indeed, when overexpressed along with Htt97Q, Sis1 led to a strong induction of the HSR, whereas another Hsp40, Ydj1, implicated in many processes related to misfolded proteins, only showed a weak effect (Figure 13C). The Sis1-dependent induction of the HSR relied on the formation of inclusions as only the expression of Htt97Q but not Htt20Q led to activity of the β-gal reporter (Figure 13C).

Sis1 affects physico-chemical aggregate properties

In order to understand how overexpression of *SIS1* confers cells with the ability to detect Htt97Q inclusions and induce the HSR, we analyzed the cellular aggregates via microscopy. Interestingly, while we observed mainly single bright inclusions at endogenous *SIS1* expression levels, co-overexpression of *SIS1* led to an altered aggregate morphology (Figure 14A). Htt97Q now formed cloud-like structures that, while still being mostly confined to the cytoplasm, expanded throughout large parts of the cell (Figure 14A).

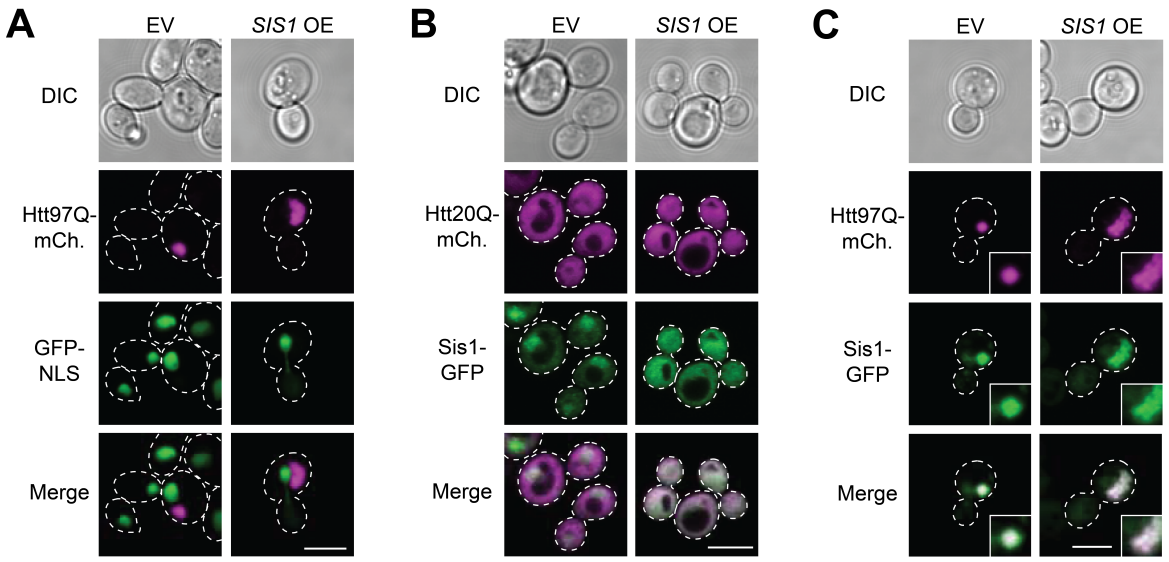

Figure 14: SIS1 overexpression changes polyQ aggregate morphology. (**A**) *SIS1* overexpression leads to the formation of cloud-like Htt97Q condensates. Representative confocal micrographs of yeast cells coexpressing Htt97Q and either an empty vector control or *SIS1*, along with *GFP-NLS*. Cultures were grown in galactose-containing media for ~21 h. Experiments were performed in triplicate. Scale bar, 5 µm. (**B**) Sis1 is found in nucleus and cytoplasm alike upon overexpression. Representative confocal micrographs of yeast cells expressing endogenously tagged *SIS1-GFP* along with Htt20Q. Cells additionally expressed an empty vector control or overexpressed *SIS1*. Cultures were grown in galactose-containing media for ~21 h. Experiments were performed in triplicate. Scale bar, 5 µm. (**C**) Sis1 localizes to Htt97Q inclusions and condensates. Representative confocal micrographs of yeast cells expressing endogenously tagged *SIS1-GFP* along with Htt97Q. Cells additionally expressed an empty vector control or overexpressed *SIS1*. Cultures were grown in galactose-containing media for ~21 h. Experiments were performed in triplicate. Scale bar, 5 µm.

To investigate whether Sis1 was directly involved in modulating aggregate morphology, we visualized Sis1 via expression of an endogenously tagged *SIS1-GFP* fusion protein. At endogenous expression levels coexpressing only the soluble Htt20Q, Sis1 was found throughout the cells but accumulated in the nucleus, in line with previous reports (Huh et al., 2003) (Figure 14B). Upon additional overexpression of *SIS1*, the Sis1-GFP signal was evenly distributed between nucleus and cytoplasm, indicating a saturation of the nucleus (Figure 14B). When coexpressing Htt97Q instead of Htt20Q, we observed the formation of dense inclusions or cloud-like condensates upon endogenous or additional overexpression of *SIS1*, respectively, as shown before (Figures 14C and A). Sis1-GFP colocalized with Htt97Q in both inclusions and condensates (Figure 14C). The sequestration of Sis1-GFP by the Htt97Q aggregates was very efficient as almost no residual Sis1 signal was detected in the rest of the cells, even under *SIS1* overexpression conditions (Figure 14C).

When we analyzed the density of Htt97Q aggregates via fluorescence analysis, we found that the cloud-like condensates, formed in the presence of *SIS1* overexpression, were

almost four times less dense than inclusions formed under endogenous Sis1 levels (Figure 15A). A complementary biochemical analysis further underlined this finding: Upon *SIS1* overexpression, the amount of Htt97Q retained in the pellet fraction after fractionation decreased and Htt97Q was almost exclusively soluble (≈ 90%) (Figure 15B). Analysis of these total and soluble fractions via semi-denaturating detergent agarose gel electrophoresis (SDD-AGE), a biochemical method to visualize protein oligomers, offered interesting insights. At endogenous Sis1 levels, Htt97Q not only formed large, SDS-insoluble inclusions (Figure 12C), but also oligomeric species (Figure 15C). These oligomers were mostly soluble as they also appeared in the soluble fraction (Figure 15C). At elevated Sis1 levels, the amount of soluble Htt97Q oligomers was strongly increased (Figure 15C), suggesting that Sis1 changed the physico-chemical properties of Htt97Q aggregates. These soluble oligomeric species appeared as cloud-like condensates on a macroscopic scale. In line with our microscopy results (Figure 14), the SDD-AGE analysis supported the idea of a direct interaction of Sis1 with Htt97Q oligomers, as they were comigrating on the gel (Figure 15C).

Given the increased solubility of Htt97Q aggregates upon *SIS1* overexpression, we were curious about the dynamic properties of these cloud-like condensates. In order to

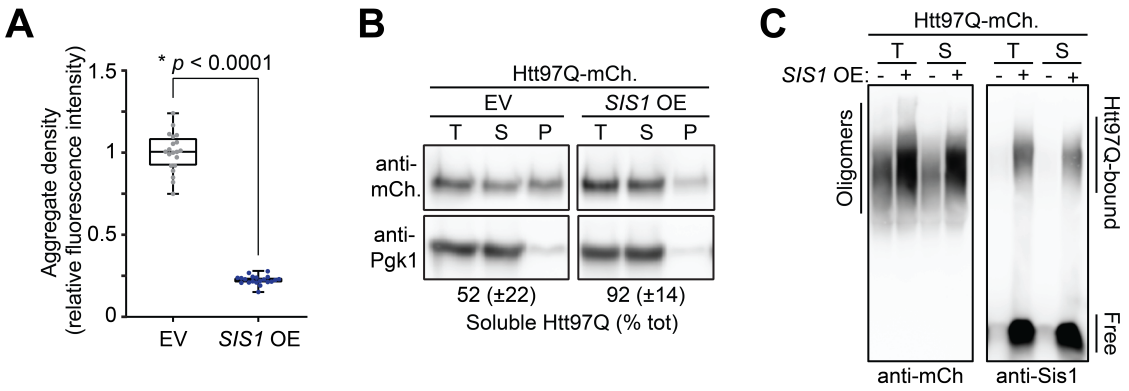

Figure 15: Sis1 affects physico-chemical characteristics of Htt97Q aggregates. (**A**) Htt97Q condensates are less dense than inclusions. The average fluorescence intensity of aggregates from Htt97Q expressing cells, coexpressing an empty vector control or overexpressing *SIS1* and grown in galactose-containing media for ~21 h was measured using confocal microscopy. Box plots represent median and 25th and 75th percentile, whiskers minimal and maximal values. *n* = 20 cells, *p*-value was calculated by unpaired, two-sided *t*-test. (**B**) Htt97Q condensates are more soluble than inclusions. Cell lysates of cells expressing Htt97Q and coexpressing either an empty vector control or overexpressing *SIS1*, grown in galactose-containing media for ~21 h, were subjected to fractionation (15'000 x g). Total lysate (T) as well as soluble (S) and pellet (P) fractions were analyzed by SDS-PAGE and immunoblotting for mCherry and Pgk1. Representative results are shown from experiments performed in triplicate. Blots were quantified by densitometry. Data represent mean ± SD. (**C**) Overexpression of *SIS1* leads to increase of soluble Htt97Q oligomers. Cells expressing Htt97Q and coexpressing either an empty vector control or overexpressing *SIS1* were grown in galactose-containing media for ~21 h. Cell lysates were fractionated and total lysate (T) and soluble fraction (S) were analyzed via SDD-AGE and immunoblotting for mCherry and Sis1. Representative results are shown from experiments performed in triplicate.

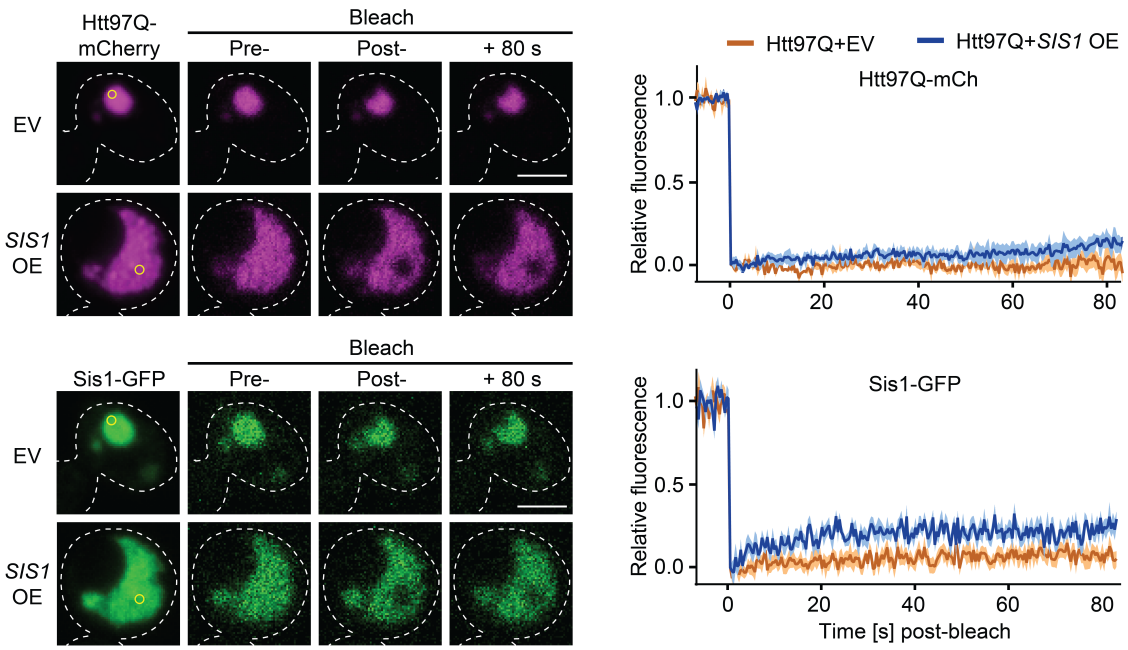

Figure 16: Htt97Q and Sis1 form static mesh. Cells expressing Htt97Q and endogenously tagged *SIS1-GFP* as well as coexpressing either an empty vector control or additionally overexpressing *SIS1* from a separate plasmid were grown in galactose-containing media for ~21 h. Htt97Q (top panel) or Sis1-GFP (bottom panel) were analyzed via fluorescent recovery after photobleaching (FRAP). Representative confocal images of cells before (pre) and after (post, +80 s) bleach are shown on the left from experiments performed at least three times. Yellow circle indicates region of interest. Scale bar, 2.5 µm. Graphs on the right depict mean ± SE relative fluorescence of region of interest over the course of 90 s.

evaluate the mobility of both Htt97Q as well as Sis1 within the aggregates, we performed fluorescence recovery after photobleaching (FRAP) experiments. When Htt97Q formed dense inclusions under endogenous Sis1 levels, both Htt97Q and Sis1 were immobile as no recovery of the bleached photo signal was detected even over an extended period of time (Figure 16). Interestingly, Htt97Q and Sis1 were also largely immobile in the cloud-like condensates formed upon *SIS1* overexpression (Figure 16). Thus, despite the increased solubility of these condensates, they did not seem to possess liquid-like properties but rather formed a static mesh-like structure, in line with their irregular shape.

Sis1 recruits Ssa1 to polyQ aggregates

Sis1 is a multidomain Hsp40 chaperone responsible for substrate recognition and binding, substrate transfer to an Hsp70 partner and the stimulation of the Hsp70 ATPase activity. We next assessed the influence of different Sis1 mutations and deletions on its ability to promote Htt97Q condensate formation. Deletion of the substrate-binding C-terminal domain as well

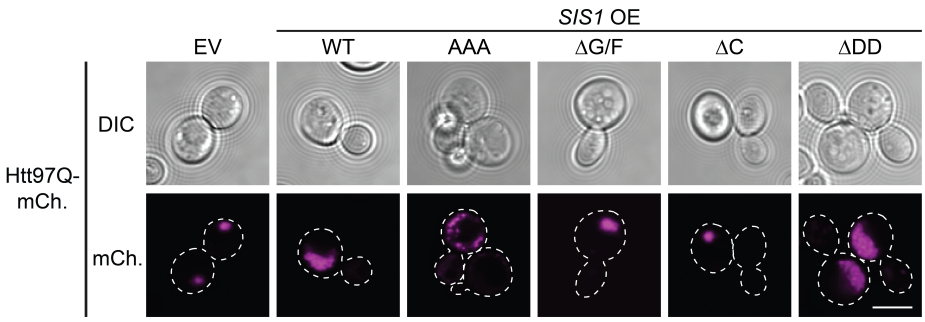

Figure 17: Formation of cloud-like Htt97Q condensates requires functional interaction of Sis1 with Hsp70. Representative confocal micrographs of yeast cells coexpressing Htt97Q and either an empty vector control, wild-type *SIS1* (WT) or a mutant form of *SIS1*. Cultures were grown in galactose-containing media for ~21 h. AAA, triple mutant converting the HPD motif into AAA; ΔG/F, deletion of the G/F domain (residues 77-121); ΔC, deletion of the C-terminus (residues 122-352); ΔDD, deletion of the dimerization domain (residues 339-352). Experiments were performed in triplicate. Scale bar, 5 µm.

as the G/F region – the function of which, while essential for cellular functions, remains to be fully characterized – led to the loss of the ability of Sis1 to form cloud-like Htt97Q condensates (Figure 17). Similarly, mutating the HPD motif of the J-domain required for stimulation of the Hsp70 ATPase activity, prevented the formation of Htt97Q condensates, instead leading to smaller, more dispersed aggregates (Figure 17). All three regions of Sis1 are required for either its interaction with substrate or the Hsp70 Ssa1, suggesting that Ssa1 participated in condensate formation. Concurrently, deletion of the Sis1 dimerization domain, not involved in interaction with substrate or Hsp70, preserved the ability of Sis1 to form cloud-like Htt97Q condensates (Figure 17). Interestingly, β-galactosidase reporter assays mirrored our microscopy results, as Htt97Q-dependent HSR induction was lost for the AAA, ΔG/F and ΔC mutants but retained for the ΔDD deletion (data not shown, see Klaips et al., 2020), suggesting that condensate formation and HSR induction were coupled.

We next analyzed the localization of Ssa1 via expression of *SSA1-GFP* and found that it localized to both the dense inclusions and the cloud-like condensates under endogenous or elevated Sis1 levels, respectively (Figure 18A). Interestingly, Ssa1 was mostly found on the surface of the dense Htt97Q inclusions formed at endogenous Sis1 levels, apparently unable to penetrate the aggregate core (Figure 18A). Conversely, Ssa1 could be found throughout the cloud-like Htt97Q condensates when *SIS1* was overexpressed, indicating that this less dense type of aggregate – even though static in nature – was permeable for cellular factors (Figure 18A). Earlier, we showed that both Htt97Q and Sis1 are immobile in the Htt97Q

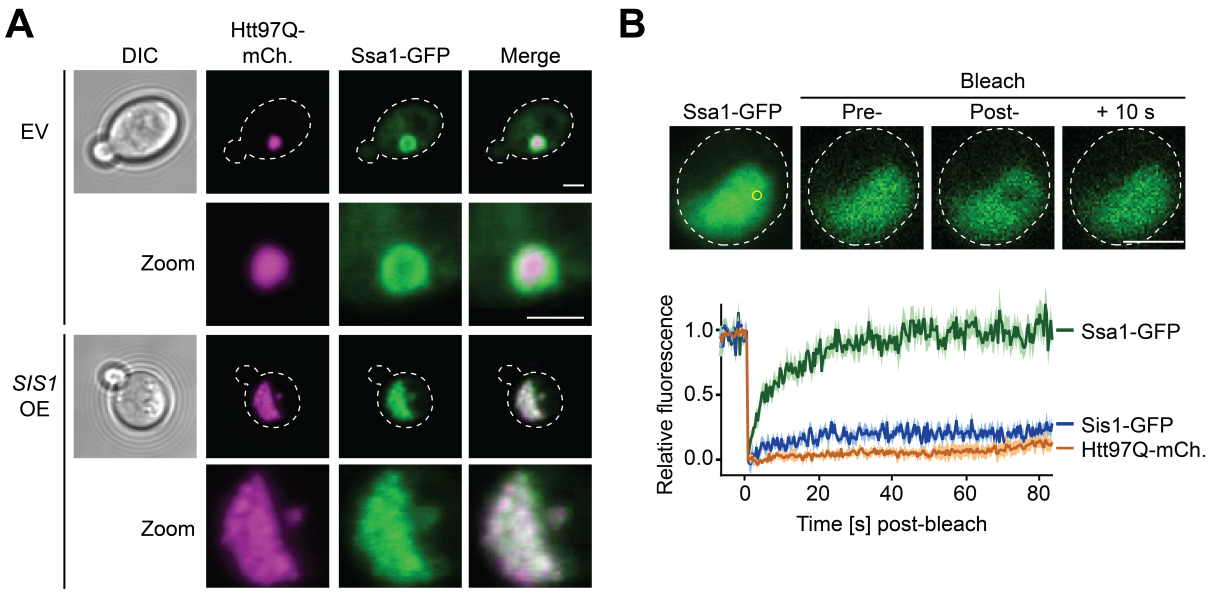

Figure 18: Ssa1 accumulates in Htt97Q condensates, forming a mobile phase. (**A**) Ssa1 can only penetrate Htt97Q condensates, not inclusions. Representative confocal micrographs of cells expressing Htt97Q and *SSA1-GFP* as well as coexpressing either an empty vector control or additionally overexpressing *SIS1*, grown in galactose-containing media for ~21 h. Experiments were performed in triplicate, scale bars, 2 µm. (**B**) Ssa1 forms mobile phase within Htt97Q condensates. Cells expressing Htt97Q and *SSA1-GFP* and additionally overexpressing *SIS1* from a separate plasmid were grown in galactose-containing media for ~21 h. Dynamics of Ssa1-GFP were analyzed via FRAP. Representative confocal micrographs of cells before (pre) and after (post, +80 s) bleach are shown on top from experiments performed at least three times. Yellow circle indicates region of interest. Scale bar, 2.5 µm. Graph below depicts mean ± SE relative fluorescence of region of interest over the course of 90 s. FRAP traces of Sis1-GFP and Htt97Q-mCherry from Figure 16 shown as references.

condensates. Finding Ssa1 to localize to the same aggregates, we investigated its dynamics via FRAP analysis as well. Surprisingly, the Ssa1 signal recovered rapidly after photobleaching ($t_{1/2}$ ~ 6s) (Figure 18B). Thus, Ssa1 seemed to be able to move through the mesh formed by Htt97Q and Sis1, interacting with both proteins.

Taken together, the altered Htt97Q aggregate morphology and composition upon overexpression of *SIS1* makes the aggregates accessible for Ssa1 and possibly allows for an effective titration of Ssa1 from Hsf1, thereby activating the HSR. Under endogenous Sis1 expression conditions, when Htt97Q forms dense, impenetrable inclusions, Ssa1 cannot be efficiently recruited to these aggregates and their presence does not lead to an induction of the HSR.

Sis1-Ssa1 interaction is important for HSR activation by heat-denatured proteins

Finally, we were wondering whether the role of Sis1 in recognizing disease-associated aggregates was a general phenomenon that was also important for the recognition of more 'physiological' protein aggregates, such as those formed upon thermal stress. Upon incubation of cells at elevated temperatures, both Sis1 and Ssa1 accumulated in distinct foci in the cytoplasm as well as the nucleus (Figure 19A), suggesting that these chaperones also cooperate under thermal heat stress conditions to identify aberrant protein species.

To test this possibility, we expressed a model protein based on conformationally destabilized firefly luciferase (FlucDM). This protein, containing two point mutations, is structurally labile and only stably folded under non-stress conditions. Elevated temperatures lead to the rapid un- and misfolding of this protein and the formation of protein aggregates (Gupta et al., 2011). When we analyzed the localization of Sis1 under thermal stress conditions in cells expressing the luciferase model protein, we made similar observations as described above for polyQ-expressing cells. At endogenous Sis1 levels, luciferase formed small aggregates in the cytoplasm and nucleus that were also bound by Sis1 (Figure 19B). Upon overexpression of *SIS1*, FlucDM accumulated into fuzzier, expanded aggregates, similarly binding Sis1 (Figure 19B). Both types of aggregates also interacted with Ssa1 (Figure 19C). However, just as for the dense polyQ inclusions, Ssa1 could not fully penetrate all luciferase aggregates that were formed under endogenous Sis1 expression levels (Figure 19C). Only upon overexpression of *SIS1* and remodeling of the luciferase aggregates did we observe efficient colocalization of Ssa1 with FlucDM (Figure 19C). When we quantitatively assessed the amount of Ssa1 colocalizing with aggregates compared to unbound, free Ssa1, we found that *SIS1* overexpression led to a three-fold increase in the amount of Ssa1 that was bound by aggregated luciferase (Figures 19C and D). Consistent with our observations for polyQ inclusions, overexpression of *SIS1* also enhanced the HSR induction caused by expression and misfolding of FlucDM at elevated temperatures (Figure 19E).

These findings support the notion that the interplay of Sis1 and Ssa1 is also important for the recognition of protein aggregates induced by thermal stress. Therefore, the central role that Sis1 plays in recognizing polyQ aggregates and inducing the HSR in response appears to be a generally conserved principle in the detection of aberrant protein species.

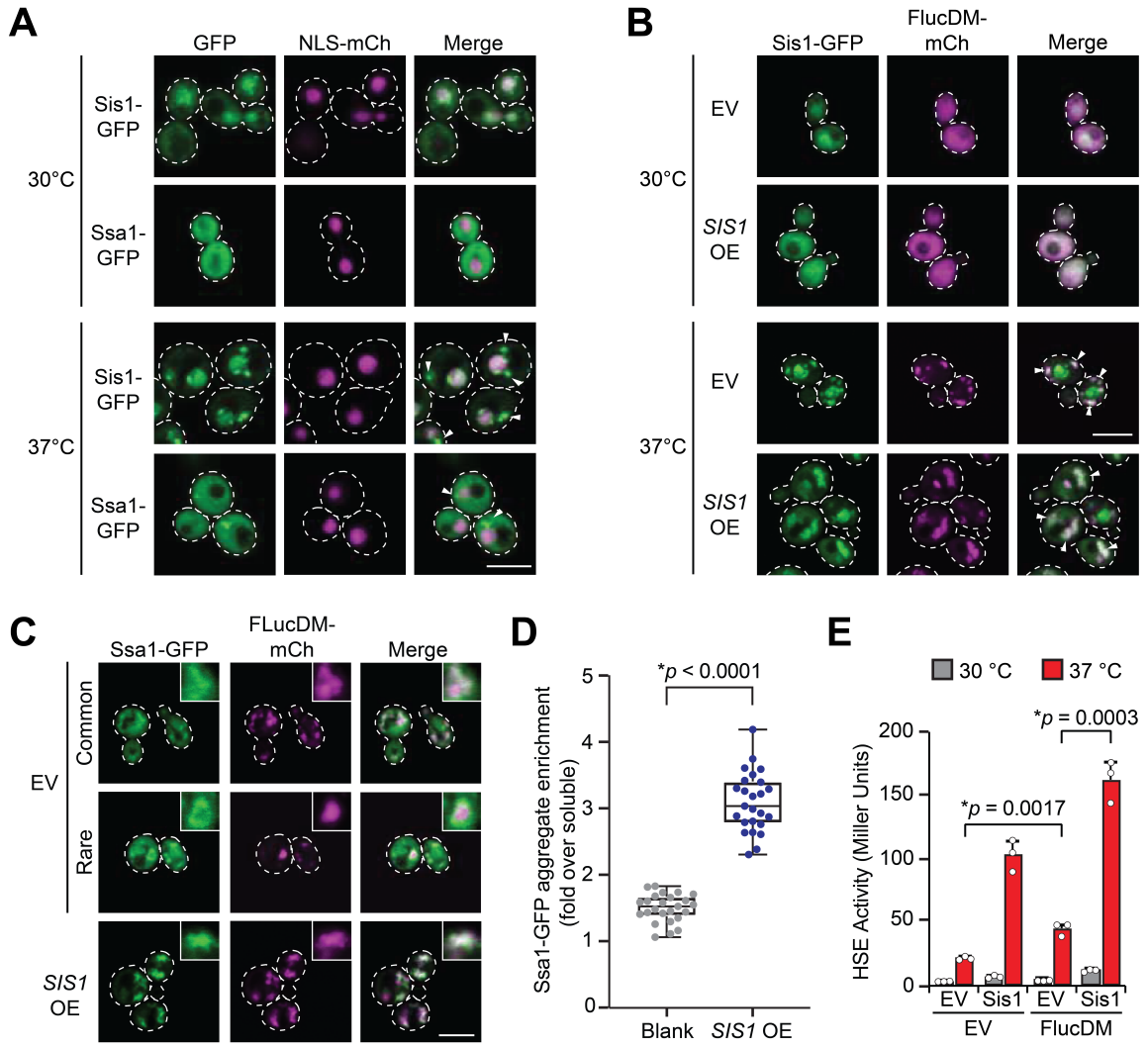

Figure 19: Sis1-Ssa1 interaction is important for HSR activation by heat-denatured proteins. (**A**) Sis1 and Ssa1 localize to foci upon heat shock. Representative confocal micrographs of yeast cells expressing either endogenously GFP-tagged *SIS1* or *SSA1-GFP* from an endogenous locus, grown at 30 °C. Cells were either maintained at 30 °C prior to imaging (top) or shifted to 37 °C for 1 h (bottom). Cells were coexpressing *NLS-mCherry* as nuclear marker. Experiments were performed in triplicate. White arrows indicate foci. Scale bar, 5 µm. (**B**) Sis1 localizes to heat-induced protein aggregates. Representative confocal micrographs of yeast cells expressing endogenously GFP-tagged *SIS1* and mCherry-tagged double mutant firefly luciferase (FlucDM-mCh). Cells were coexpressing either an empty vector control or additionally overexpressing *SIS1* from a separate plasmid. Cells were grown at 30 °C and either maintained at 30 °C (top) or shifted to 37 °C for 1 h (bottom) prior to imaging. Experiments were performed in triplicate. White arrows indicate colocalization. Scale bar, 5 µm. (**C**) *SIS1* overexpression increases recruitment of Ssa1 to heat-induced protein aggregates. Representative confocal micrographs of yeast cells expressing *SSA1-GFP* from an endogenous locus along with FlucDM-mCh. Cells were additionally coexpressing either an empty vector control or overexpressing *SIS1*. Cells were grown at 30 °C and shifted to 37 °C for 1 h prior to imaging. For the empty vector control, common and rare aggregation events are shown. Boxes show magnification of selected aggregates. Scale bar, 5 µm. (**D**) Ssa1-GFP enrichment within aggregates versus the rest of the cell in (C) were quantified via fluorescence. Box plots represent median and 25th and 75th percentile, whiskers minimal and maximal values. *n* = 25 cells, *p*-value was calculated by unpaired, two-sided *t*-test. (**E**) FlucDM-induced stress response is enhanced by Sis1. pHSELacZ reporter cells, expressing either empty vector (EV) or FlucDM-mCh (FlucDM) and coexpressing either empty vector (EV) or *SIS1* (Sis1) were grown in galactose-containing media at 30 °C for ~20 h. Cells were either maintained at 30 °C or shifted to 37 °C for 1 h prior to measurement of β-gal activity. Data represent mean + SD from at least three independent experiments, *p*-values were calculated by unpaired, two-sided *t*-test.

Discussion

Deposition of large amyloid-like aggregates is a hallmark of many diseases, including neurodegenerative disorders such as Alzheimer's, Parkinson's and Huntingtin's diseases (Chiti and Dobson, 2006; Ross and Poirier, 2004; Stefani and Dobson, 2003). These aggregates have been shown to be highly interactive and sequester a wide range of cellular proteins, thus contributing to disease (Hartl, 2017; Valastyan and Lindquist, 2014). However, despite their highly toxic nature, disease-associated protein aggregates often fail to induce defensive stress responses in affected cells (Gomez-Pastor et al., 2017; Olzscha et al., 2011; San Gil et al., 2020), although stress response pathways, when activated, have been shown to effectively ameliorate harmful aggregate effects (Balch et al., 2008; Fujimoto et al., 2005; Gomez-Pastor et al., 2018; Maheshwari et al., 2014; Neef et al., 2011).

In this study, we investigated this phenomenon in the model organism *S. cerevisiae*, expressing polyQ-expanded model proteins on the basis of Huntingtin exon 1. We confirmed that the presence of large polyQ inclusions did not elicit the cytosolic heat stress response. Screening a library of yeast chaperones identified the Hsp40 Sis1 as a key regulator for the induction of the HSR by aggregated polyQ. Overexpression of *SIS1* led to the formation of enlarged, less dense, cloud-like condensates instead of the densely packed inclusions observed at endogenous Sis1 levels (Figures 20A and B). These condensates were built of a static mesh of Sis1 and polyQ oligomers that increased the permeability of the aggregate for other cellular components such as the Hsp70 Ssa1, which could move freely through this structure. The increased capacity of these remodeled condensates to sequester Ssa1 in turn led to the induction of the HSR response, most likely by titrating away Ssa1 from Hsf1 (Figure 20B). Domain deletion experiments of Sis1 further underlined this dual function in substrate recognition and HSR induction: mutation of the J-domain HPD motif, deletion of the G/F region as well as deletion of the C-terminal domain all independently prevented polyQ condensate formation and HSR induction alike.

Interestingly, the observed mechanism of aggregate recognition and remodeling by Sis1 was not exclusive to polyQ but could also be observed for aberrant protein species appearing upon thermal stress. Luciferase aggregates, formed at elevated temperatures, were not only bound by Sis1 and directed into larger condensates upon *SIS1* overexpression,

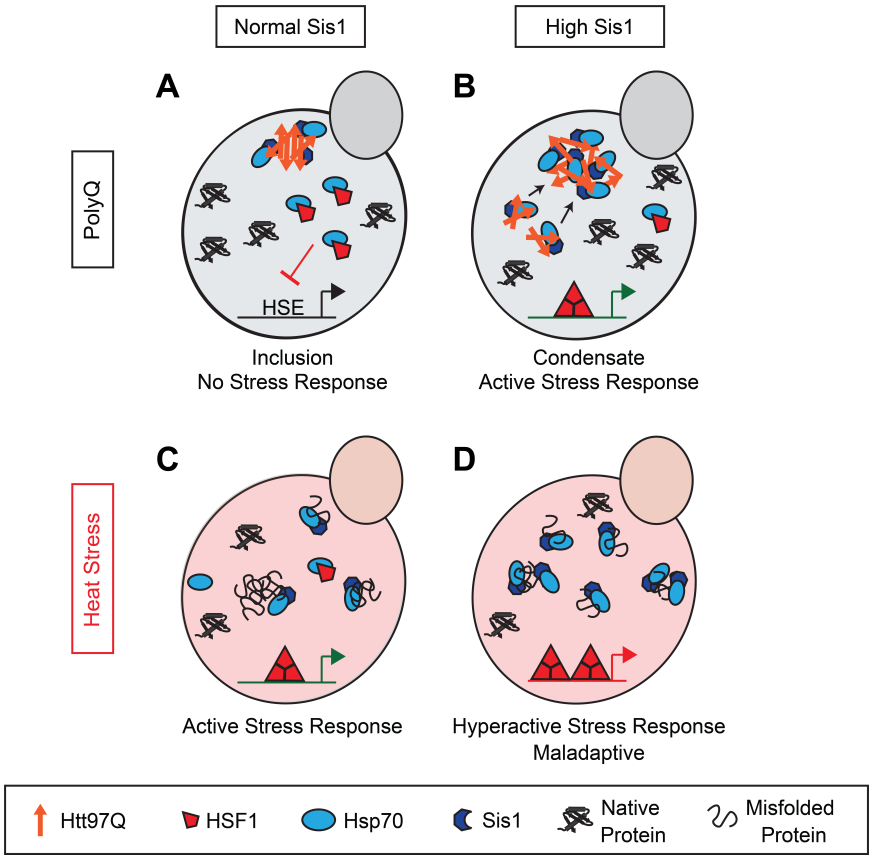

Figure 20: Model. (**A**) Under endogenous Sis1 levels, Htt97Q forms dense inclusions that are inaccessible for Ssa1. Hsf1 remains bound by Ssa1 and cannot induce the HSR. (**B**) At higher Sis1 levels, Sis1 interacts with soluble Htt97Q oligomers, forming cloud-like condensates that are permeable for Ssa1. Ssa1 accumulates in these condensates and is titrated away from Hsf1. Hsf1 is released and can activate the HSR by binding to HSEs. (**C**) Under endogenous Sis1 levels, heat stress leads to the accumulation of aberrant protein species. Sis1 recruits Ssa1 to these proteins, in turn freeing Hsf1 and allowing for an appropriate induction of the HSR. (**D**) At elevated Sis1 levels, higher amounts of Ssa1 are recruited to heat-denatured proteins, resulting in a hyperactive, maladapted HSR.

but they were also able to sequester larger amounts of Hsp70, thereby amplifying the HSR (Figures 20C and D). This argued for a general role of Sis1 in sensing aberrant protein species.

Given the beneficial effect of elevated Sis1 levels on the sensitivity of the HSR not only to heat-induced protein aggregates but also disease-associated inclusions, the question arises why cells are limiting the amounts of available Sis1, thereby risking potential harm from toxic protein aggregation. Further experiments in the context of this project suggested that a permanently elevated level of Sis1 results in a maladapted HSR. Overexpression of *SIS1* caused hypersensitivity towards even mild stress conditions resulting in an overshooting cellular response and the consumption of valuable cellular energy and chemical resources. It also led to a longer lasting stress response unable to be shut off efficiently by the cells once

activated. Our experiments demonstrated the importance of a fine-tuned HSR for the survival of cells encountering proteotoxic stress. While elevated levels of Sis1 are beneficial to recognize and deal with disease-associated protein aggregates, they can also lead to a maladapted stress response that renders cells incapable of a sensitive and dynamic response to stress. Thus, stress responses appear to have been optimized in evolution to allow cells to maintain a fine balance between these two extremes.

The function of Sis1 in regulating the HSR is conserved in mammalian cells. We found that the human Sis1 homolog DNAJB6 is critical for an efficient induction of the HSR by protein conformational stress caused by elevated temperatures and that increasing the levels of DNAJB6 amplifies this response (data not shown here, see Klaips et al., 2020). However, similar to the yeast system, levels of DNAJB6 are tightly controlled. While multiple studies found that elevated levels of DNAJB6 can prevent disease-associated protein aggregation (Gillis et al., 2013; Hageman et al., 2010; Kakkar et al., 2016), an excess of DNAJB6 has also been implicated in causing toxicity in primary neurons (Smith and D'Mello, 2016), highlighting the conservation of the importance of a balanced proteostasis network for cellular health.

Our results not only offer new mechanistic insights into the cellular recognition of aberrant protein species and efficient induction of stress response pathways but also underline the importance of a fine-tuned proteostasis system in this process. Furthermore, the findings presented here also help to outline possible strategies for pharmacological intervention with protein misfolding diseases. While a permanent elevation of proteostasis factors such as Sis1 or DNAJB6 can potentially be problematic, intermittently boosting their expression might allow specific recognition of disease-associated protein aggregates and temporal activation of the HSR to promote disease amelioration without detrimental side effects.

Chapter II

Formation of Toxic Oligomers of PolyQ-Expanded Huntingtin by Prion-Mediated Cross-Seeding

Summary

Selective cellular vulnerability is a well-known phenomenon in neurodegenerative diseases. Despite their ubiquitous expression, disease-associated proteins such as Huntingtin initially form aggregates only in a subset of neurons, revealing an underlying influence of the cellular background on pathological protein aggregation. A similar phenomenon can be observed in the yeast model *S. cerevisiae*, where the aggregation of expanded polyQ is influenced by the prion status of the strain background. PolyQ forms detergent-resistant inclusions only if the yeast prion-forming protein Rnq1 is in its prion conformation ([*PIN*$^+$]) but remains soluble if the yeast strain is cured of the Rnq1 prion ([*pin*$^-$]).

In this section of the work, we designed an optogenetic tool by coupling the photoreceptor protein CRY2 from *A. thaliana* with polyQ-expanded Huntingtin exon 1 variants, allowing us to induce polyQ aggregation even in the non-permissive [*pin*$^-$] yeast strain background by illumination with blue light. Being able to directly compare aggregation of polyQ in both [*PIN*$^+$] and [*pin*$^-$] strains for the first time enabled us to investigate influences of the cellular background on the aggregation process itself as well as the ability of polyQ aggregates to induce cellular responses such as activation of the HSR or toxic effects.

Proteomic and functional analyses revealed no evidence of general proteostasis impairment of [*PIN*$^+$] cells, arguing for a direct effect of the Rnq1 prion on the aggregation of polyQ. Artificially inducing aggregation of polyQ in [*pin*$^-$] with our optogenetic tool, we found that the presence of large SDS-insoluble inclusions was not sufficient to induce biological outcomes in this strain background. Rather, our results suggested that soluble oligomeric assemblies of polyQ are the actual bioactive species and that these oligomers only form in the presence of preexisting prions in [*PIN*$^+$]. Mass spectrometric experiments and *in vitro* reconstitution confirmed that early transient interactions of soluble polyQ with Rnq1 prions cross-seed aggregation of polyQ and lead to the formation of soluble oligomeric species responsible for HSR induction and toxicity.

The fact that prion-like proteins have also been identified to interact with soluble polyQ species in mammalian cells offers the intriguing hypothesis that the age-dependent accumulation of prion-like aggregates in the human brain may catalyze the aggregation of disease-relevant proteins ultimately causing neurodegenerative phenotypes.

Results

Work described in this chapter was published in *Molecular Cell* in October 2022 (Gropp et al., 2022).

Rnq1 prion status influences aggregation of expanded polyQ

We began our investigation by curing a prion positive [*PIN*$^+$] yeast strain via GdnHCl treatment to transiently inhibit Hsp104. The resulting prion-free [*pin*$^-$] strain is isogenic to its [*PIN*$^+$] parent and only differs in the aggregation status of the Rnq1 protein. We confirmed the prion status of the two yeast strains through expression of *RNQ1-GFP*. As expected, Rnq1-GFP formed distinct foci in the [*PIN*$^+$] strain, while it remained soluble and diffusely distributed throughout [*pin*$^-$] cells (Figure 21A).

To establish the dependence of polyQ aggregation on the prion status of the yeast strain background, we expressed a fluorescently tagged model protein based on Huntingtin exon 1 containing a disease-associated 97 Q expansion in its poly glutamine tract (97Q). 20Q, a glutamine repeat length below the threshold for aggregation, served as control. While we observed visible 97Q inclusions in the cytosol of the [*PIN*$^+$] strain, 97Q remained soluble in the majority of [*pin*$^-$] cells (Figure 21B), as previously reported (Duennwald et al., 2006a; Meriin et al., 2002; Osherovich and Weissman, 2001). 20Q was diffusely distributed throughout the cells in both strain backgrounds (Figure 21B).

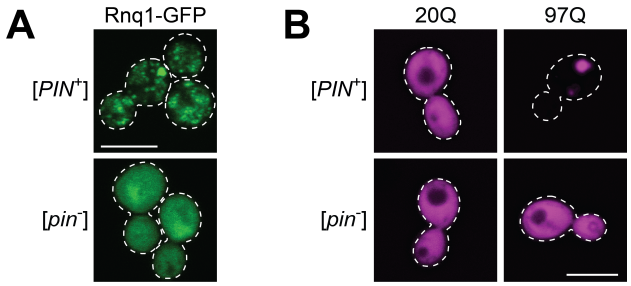

Figure 21: Rnq1 prion status influences aggregation of expanded polyQ. (**A**) GdnHCl treatment cures [*PIN*$^+$] phenotype. Representative confocal micrographs of [*PIN*$^+$] and GdnHCl-treated [*pin*$^-$] yeast cells expressing a *RNQ1-GFP* reporter. Experiments were performed in triplicate. Scale bar, 5 µm. (**B**) 97Q aggregation is dependent on [*PIN*] prion background. Representative confocal micrographs of [*PIN*$^+$] and [*pin*$^-$] yeast cells expressing either 20Q or 97Q. Experiments were performed in triplicate. Scale bar, 5 µm.

Rnq1 prion status does not detectably impair proteostasis

To investigate the influence of the yeast prion status on the aggregation of other, unrelated proteins such as polyQ, we first analyzed whether there were intrinsic distinctions between isogenic [*PIN*$^+$] and [*pin*$^-$] strains (Figure 22A). Total proteome analysis, based on the quantification of 3478 proteins by mass spectrometry, revealed only few proteins significantly enriched (> 1.5-fold; $p < 0.05$) in either condition with no GO Term correlation for any biological processes relevant for aggregation modulation, suggesting that there were no global proteome differences between the two strains (Figures 22A, left and B).

The presence of prions in yeast has been reported to limit the availability of cellular factors, especially proteostasis components, by sequestration (Douglas et al., 2008; Lopez et al., 2003; Osherovich and Weissman, 2001; Sondheimer et al., 2001). Titration of such regulatory factors that normally function as modulators of aggregation could influence the process of polyQ aggregate formation. To identify potential proteins that are bound by Rnq1 in its aggregated, amyloid form in [*PIN*$^+$] cells, we performed an immunoprecipitation (IP) experiment against Rnq1-GFP from respective yeast cells followed by mass spectrometric analysis of bound interactors (Figure 22A, right). As a reference, we performed the same IP against Rnq1-GFP in its soluble state in [*pin*$^-$] cells. Rnq1-GFP was highly interactive and bound a plethora of cellular factors in its prion conformation compared to its soluble form (Figure 22C). A GO Term enrichment analysis of interactors (> 1.5-fold enrichment; $p < 0.05$) in the [*PIN*$^+$] condition showed many factors involved in cytoskeleton organization or nuclear transport (Figure 22D).

The top hits of interactors preferentially bound by Rnq1-GFP in its aggregated state, were enriched for prion(-like) proteins (Figure 22E). Such proteins possess low complexity regions, often rich in asparagine and glutamine residues, and have been shown to be sequestered by amyloid aggregates (Olzscha et al., 2011; Park et al., 2013). However, most of these proteins have not been associated with a function in modulating aggregation. Factors that could potentially play such a role are members of the proteostasis network, especially chaperones. While we did not observe any highly significant correlation in this regard among interactors of Rnq1-GFP in [*PIN*$^+$] (Figure 22D), we found many individual proteostasis components among those interactors. Most prominently, Rnq1-GFP bound several members of the Hsp70 chaperone family (Ssa1, Ssa2, Ssa3) as well as the essential Hsp40 Sis1

(Figure 22F), known to be involved in proteostatic pathways such as protein degradation and stress response induction (see Chapter I; Klaips et al., 2020; Park et al., 2013).

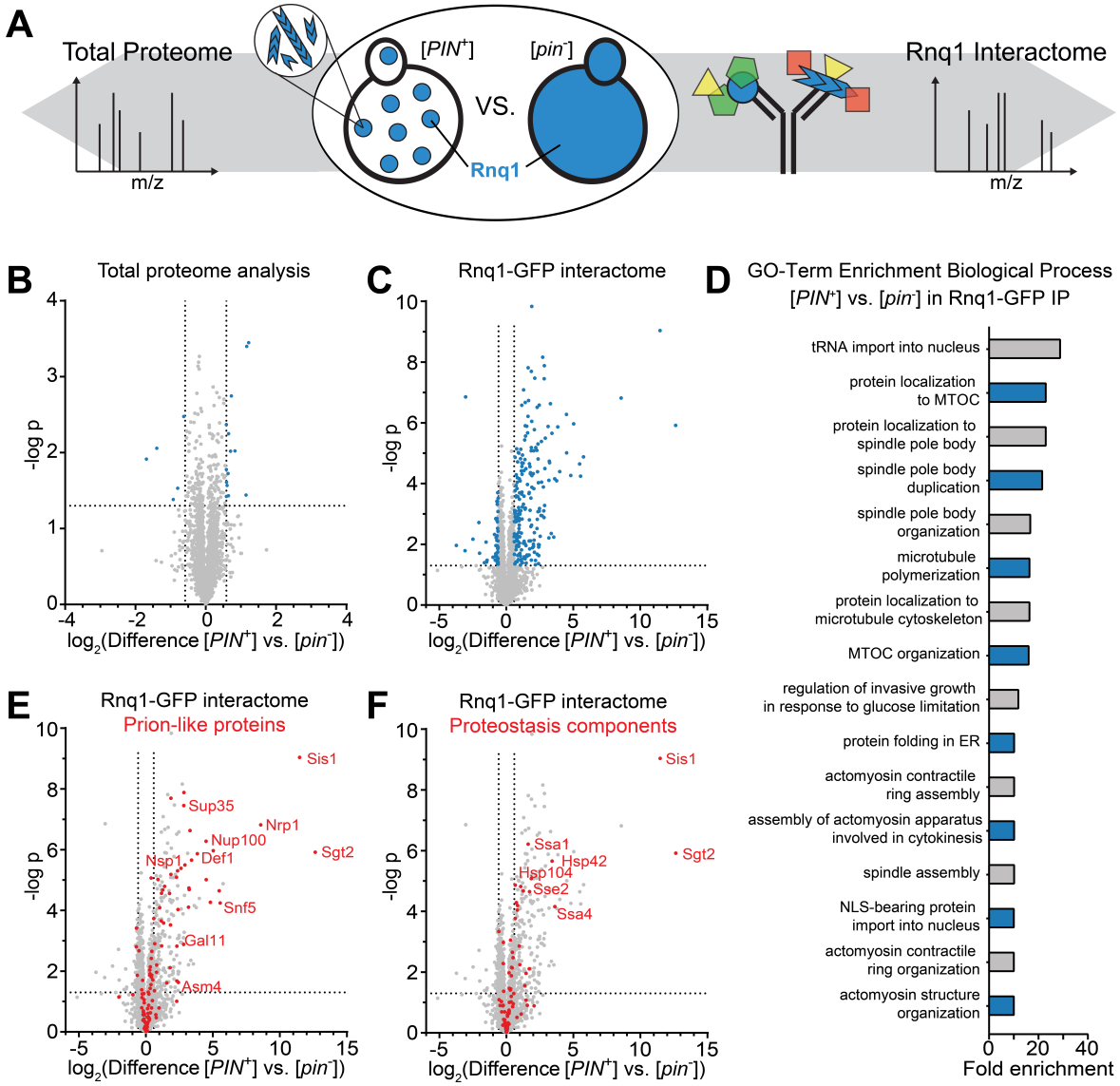

Figure 22: Rnq1 prions sequester prion-like proteins and proteostasis components. (**A**) Schematic representation of mass spectrometry experiments. [*PIN*$^+$] and [*pin*$^-$] yeast cells were compared directly with regard to total proteome differences (left) or after IP to identify specific interactors of Rnq1 (right). (**B**) Proteomes of [*PIN*$^+$] and [*pin*$^-$] cells are similar. Volcano plot representation of label-free total proteome analysis of [*PIN*$^+$] versus [*pin*$^-$] cells from four independent experiments. Significantly enriched proteins (> 1.5-fold enrichment, $p < 0.05$) are marked in blue. (**C**) Rnq1-GFP is highly interactive in its prion state. Volcano plot representation of label-free interactome analysis of Rnq1-GFP in [*PIN*$^+$] versus [*pin*$^-$] after anti-GFP IP from four independent experiments. Significant interactors (> 1.5-fold enrichment, $p < 0.05$) are marked in blue. (**D**) GO-Term enrichment analysis for *Biological Process* of interactors of Rnq1-GFP in [*PIN*$^+$] condition in (C). Enrichment of GO-Terms with a significance of $p < 0.05$ are shown. (**E**) Prion-like proteins are bound by Rnq1-GFP in [*PIN*$^+$]. Volcano plot representation from (C) with prion-like proteins labelled in red. Selected hits are annotated. (**F**) Proteostasis components are bound by Rnq1-GFP in [*PIN*$^+$]. Volcano plot representation from (C) with chaperones, Hsps and proteins with described protein folding function labelled in red. Selected hits are annotated.

To determine whether sequestration of these factors leads to proteostasis impairment, we measured the half-life of the terminally misfolded model protein cytosolic carboxypeptidase Y* fused to GFP (CG*). Upon synthesis, CG* is rapidly degraded by the proteasome, dependent on Hsp70 and Hsp40 (Sis1) (Park et al., 2013). Consequently, reduction of cellular Sis1 levels through transcriptional repression using a *tet*-off system led to a marked stabilization of CG* in a cycloheximide (CHX) chase experiment (Figures 23A and B). Degradation kinetics of CG* did not differ in [*PIN*$^+$] or [*pin*$^-$] cells (Figure 23A). Moreover, a β-galactosidase-based reporter assay revealed no HSE-mediated stress response in [*PIN*$^+$] and a similar inducibility of the HSR in [*PIN*$^+$] and [*pin*$^-$] cells upon exposure of cells to elevated temperatures (Figure 23C).

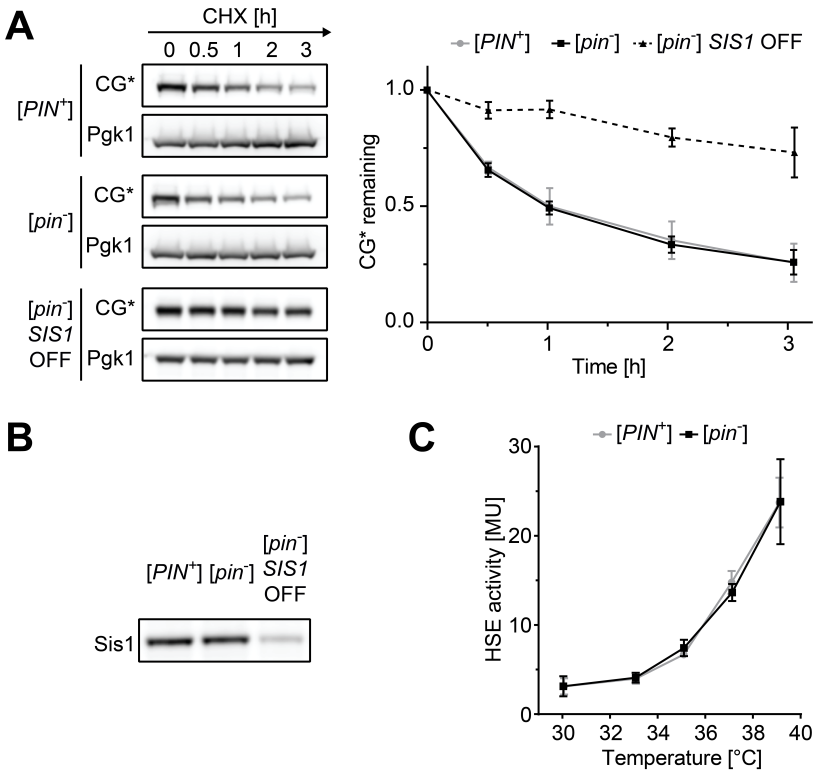

Figure 23: Rnq1 prion status does not detectably impair proteostasis. (**A**) Prion status does not influence turnover of CG*. CG* was expressed in [*PIN*$^+$] and [*pin*$^-$] yeast cells for 20 hr. Cycloheximide (CHX) was added to inhibit protein synthesis and cells were collected at the indicated times after CHX addition. As a control, a [*pin*$^-$] strain in which endogenous *SIS1* was replaced with tet-off *SIS1* was grown for 20 h in the presence of doxycycline (DOX) to shut off expression of *SIS1* (*SIS1* OFF). CHX chase was performed in a similar fashion as for *wt* samples. Samples were analyzed by SDS-PAGE and immunoblotting for GFP and Pgk1 as a loading control, followed by densitometric analysis. Data represent mean ± SD from three independent experiments. (**B**) Depletion of Sis1. Samples from (A) were analyzed via SDS-PAGE and immunoblotting for Sis1. A representative result is shown from experiments performed in triplicate. (**C**) Prion status does not influence induction of the HSR by heat. β-Galactosidase (β-Gal) activity was measured in [*PIN*$^+$] or [*pin*$^-$] cells expressing a LacZ reporter under the control of a minimal promoter containing a HSE from *SSA3* (pHSELacZ). Cells were grown at 30 °C for ~20 h, followed by a shift to the indicated temperature for 1 h prior to analysis. LacZ activity is reported in standard Miller Units. Data represent mean ± SD from four independent experiments.

Taken together, our data suggest that neither intrinsic proteome differences nor a general impairment of the proteostasis network through sequestration of proteostasis factors in [*PIN*$^+$] can explain the dependence of polyQ aggregate formation on the prion status.

Characterizing blue light-inducible protein clustering in yeast

Our proteomics data argued that it is not an intrinsic feature of the yeast strain that influences the aggregation of polyQ, but potentially a direct effect of the prion aggregates on the polyQ protein. Amyloid-forming proteins, including both Rnq1 and polyQ, are generally highly interactive once in their aggregated state, especially with other intrinsically disordered proteins (Olzscha et al., 2011; Ripaud et al., 2014) (Figure 22E). In addressing this possibility, it was of interest to experimentally circumvent the prion requirement for polyQ aggregate formation.

It has been suggested that the formation of polyQ-expanded Huntingtin exon 1 inclusions follows a multistep mechanism (Ossato et al., 2010; Vitalis and Pappu, 2011). First, protein monomers accumulate locally, as suggested for example through oligomerization, micelle formation or liquid-liquid phase separation (Jayaraman et al., 2012; Peskett et al., 2018; Thakur et al., 2009). Within these local clusters, a stochastic aberrant conformational transition takes place, generating a critical nucleus with partial β-sheet structure that triggers downstream aggregation of the protein population (Serio et al., 2000; Sinnige et al., 2021; Walters and Murphy, 2011; Yushchenko et al., 2018). Following this rational, we hypothesized that combining expanded polyQ with the *Arabidopsis thaliana* photoreceptor protein CRY2, known for its ability to rapidly form homo-oligomeric protein clusters upon a blue light stimulus, could enable directed, local concentration of the protein and thereby facilitate its aggregation even in a prion-free [*pin*$^-$] strain, thus circumventing the catalytic function of the prion phenotype.

CRY2 has been used as an important optobiochemical tool for many applications in plants, human cell culture and other model organisms (Bugaj et al., 2013; Kyung et al., 2015; Pathak et al., 2017). However, little had been known about its behavior in yeast. To examine the suitability of CRY2 for our experimental approach, we first elucidated its characteristics in yeast. We labelled the photolyase homology region (PHR) of CRY2, known for its ability to

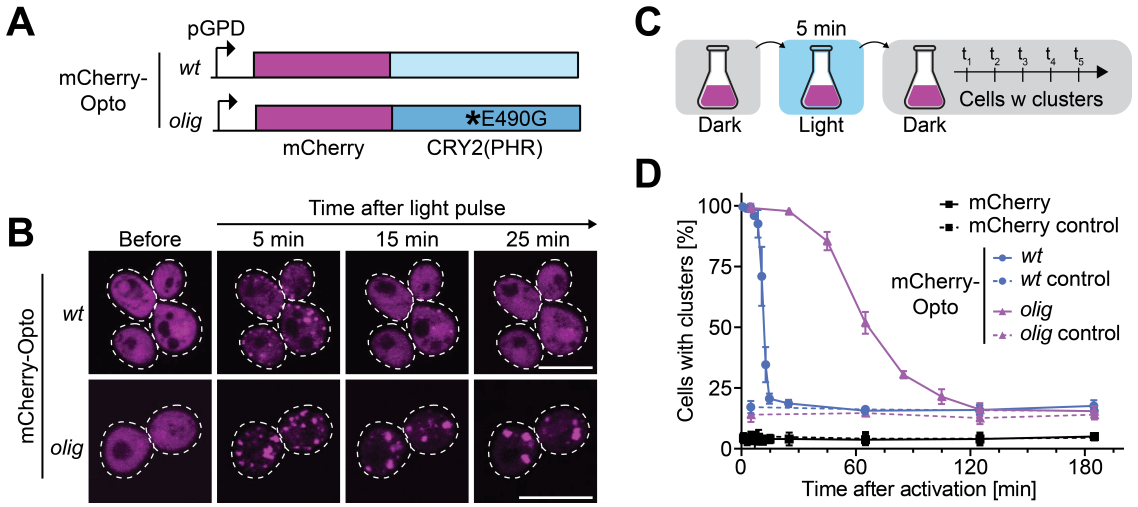

Figure 24: Characterizing blue light-inducible protein clustering in yeast. (**A**) Schematic illustration of Opto construct design. For *wt* mCherry-Opto, the CRY2 photolyase homology region (PHR) was tagged with an N-terminal mCherry fluorophore. mCherry-Opto *olig* contains a point mutation at position 490 of CRY2. Both constructs were integrated into the genome and expressed from the constitutive *GPD* promoter. (**B**) Formation of homooligomeric clusters upon light activation. Representative confocal micrographs of cells expressing *wt* or *olig* mCherry-Opto, imaged at different time points before and after activation with blue light for 30 s. Experiments were performed in triplicate. Scale bars, 5 µm. (**C**) Workflow for cluster disappearance experiment. Cells expressing mCherry-Opto constructs were grown in the dark, followed by a 5 min activation period in blue light. Cultures were returned to the dark and continued to incubate. At regular time intervals, the number of cells with visible mCherry-Opto clusters was counted. (**D**) Disappearance kinetics differ for CRY2 variants. Quantification of number of cells with visible clusters over time after illumination with blue light for 5 min or without illumination as control. Cells were expressing either mCherry alone or mCherry-Opto constructs. Each data point represents the mean ± SD from three biological replicates and 100 individual cells counted each.

allow homo-oligomerization upon illumination with blue light, with mCherry (mCherry-Opto), integrated this construct in the genome and expressed it under the control of the strong constitutive *GPD* promoter (Figure 24A). We also analyzed the behavior of the CRY2 E490G point mutant, shown to display altered clustering and dissociation kinetics (CRY2 *olig*) (Duan et al., 2017; Taslimi et al., 2014) (Figure 24A). When the mCherry-Opto constructs were expressed in yeast grown in the absence of blue light, both CRY2 variants were diffusely distributed throughout the cells and clustered upon exposure to a short (30 s) blue light pulse (Figure 24B). While CRY2 *wt* formed many small foci upon illumination, CRY2 *olig* first assembled into larger clusters that eventually merged into a few large foci per cell, persisting substantially longer than *wt* counterparts (Figure 24B). These protein clusters dissociated over time in the dark. The kinetics of this process differed between the two constructs. Counting the number of cells expressing the mCherry-Opto proteins in visible foci after a 5 min blue light pulse followed by incubation in the dark (Figure 24C) revealed that CRY2 *wt* clusters had a lifetime of only about 15 min, while foci formed by CRY2 *olig* persisted much

longer, up to 2 h after activation (Figure 24D). Since for our purposes an extended period in a locally concentrated form was desired, we chose to proceed using exclusively the PHR of the CRY2 *olig* variant for all following experiments.

To ensure the suitability of mCherry-Opto in both [*PIN*$^+$] and [*pin*$^-$] yeast cells, we tested its response to blue light illumination in both backgrounds. Independent of the prion status of the cell, mCherry-Opto was soluble when cells were grown in the absence of light, rapidly clustered upon illumination and eventually formed one or few large foci per cell when exposed to blue light for a longer period of time (Figure 25A). After short blue light illumination (5 min) and subsequent incubation in the dark, the mCherry-Opto clusters dissociated with similar kinetics in both backgrounds (Figure 25B), confirming that the prion status did not influence the behavior of this optogenetic tool.

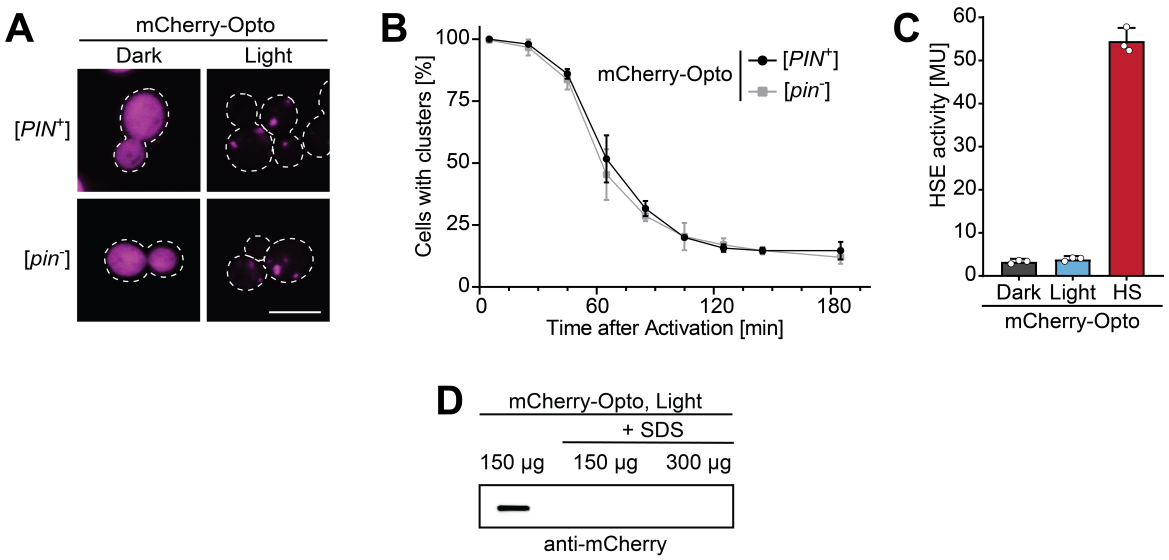

Figure 25: Light-induced mCherry-Opto clusters are inert. (**A**) [*PIN*] prion status does not influence clustering of mCherry-Opto. Representative confocal micrographs of [*PIN*$^+$] and [*pin*$^-$] cells expressing mCherry-Opto, grown in the absence (Dark) or presence of blue light (Light) for 6 h prior to imaging. Experiments were performed in triplicate. Scale bar, 5 µm. (**B**) [*PIN*] prion status does not influence disappearance of Opto clusters. Quantification of number of mCherry-Opto-expressing [*PIN*$^+$] or [*pin*$^-$] cells with visible clusters over time after illumination with blue light for 5 min. Each data point represents the mean ± SD from three biological replicates and 100 individual cells counted each. (**C**) Neither expression of mCherry-Opto nor its activation with light induce the HSR. β-Gal activity was measured in pHSELacZ-containing [*PIN*$^+$] cells expressing mCherry-Opto and grown either in the absence (Dark) or presence of blue light for 6 h (Light) prior to analysis. As a control, β-gal activity was measured in the same cells shifted to 37 °C for 1 h (HS) prior to measurement. Data represent mean + SD from three independent experiments (**D**) mCherry-Opto does not form SDS-resistant aggregates. Indicated amounts of total protein from lysates of [*PIN*$^+$] cells expressing mCherry-Opto grown in the presence of blue light for 6 h prior to harvest were filtered through a 0.2 µm cellulose acetate membrane. Indicated samples were treated with SDS/DTT before loading. The membrane was processed for immunodetection with anti-mCherry antibody. A representative result is shown from experiments performed in triplicate.

Functional analysis of the mCherry-Opto clusters revealed that their presence, even over an extended period, did not induce the HSR or interfere with its regular activation in response to elevated temperatures (Figure 25C). In line with the dynamic clustering and dissociation behavior of mCherry-Opto, the visible clusters that were formed upon blue light illumination remained soluble in the detergent SDS (Figure 25D). Together, these results suggest that the dynamic mCherry-Opto clusters are largely inert on their own.

Light-inducible polyQ aggregation

Having established the suitability of the CRY2-based optogenetic tool in yeast, we proceeded to functionalize the mCherry-Opto construct by N-terminally fusing cMyc-tagged 97Q-expanded Huntingtin exon 1 (97Q-Opto) (Figure 26A). As before, 20Q served as control (20Q-Opto) (Figure 26A). The presence of the poly proline tract C-terminal to the polyQ sequence allowed the expression of these constructs without overt toxicity in yeast, making it an ideal model system to study fundamental aggregation processes unaffected by deleterious side effects (Duennwald et al., 2006b; Holmes et al., 2014a).

To assess the influence of the polyQ tags on the behavior of the Opto construct, we performed similar experiments as before. 20Q-Opto was soluble when cells were grown in the absence of light in both [*PIN*$^+$] and [*pin*$^-$] and clustered upon illumination with blue light (Figure 26B), similar to mCherry-Opto alone (Figure 25A). 97Q-Opto showed a different behavior depending on the prion status of the strain background (Figure 26B). In [*PIN*$^+$], inclusions were observed already in the dark in a subset of cells (Figure 26B). Here, as reported in previous studies, 97Q formed aggregates independent of the influence of CRY2 (Meriin et al., 2002; Osherovich and Weissman, 2001). If these cells were illuminated with blue light, the preformed inclusions were not altered, but residual diffuse 97Q-Opto clustered into characteristic foci (Figure 26B). In the non-permissive, [*pin*$^-$] background, 97Q-Opto was soluble in the absence of light and clustered only upon illumination with blue light (Figure 26B). When exposed to blue light for a brief period (5 min), light-induced 20Q- and 97Q-Opto clusters dissociated with slower kinetics compared to the mCherry-Opto control (Figure 26C), suggesting interactions between the polyQ tags of the constructs when accumulated locally. While this short blue light pulse was apparently not sufficient to

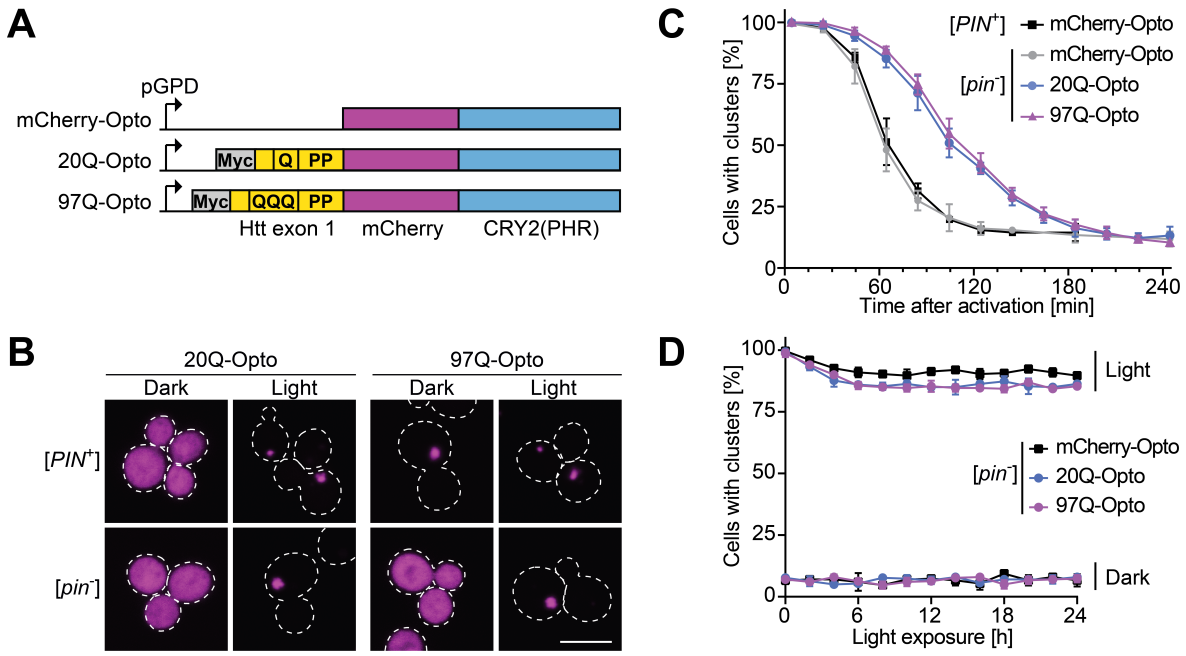

Figure 26: Light-inducible polyQ aggregation. (**A**) Schematic illustration of polyQ-Opto construct design. Functionalized Opto constructs contain Myc-tagged Huntingtin exon 1 with variable lengths of the poly glutamine expansion (Q/QQQ), including the adjacent proline-rich region (PP), N-terminal to the previously described mCherry-Opto (20Q-Opto and 97Q-Opto). Analogous to mCherry-Opto, polyQ-Opto constructs are integrated into the genome and expressed constitutively from the *GPD* promoter. (**B**) PolyQ-Opto forms clusters upon blue light illumination. Representative confocal micrographs of [*PIN*$^+$] and [*pin*$^-$] cells expressing 20Q-Opto or 97Q-Opto, grown in the absence (Dark) or presence of blue light (Light) for 6 h prior to imaging. Experiments were performed in triplicate. Scale bar, 5 µm. (**C**) PolyQ-Opto clusters persist longer than mCherry-Opto. Quantification of number of [*pin*$^-$] cells expressing either mCherry-Opto, 20Q-Opto or 97Q-Opto in visible clusters after illumination with blue light for 5 min. Each data point represents the mean ± SD from three biological replicates and 100 individual cells counted each. (**D**) Continuous illumination with blue light results in prolonged clustering of Opto constructs. Quantification of number of [*pin*$^-$] cells expressing either mCherry-Opto, 20Q-Opto or 97Q-Opto in visible clusters over time. Cultures were either grown in in the constant presence (Light) or absence (Dark) of blue light. Each data point represents the mean ± SD from three biological replicates and 100 individual cells counted each.

generate stable polyQ-Opto aggregates, clusters could be maintained through continuous illumination with blue light (Figure 26D).

Comparing the behavior of mCherry-Opto alone with polyQ-tagged Opto variants demonstrated that this functionalization preserved the basic characteristic of the photoreceptor of aggregation in response to blue light. This approach allowed us to induce the formation of protein clusters decorated with polyQ peptides in the otherwise non-permissive [*pin*$^-$] yeast strain.

Light-induced formation of polyQ aggregates in [*pin*$^-$] cells

Expanded polyQ proteins form SDS-resistant aggregates in [*PIN*$^+$] yeast and mammalian cells, a feature that these inclusions share with polyQ fibrils produced *in vitro* (Kazantsev et al., 1999; Muchowski et al., 2002; Scherzinger et al., 1997). We next analyzed the polyQ-Opto clusters via filter retardation assay in order to investigate whether they possessed similar biochemical characteristics. Neither mCherry-Opto nor 20Q-Opto formed large SDS-resistant aggregates in any condition tested (Figure 27A). For 97Q-Opto, the results were more

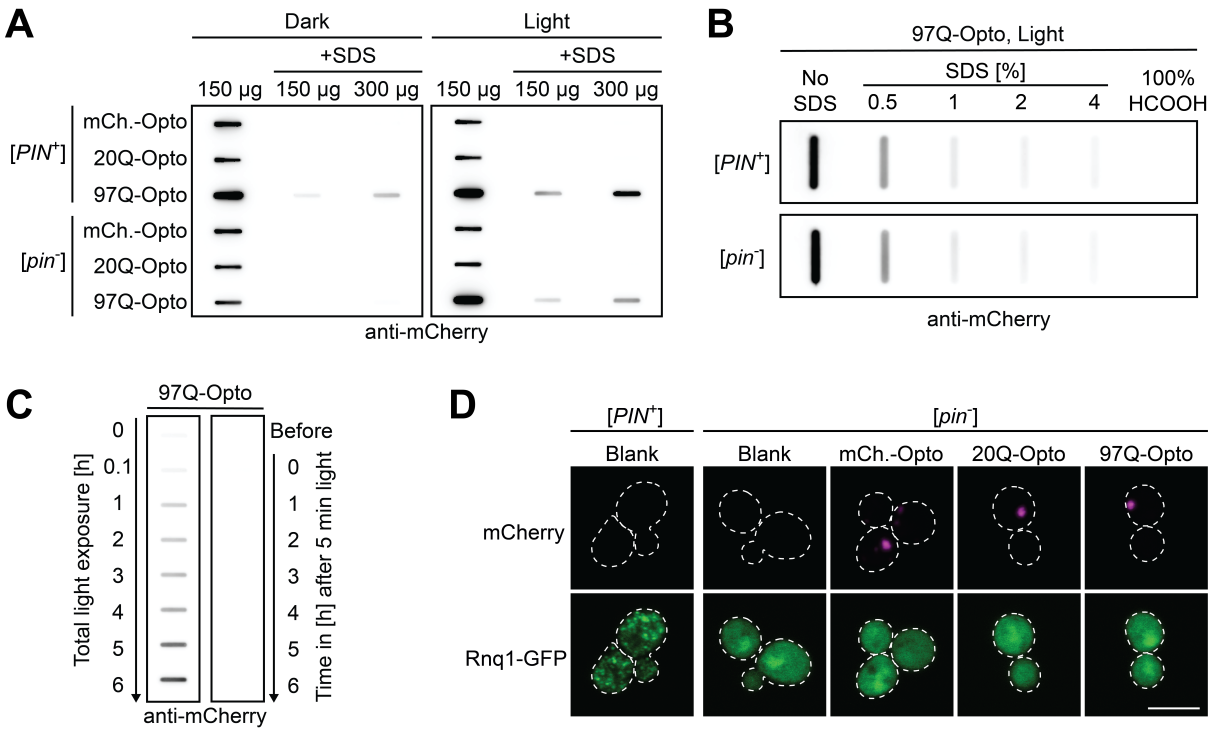

Figure 27: Formation of polyQ aggregates in [pin$^-$] cells. (**A**) 97Q-Opto forms SDS-resistant aggregates upon illumination with blue light. Indicated amounts of total protein from lysates of [*PIN*$^+$] or [*pin*$^-$] cells expressing either mCherry-Opto, 20Q-Opto or 97Q-Opto, grown either in the absence (Dark) or presence of blue light (Light) for 6 h prior to harvest, were filtered through a 0.2 µm cellulose acetate membrane. Indicated samples were treated with SDS/DTT before loading. Membrane was processed for immunodetection with anti-mCherry antibody. Representative result is shown from experiments performed in triplicate. (**B**) 97Q-Opto aggregates in [*PIN*$^+$] and [*pin*$^-$] cells share similar physico-chemical characteristics. 97Q-Opto was expressed in [*PIN*$^+$] or [*pin*$^-$] cells from a 2µ plasmid under the control of a galactose-inducible promoter in inducing media for ~23 h in the presence of blue light. Cell lysates were subjected to treatment with different amounts of SDS or 100% formic acid prior to analysis via filtration as in (A). 375 µg total protein were loaded for each [*pin*$^-$] sample, 300 µg for [*PIN*$^+$] samples. Only half the amount of total protein was applied in control samples (No SDS). 97Q-Opto was detected with anti-mCherry antibody. A representative result is shown from experiments performed in triplicate. (**C**) Formation of SDS-resistant aggregates requires prolonged activation with light. [*pin*$^-$] cells expressing 97Q-Opto were grown in the absence of blue light and shifted to blue light for the indicated times prior to harvest (left) or returned to the dark after 5 min blue light pulse (right). Cells were harvested at indicated time points. 300 µg of total protein from lysates were treated with SDS/DTT and analyzed via filtration. Membranes were processed for immunodetection with anti-mCherry antibody. Representative results are shown from experiments performed in triplicate. (**D**) Expression and light-induction of Opto constructs does not change [*PIN*] prion status. Confocal micrographs of *RNQ1-GFP* expressing [*PIN*$^+$] and [*pin*$^-$] cells coexpressing either a blank vector control, mCherry-Opto, 20Q-Opto or 97Q-Opto. Cells were grown in blue light for 6 h prior to imaging. Experiments were performed in triplicate. Scale bar, 5 µm.

complex. When expressed in the permissive [*PIN*$^+$] background, 97Q-Opto formed SDS-insoluble inclusions already in the absence of light, in agreement with our previous microscopy analysis (Figures 27A and 26B), and the trapped material increased upon blue light illumination (Figure 27A), suggesting that light-induced species were also partially SDS-resistant. As expected, we did not observe any 97Q-Opto trapped on the filter in [*pin*$^-$] cells in the absence of light (Figure 27A). However, if cells were illuminated with blue light, 97Q-Opto formed SDS-insoluble aggregates even in this non-permissive background (Figure 27A). The light-induced 97Q-Opto aggregates in [*pin*$^-$] cells exhibited comparable physico-chemical properties to the aggregates formed in the [*PIN*$^+$] strain: they showed similar susceptibility to different concentrations of SDS and readily dissolved upon treatment with formic acid (Figure 27B), as has previously been described for polyQ fibrils (Hazeki et al., 2000). Notably, the formation of SDS-resistant aggregates in [*pin*$^-$] cells required the prolonged exposure to blue light, as a short pulse of blue light followed by a further incubation in the dark was not sufficient (Figure 27C), in agreement with our previous observations (Figure 26C).

To exclude the possibility that expression and light-induction of the Opto constructs altered the [*pin*$^-$] status of the yeast strain and thereby allowed the formation of SDS-resistant 97Q-Opto aggregates, we visualized the state of the cellular Rnq1 protein via the coexpression of *RNQ1-GFP* (Figure 27D). In all tested conditions, including the expression and activation of Opto constructs, the Rnq1-GFP signal remained diffuse and did not form discrete foci characteristic of a [*PIN*$^+$] prion state. This confirmed that the SDS-insoluble aggregates we observed in the filter retardation assay were indeed formed via light-induced clustering of 97Q-Opto. Thus, by applying the optogenetic tool, we were able to induce robust formation of SDS-resistant protein aggregates of an expanded polyQ protein in a non-permissive [*pin*$^-$] background.

Previous studies, including work presented in Chapter I, have shown that polyQ aggregates directly interact with and are able to sequester cellular components such as the yeast Hsp40 Sis1 (see Chapter I; Klaips et al., 2020; Park et al., 2013; Walter et al., 2011). Furthermore, we demonstrated that the overexpression of *SIS1* increases the solubility of polyQ inclusions (see Chapter I; Klaips et al., 2020). To analyze whether light-induced 97Q-Opto aggregates in [*pin*$^-$] cells were equally influenced by cellular components, we assessed the solubility of these aggregates at endogenous and elevated Sis1 levels (Figure 28A).

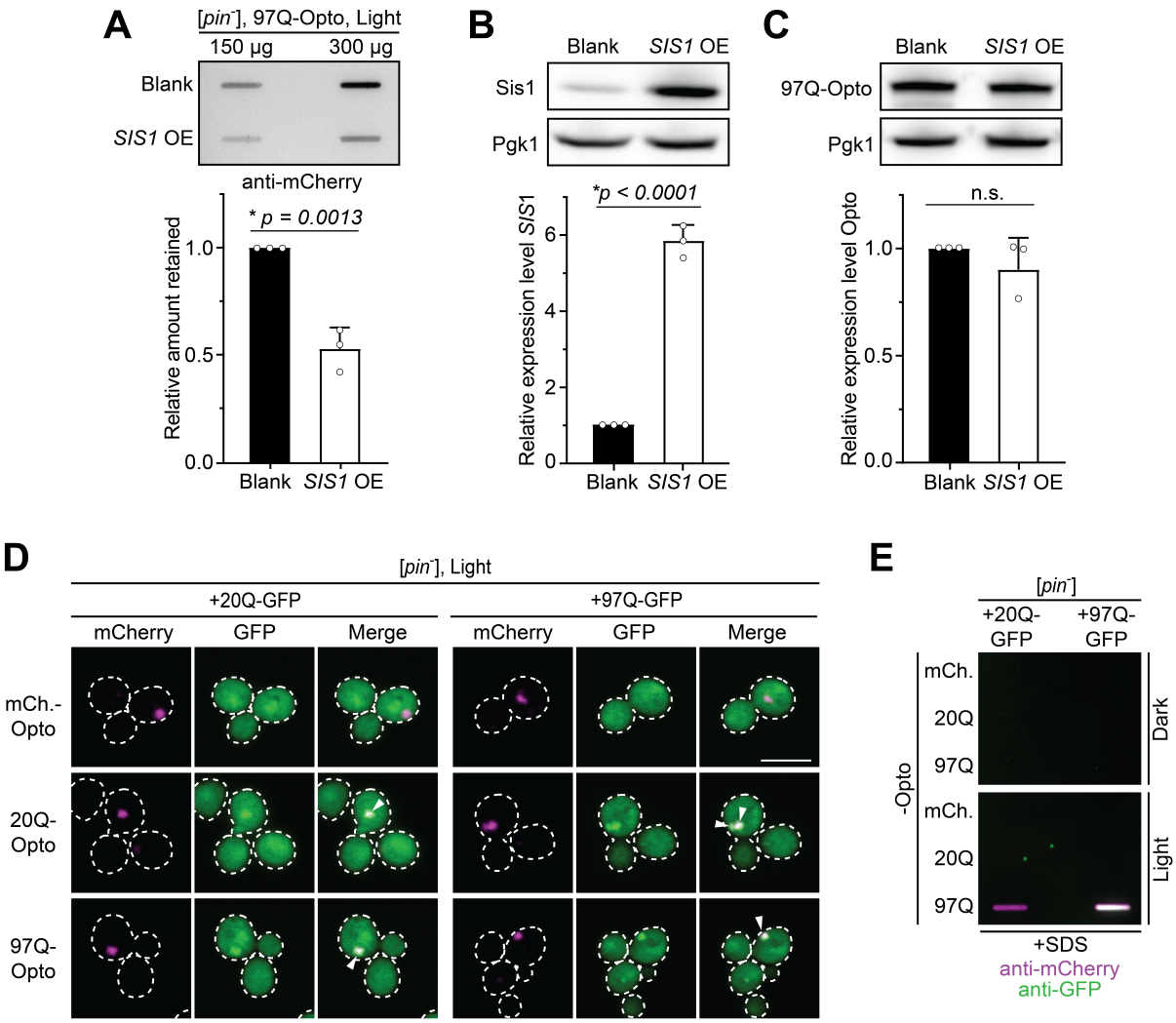

Figure 28: Light-induced 97Q-Opto aggregates resemble regular polyQ inclusions. (**A**) Overexpression of *SIS1* results in increased SDS-solubility of 97Q-Opto aggregates. [*pin*$^-$] cells expressing 97Q-Opto and coexpressing either a blank vector control (Blank) or overexpressing *SIS1* from an additional plasmid under the control of the *GPD* promoter (*SIS1* OE) were grown in blue light for 6 h prior to harvest. Indicated amounts of total protein from lysates were treated with SDS/DTT and filtered through a 0.2 µm cellulose acetate membrane. The membrane was processed for immunodetection with anti-mCherry antibody. A representative result is shown from experiments performed in triplicate. Graph depicts densitometric quantification of membranes. Bars represent mean + SD, *p*-value calculated by unpaired, two-sided *t*-test. (**B**) *SIS1* overexpression level. Samples from (A) were analyzed by SDS-PAGE and immunoblotting for Sis1 and Pgk1. A representative result is shown from experiments performed in triplicate. Graph depicts densitometric quantification of membranes. Bars represent mean + SD, *p*-value calculated by unpaired, two-sided *t*-test. (**C**) 97Q-Opto expression levels. Samples from (A) were analyzed by SDS-PAGE and immunoblotting for mCherry and Pgk1. A representative result is shown from experiments performed in triplicate. Graph depicts densitometric quantification of membranes. Bars represent mean + SD, *p*-value calculated by unpaired, two-sided *t*-test. n.s., not statistically significant. (**D**) PolyQ-Opto aggregates sequester polyQ-GFP. Representative confocal micrographs of [*pin*$^-$] cells coexpressing mCherry-Opto, 20Q-Opto or 97Q-Opto and 20Q-GFP or 97Q-GFP, grown in blue light for 6 h prior to imaging. Experiments were performed in triplicate. Arrows mark colocalization. Scale bar, 5 µm. (**E**) Light-induced 97Q-Opto aggregates sequester 97Q-GFP in detergent-insoluble aggregates. 300 µg of total protein from lysate of samples from (D) were analyzed via filtration as in (A). Membranes were processed for immunodetection with either anti-mCherry (magenta) or anti-GFP (green) antibody. Chemiluminescence signals were overlaid, matching signals appear white. Representative result is shown from experiments performed in triplicate.

Indeed, upon *SIS1* overexpression (Figure 28B), blue light illumination of [*pin*$^-$] cells expressing similar amounts of 97Q-Opto (Figure 28C) resulted in reduced amounts of SDS-insoluble aggregates, compared to an empty vector control condition (Figure 28A). This result suggested that light-induced 97Q-Opto aggregates in [*pin*$^-$] were indeed functionally interacting with cellular components such as Sis1, just as regular polyQ inclusions in [*PIN*$^+$].

Partial SDS-resistance and the ability to interact with cellular factors are hallmarks the light-induced aggregates share with regular polyQ inclusions in yeast. Another characteristic feature of expanded polyQ proteins in [*PIN*$^+$] is the ability to sequester proteins with shorter polyQ stretches, which are unable to aggregate on their own (Chen et al., 2001; Duennwald et al., 2006a; Kazantsev et al., 1999; Wang et al., 2009). To test this property for the light-induced polyQ-Opto aggregates, we coexpressed mCherry-Opto, 20Q-Opto or 97Q-Opto along with non-Opto-tagged 20Q-GFP and 97Q-GFP in [*pin*$^-$] cells. As expected, light-induced mCherry-Opto clusters failed to sequester either 20Q-GFP or 97Q-GFP (Figure 28D). In contrast, both 20Q-GFP and 97Q-GFP colocalized with aggregates formed by 20Q-Opto and 97Q-Opto (Figure 28D). The surprising finding that even light-induced 20Q-Opto aggregates were able to sequester other polyQ-containing proteins suggests polyQ co-aggregation depends mostly on high local polyQ concentrations rather than pathological polyQ expansion. Furthermore, co-aggregation did also not depend on the ability to form SDS-resistant aggregates, as 20Q-Opto aggregates remain SDS-soluble (Figures 28E and 27A). Only light-induced aggregation of 97Q-Opto and co-expression of 97Q-GFP led to the formation of SDS-resistant co-aggregates (Figure 28E).

The importance of polyQ length and protein concentration for aggregation in yeast has been previously reported (Duennwald et al., 2006b; Krobitsch and Lindquist, 2000; Scherzinger et al., 1999). While at low concentrations and short glutamine repeat lengths, polyQ is mostly found in its soluble state, an increase in the protein concentration or a longer polyQ tract can lead to the formation of protein aggregates. Having characterized the behavior of 20Q-Opto and 97Q-Opto and their light-induced aggregates thoroughly, we extended our study to constructs with polyQ stretches of intermediate length to get a better understanding of the phase dynamics of polyQ. To assess the basal level of aggregation of polyQ in the [*PIN*$^+$] background, we analyzed cultures endogenously expressing polyQ-Opto in the absence of light (Figure 29A). Under these conditions, only cells expressing 97Q-Opto

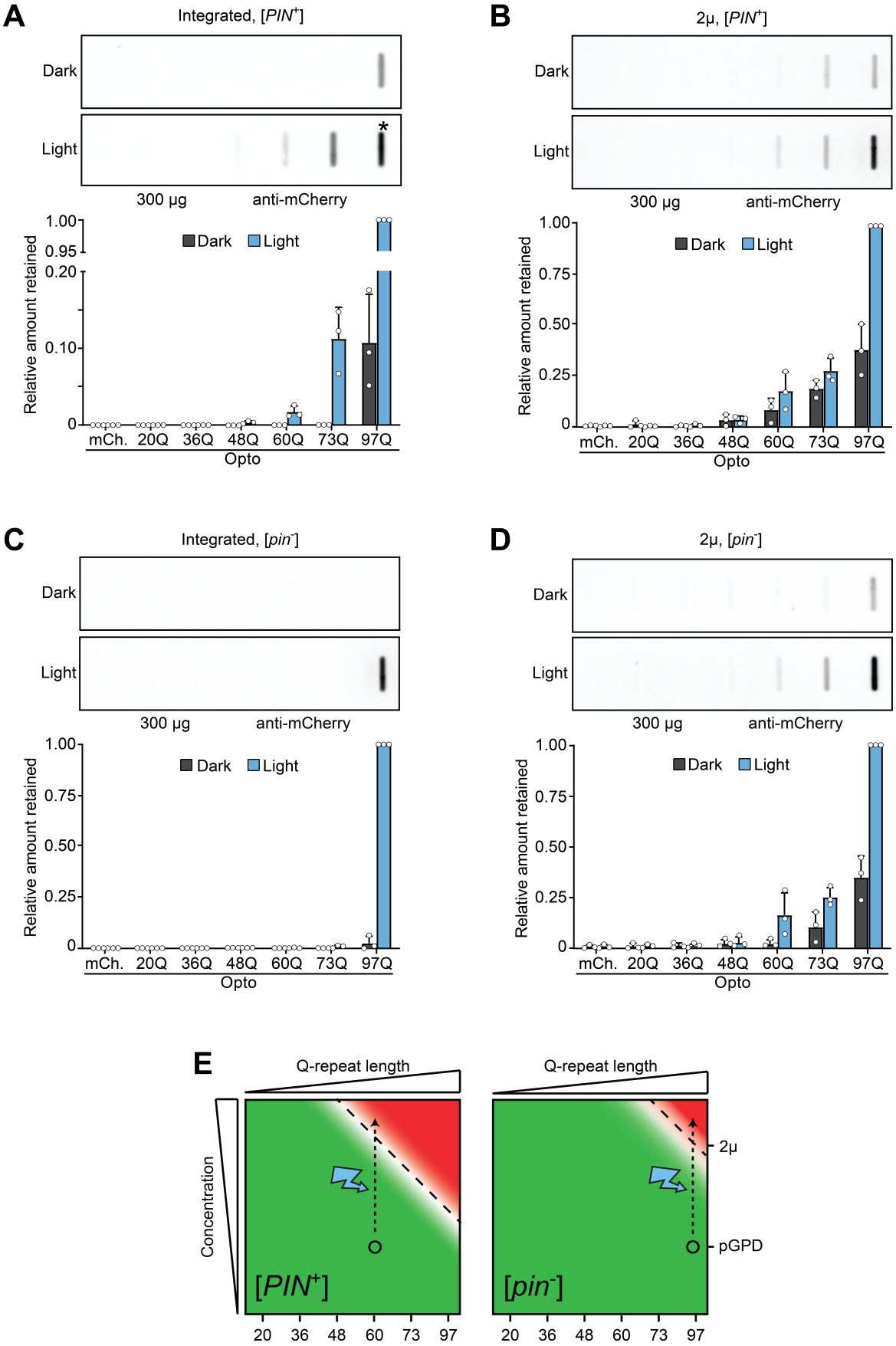
A
Integrated, [PIN+]
Dark
Light
*
300 µg
anti-mCherry
Relative amount retained
1.00
0.95
0.20
0.10
0
Dark
Light
mCh.
20Q
36Q
48Q
60Q
73Q
97Q
Opto
B
2µ, [PIN+]
Dark
Light
300 µg
anti-mCherry
Relative amount retained
1.00
0.75
0.50
0.25
0
Dark
Light
mCh.
20Q
36Q
48Q
60Q
73Q
97Q
Opto
C
Integrated, [pin-]
Dark
Light
300 µg
anti-mCherry
Relative amount retained
1.00
0.75
0.50
0.25
0
Dark
Light
mCh.
20Q
36Q
48Q
60Q
73Q
97Q
Opto
D
2µ, [pin-]
Dark
Light
300 µg
anti-mCherry
Relative amount retained
1.00
0.75
0.50
0.25
0
Dark
Light
mCh.
20Q
36Q
48Q
60Q
73Q
97Q
Opto
E
Q-repeat length
Concentration
[PIN+]
20
36
48
60
73
97
Q-repeat length
2µ
pGPD
[pin-]
20
36
48
60
73
97

Figure 29: Light induction allows dynamic movement in aggregation phase diagram. (**A**) Activation with light lowers the Q-length threshold for aggregate formation in [*PIN*$^+$]. [*PIN*$^+$] cells expressing either mCherry-Opto or polyQ-Opto from an integrated endogenous locus under the control of the *GPD* promoter were grown either in the absence (Dark) or presence of blue light (Light). 300 µg of total protein from lysates were treated with SDS/DTT and filtered through a 0.2 µm cellulose acetate membrane. Membrane was processed for immunodetection with anti-mCherry antibody. Representative result is shown from experiments performed in triplicate. *, only 60 µg of total protein was loaded. Graph depicts densitometric quantification of material retained on membranes. Data represent mean + SD. (**B**) Activation with light increases SDS-insoluble aggregation at higher expression levels. mCherry-Opto or polyQ-Opto were expressed in [*PIN*$^+$] cells from 2µ plasmids under the control of a galactose-inducible promoter through growth in inducing media for ~23 h. Samples were analyzed as in (A). Representative result from experiments performed in triplicate is shown. Data represent mean + SD. (**C**) Activation with light induces 97Q-Opto aggregate formation in [*pin*$^-$]. [*pin*$^-$] cells expressing either mCherry-Opto or polyQ-Opto from an integrated endogenous locus under the control of the *GPD* promoter were grown and analyzed as in (A). Representative result is shown from experiments performed in triplicate. Data represent mean + SD. (**D**) Activation with light lowers the Q-length threshold for aggregate formation in [*pin*$^-$] at higher expression levels. mCherry-Opto or polyQ-Opto were expressed in [*pin*$^-$] cells from 2µ plasmids under the control of a galactose-inducible promoter through growth in inducing media for ~23 h. Samples were analyzed as in (A). Representative result is shown from experiments performed in triplicate. Data represent mean + SD. (**E**) PolyQ-Opto allows dynamic movement in aggregation phase diagram. Schematic phase diagrams depicting the Q-length and concentration dependence of aggregate formation by polyQ-Opto in [*PIN*$^+$] (left) and [*pin*$^-$] (right) cells. At low expression levels and short polyQ lengths, polyQ is mostly soluble (green) whereas at high concentrations and long Q-stretches polyQ forms aggregates (red). Critical concentration and Q-length for aggregate formation are lower for [*PIN*$^+$] than for [*pin*$^-$]. Aggregation of polyQ-Opto can be induced via light-dependent clustering, increasing the local polyQ concentration and thereby allowing the crossing of phase boundaries, even for shorter Q-repeat lengths or non-permissive backgrounds.

showed a significant formation of SDS-resistant aggregates (Figure 29A). Light-induced clustering lowered the threshold for aggregate formation to 60 Q (Figure 29A) and increased the amount of SDS-resistant aggregates for 97Q-Opto (Figure 29A). In line with these results, augmenting the overall concentration of polyQ-Opto through expression from multicopy 2µ plasmids and a stronger promoter already allowed the formation of SDS-resistant aggregates at shorter polyQ length in the absence of light (Figure 29B). Light induction further increased the amount of SDS-resistant aggregates (Figure 29B). In the non-permissive [*pin*$^-$] background, only 97Q-Opto showed the light-dependent formation of SDS-insoluble aggregates at low expression levels (Figure 29C). However, aggregation still remained ~ 4-fold lower than in [*PIN*$^+$] cells under similar conditions (Figure 27A), suggesting that the [*PIN*$^+$] prion status dramatically enhances polyQ aggregation propensity. Overexpression of polyQ-Opto in [*pin*$^-$] cells and light activation mirrored previous observations in [*PIN*$^+$] with SDS-resistant aggregates forming already for 60Q-Opto (Figure 29D). Interestingly, at these high expression levels, small but detectable amounts of SDS-resistant aggregates of 97Q-Opto could even be observed without illumination. In summary, increasing the concentration of polyQ through light-induced clustering or higher expression levels decreased the threshold for aggregate formation even for proteins with shorter polyQ stretches (Figure 29E), recapitulating

previously published results on the importance of polyQ length and protein concentration on the aggregation process for our polyQ-Opto constructs.

Taken together, our experiments confirmed that light-induced polyQ-Opto aggregates share key characteristics with regular polyQ inclusions in yeast: they are partially SDS-resistant, readily dissolve in formic acid, interact with cellular factors, are able to sequester other polyQ proteins and exhibit a similar dependence on both polyQ length and protein concentration for the formation of SDS-resistant species. The possibility to induce these aggregates in both [*PIN*$^+$] and [*pin*$^-$] cells and dynamically shift the threshold for aggregate formation by illumination with blue light allowed us to study polyQ aggregation and its biological effects for the first time in isogenic yeast strains in order to shed light on the influence of the cellular background on these processes.

[*PIN*$^+$] cells accumulate polyQ oligomers responsible for HSR induction

After the biochemical characterization of polyQ-Opto aggregates, we next investigated their functional properties. In Chapter I, we showed that the induction of the HSR by expanded polyQ in yeast is dependent on the overexpression of *SIS1* (see Chapter I; Klaips et al., 2020). Here, we showed that the light-induced polyQ-Opto aggregates were able to interact with Sis1 as well (Figure 28). Thus, we tested whether these aggregates were also able to induce a Sis1-dependent HSR. Expression of 97Q-Opto in *SIS1* overexpressing [*PIN*$^+$] cells activated a heat shock element-mediated stress response in the absence of light, similar to untagged 97Q, and activation of 97Q-Opto with blue light led to a two-fold increase of the β-gal reporter activity (Figure 30A), confirming that light-induced aggregates were also biologically active. This result further underlined that the aggregation status of a polyQ protein is important for the HSR induction. As previously reported for non-Opto-tagged expanded polyQ, this result was dependent on the overexpression of *SIS1* (Figure 30B). In contrast, in [*pin*$^-$] cells, no HSR was observed for any tested condition, even when cells expressing 97Q-Opto were illuminated with blue light (Figure 30A). This was the case, although similar amounts of SDS-resistant aggregates were formed as in the [*PIN*$^+$] dark condition (Figure 30C), where a mild HSR induction was observed (Figure 30A). Furthermore, the [*pin*$^-$] strain remained capable of initiating a normal HSR at elevated temperature (Figure 30D). This suggested that in addition

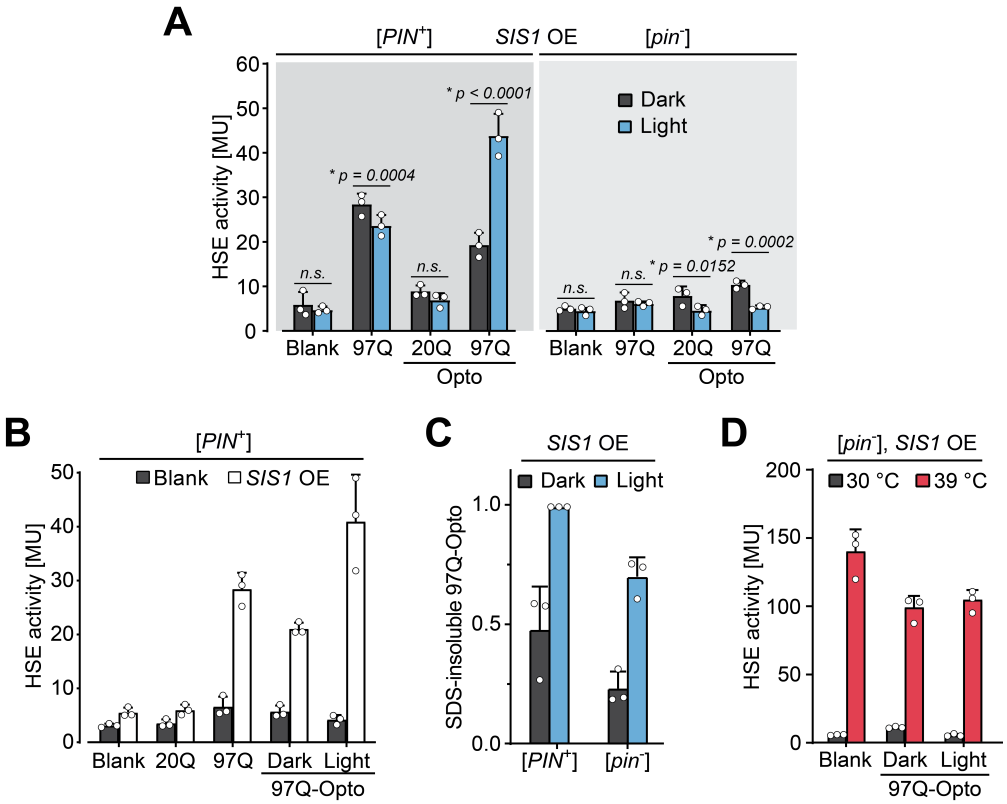

Figure 30: HSR activation by light-induced polyQ-Opto aggregates is dependent on [PIN] prion status. (**A**) Light-induced polyQ-Opto aggregates induce a cytosolic HSR in [*PIN*$^+$] but not [*pin*$^-$]. β-Gal activity is shown for pHSELacZ-containing, *SIS1*-overexpressing [*PIN*$^+$] and [*pin*$^-$] cells coexpressing a blank vector control, 97Q, mCherry-Opto, 20Q-Opto or 97Q-Opto from 2µ plasmids under the control of a galactose-inducible promoter. Cells were grown either in the absence (Dark) or presence of blue light (Light) in inducing media for ~23 h. Data represent mean + SD from three independent experiments, *p*-values calculated by two-way ANOVA with Bonferroni's multiple comparisons test. n.s., not statistically significant. (**B**) *SIS1* overexpression is required for induction of the HSR by light-induced 97Q-Opto aggregates. β-Gal activity is shown for pHSELacZ-containing [*PIN*$^+$] cells expressing a blank vector control, 20Q, 97Q or 97Q-Opto from 2µ plasmids under the control of a galactose-inducible promoter. Cells were coexpressing either an empty vector control (Blank) or overexpressing *SIS1* from an additional plasmid under the control of the *GPD* promoter (*SIS1* OE) and grown in blue light (unless indicated otherwise) in inducing media for ~23 h. Data represent mean + SD from three independent experiments. (**C**) Levels of SDS-resistant 97Q-Opto aggregates. *SIS1*-overexpressing [*PIN*$^+$] and [*pin*$^-$] cells coexpressing 97Q-Opto from a 2µ plasmid under the control of a galactose-inducible promoter were grown either in the absence (Dark) or presence of blue light (Light) in inducing media for ~23 h. Identical amounts of total protein from lysates were treated with SDS/DTT and filtered through a 0.2 µm cellulose acetate membrane. The membrane was then processed for immunodetection with anti-mCherry antibody. Graph depicts densitometric analysis of material retained on filter membranes. Data represents mean + SD from three independent experiments. (**D**) Presence of 97Q-Opto aggregates does not interfere with HSR induction by heat. β-Gal activity was measured in [*pin*$^-$] cells expressing the pHSELacZ HSR reporter with *SIS1* overexpression and coexpression of empty vector or 97Q-Opto from 2µ plasmids under the control of a galactose-inducible promoter. Cells were grown either in the absence (Dark) or presence (Light) of blue light in inducing media for ~23 h. Selected samples were subjected to a 1 h heat treatment at 39 °C prior to analysis. Data represent mean + SD from 3 independent experiments.

to facilitating the aggregation of a polyQ protein, the prion status of the cell also influences the inducibility of the HSR by polyQ aggregates.

In Chapter I, we demonstrated that soluble oligomers rather than large inclusions are responsible for induction of the HSR by expanded polyQ (see Chapter I; Klaips et al., 2020).

Analysis by SDD-AGE revealed that 97Q-Opto in the [*PIN*$^+$] background formed oligomeric assemblies (Figure 31A), in addition to the SDS-insoluble aggregates detected by filter retardation assay (Figure 30C). These oligomeric aggregates were absent in [*pin*$^-$] cells (Figure 31A). Oligomers formed in [*PIN*$^+$] cells in a polyQ-length dependent manner (Figure 31B) and unlike larger SDS-resistant aggregates, remained mostly soluble upon fractionation via centrifugation (Figure 31C). Sis1 binding to polyQ oligomers is crucial for HSR induction (see Chapter I; Klaips et al., 2020) and can explain both the induction of the cytosolic HSR in [*PIN*$^+$] cells, where soluble polyQ oligomers interact with Sis1, and the absence of a stress response in [*pin*$^-$] strains, where no oligomeric species are detected (Figures 31D and 30A), despite the presence of similar amounts of large SDS-resistant aggregates (Figure 30C).

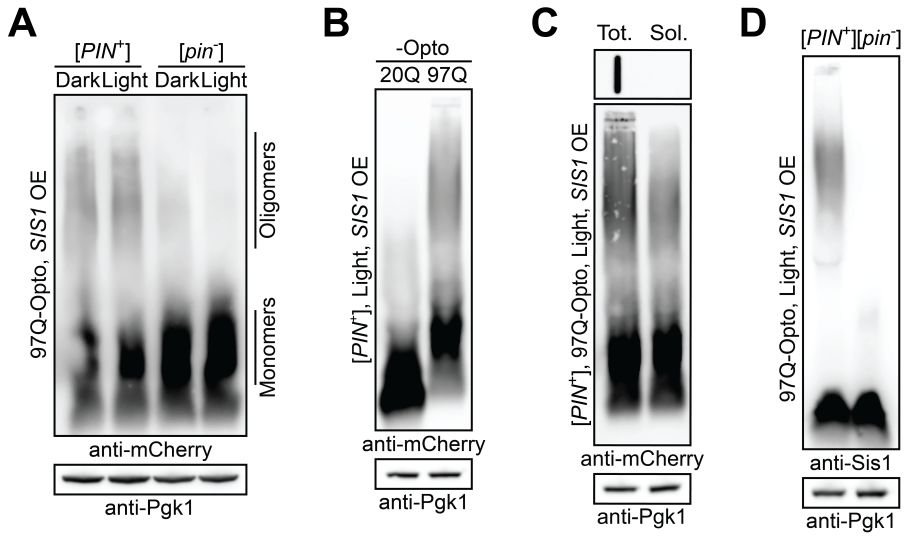

Figure 31: [PIN$^+$] cells accumulate polyQ-Opto oligomers. (**A**) 97Q-Opto forms oligomeric assemblies only in [*PIN*$^+$]. *SIS1*-overexpressing [*PIN*$^+$] and [*pin*$^-$] cells coexpressing 97Q-Opto from a 2µ plasmid under the control of a galactose-inducible promoter were grown either in the absence (Dark) or presence of blue light (Light) in inducing media for ~23 h. Lysates were analyzed by SDD-AGE. The membrane was processed for immunodetection with anti-mCherry antibody. Separate analysis by SDS-PAGE and immunoblotting for Pgk1 served as a loading control. Representative results are shown from experiments performed in triplicate. (**B**) Appearance of oligomeric species is Q-length dependent. *SIS1*-overexpressing [*PIN*$^+$] cells coexpressing either 20Q-Opto or 97Q-Opto from 2µ plasmids under the control of a galactose-inducible promoter were grown in the presence of blue light in inducing media for ~23 h. Lysates were analyzed by SDD-AGE. The membrane was processed for immunodetection with anti-mCherry antibody. Separate analysis by SDS-PAGE and immunoblotting for Pgk1 served as a loading control. Representative results are shown from experiments performed in triplicate. (**C**) Oligomeric 97Q-Opto species in [*PIN*$^+$] are largely soluble. *SIS1*-overexpressing [*PIN*$^+$] cells coexpressing 97Q-Opto from a 2µ plasmid under the control of a galactose-inducible promoter were grown as in (B). Lysate was separated into total (Tot.) and soluble (Sol.) fractions by centrifugation (15'000 x g). Samples were treated with SDS/DTT and analyzed via filtration (top) or by SDD-AGE (middle). The membranes were processed for immunodetection with anti-mCherry antibody. Separate analysis by SDS-PAGE and immunoblotting for Pgk1 served as a loading control. Representative results are shown from experiments performed in triplicate. (**D**) Sis1 binds to oligomeric 97Q-Opto in [*PIN*$^+$]. Selected samples from (A) were analyzed by SDD-AGE and the membrane was processed for immunodetection with anti-Sis1 antibody. Separate analysis by SDS-PAGE and immunoblotting for Pgk1 served as a loading control. Representative results are shown from experiments performed in triplicate.

Toxicity correlates with appearance of oligomeric polyQ species

Having established the importance of cellular background on the formation of soluble oligomeric species in the context of stress response induction, we next investigated whether these principles would hold true for other biological effects. Huntingtin exon 1 variants lacking the poly proline region following the glutamine tract in sequence have been shown to exhibit Q-length- and aggregation-dependent toxicity when expressed in yeast cells (Dehay and Bertolotti, 2006; Duennwald et al., 2006a; Duennwald et al., 2006b). To assess whether polyQ-Opto could also be used to reproduce and investigate the effects of toxic polyQ aggregation, we designed polyQΔP-Opto constructs (Figure 32A). Note that the N-terminal cMyc-tag was replaced by a Flag-tag, as this was shown to lead to enhanced toxicity (Duennwald et al., 2006b). Expression of 97QΔP-Opto in [*PIN*$^+$] cells led to a significantly reduced growth rate of cultures compared to a 25QΔP-Opto control (Figure 32B), indicative of toxicity. Growth in constant blue light further exacerbated this growth defect (Figure 32B), consistent with aggravated toxicity by enhanced aggregation through light induction. Interestingly, blue light illumination could not only enhance preexisting toxic effects but also induce the toxicity of a previously non-toxic construct. While expression of 66QΔP-Opto in [*PIN*$^+$] cells did not result in reduced growth in the absence of light, the doubling time for these cells increased significantly upon light activation (Figure 32B). Toxicity correlated inversely with the expression levels of polyQΔP-Opto, as cells are selected for low expression levels of polyQΔP-Opto whenever the conditions would allow them to be toxic. Accordingly, light activation of 66QΔP-Opto expressed in [*PIN*$^+$] cells led to a dramatic reduction in protein levels as assessed by fluorescence-activated cell sorting (FACS) (Figure 32C). Note that the expression levels of tox25Q-Opto seemed to be generally low, likely due a more rapid turnover of this construct. Analogous to our results for HSR induction (Figure 30A), we did not observe toxicity for any tested condition in the [*pin*$^-$] strain (Figure 32B). Moreover, expression levels of polyQΔP-Opto were higher than in the [*PIN*$^+$] strain (Figure 32C).

Oligomers are believed to be crucial for toxic effects of polyQ and other disease-associated proteins in neurodegenerative disorders (Arrasate et al., 2004; Behrends et al., 2006; Haass and Selkoe, 2007; Kayed et al., 2003; Kim et al., 2016; Leitman et al., 2013; Takahashi et al., 2008). We found that toxicity of polyQΔP-Opto strongly correlated with the presence of oligomeric species, as assessed via SDD-AGE analysis (Figure 32D). Not only did

the amount of detected polyQ oligomers increase for 97QΔP-Opto in [*PIN*$^+$] upon light activation, but oligomers also appeared de novo for 66QΔP-Opto in [*PIN*$^+$] cells when

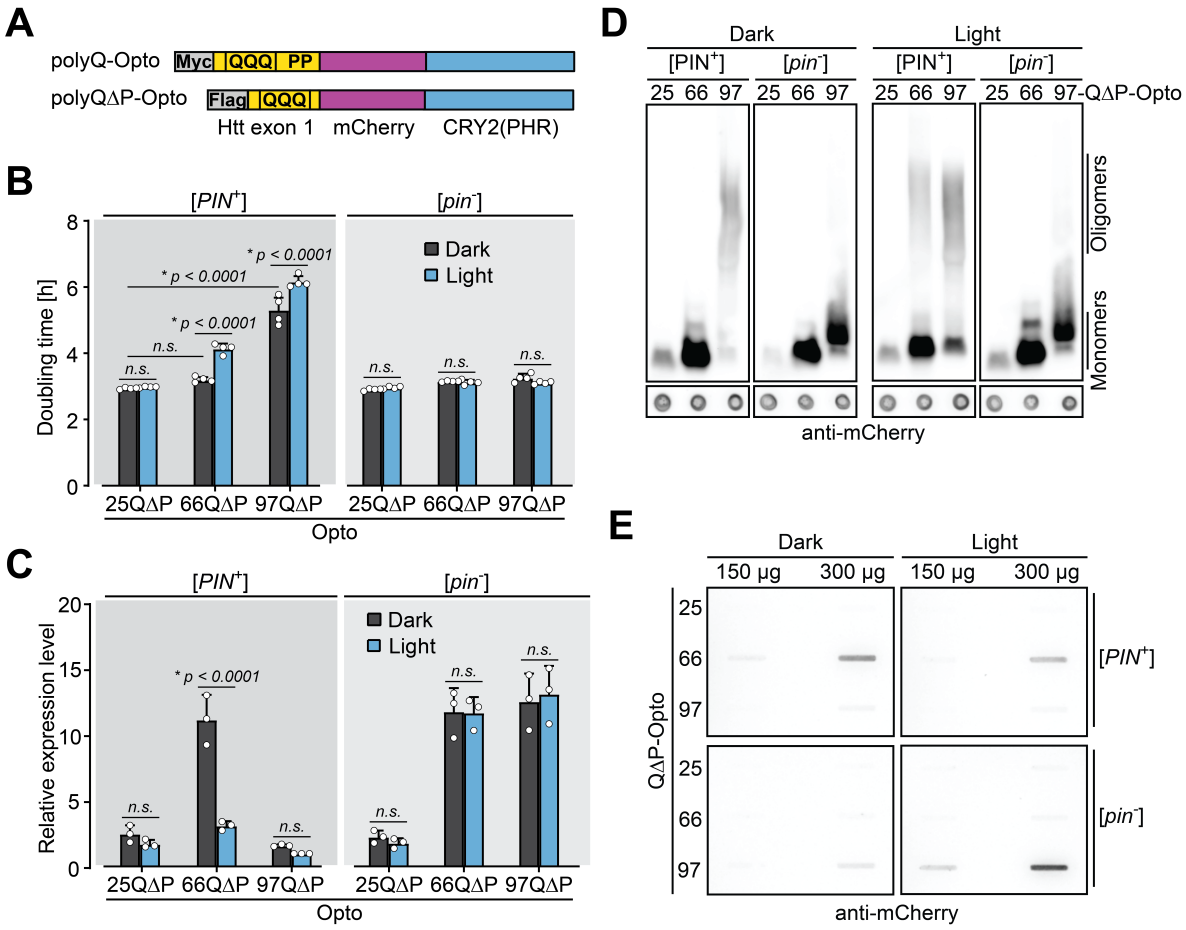

Figure 32: Toxicity coincides with presence of polyQΔP-Opto oligomers, not insoluble inclusions. (**A**) Schematic illustration of polyQΔP-Opto construct design. In contrast to polyQ-Opto, polyQΔP-Opto constructs lack the poly proline region (PP) C-terminal to the polyQ tract and contain an N-terminal Flag-instead of a Myc-tag. (**B**) Light-induced polyQΔP-Opto aggregates are toxic in [*PIN*$^+$]. [*PIN*$^+$] or [*pin*$^-$] cells expressing polyQΔP-Opto from 2µ plasmids under the control of a galactose-inducible promoter were grown either in the absence (Dark) or presence of blue light (Light) in inducing media for ~40 h. Subsequently, OD_{600} was measured at multiple time points during log phase growth and doubling times were calculated. Data represent mean + SD from four independent experiments, *p*-values were calculated by two-way ANOVA with Bonferroni's multiple comparisons test. n.s., not statistically significant. (**C**) Toxic polyQΔP-Opto samples show reduced expression. [*PIN*$^+$] or [*pin*$^-$] cells expressing polyQΔP-Opto from 2µ plasmids under the control of a galactose-inducible promoter were grown as in (B). Cells were harvest and mCherry fluorescence was analyzed via FACS. Data represent mean + SD from three independent experiments, *p*-values were calculated by two-way ANOVA with Bonferroni's multiple comparisons test. n.s., not statistically significant. (**D**) Presence of oligomeric polyQΔP-Opto coincides with toxicity. [*PIN*$^+$] or [*pin*$^-$] cells expressing polyQΔP-Opto from 2µ plasmids under the control of a galactose-inducible promoter were grown as in (B). Lysates normalized to equal amounts of polyQΔP-Opto were analyzed by SDD-AGE. Separate dot blot analysis of same samples served as a loading control. Membranes were processed for immunodetection with anti-mCherry antibody. Representative results are shown from experiments performed in triplicate. (**E**) 97QΔP-Opto forms SDS-resistant aggregates in [*pin*$^-$]. [*PIN*$^+$] or [*pin*$^-$] cells expressing polyQΔP-Opto from 2µ plasmids under the control of a galactose-inducible promoter were grown as in (B). 300 µg of total protein from lysates were treated with SDS/DTT and filtered through a 0.2 µm cellulose acetate membrane. The membrane was processed for immunodetection with anti-mCherry antibody. Representative result is shown from experiments performed in triplicate.

illuminated with blue light (Figure 32D), in line with a clear growth defect under these conditions (Figure 32B). Oligomers were only detected in lysates of [*PIN*$^+$] but not [*pin*$^-$] yeast (Figure 32D). Instead, [*pin*$^-$] cells accumulated substantial amounts of SDS-resistant aggregates (Figure 32E), further emphasizing the notion that large insoluble inclusions are not the primary toxic species.

Taken together, our results demonstrate that the presence of Rnq1 prions not only facilitates polyQ aggregation but also leads to the accumulation of polyQ oligomers exclusively in [*PIN*$^+$] cells. The presence of these soluble polyQ oligomers and their interaction with cellular factors, such as Sis1, further defines downstream biological effects of expanded polyQ including induction of the HSR and growth retardation.

Soluble polyQ interacts with Rnq1 prions

Earlier, we ruled out a general limitation of proteostasis capacity as the reason for the different aggregation behavior of polyQ in isogenic [*PIN*$^+$] and [*pin*$^-$] strains (Figures 22 and 23). Being in a position to investigate biologically relevant aggregation events in these different cell-types, we next sought to identify interactors that could modulate the aggregation process of 97Q-Opto directly and allow the formation of oligomeric species in

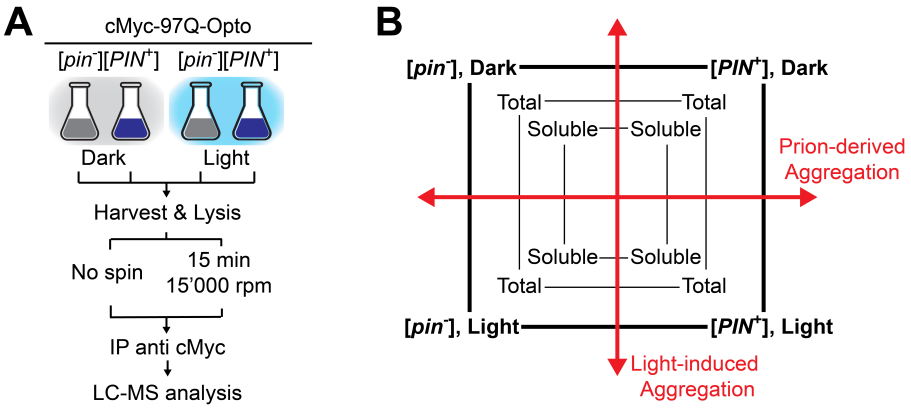

Figure 33: Experimental design of 97Q-Opto interactome analysis. (**A**) Schematic workflow for 97Q-Opto interactome analysis. [*PIN*$^+$] and [*pin*$^-$] cells expressing 97Q-Opto from an integrated endogenous locus under the control of the *GPD* promoter were either grown in the absence (Dark) or presence of blue light (Light) prior to harvest and cell lysis. Samples were split in total lysate and soluble fraction before performing an IP against the cMyc-tag on the N-terminus of 97Q-Opto. Samples were digested on column and analyzed via label-free mass spectrometry. All experimental steps from cell harvest to on column digest were performed in the absence of blue light. (**B**) Comparison of different conditions allows the uncoupling of prion-derived and light-induced aggregation and illuminate the influence of the [*PIN*] prion status on these processes.

[*PIN*$^+$] but not [*pin*$^-$] cells. To this end, we examined the interactome of 97Q-Opto via label-free proteomics following IP (Figure 33A). Inducing polyQ aggregation with light allowed us to investigate the interactome of 97Q-Opto under various conditions in isogenic strains (Figures 33A and B). The comparison of [*PIN*$^+$] and [*pin*$^-$] conditions offered insights into specific interactors that are affected by the prion status of the yeast background. Comparing conditions of growth in either the absence or presence of blue light identified interactors specific to increased aggregation. Finally, dividing each sample into a total lysate and a soluble fraction allowed to further define the stage at which potential interactions are taking place.

We detected 212 significantly enriched interactors (>1.5-fold enriched; $p < 0.05$) of 97Q-Opto in total lysate of [*PIN*$^+$] relative to [*pin*$^-$] cells (Figure 34A). Among the most enriched interactors we identified the prion proteins Rnq1, Pin3 and Sup35, as well as Gts1, Sgt2 and

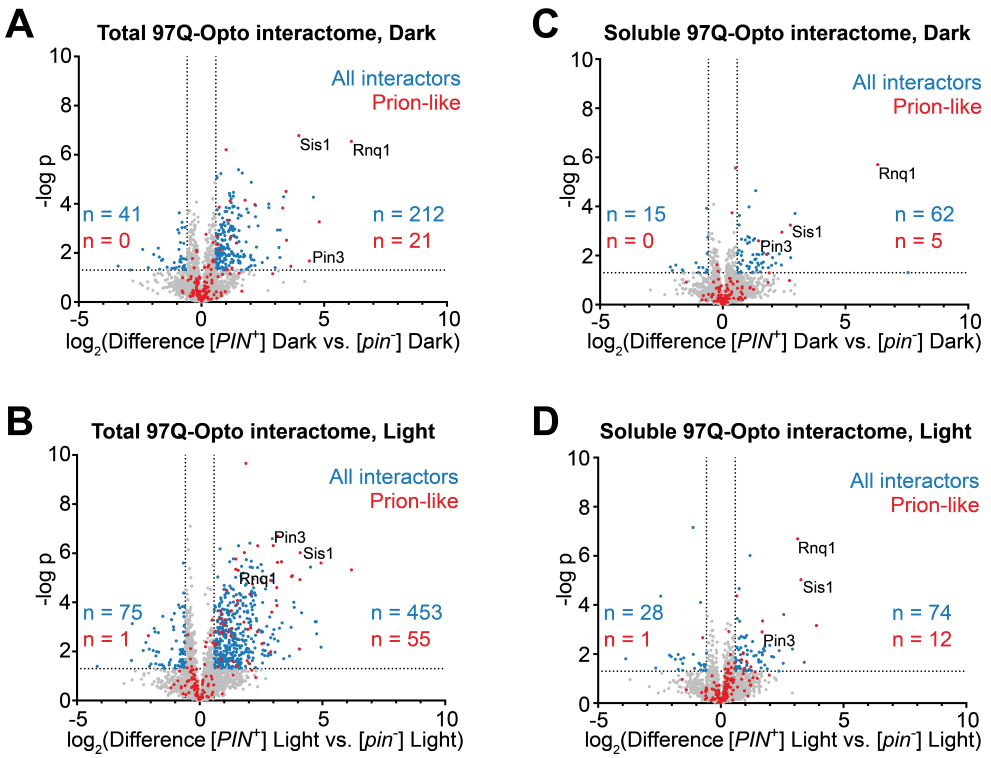

Figure 34: 97Q-Opto is highly interactive in a [PIN$^+$] strain. (**A**, **B**) 97Q-Opto interacts with other proteins preferably in [*PIN*$^+$]. Volcano plot representations of label-free interactome analyses of 97Q-Opto after anti-cMyc IP from total lysates of [*PIN*$^+$] and [*pin*$^-$] cells grown in the absence (A) or presence (B) of light. Data based on four independent experiments. Significantly enriched proteins (> 1.5-fold enrichment, $p < 0.05$) are marked in blue. Prion-like proteins are marked in red. Selected hits are annotated. (**C**, **D**) Soluble 97Q-Opto interacts with Rnq1 in [*PIN*$^+$]. Volcano plot representations of label-free interactome analyses of 97Q-Opto after anti-cMyc IP from soluble lysate fractions (supernatant after centrifugation at 15'000 x g) of [*PIN*$^+$] and [*pin*$^-$] cells grown in the absence (C) or presence (D) of light. Data based on four independent experiments. Significantly enriched proteins (> 1.5-fold enrichment, $p < 0.05$) are marked in blue. Prion-like proteins are marked in red. Selected hits are annotated.

Sis1, which have previously been described as prion-like proteins based on the presence of characteristic low complexity sequences (Alberti et al., 2009). The number of interactors increased to 453 upon illumination of cells with blue light (Figure 34B). These results were not only in line with the enhanced aggregate formation of 97Q-Opto as a result of light induction but also with previous studies showing that polyQ aggregates possess the ability to interact with and sequester a wide range of proteins, including proteostasis components and prion-like proteins (Kim et al., 2002; Kim et al., 2016; Park et al., 2013; Ripaud et al., 2014).

Given the importance of soluble polyQ oligomers in mediating biological effects, crucial interactions of 97Q-Opto and its partner most likely happen early, at a soluble level. An analysis of the soluble lysate fractions (supernatant after centrifugation at 15’000 x g)

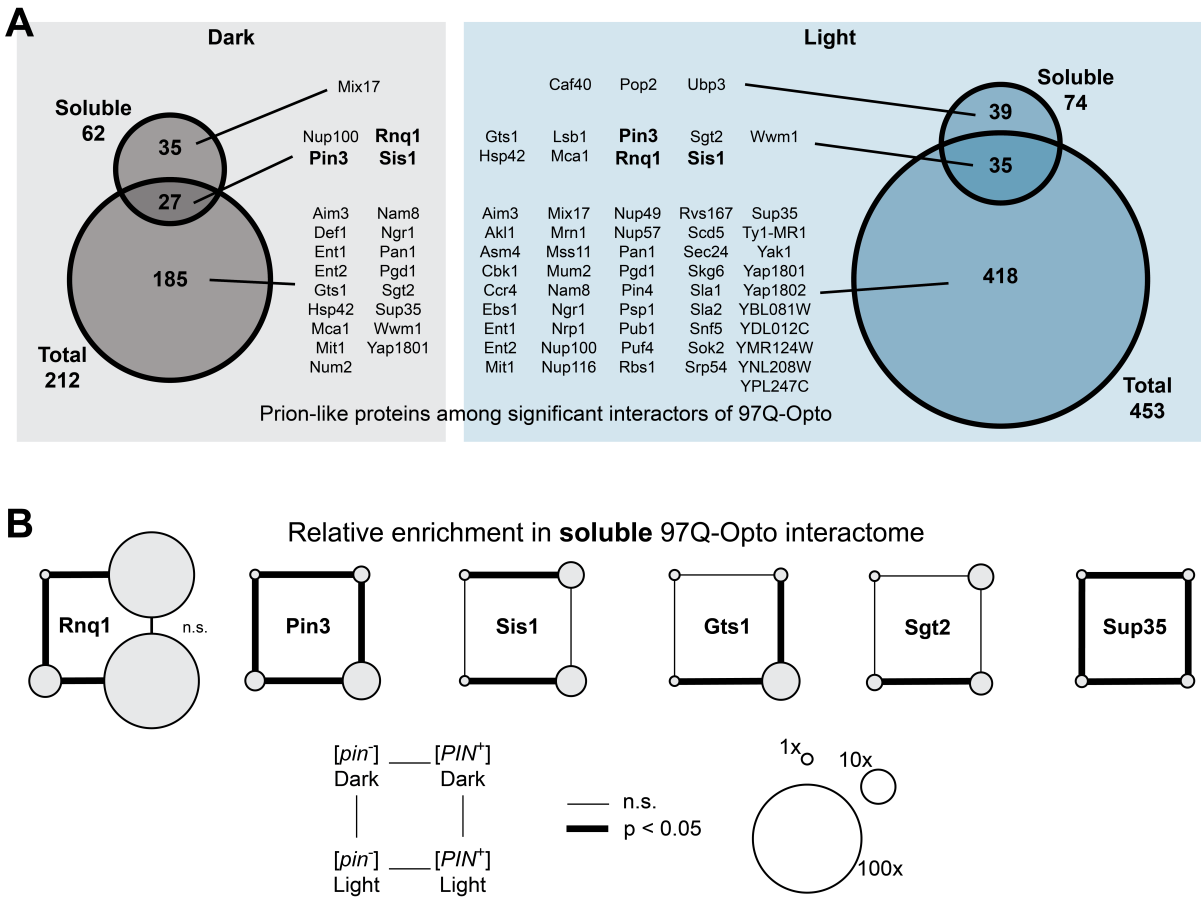

Figure 35: Soluble 97Q-Opto interacts with Rnq1 prions in [PIN⁺]. (**A**) Overlap of interactors of soluble (top circles, related to Figures 34C and D) or total (bottom circles, related to Figures 34A and B) 97Q-Opto in [*PIN*⁺] in the absence (Dark, left) or presence of blue light (Light, right). Prion-like interactors are annotated. (**B**) Schematic representation of the relative enrichment of selected prion-like proteins in the interactomes of 97Q-Opto after anti-cMyc IP from soluble lysate fractions. Data based on four independent experiments. Weight of connecting line between conditions indicates significance (bold = $p < 0.05$), area of circle represents relative enrichment normalized to the least enriched condition for each protein. n.s., not statistically significant.

detected 62 significant interactors of 97Q-Opto in [*PIN*$^+$] cells (Figure 34C), increasing only slightly to 72 upon blue light illumination (Figure 34D). Many interactors that were identified in the total 97Q-Opto interactome in [*PIN*$^+$] cells were also found among its soluble interactors, including Rnq1, Pin3 and Sis1 as well as other prion-like proteins generally rich in glutamine and asparagine residues (Figures 35A and 34). The interaction of these factors agrees with our earlier findings and previously published literature demonstrating that polyQ proteins are able to interact with proteins with similar biophysical characteristics (Kayatekin et al., 2014; Ripaud et al., 2014; Wolfe et al., 2014). Remarkably, Rnq1 was at least ~ 10-fold more enriched in the soluble 97Q-Opto interactome of [*PIN*$^+$] cells and ~ 10-100-fold more abundant (based on intensity based absolute quantification, iBAQ (Schwanhäusser et al., 2011)) than the other prion-like proteins, reaching a molar ratio of soluble polyQ to Rnq1 of ~ 5:1 (Figure 35B).

The proteomic analyses revealed that 97Q-Opto interacts strongly with cellular proteins. While its prion-dependent, aggregated form seems to be the most interactive species, interactions taking place on the soluble level are crucial for understanding the difference between the behavior of polyQ in [*PIN*$^+$] and [*pin*$^-$] strains. The interaction of soluble 97Q-Opto with Rnq1 is specific for the [*PIN*$^+$] prion state, in line with a model in which Rnq1 prions serve as a catalyst to facilitate polyQ aggregation and oligomer formation via templated cross-seeding.

PolyQ oligomers form through direct interaction with Rnq1 prions

To further test this model of prion-mediating templating, we performed *in vitro* aggregation assays of purified Huntingtin exon 1 based on a previously established protocol (Muchowski et al., 2000; Scherzinger et al., 1997) (Figure 36A). In brief, expanded polyQ protein can be expressed recombinantly and purified in a soluble form when fused to a glutathion S-transferase (GST) solubility tag. After proteolytic removal of this solubility tag via an engineered PreScission protease cleavage site, the released polyQ fragment rapidly forms SDS-insoluble aggregates. Aggregation can be monitored via filter retardation or SDD-AGE analysis. We performed experiments with a 54Q-expansion protein (Htt54Q) as proteins with longer polyQ expansions are difficult to produce recombinantly due to their high aggregation

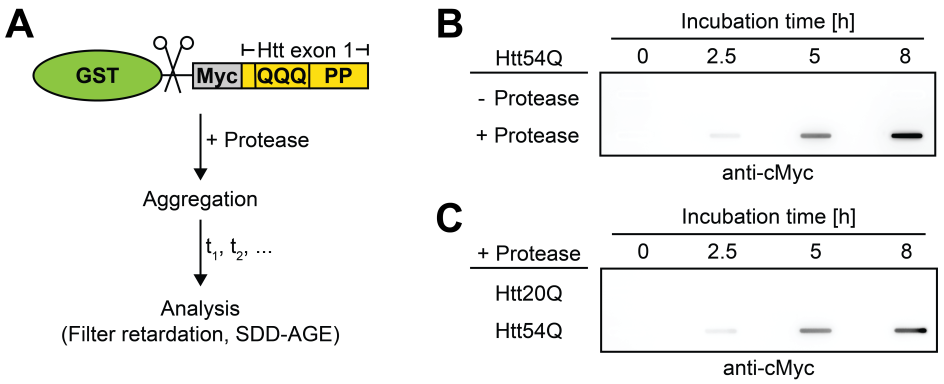

Figure 36: In vitro polyQ aggregation assay. (**A**) Workflow of *in vitro* polyQ aggregation assay. Aggregation is initiated by proteolytic cleavage of GST-cMycHtt54Q. Samples are taken after different time intervals and reactions analyzed by filter retardation assay or SDD-AGE. (**B**) PolyQ forms aggregates *in vitro* upon proteolytic removal of solubility tag. Samples of *in vitro* aggregation reactions of Htt54Q with or without the addition of protease to remove the GST solubility tag were taken at indicated time points of incubation. Samples were treated with SDS/DTT before they were filtered through a 0.2 µm cellulose acetate membrane. Membrane was processed for immunodetection with anti-cMyc antibody. A representative result is shown from experiments performed in triplicate. (**C**) Aggregation of polyQ *in vitro* is Q-length dependent. Samples of *in vitro* aggregation reactions of Htt20Q or Htt54Q were taken at indicated time points after addition of protease to remove the GST solubility tag and analyzed as in (B). A representative result is shown from experiments performed in triplicate.

propensity (Scherzinger et al., 1997). *In vitro*, Htt54Q, but not Htt20Q, selectively formed large SDS-resistant aggregates upon proteolytic removal of the GST solubility tag, as assessed via filter retardation (Figures 36B and C).

When reactions were performed in the presence of diluted cell lysate from either [*PIN*$^+$] or [*pin*$^-$] yeast cells (4.4 mg total protein/mL), formation of large SDS-resistant aggregates was delayed significantly in both samples (Figure 37A). Prevention of aggregation occurred irrespective of the prion status of the yeast strain, suggesting equal anti-aggregation activities in both strains. These observations could not be explained by a general protein effect, as the presence of ovalbumin (OVA) at equivalent concentration (4.4 mg/mL) did not delay formation of large aggregates significantly (Figure 37B). Furthermore, neither the presence of ovalbumin nor of yeast cell lysate prevented the proteolytic removal of the GST-tag from Htt54Q (Figure 37C).

We could not identify any oligomeric species when aggregation reactions in the presence of yeast lysate were analyzed via SDD-AGE (Figure 38A), suggesting that the concentration of Rnq1 prions in the diluted cell lysate was too low to recapitulate the observations *in vivo*. As the dilution of lysate is inevitable due to experimental constraints, we overexpressed *RNQ1-GFP* in [*PIN*$^+$] and [*pin*$^-$] cells to approach physiological Rnq1

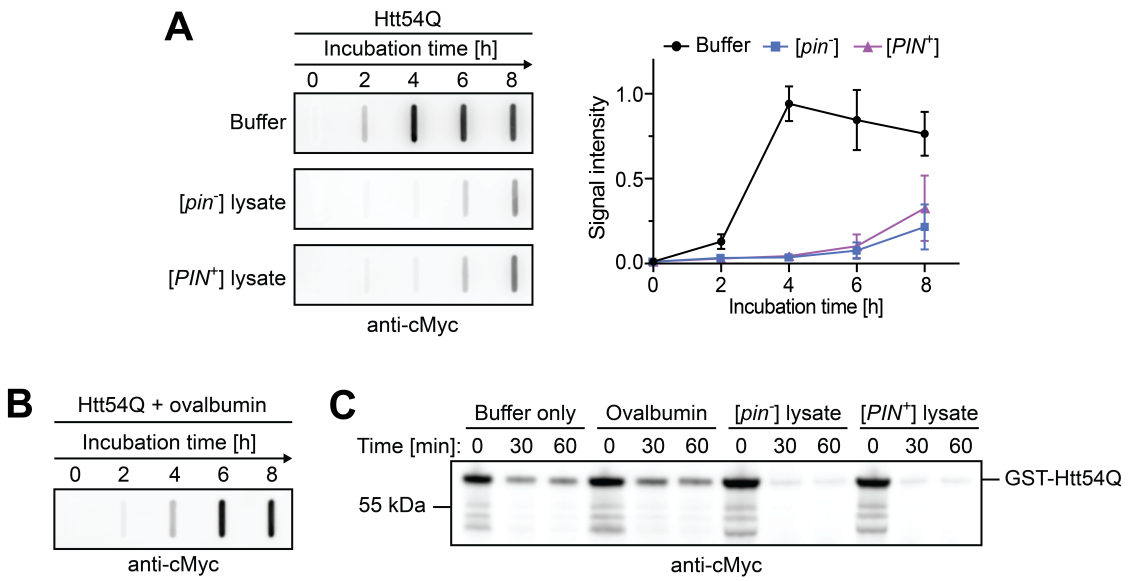

Figure 37: Addition of yeast lysate delays aggregation of polyQ in vitro. (**A**) Presence of yeast lysate delays aggregation of polyQ *in vitro*. Samples of *in vitro* aggregation reactions of Htt54Q in the presence of reaction buffer or yeast lysate (4.4 mg total protein/mL) from either [*pin*$^-$] or [*PIN*$^+$] strains were taken at indicated time points after addition of protease to remove the GST solubility tag. Samples were treated with SDS/DTT and filtered through a 0.2 µm cellulose acetate membrane. Membranes were then processed for immunodetection with anti-cMyc antibody. Representative results are shown from experiments performed in triplicate. Membranes were analyzed via densitometry. Data represent mean ± SD. Each replicate was normalized to the most intense data point. (**B**) Presence of ovalbumin does not significantly alter aggregation of polyQ *in vitro*. Samples of *in vitro* aggregation reaction of Htt54Q in the presence of ovalbumin (4.4 mg/mL) were taken at indicated time points after addition of protease to remove the GST solubility tag. Samples were analyzed via filtration as in (A). A representative result is shown from experiments performed in triplicate. (**C**) Presence of yeast lysate does not prevent the proteolytic removal of the solubility tag. *In vitro* aggregation reactions of Htt54Q were performed either in buffer only, in the presence of ovalbumin or yeast lysate from [*PIN*$^+$] or [*pin*$^-$] cells. Samples were taken at indicated time points before (0) or after (30, 60) addition of protease to remove the GST solubility tag and were analyzed by SDS-PAGE and immunoblotting for cMyc. Representative result is shown from experiments performed in triplicate.

concentrations in the *in vitro* reaction setup. As shown earlier, Rnq1-GFP is soluble in [*pin*$^-$] cells but forms prions in [*PIN*$^+$] and is therefore suited for artificially increasing the Rnq1 prion concentration in the lysate (Figure 21). Indeed, when *in vitro* aggregation reactions were performed in the presence of [*PIN*$^+$] and [*pin*$^-$] lysate of *RNQ1-GFP* overexpressing cells, oligomer formation could readily be detected in the [*PIN*$^+$] but not the [*pin*$^-$] background, recapitulating our *in vivo* observations (Figure 38B). In addition to the polyQ oligomers, we also observed the formation of larger polyQ aggregates, which migrated on the top of the SDD-AGE gel (Figure 38B). Importantly, formation of polyQ oligomers coincided with a decrease in monomeric species (Figure 38B), indicating that Rnq1 prions directly mediate the *de novo* formation of oligomers. Immunoblotting for Rnq1-GFP revealed the presence of Rnq1 prion aggregates specifically in [*PIN*$^+$] lysate (Figure 38C). These prions migrated

independently of the polyQ oligomers (Figure 38C), indicating that these two species did not interact stably under the conditions of SDD-AGE, in line with a catalytic templating function of Rnq1 prions.

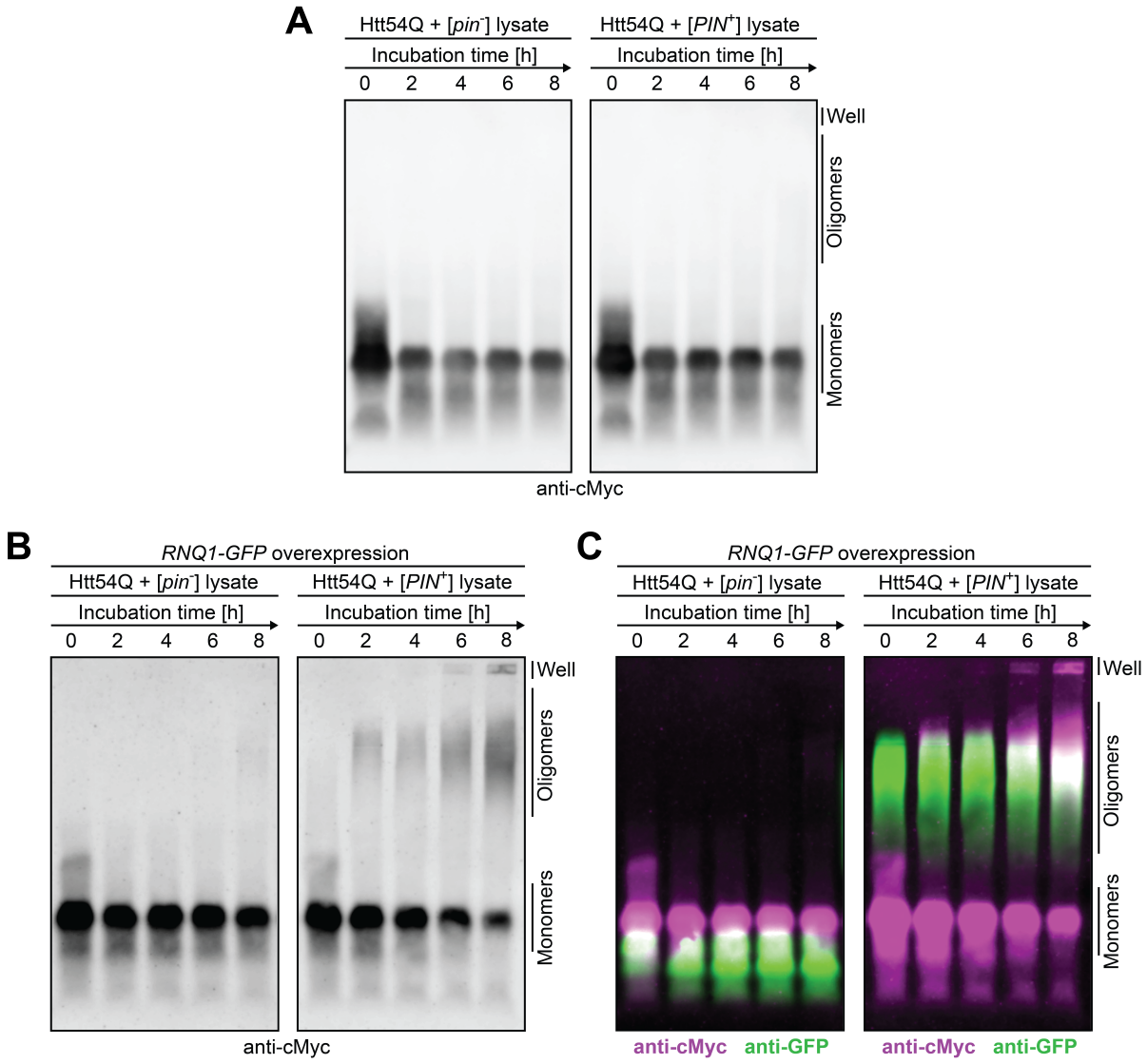

Figure 38: Interaction of soluble polyQ with Rnq1 prions catalyzes polyQ oligomer formation in vitro. (**A**) Presence of yeast lysate does not lead to oligomer formation. Samples of *in vitro* aggregation reactions of Htt54Q in the presence of yeast lysate (4.4 mg total protein/mL) from either [*pin*$^-$] or [*PIN*$^+$] strains were taken at indicated time points after addition of protease to remove the GST solubility tag. Samples were analyzed via SDD-AGE. Membranes were processed for immunodetection with anti-cMyc antibody. Representative result is shown from experiments performed in triplicate. (**B**) Interaction with Rnq1 prions leads to the formation of polyQ oligomers *in vitro*. Aggregation of Htt54Q was initiated by proteolytic removal of the GST solubility tag in *in vitro* reactions containing yeast lysate (4.4 mg total protein/mL) from [*pin*$^-$] or [*PIN*$^+$] cells overexpressing *RNQ1-GFP*. Samples were taken at indicated time points after addition of protease and analyzed by SDD-AGE as in (A). Membrane was processed for immunodetection with anti-cMyc antibody. Representative result is shown from experiments performed in triplicate. (**C**) Oligomeric species of polyQ and Rnq1-GFP prions co-migrate. Membrane shown in (B) was stripped, blocked, and processed for immunodetection with anti-GFP antibody. Signals from anti-cMyc (magenta) and anti-GFP (green) detection are overlaid. Representative result is shown from experiments performed in triplicate.

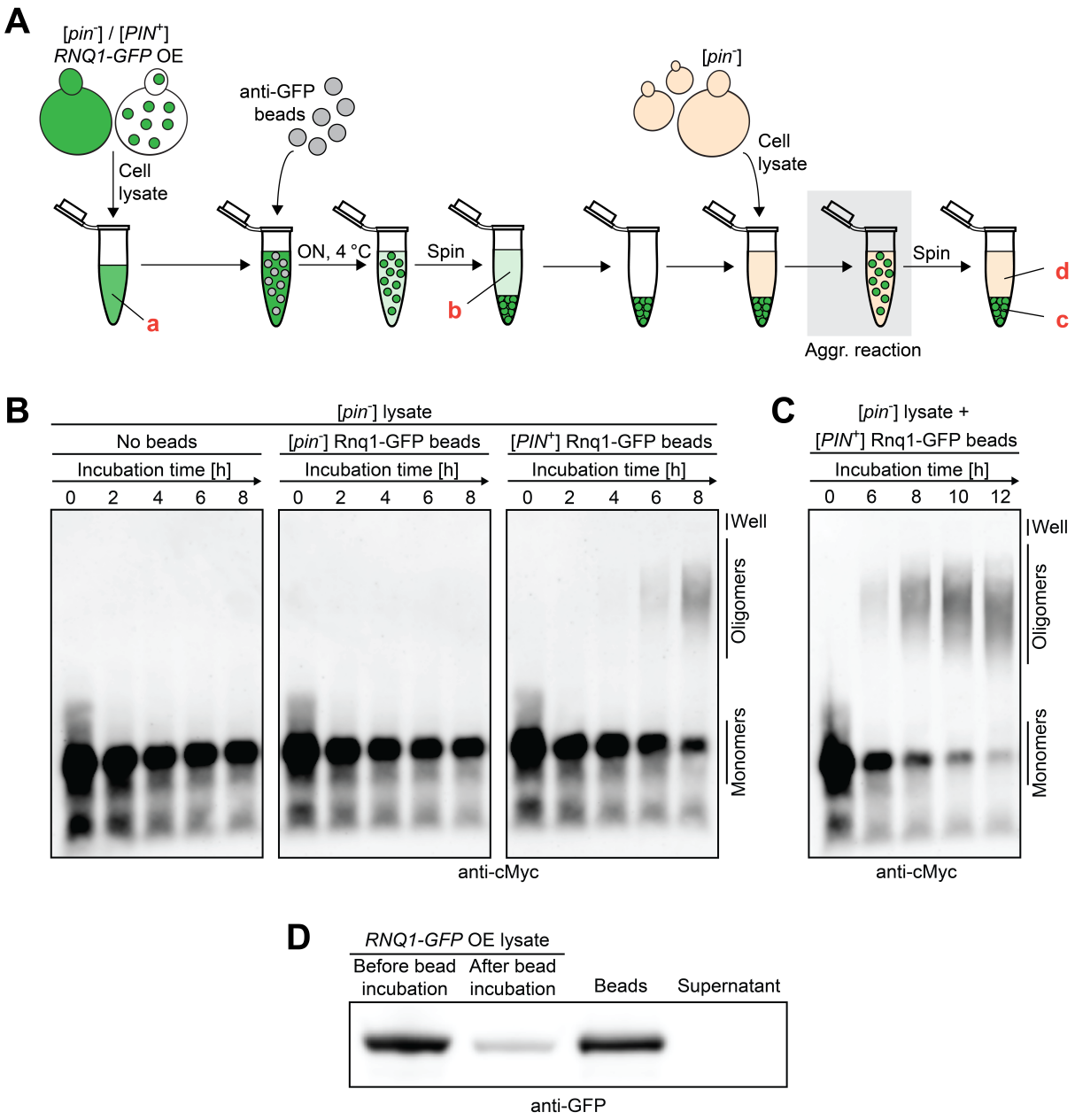

Figure 39: PolyQ oligomers form through direct interaction with Rnq1 prions. (**A**) Schematic workflow of sample preparation for *in vitro* aggregation reaction in the presence of immobilized Rnq1-GFP. Anti-GFP beads were added to lysate of [*pin*$^-$] or [*PIN*$^+$] cells overexpressing *RNQ1-GFP* and incubated overnight. Rnq1-GFP-loaded beads were isolated and mixed with [*pin*$^-$] cell lysate. Htt54Q aggregation reactions were performed in this suspension. At different time points, supernatant was separated from the beads by centrifugation and samples were taken for analysis by SDD-AGE (see (B) and (C)). Throughout the preparation process and the aggregation reaction, samples were taken for SDS-PAGE analysis (a, before bead incubation; b, after bead incubation; c, beads; d, supernatant; see (D)) (**B**) Immobilized Rnq1 prions can catalyze polyQ oligomer formation *in vitro*. Aggregation reactions were performed in [*pin*$^-$] cell lysate (4.4 mg total protein/mL) in the presence of Rnq1-GFP-loaded beads from either [*pin*$^-$] or [*PIN*$^+$] cells overexpressing *RNQ1-GFP*. As a control, aggregation reaction was performed in [*pin*$^-$] cell lysate without addition of beads. Analysis by SDD-AGE, followed by immunodetection with anti-cMyc antibody. A representative result is shown from experiments performed in triplicate. (**C**) PolyQ oligomer formation plateaus after extended reaction time. Aggregation reaction was performed as in (B), but extended time points were chosen. Analysis by SDD-AGE, followed by immunodetection with anti-cMyc antibody. A representative result is shown from experiments performed in triplicate. (**D**) Rnq1 prions remain immobilized to beads throughout the aggregation reaction. Samples taken at different stages of the experimental procedure described in (A) were analyzed for the presence of Rnq1-GFP by SDS-PAGE and immunodetection with anti-GFP antibody. Rnq1-GFP amounts loaded are directly comparable. A representative result from experiments performed in triplicate is shown.

To further test the dynamic nature of the interaction of polyQ with Rnq1 prions, we immobilized Rnq1-GFP prions on anti-GFP beads and added them to [*pin*$^-$] lysate, which does not support the formation of Htt54Q oligomers (Figures 39A and 38A). Addition of beads incubated with Rnq1-GFP aggregates of [*PIN*$^+$] cells but not with soluble Rnq1-GFP of [*pin*$^-$] cells allowed the formation of oligomeric Htt54Q even in non-permissive [*pin*$^-$] lysate (Figure 39B). The appearance of oligomers in the presence of immobilized Rnq1 prions was delayed compared to a reaction in [*PIN*$^+$] lysate with Rnq1-GFP overexpression (Figures 39B and 38B), most likely due to the limited mobility of bead-bound prions and less accessible surface. PolyQ oligomer formation plateaued after approximately 10 h of incubation (Figure 39C). While the polyQ oligomers were detected in the supernatant fraction of the aggregation reaction, Rnq1-GFP aggregates remained bound to the beads throughout the assay (Figure 39D), confirming the transient nature of the interaction of Rnq1 prions with polyQ.

Taken together, proteomic analysis and aggregation reactions *in vitro* revealed the transient interaction of soluble polyQ with Rnq1 prions specifically in the [*PIN*$^+$] background. Rnq1 prions not only function as catalysts to stimulate polyQ aggregation but also mediate the formation of polyQ oligomers, which are responsible for downstream biological effects such as HSR induction and toxicity.

Discussion

The yeast *S. cerevisiae* has proven to be an invaluable model for the study of protein aggregation associated with expanded polyQ proteins in Huntington's disease and other related polyQ pathologies (Di Gregorio and Duennwald, 2018; Duennwald, 2011; Khurana and Lindquist, 2010; Winderickx et al., 2008). While among the simplest eukaryotic model organisms, yeast resemble mammalian cells in their varied susceptibility to the aggregation propensity of polyQ proteins (Meriin et al., 2002; Osherovich and Weissman, 2001). Here we took advantage of the dependence of polyQ aggregation and toxicity on the presence of prions to obtain insight into how the cellular environment effects the aggregation process. We overcame the prion requirement using a novel optogenetic approach to induce polyQ aggregation via the photoreceptor protein CRY2 even in a non-permissive, prion-free [*pin*$^-$] yeast strain, enabling the comparison of polyQ aggregation in isogenic [*PIN*$^+$] and [*pin*$^-$] cells. While the light-induced aggregates in [*pin*$^-$] cells replicated typical characteristics of polyQ inclusions in [*PIN*$^+$] strains, including partial SDS-resistance, solubility in formic acid and the ability to sequester proteins with polyQ sequences below the threshold for aggregation, they failed to result in biological consequences such as induction of the HSR or toxicity. We presented evidence that these biological effects depend on the prion-dependent aggregation status of polyQ, specifically on the prion-mediated formation of soluble oligomers, in line with previous reports implicating toxic oligomers in neurodegeneration (see Chapter I; Arrasate et al., 2004; Behrends et al., 2006; Haass and Selkoe, 2007; Kayed et al., 2003; Kim et al., 2016; Klaips et al., 2020; Leitman et al., 2013; Takahashi et al., 2008). These toxic oligomers are not generated in [*pin*$^-$] cells, even when polyQ aggregation is induced optogentically. We found that direct interactions of soluble polyQ with Rnq1 prions, rather than an indirect effect of limited proteostasis capacity in [*PIN*$^+$] cells, is the cause of polyQ aggregation and specifically the formation of oligomeric species. We confirmed this interaction both *in vivo* and *in vitro*. Thus, while the prion requirement can be circumvented to induce large SDS-resistant aggregates artificially with polyQ-Opto in the [*pin*$^-$] background, the lack of Rnq1 prions prevents the formation of soluble oligomeric species and their biological effects (Figure 40A). In [*PIN*$^+$], the polyQ aggregation trajectory is profoundly influenced by the presence of Rnq1 prions. Here, polyQ forms large SDS-resistant aggregates as well as soluble oligomers, through direct templating on Rnq1 prions. The oligomers are highly interactive and sequester a wide

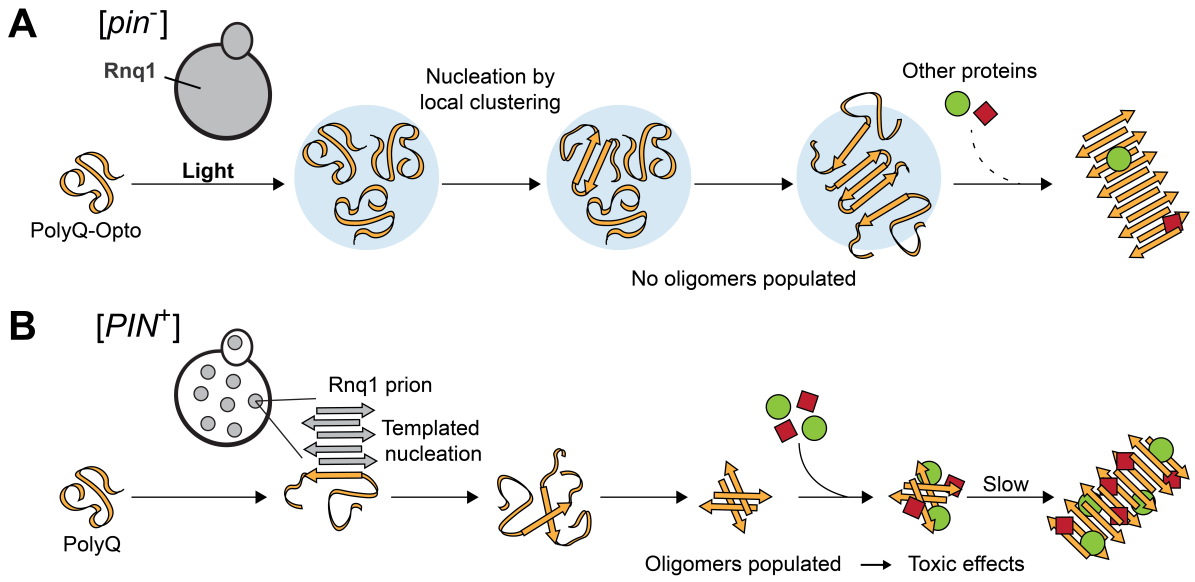

Figure 40: Model. (**A**) Optogenetic aggregation in [*pin*⁻] cells. Light-induced condensate formation of polyQ-Opto monomers facilitates aggregate nucleation of locally clustered polyQ sequences and leads to the formation of SDS-resistant aggregates with limited ability to sequester other proteins. Accumulation of soluble polyQ oligomers as aggregation intermediates is prevented. (**B**) Aggregation in [*PIN*⁺] cells. Soluble polyQ protein interacts with Rnq1 prions, which offer a surface for templating aggregation. Through this interaction, polyQ monomers adopt aggregation-competent secondary structures and interact with similarly misfolded polyQ proteins, resulting in the formation of soluble oligomers. These oligomers convert slowly to insoluble aggregates and engage in aberrant interactions with multiple endogenous proteins, resulting in toxic effects reflected in growth inhibition and the induction of the HSR.

range of cellular proteins, contributing to toxic effects such as heat stress response induction and toxicity (Figure 40B). Activation of polyQ-Opto with light in [*PIN*⁺] cells further increased formation of aggregated species and enhanced their inherent biological consequences.

The scope of the phenomenon that we describe here extends beyond the already established dependence of polyQ aggregation on the prion state of a yeast strain (Meriin et al., 2002; Osherovich and Weissman, 2001). Our finding that not a generalized proteostasis collapse but the direct interaction of polyQ with other protein aggregates – here the prion form of Rnq1 –catalyzes the aggregation of polyQ into toxic oligomeric species suggests a possible cause for the aggregation of disease-related proteins in the neuronal systems of higher organisms. However, while our results are in line with the well-established phenomenon of cross-seeding of misfolded proteins In the neuronal system (Giasson et al., 2003; Guo et al., 2013; Morales et al., 2013; Vasconcelos et al., 2016), the question arises how this hypothesis can be reconciled with the long-held belief that a general decrease in proteostasis capacity with age directly causes aggregation of disease-relevant proteins

(Douglas and Dillin, 2010; Hipp et al., 2014; Klaips et al., 2018). We propose that the well-established decline in proteostasis capacity with progressing age leads to the formation of endogenous prion-like protein aggregates, which in turn function as catalysts to template the aggregation of polyQ and lead to the formation of toxic oligomers, causing the manifestation of neurodegenerative phenotypes. Similar cross-seeding events could also play a pathological role in other neurological disorders.

To determine whether our hypothesis is compatible with previous reports in higher organisms, we collated data from three depositories for mammalian prion-like proteins (Angarica et al., 2014; Iglesias et al., 2019; March et al., 2016). Such proteins possess extended low complexity regions (LCRs), rendering them aggregation prone due to their biophysical characteristics (Kato et al., 2012; Sprunger and Jackrel, 2021; Vecchi et al., 2020; Zbinden et al., 2020). It has been shown that soluble polyQ oligomers are highly interactive in a mammalian cell culture model, binding a plethora of cellular factors ranging from proteostasis components to transcription or RNA processing factors (Kim et al., 2016). We found a significant enrichment of prion-like proteins among these interactors of soluble polyQ, similar to our observations in yeast. Among the interactors of soluble polyQ species are also TDP43 and FUS, proteins associated with other neurodegenerative diseases (Chen-Plotkin et al., 2010; Deng et al., 2014; Zbinden et al., 2020). In addition, TDP43 has been demonstrated to participate in cross-seeding aggregation of Tau *in vitro* (Montalbano et al., 2020). Interestingly, the LCR amino acid composition of many of these interactors of soluble polyQ exhibit an enrichment of glutamine, asparagine, and glycine residues, similar to LCRs found in the prion domain of yeast Rnq1 (Figure 41A).

Neurons are particularly sensitive to pathological protein aggregation, such as polyQ (Fu et al., 2018; Saudou and Humbert, 2016). We next carried out an in-depth analysis of previously published extensive proteomics data on primary cultured mouse brain cells and corresponding brain tissue samples (Sharma et al., 2015) and found a strong enrichment of aggregation-prone prion-like proteins in the proteome of neurons compared to other cell types such as oligodendrocytes, astrocytes or microglia (Figure 41B), possibly rendering them more vulnerable to general protein aggregation. Revisiting proteomics data for age-dependent protein aggregation in the nematode *C. elegans* showed that the few prion-like proteins annotated for this organism are not only among the proteins with the highest

aggregation propensity (Figure 41C), but these proteins also display pronounced age-dependence of aggregation (Vecchi et al., 2020; Walther et al., 2015) (Figure 41D), a phenomenon recently recapitulated in the aging vertebrate brain (Harel et al., 2022).

In summary, our experimental results in *S. cerevisiae* and *in vitro* combined with the analysis of previous studies in higher model organisms suggest a role of general, age-dependent protein aggregation in the pathology of neurodegenerative diseases. The decrease of proteostasis capacity with age causes many proteins, especially aggregation-prone prion-

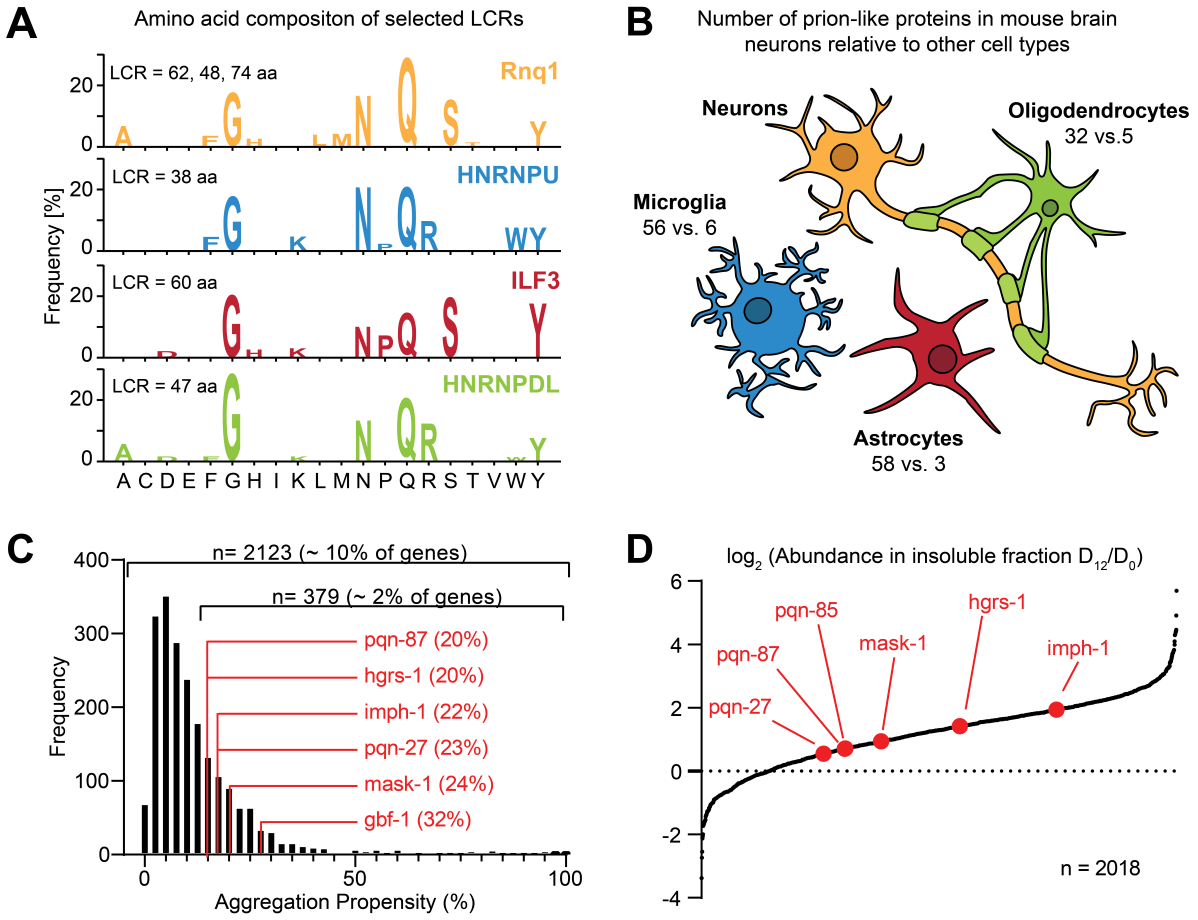

Figure 41: Prion hypothesis of polyQ aggregation. (**A**) LCRs of mammalian prion-like proteins share similarity with the prion domain of Rnq1. The amino acid composition of LCRs of yeast Rnq1 and mammalian interactors of soluble polyQ, HNRNPU, ILF3 and HNRNPDL, is shown. LCRs were identified using the SEG algorithm (Wootton and Federhen, 1993). For Rnq1 the average composition of the three LCRs located in the prion-domain is shown. Lengths of LCRs are indicated. (**B**) Prion-like proteins are enriched in neurons. Proteome analysis from Sharma et al. (2015) indicating the number of significantly enriched prion-like proteins identified in neurons extracted from mouse brain in comparison to astrocytes, microglia, and oligodendrocytes. (**C**) Prion-like proteins are among the most aggregation prone proteins in *C. elegans*. Aggregation propensities calculated in Walther et al. (2015) as percentage of protein found in the insoluble fraction relative to its total amount. Prion-like proteins are annotated. (**D**) Prion-like proteins become insoluble with age in *C. elegans*. Abundance of individual proteins found in the insoluble fraction comparing old (day 12, D_{12}) and young (day 0, D_0) worms, as determined in Walther et al. (2015). Prion-like proteins are annotated.

like proteins, to undergo aggregation. Once these aggregates are formed, they present a potent interaction partner and can cross-seed the aggregation of disease-relevant proteins such as Huntingtin. Oligomeric species that arise during this catalytic templating have the potential to confer biological consequences. Cells with high expression levels of prion-like proteins, such as neurons, are particularly at risk of experiencing global protein aggregation, explaining the selective vulnerability observed in many neurological disorders despite the ubiquitous expression pattern of disease proteins including Huntingtin or Tau. Therapeutic studies in neurodegenerative diseases have so far mainly been focused on amyloid aggregates that are notoriously tough to fight. Refocusing on reducing the load of “benign” protein aggregation through increasing proteostasis capacity could therefore present a promising strategy in reducing or delaying the aggregation of disease-relevant proteins.

Conclusions

Neurodegenerative diseases have been investigated for more than a century and yet we are far from understanding the mechanisms underlying these maladies. Despite its simple unicellular organization, the yeast *S. cerevisiae* has been an important model organism to study biochemical principles of neurodegeneration such as disease-associated protein misfolding and aggregation. Many findings could be reproduced in higher model organisms and mammalian neuronal cell culture, underscoring the immense contribution research in *S. cerevisiae* has made towards tackling of what amounts to one of the major medical challenges of our time. In this work, we used a model protein based on polyQ-expanded Huntington exon 1 and applied recent technological advances in the field of optogenetics. We demonstrated how pathological protein aggregation is influenced by the yeast strain background, how cellular factors such as chaperones can influence aggregate formation and morphology, and how all of these contributions define downstream biological effects such as heat stress response induction and toxicity. Based on our results obtained in *S. cerevisiae*, we confirmed conservation of these principles in mammalian cells.

The phenomenon of selective vulnerability to protein aggregation known from the neuronal system has also been observed in yeast. Here, we demonstrated how preexisting protein aggregates in the form of the Rnq1 prion catalyze the aggregation of expanded polyQ, both *in vivo* and *in vitro*, and showed that this transient cross-seeding mechanism leads to the formation of soluble polyQ oligomers responsible for biological effects such as toxicity. After in-depth analysis of previously published proteomics data, we suggest a similar underlying principle of templated cross-seeding for pathological protein aggregation in higher eukaryotic organisms. Our findings offer a synthesis of two prevalent models explaining the appearance of disease-associated protein aggregates: cross-seeding and proteostasis decline. We suggest that age-associated decline in proteostasis capacity increases the risk of aggregation of prion-like proteins, which, in turn, could template aggregation of disease-relevant proteins such as Huntingtin in neurological disorders.

The cytosolic heat stress response is a powerful defense mechanism of cells to counteract proteostasis imbalance and the aberrant misfolding and aggregation of proteins. We observed that higher levels of the Hsp40 Sis1 lead to a more effective recognition of

pathological protein aggregates and the activation of beneficial stress response pathways. However, cells limit the expression of Sis1 to avoid maladaptation and overshooting stress responses. Our finding illustrates how the proteostasis network has evolved to a fine-tuned system that needs to keep the balance between sensitive and dynamic responses towards compromising conditions and safeguarding valuable energy and chemical resources to remain able to fight detrimental stresses effectively.

The findings we presented in this work not only help advance our understanding of biochemical principles of disease-relevant protein aggregation and cellular responses to it, but they also offer important insights for the development of therapeutic strategies for neurodegenerative diseases. So far, therapies have been focused on the clearance of specific pathological inclusions, rather than on ways to generally improve proteostasis, in order to reduce toxicity. Our work, together with many previously published studies, suggests that not large SDS-resistant inclusion but soluble oligomeric species represent the primary toxic species. Thus, intervention at later stages of aggregate manifestation may miss the real problem. In contrast, boosting proteostasis capacity, e.g., through intermittent pharmacologic induction of the cytosolic stress response, has the potential to decrease the load of prion-like protein aggregates that naturally appear with an age-dependent decline in proteostasis capacity. In turn, this can help reduce the likelihood of disease-associated protein aggregation, as critical interaction partners for cross-seeding are reduced. We demonstrated that the HSR can be induced in a specific aggregate dependent way by the overexpression of a single proteostasis component, thus minimizing the risk of possible side effects.

Materials and Methods

General materials and methods

In this section, information regarding all materials and methods relevant for both chapters of this work are listed.

Materials

Listed here you will find all materials used in this work, their source (manufacturer, website, etc.) and unique identifier (catalogue number, accession number, etc.).

Antibodies

Antibodies used in this work can be found in Table 1. Listed are the manufacturer as well as the respective catalogue number and unique antibody identifier (RRID).

Table 1: Antibodies used in this work.

Antibodies	Source	Identifier
mCherry Monoclonal Antibody (16D7)	Invitrogen	Cat.#M11217; RRID:AB_2536611
PGK1 Monoclonal Antibody (22C5D8)	Invitrogen	Cat.#459250; RRID:AB_2532235
Anti Sis1(Dnaj) pAb (Rabbit)	Cosmo Bio USA	Cat.#COP-080051; RRID:AB_10709957
Monoclonal Anti-c-Myc antibody produced in mouse	Sigma	Cat.#M5546; RRID:AB_260581
Anti-Rat IgG (whole molecule)–Peroxidase antibody produced in goat	Sigma	Cat.#A9037; RRID:AB_258429
Anti-Mouse IgG (whole molecule)–Peroxidase antibody produced in goat	Sigma	Cat.#A4416; RRID:AB_258167
Anti-Rabbit IgG (whole molecule)–Peroxidase antibody produced in goat	Sigma	Cat.#A9169; RRID:AB_258434

Bacteria strains

Table 2 contains information on bacteria strains that were used in this work, their manufacturer and respective catalogue number.

Table 2: Bacteria strains used in this work.

Bacteria strains	Source	Identifier
E. coli Bl21(DE3)	Sigma	Cat.#69450
E. coli DH5α	Invitrogen	Cat.#18265017

Chemicals, peptides and recombinant proteins

All basic chemical compounds used in this work were either purchased from *Sigma-Aldrich* or *Carl Roth*. Other, specific chemicals, peptides and recombinant proteins are listed in Table 3.

Table 3: Chemicals, peptides and recombinant proteins used in this work.

Chemicals, peptides, and recombinant proteins	Source	Identifier
2-Nitrophenyl β-D-galactopyranoside (ONPG)	Sigma	Cat.#N1127
AatII restriction enzyme	New England BioLabs	Cat.#R0117
AflII restriction enzyme	New England BioLabs	Cat.#R0520
BamHI restriction enzyme	New England BioLabs	Cat#R0136
BD Difco Yeast Nitrogen Base w/o Amino Acids	Fisher Scientific	Cat.#291920
BglII restriction enzyme	New England BioLabs	Cat.#R0144
BsgI restriction enzyme	New England BioLabs	Cat.#R0559
Bsu36I restriction enzyme	New England BioLabs	Cat.#R0524
cOmplete, EDTA-free Protease Inhibitor Cocktail	Roche	Cat.#COEDTAF-RO
Concanavalin A from *Canavalia ensiformis*	Sigma	Cat.#C2010
Cycloheximide	Sigma	Cat.#01810
Doxycycline	Sigma	Cat.#D3072
DraIII restriction enzyme	New England BioLabs	Cat.#R3510
EcoRI restriction enzyme	New England BioLabs	Cat.#R3101
Gibco Geneticin Selective Antibiotic (G418 Sulfate)	Thermo Scientific	Cat.#10131027
Gibco Bacto Peptone	Thermo Scientific	Cat.#211820
Gibco Bacto Yeast Extract	Thermo Scientific	Cat.#212750
Gibson Assembly Master Mix	New England BioLabs	Cat.#2611
GST-PreScission Protease	MPI Biochemistry	N/A
Guanidine-HCl Solution (8M)	Thermo Scientific	Cat.#24115
Herring Sperm DNA Solution	Thermo Scientific	Cat.#15634017
Isopropyl β-D-1-thiogalactopyranoside (IPTG)	Roth	Cat.#CN08.3
KpnI restriction enzyme	New England BioLabs	Cat.#R3142
MluI restriction enzyme	New England BioLabs	Cat#R0198
NdeI restriction enzyme	New England BioLabs	Cat.#R0111
n-Octyl-β-D-glucopyranoside (OGP)	Roth	Cat.#CN23.1
PvuI restriction enzyme	New England BioLabs	Cat.#R0150
Q5 High-fidelity DNA Polymerase	New England BioLabs	Cat.#0491
SacI restriction enzyme	New England BioLabs	Cat.#R3156
SalI restriction enzyme	New England BioLabs	Cat.#R3138
Serratia marcescens DNase	MPI Biochemistry	N/A
SpeI restriction enzyme	New England BioLabs	Cat.#R3133
StuI restriction enzyme	New England BioLabs	Cat.#R0187
T7 DNA Ligase	New England BioLabs	Cat.#0318

Chemicals, peptides, and recombinant proteins	Source	Identifier
Trypsin recombinant, Proteomics Grade	Roche	Cat.#RTRYP-RO
XbaI restriction enzyme	New England BioLabs	Cat.#R0145
XhoI restriction enzyme	New England BioLabs	Cat.#R0146
XmaI restriction enzyme	New England BioLabs	Cat#R0180
SYBR Safe DNA Gel Stain	Thermo Scientific	Cat.#S33102

Commercial assays and kits

All commercial assays and kits that were used in this work are listed in Table 4. The respective manufacturer and corresponding catalogue numbers are specified as well.

Table 4: Commercial assays and kits used in this work.

Commercial assays and kits	Source	Identifier
Bio-Rad Protein Assay Kit	Bio-Rad Laboratories	Cat.#5000001
Immobilon Classico Western HRP Substrate	Millipore	Cat.#WBLUC0500
Pierce Rapid Gold BCA Protein Assay Kit	Thermo Scientific	Cat.#A53227
QIAprep Spin Miniprep Kit	QIAGEN	Cat.#27106X4
Wizard SV Gel and PCR Clean-Up System	Promega	Cat.#A9282

Data

This work produced new mass spectrometry data sets and reanalyzed previously published ones. Information on the source of these data sets as well as their accession number for the public ProteomeXchange database are listed in Table 5.

Table 5: Data generated and analyzed in this work.

Deposited data	Source	Identifier
Proteomic dataset	Chapter II of this study; Gropp et al., 2022	Figures 22, 34, 35 ProteomeXchange: PXD031337
Proteomic dataset (related to Chapter II Discussion)	Kim et al., 2016	Figure 41 ProteomeXchange: PXD003446
Proteomic dataset (related to Chapter II Discussion)	Sharma et al., 2015	Figure 41 ProteomeXchange: PXD001250
Proteomic dataset (related to Chapter II Discussion)	Hosp et al., 2017	Figure 41 ProteomeXchange: PXD004973
Proteomic dataset (related to Chapter II Discussion)	Walther et al., 2015	Figure 41 ProteomeXchange: PXD001364

Software and algorithms

For the analysis of experimental data and acquired images, specialized software platforms and algorithms were used that are listed in Table 6. Wherever applicable, the original publication is referenced together with an online link.

Table 6: Software and algorithms used in this work.

Software and algorithms	Source	Identifier
Fiji – ImageJ Image processing package v1.52p	Schindelin et al., 2012	https://imagej.net/software/fiji/
GO Enrichment Analysis	Ashburner et al., 2000; Gene Ontology, 2021; Mi et al., 2019	http://geneontology.org/
GraphPad Prism v9.3.1	GraphPad Software	https://www.graphpad.com/scientific-software/prism/
MaxQuant v1.6.17.0	Cox and Mann, 2008	https://maxquant.net/maxquant/
Perseus v1.6.12.0	Tyanova et al., 2016	https://maxquant.net/perseus/

Other materials

All other materials that were not listed in tables above are listed in Table 7. For each of these materials the manufacturer and – wherever available – catalogue number is mentioned.

Table 7: Other material used in this work.

Other	Source	Identifier
µMACS c-myc Isolation Kit	Miltenyi Biotec	Cat.#130-091-123
µMACS Columns	Miltenyi Biotec	Cat.#130-042-701
µMACS GFP Isolation Kit	Miltenyi Biotec	Cat.#130-091-125
µ-Slide VI-Flat Imaging Chambers	Ibidi	Cat.#80621
Amersham ImageQuant 800 Western Blot Imaging System	Cytiva Life Sciences	Cat.#29399481
Amersham Protran Western Blotting Membranes, nitrocellulose	Merck	Cat.#GE10600002
Attune NxT Flow Cytometer	Thermo Scientific	N/A
Biometra TRIO Thermocycler	Analytik Jena	Cat.#846-2-070-724
Bioruptor Plus sonication device	Diagenode	Cat.#B01020001
Cellulose acetate Membrane - OE66	Cytiva Life Sciences	Cat.#10404131
EmulsiFlex-C5 High Pressure Homogenizer	Avestin	N/A
Eppendorf BioSpectrometer basic	Eppendorf	Cat.#6135000009
FastPrep-24 Classic Bead Beating Grinder and Lysis System	MP Biomedicals	Cat.#116004500
GFP-Trap Agarose	ChromoTek	Cat#gta
GSTPrep Fast Flow 16/10	Cytiva Life Sciences	Cat.#GE28-9365-50
HiPrep 26/60 Sephacryl S-100 HR	Cytiva Life Sciences	Cat.#GE17-1194-01

Other	Source	Identifier
LED Dash 1.23 m LED Tube 18 Watt 1800 Lumens Blue	Orgon	ASIN#B071GNZ5YW
NanoDrop One/One^{C} Microvolume UV-Vis Spectrophotometer	Thermo Scientific	Cat.#ND-ONE-W
NuPAGE 4-12% Bis-Tris Gels, 1mm, 10 wells	Invitrogen	Cat.#NP0321BOX
NuPAGE 4-12% Bis-Tris Gels, 1mm, 12 wells	Invitrogen	Cat.#NP0322BOX
NuPAGE 4-12% Bis-Tris Gels, 1mm, 15 wells	Invitrogen	Cat.#NP0323BOX
NuPAGE MOPS SDS Running Buffer (20X)	Invitrogen	Cat.#NP0001
Olympus FV1000 Confocal Microscope	Olympus Life Sciences	N/A
PR648 Slot Blot Blotting Manifold	Hoefer	Cat.#12004787
Q Exactive HF-X Hybrid Quadrupole-Orbitrap Mass Spectrometer	Thermo Scientific	N/A
ReproSil-Pur C18-AQ 1.9-micron beads	Dr. Maisch	Cat.#r119.aq.
Restore Western Blot Stripping Buffer	Thermo Scientific	Cat.#21059
Thermo Easy-nLC 1200	Thermo Scientific	Cat.#LC140
Type 45 Ti Fixed-Angle Titanium Rotor	Beckman Coulter	Cat.#339160
Vivaspin 6, 30 kDa MWCO	Cytiva Life Sciences	Cat.#GE28-9323-17
Zeiss Plan-Apochromat 63x/1,4 Oil DIC M27	Carl Zeiss	Cat.#420782-9900-799
Zeiss Plan-Apochromat 63×/1.46 Oil Korr M27	Carl Zeiss	Cat.#420780-9971-000
Zeiss LSM780 Confocal Laser Scanning Microscope	Carl Zeiss	N/A

Molecular biological methods

Plasmid DNA purification

Plasmid DNA was prepared from *E. coli* DH5α cultures following the *QIAprep Spin Miniprep Kit* (QIAGEN) protocol. In brief, 3 mL of saturated *E. coli* culture were pelleted and resuspended in Buffer P1, cells were lysed by the addition of Buffer B and incubation for 5 min. After addition of Buffer N3, sample was cleared by centrifugation and supernatant was applied to a spin column. Sample was passed through the column by applying vacuum. Column was washed with Buffer PB and Buffer PE and DNA was eluted from the column by applying nuclease free water. DNA concentration was determined using a *NanoDrop One/OneC Microvolume UV-Vis Spectrophotometer* (Thermo Scientific).

DNA sequencing

DNA sequencing was performed in cooperation with *Eurofins Genomics Germany GmbH* (Ebersberg, Germany) or *Microsynth Seqlab* (Göttingen, Germany). Samples were prepared according to company-specific requirements.

DNA restriction digest

DNA restriction enzymes were purchased from *New England Biolabs* (Ipswich, USA) and digestions were performed according to manufacturer's protocol. Shortly, sample DNA was diluted into enzyme-specific reaction buffer and restriction enzyme was added to a final concentration of 10 U per µg DNA. Restriction reactions were incubated at 37 °C for 1 h unless stated otherwise.

Agarose gel electrophoresis

For analysis of DNA, 1% (w/v) agarose gel was prepared as follows. Agarose was dissolved in 1x TAE buffer (40 mM Tris-acetate, 1 mM EDTA) through boiling. *SYBR Safe DNA Gel Stain* (Thermo Scientific) was added (1:10'000) to the hot agarose solution and mixed well. Solution was poured into a gel cast station. After solidification, the gel was placed in a running chamber and fully immersed in 1x TAE buffer. DNA samples were prepared by mixing with appropriate amounts of 6x DNA Loading Buffer (30% glycerol, 0.25% bromophenol blue, 0.25% xylene cyanol FF). Samples were loaded in gel pockets and DNA was separated by electrophoresis for 30 min at 100 V. DNA bands were visualized via UV/blue light imaging.

DNA gel extraction and purification

For DNA extraction and purification of DNA from agarose gels, *Wizard SV Gel and PCR Clean-Up System* (Promega) was used following the manufacturer's protocol. Briefly, gel bands containing the DNA fragment of interest were cut out and dissolved in Membrane Binding Solution. Sample was applied to an SV Minicolumn and passed through via centrifugation. Membrane-bound DNA was washed twice with Membrane Wash Solution and eluted by applying nuclease free water. DNA concentration was determined using a *NanoDrop One/OneC Microvolume UV-Vis Spectrophotometer* (Thermo Scientific).

Polymerase chain reaction

For amplification of DNA, polymerase chain reaction (PCR) was performed using *Q5 High Fidelity DNA Polymerase* (New England Biolabs) following the manufacturer's protocol.

Reactions were set up on ice containing 10 mM dNTPs, 10 µM forward primer, 10 µM reverse primer and 50 ng template DNA in a total volume of 50 µL 1x Q5 Reaction Buffer. Lastly, 0.25 µL polymerase was added and reactions placed into a *Biometra TRIO thermocycler* (Analytik Jena). Thermocycling started with an initial denaturation step for 30 s at 98 °C, followed by 35 cycles of 1) denaturation (15 s, 98 °C), 2) annealing (15 s, 50-72 °C depending on melting temperatures of the primer pair) and 3) elongation (30 s per kb, 72 °C). At the end, a final extension was performed for 2 min at 72 °C. Samples were kept at 4 °C for short term storage until further use.

Ligation of DNA fragments

T7 DNA Ligase (New England Biolabs) was used for ligation of DNA fragments with complementary sticky ends. Reactions were performed according to the manufacturer's protocol. In brief, ligation reactions containing vector and insert DNA at a molar ratio of 1:3 (total of approx. 100 ng) and 1 µL T7 DNA Ligase were set up in a total volume of 20 µL T7 DNA Ligase Reaction Buffer. Samples were incubated at room temperature for 30 min. Samples were stored at 4 °C until further use.

Gibson Assembly

DNA fragments with complementary sequences were assembled using *Gibson Assembly Master Mix* (New England Biolabs) according to the manufacturer's protocol. Shortly, Gibson Assembly reactions were set up on ice by mixing vector and insert DNA in a molar ratio of 1:3 (total of approx. 100 ng) in a total volume of 10 µL nuclease free water. 10 µL Gibson Assembly Master Mix were added to the reactions on ice, mixed by pipetting up and down, and immediately transferred to a preheated (50 °C) thermocycler. Reactions were incubated for at least 15 min at 50 °C. Samples were stored at 4 °C until further use.

E. coli DNA transformation

Chemically competent *E. coli* cells were thawed on ice. 50 ng of plasmid DNA were added to 50 µL cell suspension and gently mixed by flicking the tube. Cells were incubated for 30 min

on ice followed by incubation in a preheated (42 °C) water bath for 40 s. Cells were put back on ice for 5 min. LB medium was added and cells were allowed to recover for 1 h at 37 °C. Cells were plated on LB Agar plates containing appropriate antibiotics for selection and plates were incubated overnight at 37 °C until colonies appeared.

Yeast methods

Yeast culture growth and handling

For liquid cultures, yeast cells were either grown in rich (YP; 2% Bacto peptone, 1% Bacto yeast extract) or synthetic complete dropout (SC; 0.67% yeast nitrogen base w/o amino acids, 0.2% amino acid dropout mix (2 g L-alanine, 2 g L-arginine, 2 g L-asparagine, 2 g L-aspartic acid, 2 g L-cysteine, 2 g L-glutamine, 2 g L-glutamic acid, 2 g L-glycine, 2 g L-methionine, 2 g L-isoleucine, 2 g L-phenylalanine, 2 g L-proline, 2 g L-serine, 2 g L-threonine, 2 g L-tyrosine, 2 g L-valine, 2 g myo-inositol, 0.2 g 4-aminobenzoic acid (all *Sigma*))) media. Media contained either 2% glucose (YPD, SD), 2% raffinose (SCRaf), or 1% raffinose and 3% galactose (SCRafGal). For cells carrying extrachromosomal expression plasmids, respective organic compounds were omitted in SC for auxotrophic selection. Generally, cells were grown in liquid media for at least 18 h at 30 °C with back dilution, prior to harvest during log phase growth, unless stated otherwise. Generally, 30 OD_{600} equivalents of cells were harvested. OD_{600} was measured with an *Eppendorf BioSpectrometer basic* (Eppendorf).

Yeast plates were prepared as described for respective liquid media, but 2% agarose was added and dissolved by heating. Plates were poured with hot agar solution.

Yeast transformation

Lithium acetate (LiOAc) yeast transformation was performed as described (Schiestl and Gietz, 1989). Yeast cells were grown overnight in YPD and back diluted to an OD_{600} of 0.2 in 5 mL fresh media for each transformation. Cultures were grown for four more hours before cells were harvested, washed once with water, and transferred to a reaction tube. Cells were washed with 100 mM LiOAc. Transformation reagents were added to the cell pellet in the following order without mixing: 240 µL 50% PEG-3350, 36 µL 1 M LiOAc, 10 µL pre-boiled herring sperm DNA, target DNA, 20 µL DMSO and H_2O to a total of 360 µL. Depending on the

type of transformation, different types and amounts of target DNA were used: for simple expression plasmid transformation, 100 ng yeast vector DNA were added, for integration of plasmids, 1 µg yeast vector DNA was cleaved with an appropriate restriction enzyme, for integration of cassettes, DNA fragments with complementary overhangs were generated in a PCR reaction. Samples were vortexed for 1 min and incubated at 30 °C for 30 min, followed by a 20 min heat shock at 42 °C. Subsequently, cells were pelleted, resuspended in sterile water and transferred to appropriate yeast plates for selection: for auxotrophic selection, cells were plated on respective SD dropout plates while for antibiotic selection, cells were plated on YPD first and replicate plated on respective antibiotic-containing plates after one day of recovery. Plates were incubated at 30 °C until colonies appeared.

GdnHCl treatment

Yeast strains were cured of the [*PIN*$^+$] prion through three passages on YPD plates containing 3 mM GdnHCl, as described previously (Cox et al., 2007; Derkatch et al., 1997; Tuite et al., 1981). Successful curing and resulting [*pin*$^-$] status was checked by transient expression of *RNQ1-GFP* and visualization of the soluble Rnq1-GFP signal.

Yeast colony PCR

In order to verify the successful integration of vectors or confirm knock-in and knock-out experiments, a yeast colony PCR was performed. Yeast colonies were picked and resuspended in 50 µL 20 mM NaOH. Cell suspension was heated to 95 °C for 15 min followed by extensive vortexing. Cell debris was pelleted and genomic DNA-containing supernatant was used in a subsequent PCR reaction as template. PCR reaction was performed as described above with appropriate primer pairs covering the genomic region of interest. PCR products were analyzed via agarose gel electrophoresis.

Cycloheximide chase

For the cycloheximide chase experiment, wild-type [*PIN*$^+$] or [*pin*$^-$] strains as well as the tet-off *SIS1* strain were grown for at least 18 h prior to harvest of 25 OD_{600} equivalents of cells.

For the *SIS1* shut off, media additionally contained 10 µg mL^{-1} doxycycline. Cells were resuspended in media containing 0.5 mg mL^{-1} cycloheximide and continued to incubate as before. At different time points, 4 OD_{600} equivalents of cells were harvested, and flash frozen in liquid nitrogen. Sample pellets were subsequently processed via alkaline lysis and TCA precipitation and analyzed via SDS-PAGE as described below.

β-Galactosidase activity assay

Measurement of the cytosolic heat stress response induction was performed based on a previously published protocol (Rupp, 2002). Yeast cells carried a vector encoding a β-galactosidase reporter under the control of a promoter containing heat shock elements (HSEs) and – where applicable – were coexpressing other proteins. Cultures were grown as specified in respective figure legends. For experiments with elevated temperatures, cultures were shifted to the indicated temperature for 1 h prior to harvest. Once cells reached log phase growth, 3 OD_{600} equivalents of cells were harvested and washed once with water. Pellets were resuspended in 700 uL Z buffer (100 mM NaH_2PO_4/Na_2HPO_4 pH 7.0, 10 mM KCl, 1 mM $MgSO_4$, 2 mM β-mercaptoethanol) and 50 uL 0.1 % SDS as well as 50 uL chloroform were added. Samples were vortexed briefly and incubated for 5 min at 30 °C to lyse cells. 200 uL 2-nitrophenyl-β-D-galactopyranoside (ONPG, 4 mg mL^{-1}) were added to the samples and incubated for 5-8 min at 30 °C. Reactions were stopped by the addition of 350 uL 1 M Na_2CO_3. Samples were centrifuged for 3 min at 500 x g and absorbance at 420 nm (A_{420}) of supernatant was measured on *Eppendorf BioSpectrometer basic* (Eppendorf) photometer. Induction of the cytosolic heat stress response is described in Miller Units (MU) and calculated as:

$$1000*((A_{420})/(OD_{600}\ \text{harvested} * \text{ONPG incubation time}))$$

Growth assay

To analyze the doubling time of cells expressing polyQΔP-Opto, cultures carrying respective expression plasmids were grown for ~ 40 h in SCRafGal with regular back dilution. Subsequently, OD_{600} of cultures was measured multiple times during log phase growth.

Experimental data were fitted with exponential equations in *GraphPad Prism* to obtain doubling times.

Fluorescence-activated cell sorting

Expression levels of polyQΔP-Opto were determined via fluorescence-activated cell sorting (FACS). Cultures carrying respective expression plasmids were grown for ~ 48 h in SCRafGal with regular back dilution. 5 OD_{600} equivalents of cells were harvested, washed twice with PBS (175 mM NaCl, 8.41 mM Na_2HPO_4, 1.86 mM NaH_2PO_4) and resuspended in PBS. Cells were analyzed with an *Attune NxT Flow Cytometer* (Thermo Scientific). For detection of the mCherry signal, the 561 nm laser was chosen. Relative expression levels are based on average mCherry fluorescence for each sample.

Biochemical methods

Preparation of yeast cell extracts

Yeast cell pellets were resuspended in lysis buffer (10 mM Tris pH 7.5, 150 mM NaCl, 0.5 mM EDTA, 0.5% *IGEPAL* CA-630, 5% Glycerol, 1 mM PMSF, Complete Protease Inhibitor Cocktail, EDTA-free). An equal volume of glass beads was added and cells were lysed by vortexing 3 x 20 s on a *FastPrep-24 Classic Bead Beating Grinder and Lysis System* (MP Biomedicals). Cell lysates were cleared by centrifugation twice at 500 x g for 5 min. Total protein concentration of cell lysates was determined using either *Pierce Rapid Gold BCA Protein Assay Kit* (ThermoFisher Scientific) or *Bio-Rad Protein Assay Kit* (Bio-Rad Laboratories).

Alkaline lysis and TCA precipitation

Cell pellets were resuspended in 1 mL ice cold water. 150 µL alkaline lysis buffer (138.75 µL 2 M NaOH + 11.25 µL β-Mercaptoethanol) were added and samples incubated on ice for 5 min with regular vortexing. Subsequently, 10 µL of 2% (w/v) sodium deoxycholate were added and samples further incubated for 15 min on ice. After addition of 100 µL 100% (w/v) trichloroacetic acid (TCA), proteins were precipitated on ice for 30 min followed by centrifugation for 30 min at 20'000 x g and 4 °C. Protein pellets were washed with ice cold

acetone and dried on air. 100 µL HU buffer (8 M Urea, 200 mM Tris pH 6.8, 1 mM EDTA, 5% SDS, 0.03% bromphenol blue, 100 mM DTT) were added and pellets resuspended by shaking for 15 min at 1'400 rpm and 70 °C. Samples were analyzed by SDS-PAGE.

SDS-PAGE

Yeast cell lysate was prepared as described. Protein samples were mixed with an equal volume of 2x SDS sample buffer (100 mM Tris pH 6.8, 4% SDS, 20% glycerol, 10% β-mercaptoethanol, bromophenol blue) and heated for 5 min at 95 °C. Proteins were resolved on *NuPAGE 4-12% Bis-Tris Protein Gel* (Invitrogen) through electrophoresis in *NuPAGE MOPS SDS Running Buffer* (Invitrogen) for 55 min at 200 V.

SDD-AGE

Yeast cell lysate was prepared as described. Protein samples were mixed with a respective volume of 4x SDD-AGE sample buffer (240 mM Tris pH 6.8, 8% SDS, 15% glycerol, bromophenol blue) and incubated for 7 min at 30 °C. Proteins were resolved on an agarose gel (1.5% agarose, 20 mM Tris base, 200 mM glycine, 0.1% SDS) through electrophoresis in SDD-AGE running buffer (20 mM Tris base, 200 mM glycine, 0.1% SDS) for 105 min at 125 V and 4 °C.

Immunoblotting

Protein gels were electroblotted on *Amersham Protran Nitrocellulose Western Blotting Membranes* (Merck). SDS-PAGE gels were transferred in SDS-PAGE transfer buffer (25 mM Tris, 192 mM glycine, 20% methanol, 0.037% SDS) for 2 h at 70 V, SDD-AGE gels in SDD-AGE transfer buffer (25 mM Tris, 192 mM glycine, 20% methanol, 0.01% SDS) for 14.5 h at 7 V. Membranes were blocked in 5% milk in TBS-T (10 mM Tris-HCl pH 7.4, 150 mM NaCl, 0.1% Tween-20) for at least 30 min at room temperature followed by incubation with respective primary antibody in 5% milk in TBS-T over night at 4 °C. Membranes were washed three times in TBS-T and incubated with secondary antibody diluted in TBS-T for 1 h at room temperature. After three final washes with TBS-T, chemiluminescence was detected with *Immobilon*

Classico Western HRP Substrate (Millipore) using an *Amersham ImageQuant 800 Western Blot Imaging System* (Cytiva Life Sciences). Image analysis and densitometric quantification were conducted using *Fiji – ImageJ Image processing package v1.52p* (Schindelin et al., 2012). For repeated blotting, membrane was incubated in *Restore Western Blot Stripping Buffer* (ThermoFisher Scientific) for 15 min at 60 °C and 15 min at room temperature. After washing thoroughly with TBS-T, immunoblotting was performed as described above.

Filter retardation assay

Yeast cell lysate was prepared as described above. Samples were diluted to the indicated protein concentration in lysis buffer and incubated with 100 U benzonase at 4 °C for 30 min. Wherever indicated, SDS/DTT was added to the samples to a final concentration of 4%/50 mM and heated for 5 min at 95 °C. Control samples were only diluted with lysis buffer and not boiled. Samples treated with formic acid were first precipitated with TCA as described above before resuspension in 100% formic acid and incubation at 37 °C for 30 min (Hazeki et al., 2000). Subsequently, formic acid was evaporated and samples resuspended in SDS/DTT and boiled as described above. Samples were applied to a pre-wetted (0.1% SDS) *cellulose acetate membrane - OE66* (0.2 µm pore size; Cytiva Life Sciences) in a *PR648 Slot Blot Blotting Manifold* (Hoefer) and washed three times with 0.1% SDS. Retained material was visualized as described for immunoblotting analysis.

Dot blot analysis

Yeast cell lysate was prepared as described above. Samples were mixed with an equal volume of 2x SDS sample buffer (100 mM Tris pH 6.8, 4% SDS, 20% glycerol, 10% β-mercaptoethanol, bromophenol blue) and heated for 5 min at 95 °C. Samples were applied directly on *Amersham Protran Nitrocellulose Western Blotting Membranes* (Merck) with a multichannel pipette. Membrane was allowed to dry at room temperature for at least 1 h before it was rinsed thoroughly with TBS-T until any residual bromophenol blue dye was washed out. Membrane-bound proteins were visualized as described for immunoblotting analysis.

Cell fractionation

Yeast cell lysate, prepared as described above, was subjected to centrifugation for 15 min at 15'000 x g and 4 °C in order to pellet large protein aggregates. Pellet and supernatant were carefully separated and containing proteins were analyzed by SDD-AGE, SDS-PAGE, and filter retardation assay.

Proteomics

Sample preparation for total proteome analysis

For total proteome analysis, yeast cell pellets were resuspended in total proteome lysis buffer (100 mM Tris pH 8.0, 1% sodium deoxycholate, 40 mM 2-Cloroacetamide, 10 mM tris(2-carboxyethyl) phosphine). Cells were lysed by boiling for 2 min at 95 °C and subsequent sonication using a *Bioruptor Plus Sonication System* (Diogenode) for 10 x 30 s at high intensity. Proteins were digested sequentially by treatment with, first, LysC (final 5 µg mL^{-1}) for 4 h at 37 °C and, second, trypsin (final 5 µg mL^{-1}) overnight at 37 °C. After digestion, trifluoroacetic acid was added to the samples to a final concentration of 1%, followed by purification and desalting of peptides with home-made SCX stage-tips (Rappsilber et al., 2007).

Sample preparation for Rnq1-GFP interactome analysis

In order to investigate the interactome of Rnq1-GFP in either [*PIN*$^+$] or [*pin*$^-$] yeast cells, SCRaf was inoculated with respective strains carrying a plasmid encoding *RNQ1-GFP* under the control of the inducible galactose promoter. Cultures were grown overnight and back diluted in the morning. Four hours before cell harvest, galactose was added to the cultures to a final concentration of 2% to induce the expression of *RNQ1-GFP*. 30 OD equivalents of cells were harvested during mid-log phase. Cell pellets were resuspended in triton lysis buffer (10 mM Tris pH 7.5, 150 mM NaCl, 0.5 mM EDTA, 0.2% Triton X-100, 5% Glycerol, 1 mM PMSF, Complete Protease Inhibitor Cocktail, EDTA-free) and cells were lysed by vortexing with glass beads using a *FastPrep-24 Classic Bead Beating Grinder and Lysis System* (MP Biomedicals) as described above. 2 mg of total protein were mixed with 50 µL *anti-GFP µMACS beads* (Miltenyi Biotec) and samples were nutated at 4 °C for 1 h. Magnetic beads were separated using *µMACS columns* (Miltenyi Biotec). Beads were washed three times with triton lysis

buffer and twice with wash buffer (20 mM Tris pH 7.5). Proteins were digested on the column following a protocol described in Hubner et al., 2010. First, proteins were predigested with trypsin through the addition of elution buffer 1 (2 M Urea, 50 mM Tris pH 7.5, 1 mM DTT, 5 µg mL^{-1} trypsin) and incubation for 30 min at room temperature. Proteins were then eluted from the beads by the addition of elution buffer 2 (2 M Urea, 50 mM Tris pH 7.5, 5 mM chloroacetamide). Digestions were allowed to proceed overnight. Reactions were stopped by the addition of trifluoroacetic acid to a final concentration of 1% followed by purification and desalting of peptides with home-made SCX stage-tips (Rappsilber et al., 2007).

Sample preparation for 97Q-Opto interactome analysis

For the 97Q-Opto interactome analysis, [*PIN*$^{+}$] and [*pin*$^{-}$] cells expressing 97Q-Opto from an endogenous locus under the control of the *GPD* promoter were grown in the absence or presence of blue light for at least 18 h prior to harvest of 30 OD equivalents of cells during mid-log growth. Cell pellets were resuspended in lysis buffer (10 mM Tris pH 7.5, 150 mM NaCl, 0.5 mM EDTA, 0.5% IGEPAL CA-630, 5% Glycerol, 1 mM PMSF, Complete Protease Inhibitor Cocktail, EDTA-free) and cells were lysed by vortexing with glass beads using a *FastPrep-24 Classic Bead Beating Grinder and Lysis System* (MP Biomedicals) as described above. A TOTAL sample was set aside and the remaining lysate was cleared by spinning for 15 min at 15'000 x g and 4 °C. Supernatant was carefully removed and used as SOLUBLE sample. 4 mg of total protein were mixed with 50 µL *anti-c-Myc µMACS beads* (Miltenyi Biotec) and samples were nutated at 4 °C for 1 h. Bead separation, washing, on column trypsin digest and subsequent sample preparation steps were performed as described above for Rnq1-GFP.

LC-MS/MS

LC-MS/MS and initial data analysis were performed by Barbara Steigenberger, Nicole Krombholz and Anja Wehner at the MPI Mass Spectrometry Core Facility. I am grateful for their help and appreciate their support concerning any questions related to mass spectrometry.

The following protocol was used for the analysis of the total proteome samples. Peptide samples were vacuum dried and resuspended in 6 µl 0.1% formic acid. The peptides were loaded onto a 30-cm column (inner diameter: 75 microns; packed in-house with *ReproSil-Pur C18-AQ 1.9-micron beads*, Dr. Maisch GmbH) via the autosampler of the *Thermo Easy-nLC 1200* (Thermo Fisher Scientific) at 60 °C. Eluting peptides were directly sprayed onto the benchtop *Orbitrap mass spectrometer Q Exactive HF* (Thermo Fisher Scientific). Liquid chromatography with the *Easy-nLC 1200* was performed by loading the peptides in 0.1% formic acid at a flow rate of 1.25 µl min^{-1} and peptides were separated with a flow rate of 250 nL min^{-1} by a gradient of buffer B (80% ACN, 0.1% formic acid) from 2% to 30% over 120 min followed by a ramp to 60% over 10 min then 95% over the next 5 min and finally the percentage of buffer B was maintained at 95% for another 5 min. The mass spectrometer was operated in a data-dependent mode with survey scans from 300 to 1750 m/z (resolution of 60'000 at m/z = 200), and up to 15 of the top precursors were selected and fragmented using higher energy collisional dissociation (HCD with a normalized collision energy of value of 28). The MS2 spectra were recorded at a resolution of 15'000 (at m/z = 200). AGC target for MS1 and MS2 scans were set to 3 x 10^6 and 1 x 10^5 respectively within a maximum injection time of 100 and 25 ms for MS and MS2 scans, respectively.

For the interactome analyses of Rnq1-GFP and 97Q-Opto, a similar protocol was used with minor changes: for the liquid chromatography, a gradient from 7% to 30% over 60 min was followed by a ramp to 60% over 15 min, then ramp to 95% over the next 5 min and finally the percentage of buffer B was maintained at 95% for another 5 min. For the MS analyses, up to 10 of the top precursors were selected and fragmented. Maximum injection time of 100 and 60 ms for MS and MS2 scans were chosen, respectively.

Data analysis and visualization

Raw data were processed using the *MaxQuant computational platform* (version 1.6.17.0) with standard settings applied. The peak list was searched against the data base of *S. cerevisiae* with an allowed precursor mass deviation of 4.5 ppm and an allowed fragment mass deviation of 20 ppm. *MaxQuant* by default enables individual peptide mass tolerances, which was used in the search. Cysteine carbamidomethylation was set as static modification, and methionine

oxidation and N-terminal acetylation as variable modifications. Proteins were quantified across samples using the label-free quantification algorithm in *MaxQuant* generating label-free quantification (LFQ) intensities. Data analysis was performed using *Perseus* (Tyanova et al., 2016) and *Go Term Enrichment* (Ashburner et al., 2000; GeneOntologyConsortium, 2021; Mi et al., 2019). *p*-values for volcano blots were calculated by Student's *t*-test for proteins detected in all four biological replicates in each group (total proteome analysis) or in three out of four biological replicates in at least one group (interactome analyses).

In vitro methods

Recombinant protein expression

For recombinant expression of proteins, respective expression plasmids were transformed into competent *E. coli* Dl21 (DE3) cells as described above. Terrific broth medium (12 g tryptone, 24 g yeast extract, 5 mL glycerol, 72 mM K_2HPO_4, 17 mM KH_2PO_4) was inoculated with a single transformation colony and incubated shaking at 140 rpm and 37 °C. Once culture reached an OD_{600} of ~ 0.4, flask was transferred to 18 °C and allowed to cool down. Isopropyl β-D-1-thiogalactopyranoside (IPTG) was added to a final concentration of 0.4 mM to induce expression of the target protein. Cultures were further incubated on the shaker overnight before cells were harvested and washed once with ice cold PBS.

Recombinant protein purification

For the purification of recombinantly expressed GST-polyQ from *E. coli*, a protocol described in Scherzinger et al., 1997 was followed with adjustments. To retain the activity and prevent the aggregation of the purified proteins, all purification steps were performed on ice or at 4 °C.

A cell pellet was generated as described above and resuspended in buffer A (50 mM NaH_2PO_4 pH 7.4, 150 mM NaCl, 1 mM EDTA, Complete Protease Inhibitor Cocktail, EDTA-free). Lysozyme was added to a final concentration of 1 mg mL^{-1}, DNase to a final concentration of 2.5 U mL^{-1} and cell suspension was stirred for 45 min. Cells were lysed through multiple passages on an *EmulsiFlex-C5 high pressure homogenizer* (Avestin). n-Octyl-β-D-glucopyranoside (OGP) was added to a final concentration of 0.1%, mixed well and

incubated for 5 min. Lysate was spun at 125'000 x g for 1 h at 4 °C using a *Type 45 Ti Fixed-Angle Titanium Rotor* (Beckman Coulter) to pellet cell debris and insoluble proteins. Supernatant was carefully removed and applied onto a *GSTPrep Fast Flow 16/10* (Cytiva Life Sciences) affinity column which had been pre-equilibrated in buffer B (50 mM NaH_2PO_4 pH 7.4, 150 mM NaCl, 1 mM EDTA**,** 1% OGP). The column was washed with five column volumes (CV) of buffer B before eluting the protein with two CV of buffer C (50 mM NaH_2PO_4 pH 7.4, 150 mM NaCl, 1 mM EDTA, 15 mM glutathione). Fractions containing the GST-polyQ protein were pooled, concentrated using a *Vivaspin 6 30 kDa concentrator* (Cytiva Life Sciences) and applied onto a *HiPrep 26/60 Sephacryl S-100 HR* (Cytiva Life Sciences) size exclusion column, pre-equilibrated in SEC buffer (50 mM Tris pH 7.4, 150 mM NaCl, 1 mM EDTA, 5% glycerol, 1 mM DTT). GST-polyQ-containing fractions were pooled, the quality of the purification assessed via SDS-PAGE, and the concentration of the purified protein determined with a *NanoDrop One/OneC Microvolume UV-Vis Spectrophotometer* (Thermo Scientific). Glycerol was added to a final concentration of 10%. Aliquoted protein samples were flash frozen in liquid nitrogen and stored at -80 °C.

In vitro aggregation assay

In vitro aggregation assays of GST-polyQ were performed according to protocols described by Scherzinger et al., 1999 and Muchowski et al., 2000. Purified GST-polyQ was diluted to a final concentration of 3 µM in *in vitro* reaction buffer (10 mM Tris pH 7.5, 150 mM NaCl, 0.5 mM EDTA, 1 mM DTT, 1 mM PMSF, Complete Protease Inhibitor Cocktail, EDTA-free) in a total reaction volume of 1 mL. 25 U GST-PreScission protease were added and mixed by inverting the tube ten times to start the reaction. Sample was incubated at 30 °C, shaking at 300 rpm. At different time points samples were taken for SDD-AGE, SDS-PAGE, or filter retardation analysis. For the preparation of SDD-AGE samples, 75 µL of sample were mixed with 4x SDD-AGE sample buffer (240 mM Tris pH 6.8, 8% SDS, 15% glycerol, 0.03% bromophenol blue). SDS-PAGE samples were prepared by mixing 20 µL of sample with an equal volume of 2x SDS-PAGE sample buffer (100 mM Tris pH 6.8, 4% SDS, 20% glycerol, 0.03% bromophenol blue, 200 mM DTT) and heating at 95 °C for 5 min. For samples analyzed via filter retardation assay, 100 µL of sample were mixed with an equal volume of 4% SDS/100 mM DTT and heated at

95 °C for 5 min. All samples were flash frozen in liquid nitrogen and stored at -80 °C until further analysis.

For reactions in the presence of cell lysate, [*PIN*$^+$] or [*pin*$^-$] yeast cells with and without overexpression of *RNQ1-GFP* were harvested during log growth. Cells were lysed as described above but *in vitro* reaction buffer (10 mM Tris pH 7.5, 150 mM NaCl, 0.5 mM EDTA, 1 mM DTT, 1 mM PMSF, Complete Protease Inhibitor Cocktail, EDTA-free) was employed instead of the detergent-containing lysis buffer that is normally used. For the actual assays, GST-polyQ was diluted into cell lysate at a concentration of 4.4 mg mL^{-1}. Reaction was otherwise conducted as described above.

For aggregation assays in the presence of beads preloaded with Rnq1-GFP, 400 µL GFP-Trap agarose beads (ChromoTek) were incubated with 4.4 mg total lysate from [*pin*$^-$] or [*PIN*$^+$] cells overexpressing *RNQ1-GFP* in a total reaction volume of 1.4 mL overnight at 4 °C. Beads were separated from supernatant at 2'500 x g for 5 min at 4 °C and washed twice with *in vitro* reaction buffer. For the aggregation reaction, GST-Htt54Q protein was diluted into [*pin*$^-$] cell lysate in a total volume of 1 mL and mixed with 400 µL Rnq1-GFP-loaded beads. Reaction was started by the addition of GST-PreScission protease and incubated rotating end-over-end at 10 rpm and 30 °C. At indicated time points, beads were sedimented at 500 x g for 5 min and samples were taken from the supernatant fraction for analysis via SDD-AGE.

Microscopy

All microscopy experiments described below, with the exception of the FRAP analysis, were conducted on an *Olympus FV1000 confocal microscope* (Olympus), equipped with a *Zeiss Plan-Apochromat 63x/1,4 Oil DIC M27 objective* (Carl Zeiss). FRAP experiments were performed at the MPIB Imaging Facility (Martinsried, Germany) on a *Zeiss LSM780 confocal laser scanning microscope*, equipped with a *Zeiss Plan-Apochromat 63×/1.46 Oil Korr M27 objective* (both Carl Zeiss). For detection of the GFP fluorophore an excitation wavelength of 488 nm and emission of 505–540 nm was chosen. For the mCherry fluorophore wavelengths of 559 nm for excitation and 575–675 nm for emission were used. Image analysis was conducted using the *Fiji – ImageJ Image processing package v1.52p* (Schindelin et al., 2012).

Confocal imaging

After growth to mid-log phase, yeast cells were fixed in 3% formaldehyde for 5 min. Fixed cells were applied to the chamber of a concanavalin A-coated *µ-Slide* (ibidi) and allowed to adhere for 5 min at room temperature. After washing with PBS to remove non-adherent cells, immobilized cells were imaged as described above.

Analysis of aggregate density

Mid-log cells were applied to the chamber of a concanavalin-A-coated *µ-Slide* (ibidi) without prior fixation. Non-adherent cells were removed by washing with media. Live cells were imaged as described above. Importantly, the same non-saturating acquisition settings were used for all samples. To analyze the fluorescent density of aggregates, circular regions within the aggregate were selected and the average fluorescence signal was compared between samples. To obtain the total cellular fluorescence signal, the integrated fluorescence density over the whole area of the analyzed cell was determined.

Analysis of Ssa1 enrichment

Live cells were prepared and imaged as described above, using the same non-saturating acquisition settings for all samples. Regions of interest were selected outlining the FLuc aggregate as well as a large area in the cell not containing any aggregate (soluble). The enrichment of Ssa1 in aggregates over soluble signal was calculated as the ratio between the average fluorescence of Ssa1 in these two regions. To obtain the total cellular fluorescence signal, the integrated fluorescence density over the whole area of the analyzed cells was calculated.

Cluster disappearance

Yeast cultures were grown in the dark. After reaching log phase growth, cells were illuminated with blue light for 5 min using an *LED Dash 1,23 m LED Tube 18 Watt 1800 Lumens Blue* (Orgon) light source. Cultures were returned to the dark and further incubated. At indicated time points, cells were fixed and applied to the chamber of a *µ-Slide* (ibidi) as described above.

Using the EPI fluorescence light, the number of cells with visible inclusions was counted. 100 cells were counted for each single replicate data point.

Fluorescence recovery after photobleaching

Live cell samples were prepared as described above. For fluorescence recovery after photobleaching experiments, circular regions of constant size were bleached after 20 frames and monitored for at least 80 s (0.38 s/frame) for fluorescence recovery in a single focal plane. Fluorescence intensity data were corrected for photobleaching and normalized to the average fluorescence intensity before (1) and after (0) bleaching (relative fluorescence).

Cloning and yeast strains related to Chapter I

Here, cloning and yeast strains related to experiments in Chapter I of this work are described. This section is only an addition to the general Materials and Methods section and both have to be considered together to get a complete overview over the information related to Chapter I.

Molecular cloning

Conventional cloning was done as described in the general Materials and Methods section. Here we describe in detail how each vector used in Chapter I of this work was produced. A list of all of these vectors as well as primers that were used to generate them, can be found in the appendix (Tables X1 and X2).

pCLK207 and pCLK181 expressing the nuclear markers GST-GFP-NLS and GST-mCherry-NLS, respectively, were generated by three-way ligation. First, a DNA fragment encoding *GST* was generated by PCR by amplifying pGEX-2T-Tev (GE Lifesciences) with the primer pair oCLK1/oCLK2. GFP-NLS was generated through amplification of pFA6A-GFP(S65T)-KanMX6 (Bähler et al., 1998) with oCLK3/oCLK4, mCherry-NLS through amplification of pYES2-myc-20QmCh (Park et al., 2013) with oCLK5/oCLK6. Subsequently, pRS306pGPD (Mumberg et

al., 1995) was digested with XbaI and SalI, GST with XbaI and BamHI and GFP-NLS or mCherry-NLS with BamHI and SalI. Fragments were ligated together in a single reaction.

To generate pCLK263 for the expression of *HSF1*, *HSF1* was amplified from pRS426Hsf1 (Holmes et al., 2014b) using oCLK7/oCLK8. The resulting DNA fragment was digested with EcoRI and XhoI and ligated into the similarly cleaved pRS414pGPD (Mumberg et al., 1995) vector.

In order to generate pCLK253 and pCLK254, expressing 20Q-mCherry and 97Q-mCherry, respectively, pYES2-myc-20QmCherry or pYES2-myc-97QmCh (Park et al., 2013) were digested with BamHI and MluI and the obtained fragments ligated into a similarly digested pESCLeu vector (Agilent).

For the generation of the heat shock reporter pCLK270, the heat-stress inducible promoter and LacZ region were amplified from plasmid Ssa3-LacZ-Leu (Liu et al., 1997) using oCLK9/oCLK10. Subsequently, the resulting PCR product was digested with BglII and SalI and ligated into the pRS313 backbone (Sikorski and Hieter, 1989), previously cleaved with BamHI and SalI.

For the chaperone overexpression screen, relevant overexpression vectors were isolated from the Yeast ORF Collection (Dharmacon). Target proteins were encoded on multicopy 2µ vectors, expressed under the control of a galactose-inducible promoter.

To generate pCLK323, expressing *YDJ1*, *YDJ1* was amplified form the genome of the wild type YPH499 strain using the primer pair oCLK11/oCLK12. The PCR product was further digested with SpeI and BamHI. pRS414pGPDSis1 (Douglas et al., 2008) was digested in a similar fashion to generate the pRS414pGPD backbone that the *YDJ1* insert was ligated into.

For the generation of pCLK301, pCLK302 and pCLK304, expressing HA-tagged wild type Sis1, Sis1 with its HPD motif mutated to AAA or Sis1 lacking the G/F region (residues 71-121), respectively, DNA fragments were subcloned with their promoters from pRS415P_{GAL}-HA-Sis1, pRS415P_{GAL}-HA-Sis1(AAA), or pRS415P_{GAL}-HA-Sis1ΔG/F (Park et al., 2013) into a pRS414 vector (Sikorski and Hieter, 1989). pCLK313 and pCLK315, encoding the HA-tagged N-terminal 121 or 338 amino acids of Sis1, respectively, were generated by amplifying fragments of *SIS1* from pRS414P_{GAL}-HA-Sis1 with primers oCLK13/oCLK15 or oCLK13/oCLK16. PCR products were

digested with SpeI and BamHI and ligated into a backbone generated by the similar digestion of pCLK301 to replace wild type *SIS1*.

In order to create pCLK295, expressing GFP-tagged *SSA1*, first *SSA1* was cleaved from pRS426pGALSsa1 (Muchowski et al., 2000) with BamHI and XhoI and ligated into a similarly digested pRS413pGPD vector (Mumberg et al., 1995), generating pCLK242. pCLK242 was then amplified with oCLK17/oCLK18 to generate a PCR fragment encoding *SSA1* with compatible overhang with a GFP fragment amplified from pFA6A-GP(S65T)-KanMX6 with primer oCLK19 & oCLK20. Both fragments were fused by a PCR using oCLK17/oCLK20. The *SSA1-GFP* fusion product was then inserted into a pRS405pADH backbone (Mumberg et al., 1995) amplified with oCLK21/oCLK22 in a Gibson Assembly reaction.

pCLK332, expressing mCherry-tagged FlucDM, was generated by first cleaving FlucDM from pCIneo-FlucDM (Gupta et al., 2011) with XhoI and XmaI and ligating it into a similarly digested mCherry-N1 vector (Clontech). Subsequently, the FlucDM-mCherry fusion was subcloned into a pYES2 vector backbone (Invitrogen) using KpnI and XbaI.

All constructs were verified by DNA sequencing.

Yeast strains

Standard yeast methods are described in the general Materials and Methods section. All yeast strains used in Chapter I of this work are derived from the *S. cerevisiae* YPH499 strain and are listed in the appendix (Table X3). Here, we describe how these stains were generated.

In order to generate yCLK225, expressing GST-GFP-NLS under the control of the *GPD* promoter from an endogenous locus, YPH499 (Sikorski and Hieter, 1989) was transformed with pCLK207, linearized with BsmI prior to transformation. Cells were selected on media lacking uracil.

yCLK250, expressing *SSA1-GFP* under the control of the *ADH* promoter from an endogenous locus, was created by transforming YPH499 (Sikorski and Hieter, 1989) with BstEII-cut pCLK295 and selection on media lacking leucine.

In order to GFP-tag endogenous *SIS1* in yCLK207, a PCR generated cassette was generated by amplification of pFA6a-GFP(S65T)-KanMX6 (Bähler et al., 1998) with

oCLK23/oCLK24. Subsequently, the PCR product was transformed into YPH499 (Sikorski and Hieter, 1989). Clones were selected by growth on media containing 300 µg mL^{-1} G418 and confirmed by colony PCR (e.g., with oCLK25/oCLK4).

yCLK255 and yCLK256, coexpressing GST-mCherry-NLS under the control of the *GPD* promoter from an endogenous locus along with *SSA1-GFP* or *SIS1-GFP*, respectively, were created by transforming yCLK250 or yCLK207 with pCLK181, linearized with BsmI prior to transformation. Cells were selected on media lacking uracil.

Cloning and yeast strains related to Chapter II

Here, cloning, yeast strains and experimental procedures relevant for experiments in Chapter II of this work are described. This section is only an addition to the general Materials and Methods section and both have to be considered together to get a complete overview over the information related to Chapter II.

Molecular cloning

Conventional cloning was done as described in the general Materials and Methods section. Here we describe in detail how each vector used in Chapter II of this work was produced. A list of all of these vectors as well as primers that were used to generate them, can be found in the appendix (Tables X4 and X5).

pMG6 and pMG7 were generated by excising the *GPD* or the *GAL* promotor (and the corresponding *CYC* terminator) from pRS416pGPD and pRS416pGAL (Mumberg et al., 1994; 1995), respectively, with the restriction enzymes SacI and KpnI and ligating it into pRS316 (Sikorski and Hieter, 1989) that was cut in a similar fashion.

In order to generate pMG18 and pMG88, for the expression of mCherry-CRY2, mCherry-CRY2 was amplified from pHR-mCh-Cry2olig (Shin et al., 2017) with oMG22/oMG23 and integrated into the SalI-linearized backbones of pMG6 and pMG7, respectively, via Gibson Assembly. pMG60 and pMG90 were generated by subcloning of pMG18 or pMG88 into

pRS305 (Sikorski and Hieter, 1989): pMG18 or pMG88 were amplified with oMG44/oMG45, pRS305 with oMG42/oMG43 in two separate PCR reactions and the two products were fused via Gibson Assembly.

For pMG148 expressing 97Q-Opto, Huntingtin exon 1 including an N-terminal cMyc-tag as well as the C-terminal poly proline region was amplified from pYES2-myc-97QmCh (Park et al., 2013) with oMG113/oMG114 and fused with the pMG60 backbone amplified with oMG111/oMG112 via Gibson Assembly. pMG150, for the expression of 97Q-mCherry, was generated based on pMG148: pMG148 was amplified with oMG113/oMG143 as well as oMG88/oMG112 in two separate PCR reactions. The PCR products were ligated via Gibson Assembly.

pMG154 and pMG155, for the expression of 20Q-Opto or 20Q-mCherry, respectively, were generated by excising Huntingtin exon 1, including the N-terminal cMyc tag as well as the C-terminal poly proline region, from pYES2-myc-20QmCh (Park et al., 2013) with EcoRI and BglII and ligating it into the backbones, generated by amplifying either pMG148 or pMG150 with oMG146/oMG147, via Gibson Assembly.

In order to generate pMG160, for the expression of 97Q-GFP from pRS304, a two-step approach was taken. First, GFP was amplified with oMG149/oMG150 from pFA6aGFP(S65T)kanMX6 (Bähler et al., 1998) and integrated into a backbone generated by amplifying pMG150 with oMG148/oMG88 to obtain pMG158. Next, 97Q-GFP including its promoter was amplified from pMG158 with oMG44/oMG45 and subcloned into a backbone generated by amplifying pRS304 (Sikorski and Hieter, 1989) with oMG42/oMG43 to generate pMG160. Both steps were done using Gibson Assembly reactions.

pMG159, for the expression of 20Q-GFP from pRS305, was generated by replacing mCherry in pMG155 with GFP: GFP was excised from pMG158 with BsgI and XhoI and ligated into the pMG155 backbone that was cleaved in an analogous manner. Subsequently, in order to make pMG161 for expression of 20Q-GFP from pRS304, the *LEU* auxotrophy cassette in pMG159 was replaced with the *TRP* auxotrophy marker: the *TRP* marker was excised from pRS304 (Sikorski and Hieter, 1989) with AatII and DraIII and used to replace the *LEU* marker in pMG159 that was cleaved with the same restriction enzymes.

pMG185-pMG189, for expression of mid length polyQ-mCherry, were generated in two steps: first, pBacMam2-DiEx-LIC-C-flag_huntingtin_full-length_Q36, _Q48, _Q54, _Q60 and _Q73 (Harding et al., 2019) were cleaved with XhoI and PvuI to obtain 4.5 kb fragments containing the polyQ region of interest. These fragments were purified and digested again with BsgI and StuI. The products of this second digestion were integrated into the pMG150 vector backbone, which had been digested in a similar fashion to remove the 97Q portion in this vector. To generate pMG190-pMG194 expressing mid length polyQ-Opto, polyQ stretches were excised from pMG185-pMG189 with NdeI and SpeI and ligated into the pMG148 backbone that was treated in a similar fashion to remove the 97Q region.

In order to obtain pMG202 and pMG205 for recombinant expression of GST-20Q and GST-54Q, respectively, we excised the polyQ regions from pMG155 and pMG187 with NdeI and XbaI. The resulting fragments were integrated into the pGEX backbone, generated by amplifying pGEX-Htt53Q (Schaffar et al., 2004) with oMG169/oMG170, via Gibson Assembly.

For pMG267 and pMG268, expressing 25QΔP-Opto and 97QΔP-Opto, respectively, toxic Huntingtin exon 1 without poly proline and including an N-terminal FLAG-tag was amplified from pYES2-Htt25Q-GFP or pYES2-Htt97Q-GFP (Ripaud et al., 2014), with oMG151/oMG152 and integrated into a backbone, generated by amplifying pMG245 with oMG111/oMG112, via Gibson Assembly. pMG210, expressing 66QΔP-Opto was generated in this process coincidentally as amplification of expanded polyQ stretches via PCR may lead to a loss of Q.

In order to generate pMG245 to conditionally express mCherry-Opto from pRS426, the mCherry-Opto fragment was excised from pMG90 with KpnI and SacI and ligated into a similarly digested pRS426 vector (Christianson et al., 1992). Having created pMG245, we generated pMG246-pMG252, conditionally expressing polyQ-Opto from pRS426, by excising polyQ-Opto fragments from pMG154, pMG190-pMG194 and pMG148 with XhoI and SpeI and ligated them into the similarly digested pMG245 backbone.

pMG269, for expression of *RNQ1-GFP* from pRS306, was generated by amplifying pESC-URA-Rnq1-GFP (Kaganovich et al., 2008) with oMG199/oMG142 and ligating the resulting fragment into a backbone, generated by amplifying pRS306pADH (Mumberg et al., 1995) with oMG137/oMG138.

pMG271, for expression of *RNQ1-GFP* lacking the cMyc tag, was generated by performing two separate PCR reactions with template pESC-URA-Rnq1-GFP (Kaganovich et al., 2008) and the primer pairs oMG207/oMG208 and oMG209/oMG210 to generate fragments with complementary overhangs excluding the cMyc tag. Fragments were fused in a Gibson Assembly reaction.

All constructs were verified by DNA sequencing.

Yeast strains

Standard yeast methods are described in the general Materials and Methods section. All yeast strains used in Chapter II of this work are derived from the *S. cerevisiae* YPH499 or 74-D694 strains and are listed in the appendix (Table X6). Here, we describe how these stains were generated.

yMG33 is the [*PIN*$^+$] parent strain from which all yeast strains with integrated expression vectors used in this study are derived. It was generated by transforming SY197 (Klaips et al., 2014) with a cassette generated by amplifying the kanamycin resistance gene from pFA6-kanMX4 with oMG1/oMG2 to delete endogenous *PDR5*. Transformants were selected by growth of cells on plates containing 300 µg mL^{-1} G418. Clones were verified by colony PCR (with oMG3/oMG4).

Other [*PIN*$^+$] strains were generated based on yMG33 by integrating plasmids containing the desired gene into an auxotrophy marker locus and selecting transformants on media lacking the respective organic compound; see strain identifiers for details on host strain and plasmid used for integration (Table X6). pRS304-based plasmids were linearized with Bsu36I, pRS305 with AflII and pRS306 with StuI prior to transformation.

[*pin*$^-$] strains are derived from respective [*PIN*$^+$] strains via curing of the Rnq1 prion through three passages on YPD plates containing 3 mM GdnHCl (Cox et al., 2007; Derkatch et al., 1997; Tuite et al., 1981). The exceptions are yMG103, yMG104, yMG106, yMG120, yMG132 and yMG122, where a second integrating plasmid was transformed into an already existing [*pin*$^-$] background.

The prion status of all strains was determined by transient expression of *RNQ1-GFP* and examination of Rnq1-GFP state by microscopy.

Yeast culture growth and handling

In order to prevent the premature activation of Opto constructs, all cell culture and sample handling steps in Chapter II were performed in the dark (no light or red light as only light source). Whenever indicated, cultures were exposed to the blue light of a *LED Dash 1.23 m LED Tube 18 Watt 1800 Lumens* (Orgon) for various amounts of time. Once denaturing conditions were applied (e.g., addition of SDS-PAGE sample buffer, boiling, etc.), samples were further handled in normal light conditions.

References

Ahmad, M. (2016). Photocycle and signaling mechanisms of plant cryptochromes. Curr Opin Plant Biol *33*, 108-115. 10.1016/j.pbi.2016.06.013.

Alberti, S., Halfmann, R., King, O., Kapila, A., and Lindquist, S. (2009). A systematic survey identifies prions and illuminates sequence features of prionogenic proteins. Cell *137*, 146-158. 10.1016/j.cell.2009.02.044.

Ali, M.M., Roe, S.M., Vaughan, C.K., Meyer, P., Panaretou, B., Piper, P.W., Prodromou, C., and Pearl, L.H. (2006). Crystal structure of an Hsp90-nucleotide-p23/Sba1 closed chaperone complex. Nature *440*, 1013-1017. 10.1038/nature04716.

AlzheimerAssociation (2021). 2021 Alzheimer's disease facts and figures. Alzheimers Dement. *3*, 327-406. 10.1002/alz.12328

Amin, J., Ananthan, J., and Voellmy, R. (1988). Key features of heat shock regulatory elements. Mol Cell Biol *8*, 3761-3769. 10.1128/mcb.8.9.3761-3769.1988

Anckar, J., and Sistonen, L. (2011). Regulation of HSF1 function in the heat stress response: implications in aging and disease. Annu Rev Biochem *80*, 1089-1115. 10.1146/annurev-biochem-060809-095203.

Anfinsen, C.B. (1973). Principles that govern the folding of protein chains. Science *181*, 223-230. 10.1126/science.181.4096.223.

Angarica, V.E., Angulo, A., Giner, A., Losilla, G., Ventura, S., and Sancho, J. (2014). PrionScan: an online database of predicted prion domains in complete proteomes. BMC Genomics *15*, 102. 10.1186/1471-2164-15-102.

Arndt, V., Rogon, C., and Hohfeld, J. (2007). To be, or not to be - molecular chaperones in protein degradation. Cell Mol Life Sci *64*, 2525-2541. 10.1007/s00018-007-7188-6.

Aron, R., Lopez, N., Walter, W., Craig, E.A., and Johnson, J. (2005). In vivo bipartite interaction between the Hsp40 Sis1 and Hsp70 in Saccharomyces cerevisiae. Genetics *169*, 1873-1882. 10.1534/genetics.104.037242.

Arrasate, M., and Finkbeiner, S. (2012). Protein aggregates in Huntington's disease. Exp Neurol *238*, 1-11. 10.1016/j.expneurol.2011.12.013.

Arrasate, M., Mitra, S., Schweitzer, E.S., Segal, M.R., and Finkbeiner, S. (2004). Inclusion body formation reduces levels of mutant Huntingtin and the risk of neuronal death. Nature *431*, 805-810. 10.1038/nature02998.

Arthur, K.C., Calvo, A., Price, T.R., Geiger, J.T., Chio, A., and Traynor, B.J. (2016). Projected increase in amyotrophic lateral sclerosis from 2015 to 2040. Nat Commun *7*, 12408. 10.1038/ncomms12408.

Ashburner, M., Ball, C.A., Blake, J.A., Botstein, D., Butler, H., Cherry, J.M., Davis, A.P., Dolinski, K., Dwight, S.S., Eppig, J.T., et al. (2000). Gene ontology: tool for the unification of biology. Nat Genet *25*, 25-29. 10.1038/75556.

Bähler, J., Wu, J.-Q., Longtine, M.S., Shah, N.G., McKenzie III, A., Steever, A.B., Wach, A., Philippsen, P., and Pringle, J.R. (1998). Heterologous modules for efficient and versatile PCR-based gene targeting in Schizosaccharomyces pombe. Yeast *14*, 943-951. 10.1002/(SICI)1097-0061(199807)14:10<943::AID-YEA292>3.0.CO;2-Y.

Balch, W.E., Morimoto, R.I., Dillin, A., and Kelly, J.W. (2008). Adapting proteostasis for disease intervention. Science *319*, 916-919. 10.1126/science.1141448.

Balchin, D., Hayer-Hartl, M., and Hartl, F.U. (2016). In vivo aspects of protein folding and quality control. Science *353*, aac4354. 10.1126/science.aac4354.

Balchin, D., Hayer-Hartl, M., and Hartl, F.U. (2020). Recent advances in understanding catalysis of protein folding by molecular chaperones. FEBS Lett *594*, 2770-2781. 10.1002/1873-3468.13844.

Balchin, D., Milicic, G., Strauss, M., Hayer-Hartl, M., and Hartl, F.U. (2018). Pathway of actin folding directed by the eukaryotic chaperonin TRiC. Cell *174*, 1507-1521. 10.1016/j.cell.2018.07.006.

Barrott, J.J., and Haystead, T.A. (2013). Hsp90, an unlikely ally in the war on cancer. FEBS J *280*, 1381-1396. 10.1111/febs.12147.

Baumschlager, A., and Khammash, M. (2021). Synthetic biological approaches for optogenetics and tools for transcriptional light-control in bacteria. Adv Biol *5*, e2000256. 10.1002/adbi.202000256.

Becher, M.W., Kotzuk, J.A., Sharp, A.H., Davies, S.W., Bates, G.P., Price, D.L., and Ross, C.A. (1998). Intranuclear neuronal inclusions in Huntington's disease and dentatorubral and pallidoluysian atrophy: correlation between the density of inclusions and IT15 CAG triplet repeat length. Neurobiol Dis *6*, 387-397. 10.1006/nbdi.1998.0168

Behrends, C., Langer, C.A., Boteva, R., Bottcher, U.M., Stemp, M.J., Schaffar, G., Rao, B.V., Giese, A., Kretzschmar, H., Siegers, K., and Hartl, F.U. (2006). Chaperonin TRiC promotes the assembly of polyQ expansion proteins into nontoxic oligomers. Mol Cell *23*, 887-897. 10.1016/j.molcel.2006.08.017.

Ben-Zvi, A., Miller, E.A., and Morimoto, R.I. (2009). Collapse of proteostasis represents an early molecular event in Caenorhabditis elegans aging. PNAS *106*, 14914-14919. 10.1073/pnas.0902882106.

Bett, J.S. (2016). Proteostasis regulation by the ubiquitin system. Essays Biochem *60*, 143-151. 10.1042/EBC20160001.

Bolton, D.C., McKinley, M.P., and Prusiner, S.B. (1982). Identification of a protein that purifies with the scrapie prion. Science *218*, 1309-1311. 10.1126/science.6815801

Botstein, D., Chervitz, S.A., and Cherry, M. (1997). Yeast as a model organism. Science *277*, 1259-1260. 10.1126/science.277.5330.1259.

Botstein, D., and Fink, G.R. (1988). Yeast: an experimental organism for modern biology. Science *240*, 1439-1443. 10.1126/science.3287619

Braak, H., Alafuzoff, I., Arzberger, T., Kretzschmar, H., and Del Tredici, K. (2006). Staging of Alzheimer disease-associated neurofibrillary pathology using paraffin sections and immunocytochemistry. Acta Neuropathol *112*, 389-404. 10.1007/s00401-006-0127-z.

Braak, H., Del Tredici, K., Rüb, U., de Vos, R.A., Jansen Steur, E.N.H., and Braak, E. (2003). Staging of brain pathology related to sporadic Parkinson's disease. Neurobiol Aging *24*, 197-211. 10.1016/s0197-4580(02)00065-9

Bradley, M.E., Edskes, H.K., Hong, J.Y., Wickner, R.B., and Liebman, S.W. (2002). Interactions among prions and prion "strains" in yeast. PNAS *99*, 16392-16399. 10.1073/pnas.152330699.

Brettschneider, J., Del Tredici, K., Lee, V.M., and Trojanowski, J.Q. (2015). Spreading of pathology in neurodegenerative diseases: a focus on human studies. Nat Rev Neurosci *16*, 109-120. 10.1038/nrn3887.

Bruce, M.E., Will, R.G., Ironside, J.W., McConnell, I., Drummond, D., Suttie, A., McCardle, L., Chree, A., Hope, J., Birkett, C., et al. (1997). Transmissions to mice indicate that 'new variant' CJD is caused by the BSE agent Nature *389*, 498-501. 10.1038/39057

Bugaj, L.J., Choksi, A.T., Mesuda, C.K., Kane, R.S., and Schaffer, D.V. (2013). Optogenetic protein clustering and signaling activation in mammalian cells. Nat Methods *10*, 249-252. 10.1038/nmeth.2360.

Carra, S., Alberti, S., Arrigo, P.A., Benesch, J.L., Benjamin, I.J., Boelens, W., Bartelt-Kirbach, B., Brundel, B., Buchner, J., Bukau, B., et al. (2017). The growing world of small heat shock proteins: from structure to functions. Cell Stress Chaperones *22*, 601-611. 10.1007/s12192-017-0787-8.

Cascarina, S.M., and Ross, E.D. (2014). Yeast prions and human prion-like proteins: sequence features and prediction methods. Cell Mol Life Sci *71*, 2047-2063. 10.1007/s00018-013-1543-6.

Cheetham, M.E., and Caplan, A.J. (1998). Structure, function and evolution of DnaJ: conservation and adaptation of chaperone function. Cell Stress and Chaperones *3*, 28-36. 10.1379/1466-1268(1998)003<0028:sfaeod>2.3.co;2

Chen-Plotkin, A.S., Lee, V.M., and Trojanowski, J.Q. (2010). TAR DNA-binding protein 43 in neurodegenerative disease. Nat Rev Neurol *6*, 211-220. 10.1038/nrneurol.2010.18.

Chen, B., Retzlaff, M., Roos, T., and Frydman, J. (2011). Cellular strategies of protein quality control. Cold Spring Harb Perspect Biol *3*, a004374. 10.1101/cshperspect.a004374.

Chen, S., Berthelier, V., Yang, W., and Wetzel, R. (2001). Polyglutamine aggregation behavior in vitro supports a recruitment mechanism of cytotoxicity. J Mol Biol *311*, 173-182. 10.1006/jmbi.2001.4850.

Chen, S., Ferrone, F.A., and Wetzel, R. (2002). Huntington's disease age-of-onset linked to polyglutamine aggregation nucleation. PNAS *99*, 11884-11889. 10.1073/pnas.182276099.

Chernoff, Y.O., Lindquist, S., Ono, B., Inge-Vechtomov, S.G., and Liebman, S.W. (1995). Role of the chaperone protein Hsp104 in propagation of the yeast prion-like factor [PSI+]. Science *268*, 880-884. 10.1126/science.7754373

Chiti, F. (2006). Relative importance of hydrophobicity, net charge, and secondary structure propensities in protein aggregation. In Protein Misfolding, Aggregation, and Conformational Diseases, Uversky V.N., and F. A.L., eds. (Springer), pp. 43-59. 10.1007/0-387-25919-8_3.

Chiti, F., and Dobson, C.M. (2006). Protein misfolding, functional amyloid, and human disease. Annu Rev Biochem *75*, 333-366. 10.1146/annurev.biochem.75.101304.123901

Chiti, F., and Dobson, C.M. (2017). Protein misfolding, amyloid formation, and human disease: a summary of progress over the last decade. Annu Rev Biochem *86*, 27-68. 10.1146/annurev-biochem-061516-045115.

Christianson, T.W., Sikorski, R.S., Dante, M., Shero, J.H., and Hieter, P. (1992). Multifunctional yeast high-copy-number shuttle vectors. Gene *110*, 119-122. 10.1016/0378-1119(92)90454-W.

Clerico, E.M., Tilitsky, J.M., Meng, W., and Gierasch, L.M. (2015). How hsp70 molecular machines interact with their substrates to mediate diverse physiological functions. J Mol Biol *427*, 1575-1588. 10.1016/j.jmb.2015.02.004.

Cliff, M.J., Limpkin, C., Cameron, A., Burston, S.G., and Clarke, A.R. (2006). Elucidation of steps in the capture of a protein substrate for efficient encapsulation by GroE. J Biol Chem *281*, 21266-21275. 10.1074/jbc.M601605200.

Cohen, F.E., Pan, K.M., Huang, Z., Baldwin, M., Fletterick, R.J., and Prusiner, S.B. (1994). Structural clues to prion replication. Science *264*, 530-531. 10.1126/science.7909169

Coletta, A., Pinney, J.W., Solis, D.Y., Marsh, J., Pettifer, S.R., and Attwood, T.K. (2010). Low-complexity regions within protein sequences have position-dependent roles. BMC Syst Biol *4*, 43. 10.1186/1752-0509-4-43.

Cox, B.S. (1994). Cytoplasmic inheritance. Prion-like factors in yeast. Curr Biol *4*, 744-748. 10.1016/s0960-9822(00)00167-6

Cox, B.S., Byrne, L.J., and Tuite, M.F. (2007). Prion stability. Prion *1*, 170-178. 10.4161/pri.1.3.4839.

Cox, J., and Mann, M. (2008). MaxQuant enables high peptide identification rates, individualized p.p.b.-range mass accuracies and proteome-wide protein quantification. Nat Biotechnol *26*, 1367-1372. 10.1038/nbt.1511.

Craig, E.A., Huang, P., Aron, R., and Andrew, A. (2006). The diverse roles of J-proteins, the obligate Hsp70 co-chaperone. In Rev Physiol Biochem Pharmacol, S. Amara, ed. (Springer, Berlin, Heidelberg), pp. 1-21. 10.1007/s10254-005-0001-0.

Cunningham, C.N., Krukenberg, K.A., and Agard, D.A. (2008). Intra- and intermonomer interactions are required to synergistically facilitate ATP hydrolysis in Hsp90. J Biol Chem *283*, 21170-21178. 10.1074/jbc.M800046200.

Darwich, N.F., Phan, J.M., Kim, B., Suh, E., Papatriantafyllou, J.D., Changolkar, L., Nguyen, A.T., O'Rourke, C.M., He, Z., Porta, S., et al. (2020). Autosomal dominant VCP hypomorph mutation impairs disaggregation of PHF-Tau. Science *370*, eaay8826. 10.1126/science.aay8826.

Davies, S.W., Turmaine, M., Cozens, B.A., DiFiglia, M., Sharp, A.H., Ross, C.A., Scherzinger, E., Wanker, E.E., Mangiarini, L., and Bates, G.P. (1997). Formation of neuronal intranuclear inclusions underlies the neurological dysfunction in mice transgenic for the HD mutation. Cell *90*, 537-548. 10.1016/S0092-8674(00)80513-9.

Dehay, B., and Bertolotti, A. (2006). Critical role of the proline-rich region in Huntingtin for aggregation and cytotoxicity in yeast. J Biol Chem *281*, 35608-35615. 10.1074/jbc.M605558200.

Deng, H., Gao, K., and Jankovic, J. (2014). The role of FUS gene variants in neurodegenerative diseases. Nat Rev Neurol *10*, 337-348. 10.1038/nrneurol.2014.78.

Derkatch, I.L., Bradley, M.E., Hong, J.Y., and Liebman, S.W. (2001). Prions affect the appearance of other prions: the story of [PIN+]. Cell *106*, 171-182. 10.1016/s0092-8674(01)00427-5.

Derkatch, I.L., Bradley, M.E., Masse, S.V.L., Zadorsky, S.P., Polozkov, G.V., Inge-Vechtomov, S.G., and Lieberman, A.P. (2000). Dependence and independence of [PSI+] and [PIN+]: a two-prion system in yeast? EMBO J *19*, 1942-1952. 10.1093/emboj/19.9.1942.

Derkatch, I.L., Bradley, M.E., Zhou, P., Chernoff, Y.O., and Lieberman, A.P. (1997). Genetic and environmental factors affecting the de novo appearance of the [PSI+] prion in Saccharomyces cerevisiae. Genetics *147*, 507-519. 10.1093/genetics/147.2.507.

Derkatch, I.L., Uptain, S.M., Outeiro, T.F., Krishnan, R., Lindquist, S.L., and Liebman, S.W. (2004). Effects of Q/N-rich, polyQ, and non-polyQ amyloids on the de novo formation of the [PSI+] prion in yeast and aggregation of Sup35 in vitro. PNAS *101*, 12934-12939. 10.1073/pnas.0404968101.

DeSantis, M.E., Leung, E.H., Sweeny, E.A., Jackrel, M.E., Cushman-Nick, M., Neuhaus-Follini, A., Vashist, S., Sochor, M.A., Knight, M.N., and Shorter, J. (2012). Operational plasticity enables Hsp104 to disaggregate diverse amyloid and nonamyloid clients. Cell *151*, 778-793. 10.1016/j.cell.2012.09.038.

Dhakal, S., Wyant, C.E., George, H.E., Morgan, S.E., and Rangachari, V. (2021). Prion-like C-terminal domain of TDP-43 and alpha-Synuclein interact synergistically to generate neurotoxic hybrid fibrils. J Mol Biol *433*, 166953. 10.1016/j.jmb.2021.166953.

Di Gregorio, S.E., and Duennwald, M.L. (2018). ALS yeast models - past success stories and new opportunities. Front Mol Neurosci *11*, 394. 10.3389/fnmol.2018.00394.

Diack, A.B., Head, M.W., McCutcheon, S., Boyle, A., Knight, R., Ironside, J.W., Manson, J.C., and Will, R.G. (2014). Variant CJD. 18 years of research and surveillance. Prion *8*, 286-295. 10.4161/pri.29237.

DiFiglia, M., Sapp, E., Chase, K.O., Davies, S.W., Bates, G.P., Vonsattel, J.-P., and Aronin, N. (1997). Aggregation of Huntingtin in neuronal intranuclear inclusions and dystrophic neurites in brain. Sciene *277*, 1990-1993. 10.1126/science.277.5334.1990

Dobson, C.M. (2004). Principles of protein folding, misfolding and aggregation. Semin Cell Dev Biol *15*, 3-16. 10.1016/j.semcdb.2003.12.008.

Dobson, C.M., Sali, A., and Karplus, M. (1998). Protein folding: a perspective from theory and experiment. Angew Chem Int Ed *37*, 868-893. 10.1002/(SICI)1521-3773(19980420)37:7<868::AID-ANIE868>3.0.CO;2-H. .

Douglas, N.R., Reissmann, S., Zhang, J., Chen, B., Jakana, J., Kumar, R., Chiu, W., and Frydman, J. (2011). Dual action of ATP hydrolysis couples lid closure to substrate release into the group II chaperonin chamber. Cell *144*, 240-252. 10.1016/j.cell.2010.12.017.

Douglas, P.M., and Dillin, A. (2010). Protein homeostasis and aging in neurodegeneration. J Cell Biol *190*, 719-729. 10.1083/jcb.201005144.

Douglas, P.M., Treusch, S., Ren, H.Y., Halfmann, R., Duennwald, M.L., Lindquist, S., and Cyr, D.M. (2008). Chaperone-dependent amyloid assembly protects cells from prion toxicity. PNAS *105*, 7206-7211. 10.1073/pnas.0802593105.

Doyle, S.M., Genest, O., and Wickner, S. (2013). Protein rescue from aggregates by powerful molecular chaperone machines. Nat Rev Mol Cell Biol *14*, 617-629. 10.1038/nrm3660.

Drummond, D.A., and Wilke, C.O. (2008). Mistranslation-induced protein misfolding as a dominant constraint on coding-sequence evolution. Cell *134*, 341-352. 10.1016/j.cell.2008.05.042.

Duan, L., Hope, J., Ong, Q., Lou, H.Y., Kim, N., McCarthy, C., Acero, V., Lin, M.Z., and Cui, B. (2017). Understanding CRY2 interactions for optical control of intracellular signaling. Nat Commun *8*, 547. 10.1038/s41467-017-00648-8.

Duennwald, M.L. (2011). Polyglutamine misfolding in yeast: toxic and protective aggregation. Prion *5*, 285-290. 10.4161/pri.5.4.18071.

Duennwald, M.L., Jagadish, S., Giorgini, F., Muchowski, P.J., and Lindquist, S. (2006a). A network of protein interactions determines polyglutamine toxicity. PNAS *103*, 11051-11056. 10.1073/pnas.0604548103.

Duennwald, M.L., Jagadish, S., Muchowski, P.J., and Lindquist, S. (2006b). Flanking sequences profoundly alter polyglutamine toxicity in yeast. PNAS *103*, 11045-11050. 10.1073/pnas.0604547103.

Dugger, B.N., and Dickson, D.W. (2017). Pathology of neurodegenerative diseases. Cold Spring Harb Perspect Biol *9*, a028035. 10.1101/cshperspect.a028035.

Ecroyd, H., Meehan, S., Horwitz, J., Aquilina, J.A., Benesch, J.L., Robinson, C.V., Macphee, C.E., and Carver, J.A. (2007). Mimicking phosphorylation of alphaB-crystallin affects its chaperone activity. Biochem J *401*, 129-141. 10.1042/BJ20060981.

Ellis, J. (1987). Proteins as molecular chaperones. Nature *328*, 378-379. 10.1038/328378a0.

Ellis, R.J., and Minton, A.P. (2006). Protein aggregation in crowded environments. Biol Chem *387*, 485-497. 10.1515/BC.2006.064.

Escusa-Toret, S., Vonk, W.I., and Frydman, J. (2013). Spatial sequestration of misfolded proteins by a dynamic chaperone pathway enhances cellular fitness during stress. Nat Cell Biol *15*, 1231-1243. 10.1038/ncb2838.

Fan, C.-Y., Lee, S., Ren, H.Y., and Cyr, D.M. (2004). Exchangeable chaperone modules contribute to specification of type I and type II Hsp40 cellular function. Mol Biol Cell *15*, 761-773. 10.1091/mbc.e03-03-0146.

Farr, G.W., Furtak, K., Rowland, M.B., Ranson, N.A., Saibil, H.R., Kirchhausen, T., and Horwich, A.L. (2000). Multivalent binding of nonnative substarte proteins by the chaperonin GroEL. Cell *100*, 561-573. 10.1016/S0092-8674(00)80692-3.

Feder, Z.A., Ali, A., Singh, A., Krakowiak, J., Zheng, X., Bindokas, V.P., Wolfgeher, D., Kron, S.J., and Pincus, D. (2021). Subcellular localization of the J-protein Sis1 regulates the heat shock response. J Cell Biol *220*, e202005165. 10.1083/jcb.202005165.

Ferreira, P.C., Ness, F., Edwards, S.R., Cox, B.S., and Tuite, M.F. (2001). The elimination of the yeast [PSI+] prion by guanidine hydrochloride is the result of Hsp104 inactivation. Mol Microbiol *40*, 1357-1369. 10.1046/j.1365-2958.2001.02478.x

Fink, A.L. (1998). Protein aggregation: folding aggregates, inclusion bodies and amyloid. Fold Des *3*, R9-R23. 10.1016/s1359-0278(98)00002-9.

Fraser, P.E. (2014). Prions and prion-like proteins. J Biol Chem *289*, 19839-19840. 10.1074/jbc.R114.583492.

Fu, H., Hardy, J., and Duff, K.E. (2018). Selective vulnerability in neurodegenerative diseases. Nat Neurosci *21*, 1350-1358. 10.1038/s41593-018-0221-2.

Fujimoto, M., Takaki, E., Hayashi, T., Kitaura, Y., Tanaka, Y., Inouye, S., and Nakai, A. (2005). Active HSF1 significantly suppresses polyglutamine aggregate formation in cellular and mouse models. J Biol Chem *280*, 34908-34916. 10.1074/jbc.M506288200.

Gandhi, J., Antonelli, A.C., Afridi, A., Vatsia, S., Joshi, G., Romanov, V., Murray, I.V.J., and Khan, S.A. (2019). Protein misfolding and aggregation in neurodegenerative diseases: a review of pathogeneses, novel detection strategies, and potential therapeutics. Rev Neurosci *30*, 339-358. 10.1515/revneuro-2016-0035.

Gao, X., Carroni, M., Nussbaum-Krammer, C., Mogk, A., Nillegoda, N.B., Szlachcic, A., Guilbride, D.L., Saibil, H.R., Mayer, M.P., and Bukau, B. (2015). Human Hsp70 disaggregase reverses Parkinson's-linked alpha-synuclein amyloid fibrils. Mol Cell *59*, 781-793. 10.1016/j.molcel.2015.07.012.

Garg, A., Kumari, B., and Kumar, M. (2018). Emerging role of hsp70 in human disease. In Hsp70 in human diseases and disorders, A.A.A. Asea, and P. Kaur, eds. (Springer Cham), pp. 291-304. 10.1007/978-3-319-89551-2.

Gates, S.N., Yokom, A.L., Lin, J., Jackrel, M.E., Rizo, A.N., Kendsersky, N.M., Buell, C.E., Sweeny, E.A., Mack, K.L., Chuang, E., et al. (2017). Ratchet-like polypeptide translocation mechanism of the AAA+ disaggregase Hsp104. Science *357*, 273-279. 10.1126/science.aan1052

GeneOntologyConsortium (2021). The Gene Ontology resource: enriching a GOld mine. Nucleic Acids Res *49*, D325-D334. 10.1093/nar/gkaa1113.

Ghazaei, C. (2017). Role and mechanism of the Hsp70 molecular chaperone machines in bacterial pathogens. J Med Microbiol *66*, 259-265. 10.1099/jmm.0.000429.

Giasson, B.I., Forman, M.S., Higuchi, M., Golbe, L.I., Graves, C.L., Kotzbauer, P.T., Trojanowski, J.Q., and Lee, V.M. (2003). Initiation and synergistic fibrillization of Tau and alpha-Synuclein. Science *300*, 636-640. 10.1126/science.1082324.

Gillis, J., Schipper-Krom, S., Juenemann, K., Gruber, A., Coolen, S., van den Nieuwendijk, R., van Veen, H., Overkleeft, H., Goedhart, J., Kampinga, H.H., and Reits, E.A. (2013). The DNAJB6 and DNAJB8 protein chaperones prevent intracellular aggregation of polyglutamine peptides. J Biol Chem *288*, 17225-17237. 10.1074/jbc.M112.421685.

Glover, J.R., and Lindquist, S. (1998). Hsp104, Hsp70, and Hsp40: a novel chaperone system that rescues previously aggregated proteins. Cell *94*, 73-82. 10.1016/s0092-8674(00)81223-4.

Glover, J.R., and Tkach, J.M. (2001). Crowbars and ratchets: Hsp100 chaperones as tools in reversing protein aggregation. Biochem Cell Biol *79*, 557-568. 10.1139/bcb-79-5-557.

Glynn, C., Sawaya, M.R., Ge, P., Gallagher-Jones, M., Short, C.W., Bowman, R., Apostol, M., Zhou, Z.H., Eisenberg, D.S., and Rodriguez, J.A. (2020). Cryo-EM structure of a human prion fibril with a hydrophobic, protease-resistant core. Nat Struct Mol Biol *27*, 417-423. 10.1038/s41594-020-0403-y.

Goffeau, A., Barrell, B.G., Bussey, H., Davis, R.W., Dujon, B., Feldmann, H., Galibert, F., Hoheisel, J.D., Jacq, C., Johnston, M., et al. (1996). Life with 6000 genes. Science *274*, 563-567. 10.1126/science.274.5287.546

Gomez-Pastor, R., Burchfiel, E.T., Neef, D.W., Jaeger, A.M., Cabiscol, E., McKinstry, S.U., Doss, A., Aballay, A., Lo, D.C., Akimov, S.S., et al. (2017). Abnormal degradation of the neuronal stress-protective transcription factor HSF1 in Huntington's disease. Nat Commun *8*, 14405. 10.1038/ncomms14405.

Gomez-Pastor, R., Burchfiel, E.T., and Thiele, D.J. (2018). Regulation of heat shock transcription factors and their roles in physiology and disease. Nat Rev Mol Cell Biol *19*, 4-19. 10.1038/nrm.2017.73.

Grantham, J. (2020). The molecular chaperone CCT/TRiC: an essential component of proteostasis and potential modulator of protein aggregation. Front Genet *11*, 172. 10.3389/fgene.2020.00172.

Greene, M.K., Maskos, K., and J., L.S. (1998). Role of the J-domain in the cooperation of Hsp40 with Hsp70. PNAS *95*, 6108-6113. 10.1073/pnas.95.11.6108

Gropp, M.H.M., Klaips, C.L., and Hartl, F.U. (2022). Formation of toxic oligomers of polyQ-expanded Huntingtin by prion-mediated cross-seeding. Mol Cell *82*(22), 4290-4306. 10.1016/j.molcel.2022.09.031.

Gruber, A., Hornburg, D., Antonin, M., Krahmer, N., Collado, J., Schaffar, M., Zubaite, G., Lüchtenborg, C., Sachsenheimer, T., Brügger, B., et al. (2018). Molecular and structural architecture of polyQ aggregates in yeast. PNAS *115*, 3446-3453. 10.1073/pnas.1717978115.

Grune, T., Jung, T., Merker, K., and Davies, K.J. (2004). Decreased proteolysis caused by protein aggregates, inclusion bodies, plaques, lipofuscin, ceroid, and 'aggresomes' during oxidative stress, aging, and disease. Int J Biochem Cell Biol *36*, 2519-2530. 10.1016/j.biocel.2004.04.020.

Guo, J.L., Covell, D.J., Daniels, J.P., Iba, M., Stieber, A., Zhang, B., Riddle, D.M., Kwong, L.K., Xu, Y., Trojanowski, J.Q., and Lee, V.M. (2013). Distinct alpha-Synuclein strains differentially promote Tau inclusions in neurons. Cell *154*, 103-117. 10.1016/j.cell.2013.05.057.

Gupta, A.J., Haldar, S., Milicic, G., Hartl, F.U., and Hayer-Hartl, M. (2014). Active cage mechanism of chaperonin-assisted protein folding demonstrated at single-molecule level. J Mol Biol *426*, 2739-2754. 10.1016/j.jmb.2014.04.018.

Gupta, R., Kasturi, P., Bracher, A., Loew, C., Zheng, M., Villella, A., Garza, D., Hartl, F.U., and Raychaudhuri, S. (2011). Firefly luciferase mutants as sensors of proteome stress. Nat Methods *8*, 879-884. 10.1038/nmeth.1697.

Haass, C., and Selkoe, D.J. (2007). Soluble protein oligomers in neurodegeneration: lessons from the Alzheimer's Amyloid β-peptide. Nat Rev Mol Cell Biol *8*, 101-112. 10.1038/nrm2101.

Hageman, J., Rujano, M.A., van Waarde, M.A., Kakkar, V., Dirks, R.P., Govorukhina, N., Oosterveld-Hut, H.M., Lubsen, N.H., and Kampinga, H.H. (2010). A DNAJB chaperone subfamily with HDAC-dependent activities suppresses toxic protein aggregation. Mol Cell *37*, 355-369. 10.1016/j.molcel.2010.01.001.

Halfmann, R., Alberti, S., and Lindquist, S. (2010). Prions, protein homeostasis, and phenotypic diversity. Trends Cell Biol *20*, 125-133. 10.1016/j.tcb.2009.12.003.

Hanson, P.I., and Whiteheart, S.W. (2005). AAA+ proteins: have engine, will work. Nat Rev Mol Cell Biol *6*, 519-529. 10.1038/nrm1684.

Harding, R.J., Loppnau, P., Ackloo, S., Lemak, A., Hutchinson, A., Hunt, B., Holehouse, A.S., Ho, J.C., Fan, L., Toledo-Sherman, L., et al. (2019). Design and characterization of mutant and wildtype Huntingtin proteins produced from a toolkit of scalable eukaryotic expression systems. J Biol Chem *294*, 6986-7001. 10.1074/jbc.RA118.007204

Harel, I., Chen, Y.R., Ziv, I., Singh, P.P., Negredo, P.N., Goshtchevsky, U., Wang, W., Astre, G., Moses, E., McKay, A., et al. (2022). Identification of protein aggregates in the aging vertebrate brain with prion-like and phase separation properties. bioRxiv. 10.1101/2022.02.26.482115.

Hartl, F.U. (1996). Molecular chaperones in cellular protein folding. Nature *381*, 571-580. doi.org/10.1038/381571a0.

Hartl, F.U. (2016). Cellular homeostasis and aging. Annu Rev Biochem *85*, 1-4. 10.1146/annurev-biochem-011116-110806.

Hartl, F.U. (2017). Protein misfolding diseases. Annu Rev Biochem *86*, 21-26. 10.1146/annurev-biochem-061516-044518.

Hartl, F.U., Bracher, A., and Hayer-Hartl, M. (2011). Molecular chaperones in protein folding and proteostasis. Nature *475*, 324-332. 10.1038/nature10317.

Haslbeck, M., Franzmann, T., Weinfurtner, D., and Buchner, J. (2005a). Some like it hot: the structure and function of small heat-shock proteins. Nat Struct Mol Biol *12*, 842-846. 10.1038/nsmb993.

Haslbeck, M., Miess, A., Stromer, T., Walter, S., and Buchner, J. (2005b). Disassembling protein aggregates in the yeast cytosol. The cooperation of Hsp26 with Ssa1 and Hsp104. J Biol Chem *280*, 23861-23868. 10.1074/jbc.M502697200.

Haslbeck, M., and Vierling, E. (2015). A first line of stress defense: small heat shock proteins and their function in protein homeostasis. J Mol Biol *427*, 1537-1548. 10.1016/j.jmb.2015.02.002.

Haslbeck, M., Weinkauf, S., and Buchner, J. (2019). Small heat shock proteins: simplicity meets complexity. J Biol Chem *294*, 2121-2132. 10.1074/jbc.REV118.002809.

Hayer-Hartl, M., Bracher, A., and Hartl, F.U. (2016). The GroEL-GroES chaperonin machine: a nano-cage for protein folding. Trends Biochem Sci *41*, 62-76. 10.1016/j.tibs.2015.07.009.

Hazeki, N., Tukamoto, T., Goto, J., and Kanazawa, I. (2000). Formic acid dissolves aggregates of an N-terminal huntingtin fragment containing an expanded polyglutamine tract: applying to quantification of protein components of the aggregates. Biochem Biophys Res Commun *277*, 386-393. 10.1006/bbrc.2000.3682.

Hendrick, J.P., and Hartl, F.U. (1993). Molecular chaperone functions of heat-shock proteins. Annu Rev Biochem *62*, 349-384. 10.1146/annurev.bi.62.070193.002025

Hessling, M., Richter, K., and Buchner, J. (2009). Dissection of the ATP-induced conformational cycle of the molecular chaperone Hsp90. Nat Struct Mol Biol *16*, 287-293. 10.1038/nsmb.1565.

Hill, A.F., Desbruslais, M., Joiner, S., Sidle, K.C., Gowland, I., Collinge, J., Doey, L.J., and Lantos, P. (1997). The same prion strain causes vCJD and BSE. Nature *389*, 448-450. 10.1038/38925

Hipp, M.S., Park, S.H., and Hartl, F.U. (2014). Proteostasis impairment in protein-misfolding and -aggregation diseases. Trends Cell Biol *24*, 506-514. 10.1016/j.tcb.2014.05.003.

Holmes, W.M., Klaips, C.L., and Serio, T.R. (2014a). Defining the limits: protein aggregation and toxicity in vivo. Crit Rev Biochem Mol Biol *49*, 294-303. 10.3109/10409238.2014.914151.

Holmes, W.M., Mannakee, B.K., Gutenkunst, R.N., and Serio, T.R. (2014b). Loss of amino-terminal acetylation suppresses a prion phenotype by modulating global protein folding. Nat Commun *5*, 4383. 10.1038/ncomms5383.

Hubner, N.C., Bird, A.W., Cox, J., Splettstoesser, B., Bandilla, P., Poser, I., Hyman, A., and Mann, M. (2010). Quantitative proteomics combined with BAC TransgeneOmics reveals in vivo protein interactions. J Cell Biol *189*, 739-754. 10.1083/jcb.200911091.

Huh, W.K., Falvo, J.V., Gerke, L.C., Carroll, A.S., Howson, R.W., Weissman, J.S., and O'Shea, E.K. (2003). Global analysis of protein localization in budding yeast. Nature *425*, 686-691. 10.1038/nature02026

Iglesias, V., Paladin, L., Juan-Blanco, T., Pallares, I., Aloy, P., Tosatto, S.C.E., and Ventura, S. (2019). In silico characterization of human prion-like proteins: beyond neurological diseases. Front Physiol *10*, 314. 10.3389/fphys.2019.00314.

Imamoglu, R., Balchin, D., Hayer-Hartl, M., and Hartl, F.U. (2020). Bacterial Hsp70 resolves misfolded states and accelerates productive folding of a multi-domain protein. Nat Commun *11*, 365. 10.1038/s41467-019-14245-4.

Irobi, J., Van Impe, K., Seeman, P., Jordanova, A., Dierick, I., Verpoorten, N., Michalik, A., De Vriendt, E., Jacobs, A., Van Gerwen, V., et al. (2004). Hot-spot residue in small heat-shock protein 22 causes distal motor neuropathy. Nat Genet *36*, 597-601. 10.1038/ng1328.

Jackson, M.P., and Hewitt, E.W. (2016). Cellular proteostasis: degradation of misfolded proteins by lysosomes. Essays Biochem *60*, 173-180. 10.1042/EBC20160005.

Jayaraj, G.G., Hipp, M.S., and Hartl, F.U. (2020). Functional modules of the proteostasis network. Cold Spring Harb Perspect Biol *12*, a033951. 10.1101/cshperspect.a033951.

Jayaraman, M., Mishra, R., Kodali, R., Thakur, A.K., Koharudin, L.M., Gronenborn, A.M., and Wetzel, R. (2012). Kinetically competing Huntingtin aggregation pathways control amyloid polymorphism and properties. Biochemistry *51*, 2706-2716. 10.1021/bi3000929.

Jeffrey, M., and Gonzales, L. (2004). Pathology and pathogenesis of bovine spongiform encephalopathy and scrapie In Mad Cow Disease and Related Spongiform Encephalopathies, D.A. Harris, ed. (Springer, Berlin, Heidelberg), pp. 65-98. 10.1007/978-3-662-08441-0_3.

Kaganovich, D., Kopito, R., and Frydman, J. (2008). Misfolded proteins partition between two distinct quality control compartments. Nature *454*, 1088-1095. 10.1038/nature07195.

Kakkar, V., Mansson, C., de Mattos, E.P., Bergink, S., van der Zwaag, M., van Waarde, M., Kloosterhuis, N.J., Melki, R., van Cruchten, R.T.P., Al-Karadaghi, S., et al. (2016). The S/T-rich motif in the DNAJB6 chaperone delays polyglutamine aggregation and the onset of disease in a mouse model. Mol Cell *62*, 272-283. 10.1016/j.molcel.2016.03.017.

Kakkar, V., Meister-Broekema, M., Minoia, M., Carra, S., and Kampinga, H.H. (2014). Barcoding heat shock proteins to human diseases: looking beyond the heat shock response. Dis Model Mech *7*, 421-434. 10.1242/dmm.014563.

Kampinga, H.H., and Craig, E.A. (2010). The HSP70 chaperone machinery: J proteins as drivers of functional specificity. Nat Rev Mol Cell Biol *11*, 579-592. 10.1038/nrm2941.

Kastano, K., Mier, P., and Andrade-Navarro, M.A. (2021). The Role of Low Complexity Regions in Protein Interaction Modes: An Illustration in Huntingtin. Int J Mol Sci *22*. 10.3390/ijms22041727.

Kato, M., Han, T.W., Xie, S., Shi, K., Du, X., Wu, L.C., Mirzaei, H., Goldsmith, E.J., Longgood, J., Pei, J., et al. (2012). Cell-free formation of RNA granules: low complexity sequence domains form dynamic fibers within hydrogels. Cell *149*, 753-767. 10.1016/j.cell.2012.04.017.

Kayatekin, C., Matlack, K.E., Hesse, W.R., Guan, Y., Chakrabortee, S., Russ, J., Wanker, E.E., Shah, J.V., and Lindquist, S. (2014). Prion-like proteins sequester and suppress the toxicity of Huntingtin exon 1. PNAS *111*, 12085-12090. 10.1073/pnas.1412504111.

Kayed, R., Head, E., Thompson, J.L., McIntire, T.M., Milton, S.C., Cotman, C.W., and Glabe, C.G. (2003). Common structure of soluble amyloid oligomers implies common mechanism of pathogenesis. Science *300*, 486-489. 10.1126/science.1079469.

Kazantsev, A., Preisinger, E., Dranovsky, A., Goldgaber, D., and Housman, D. (1999). Insoluble detergent-resistant aggregates form between pathological and nonpathological lengths of polyglutamine in mammalian cells. PNAS *96*, 11404-11409. 10.1073/pnas.96.20.11404.

Kerner, M.J., Naylor, D.J., Ishihama, Y., Maier, T., Chang, H.C., Stines, A.P., Georgopoulos, C., Frishman, D., Hayer-Hartl, M., Mann, M., and Hartl, F.U. (2005). Proteome-wide analysis of chaperonin-dependent protein folding in Escherichia coli. Cell *122*, 209-220. 10.1016/j.cell.2005.05.028.

Khurana, V., and Lindquist, S. (2010). Modelling neurodegeneration in Saccharomyces cerevisiae: why cook with baker's yeast? Nat Rev Neurosci *11*, 436-449. 10.1038/nrn2809.

Kim, S., Nollen, E.A., Kitagawa, K., Bindokas, V.P., and Morimoto, R.I. (2002). Polyglutamine protein aggregates are dynamic. Nat Cell Biol *4*, 826-831. 10.1038/ncb863.

Kim, Y.E., Hipp, M.S., Bracher, A., Hayer-Hartl, M., and Hartl, F.U. (2013). Molecular chaperone functions in protein folding and proteostasis. Annu Rev Biochem *82*, 323-355. 10.1146/annurev-biochem-060208-092442.

Kim, Y.E., Hosp, F., Frottin, F., Ge, H., Mann, M., Hayer-Hartl, M., and Hartl, F.U. (2016). Soluble oligomers of polyQ-expanded Huntingtin target a multiplicity of key cellular factors. Mol Cell *63*, 951-964. 10.1016/j.molcel.2016.07.022.

Klaips, C.L., Gropp, M.H.M., Hipp, M.S., and Hartl, F.U. (2020). Sis1 potentiates the stress response to protein aggregation and elevated temperature. Nat Commun *11*, 6271. 10.1038/s41467-020-20000-x.

Klaips, C.L., Hochstrasser, M.L., Langlois, C.R., and Serio, T.R. (2014). Spatial quality control bypasses cell-based limitations on proteostasis to promote prion curing. Elife *3*, e04288. 10.7554/eLife.04288.

Klaips, C.L., Jayaraj, G.G., and Hartl, F.U. (2018). Pathways of cellular proteostasis in aging and disease. J Cell Biol *217*, 51-63. 10.1083/jcb.201709072.

Kobayashi, Y., and Sobue, G. (2001). Protective effect of chaperones on polyglutamine diseases. Brain Res Bulletin *56*, 165-168. 10.1016/s0361-9230(01)00593-7

Kremer, B., Goldberg, P., Andrew, S.E., Theilmann, J., Telenius, H., Zeisler, J., Squitieri, F., Lin, B., Bassett, A., Amlqvist, E., et al. (1994). A worldwide study of the Huntingtons's disease mutation. N Engl J Med *330*, 1401-1406. 10.1056/NEJM199405193302001.

Krobitsch, S., and Lindquist, S. (2000). Aggregation of Huntingtin in yeast varies with the length of the polyglutamine expansion and the expression of chaperone proteins. PNAS *97*, 1589-1594. 10.1073/pnas.97.4.1589.

Kushnirov, V.V., and Ter-Avenesyan, M.D. (1998). Structure and replication of yeast prions. Cell *94*, 13-16. 10.1016/s0092-8674(00)81216-7

Kyung, T., Lee, S., Kim, J.E., Cho, T., Park, H., Jeong, Y.M., Kim, D., Shin, A., Kim, S., Baek, J., et al. (2015). Optogenetic control of endogenous Ca(2+) channels in vivo. Nat Biotechnol *33*, 1092-1096. 10.1038/nbt.3350.

Labbadia, J., and Morimoto, R.I. (2015). The biology of proteostasis in aging and disease. Annu Rev Biochem *84*, 435-464. 10.1146/annurev-biochem-060614-033955.

Landles, C., Sathasivam, K., Weiss, A., Woodman, B., Moffitt, H., Finkbeiner, S., Sun, B., Gafni, J., Ellerby, L.M., Trottier, Y., et al. (2010). Proteolysis of mutant Huntingtin produces an exon 1 fragment that accumulates as an aggregated protein in neuronal nuclei in Huntington disease. J Biol Chem *285*, 8808-8823. 10.1074/jbc.M109.075028.

Landreh, M., Sawaya, M.R., Hipp, M.S., Eisenberg, D.S., Wuthrich, K., and Hartl, F.U. (2016). The formation, function and regulation of amyloids: insights from structural biology. J Intern Med *280*, 164-176. 10.1111/joim.12500.

Langer, T., Lu, C., Echols, H., Flanagan, J., Hayer, M.K., and Hartl, F.U. (1992). Successive action of DnaK, DnaJ and GroEL along the pathway of chaperone-mediated protein folding. Nature *356*, 683-689. 10.1038/356683a0.

Laufen, T., Mayer, M.P., Beisel, C., Klostermeier, D., Mogk, A., Reinstein, J., and Bukau, B. (1999). Mechanism of regulation of hsp70 chaperones by DnaJ cochaperones. PNAS *96*, 5452-5457. 10.1073/pnas.96.10.5452

Lee, S., Sielaff, B., Lee, J., and Tsai, F.T. (2010). CryoEM structure of Hsp104 and its mechanistic implication for protein disaggregation. PNAS *107*, 8135-8140. 10.1073/pnas.1003572107.

Lee, S., Sowa, M.E., Watanabe, Y., Sigler, P.B., Chiu, W., Yoshida, M., and Tsai, F.T.F. (2003). The structure of ClpB: a molecular chaperone that rescues proteins from an aggregated state. Cell *115*, 229-240. 10.1016/s0092-8674(03)00807-9. .

Leitman, J., Ulrich Hartl, F., and Lederkremer, G.Z. (2013). Soluble forms of polyQ-expanded Huntingtin rather than large aggregates cause endoplasmic reticulum stress. Nat Commun *4*, 2753. 10.1038/ncomms3753.

Leopold, A.V., Chernov, K.G., and Verkhusha, V.V. (2018). Optogenetically controlled protein kinases for regulation of cellular signaling. Chem Soc Rev *47*, 2454-2484. 10.1039/c7cs00404d.

Levinthal, C. (1968). Are there pathways for protein folding? J Chim Phys *65*, 44-45. 10.1051/jcp/1968650044

Levinthal, C. (1969). How to fold graciously.

Li, H., Li, S.-H., Johnston, H., Shelbourne, P.F., and Li, X.-J. (2000). Amino-terminal fragments of mutant Huntingtin show selective accumulation in striatal neurons and synaptic toxicity. Nat Genet *25*, 385-389. 10.1038/78054

Li, J., Soroka, J., and Buchner, J. (2012). The Hsp90 chaperone machinery: conformational dynamics and regulation by co-chaperones. Biochim Biophys Acta *1823*, 624-635. 10.1016/j.bbamcr.2011.09.003.

Liebman, S.W., and Chernoff, Y.O. (2012). Prions in yeast. Genetics *191*, 1041-1072. 10.1534/genetics.111.137760.

Lindquist, S. (2009). Protein folding sculpting evolutionary change. Cold Spring Harb Symp Quant Biol *74*, 103-108. 10.1101/sqb.2009.74.043

Lindquist, S., and Craig, E.A. (1988). The heat-shock proteins. Annu Rev Genet *22*, 631-677. 10.1146/annurev.ge.22.120188.003215

Litt, M., Kramer, P., LaMorticella, D.M., Murphey, W., Lovrien, E.W., and Weleber, R.G. (1998). Autosomal dominant congenital cataract associated with a missense mutation in the human alpha crystallin gene CRYAA. Hum Mol Genet *7*, 471-474. 10.1093/hmg/7.3.471.

Liu, X.-D., Liu, P.C.C., Santoro, N., and Thiele, D.J. (1997). Conservation of a stress response: human heat shock transcription factors functionally substitute for yeast HSF. EMBO J *16*, 6466-6477. 10.1093/emboj/16.21.6466.

Lopez, N., Aron, R., and Craig, E.A. (2003). Specificity of class II Hsp40 Sis1 in maintenance of yeast prion [RNQ+]. Mol Biol Cell *14*, 1172-1181. 10.1091/mbc.e02-09-0593.

Lopez, T., Dalton, K., and Frydman, J. (2015). The mechanism and function of group II chaperonins. J Mol Biol *427*, 2919-2930. 10.1016/j.jmb.2015.04.013.

Lu, X., Shen, Y., and Campbell, R.E. (2020). Engineering photosensory modules of non-opsin-based optogenetic actuators. Int J Mol Sci *21*, 6522. 10.3390/ijms21186522.

Lu, Z., and Cyr, D.M. (1998). Protein folding activity of Hsp70 is modified differentially by the Hsp40 co-chaperones Sis1 and Ydj1. J Biol Chem *273*, 2782427830. 10.1074/jbc.273.43.27824.

Luke, M.M., Sutton, A., and Arndt, K.T. (1991). Characterization of SIS1, a Saccharomyces cerevisiae homologue of bacterial dnaJ proteins. J Cell Biol *114*, 623-638. 10.1083/jcb.114.4.623

Luo, W., Sun, W., Taldone, T., Rodina, A., and Chiosis, G. (2010). Heat shock protein 90 in neurodegenerative diseases. Mol Neurodegener *5*, 24. 10.1186/1750-1326-5-24

Ma, L., Guan, Z., Wang, Q., Yan, X., Wang, J., Wang, Z., Cao, J., Zhang, D., Gong, X., and Yin, P. (2020). Structural insights into the photoactivation of Arabidopsis CRY2. Nat Plants *6*, 1432-1438. 10.1038/s41477-020-00800-1.

Macario, A.J., Grippo, T.M., and Conway de Macario, E. (2005). Genetic disorders involving molecular-chaperone genes: a perspective. Genet Med *7*, 3-12. 10.1097/01.gim.0000151351.11876.c3.

Maheshwari, M., Bhutani, S., Das, A., Mukherjee, R., Sharma, A., Kino, Y., Nukina, N., and Jana, N.R. (2014). Dexamethasone induces heat shock response and slows down disease progression in mouse and fly models of Huntington's disease. Hum Mol Genet *23*, 2737-2751. 10.1093/hmg/ddt667.

March, Z.M., King, O.D., and Shorter, J. (2016). Prion-like domains as epigenetic regulators, scaffolds for subcellular organization, and drivers of neurodegenerative disease. Brain Res *1647*, 9-18. 10.1016/j.brainres.2016.02.037.

Marques Sousa, C., and Humbert, S. (2013). Huntingtin: here, there, everywhere! J Huntingtons Dis *2*, 395-403. 10.3233/JHD-130082.

Martindale, D., Hackam, A., Wieczorek, A., Ellerby, L., Wellington, C.L., McCutcheon, K., Singaraja, R., Kazemi-Esfarjani, P., Devon, R., Kim, S.U., et al. (1998). Length of Huntingtin and its polyglutamine tract influences localization and frequency of intracellular aggregates. Nature Genetics *18*, 150-154. 10.1038/ng0298-150.

Mas, P., Devlin, P.F., Panda, S., and Kay, S.A. (2000). Functional interaction of Phytochrome B and Cryptochrome 2. Nature *408*, 207-211. 10.1038/35041583.

Masser, A.E., Ciccarelli, M., and Andreasson, C. (2020). Hsf1 on a leash - controlling the heat shock response by chaperone titration. Exp Cell Res *396*, 112246. 10.1016/j.yexcr.2020.112246.

Masser, A.E., Kang, W., Roy, J., Mohanakrishnan Kaimal, J., Quintana-Cordero, J., Friedlander, M.R., and Andreasson, C. (2019). Cytoplasmic protein misfolding titrates Hsp70 to activate nuclear Hsf1. Elife *8*, e47791. 10.7554/eLife.47791.

Mayer, M.P. (2010). Gymnastics of molecular chaperones. Mol Cell *39*, 321-331. 10.1016/j.molcel.2010.07.012.

Mayer, M.P. (2013). Hsp70 chaperone dynamics and molecular mechanism. Trends Biochem Sci *38*, 507-514. 10.1016/j.tibs.2013.08.001.

Mayer, M.P. (2021). The Hsp70-chaperone machines in bacteria. Front Mol Biosci *8*, 694012. 10.3389/fmolb.2021.694012.

Mayer, M.P., and Bukau, B. (2005). Hsp70 chaperones: cellular functions and molecular mechanism. Cell Mol Life Sci *62*, 670-684. 10.1007/s00018-004-4464-6.

Meriin, A.B., Zhang, X., He, X., Newnam, G.P., Chernoff, Y.O., and Sherman, M.Y. (2002). Huntington toxicity in yeast model depends on polyglutamine aggregation mediated by a prion-like protein Rnq1. J Cell Biol *157*, 997-1004. 10.1083/jcb.200112104.

Meyer, P., Prodromou, C., Hu, B., Vaughan, C., Roe, S.M., Panaretou, B., Piper, P.W., and Pearl, L.H. (2003). Structural and functional analysis of the middle segment of Hsp90: implications for ATP hydrolysis and client protein and cochaperone interactions. Mol Cell *11*, 647-658. 10.1016/s1097-2765(03)00065-0.

Mi, H., Muruganujan, A., Ebert, D., Huang, X., and Thomas, P.D. (2019). PANTHER version 14: more genomes, a new PANTHER GO-slim and improvements in enrichment analysis tools. Nucleic Acids Res *47*, D419-D426. 10.1093/nar/gky1038.

Mogk, A., Kummer, E., and Bukau, B. (2015). Cooperation of Hsp70 and Hsp100 chaperone machines in protein disaggregation. Front Mol Biosci *2*, 22. 10.3389/fmolb.2015.00022.

Montalbano, M., McAllen, S., Cascio, F.L., Sengupta, U., Garcia, S., Bhatt, N., Ellsworth, A., Heidelman, E.A., Johnson, O.D., Doskocil, S., and Kayed, R. (2020). TDP-43 and Tau oligomers in Alzheimer's disease, amyotrophic lateral sclerosis, and frontotemporal dementia. Neurobiol Dis *146*, 105130. 10.1016/j.nbd.2020.105130.

Morales, R., Moreno-Gonzales, I., and Soto, C. (2013). Cross-seeding of misfolded proteins: implications for etiology and pathogenesis of protein misfolding diseases. PLOS Pathog *9*, e1003537. 10.1371/journal.ppat.1003537.g001.

Moriyama, H., Edskes, H.K., and Wickner, R.B. (2000). [URE3] prion propagation in Saccharomyces cerevisiae: requirement for chaperone Hsp104 and curing by overexpressed chaperone Ydj1p. Mol Cell Biol *20*, 8916-8922. 10.1128/MCB.20.23.8916-8922.2000.

Muchowski, P.J., Ning, K., D'Souza-Schorey, C., and Fields, S. (2002). Requirement of an intact microtubule cytoskeleton for aggregation and inclusion body formation by a mutant Huntingtin fragment. PNAS *99*, 727-732. 10.1073/pnas.022628699.

Muchowski, P.J., Schaffar, G., Sittler, A., Wanker, E.E., Hayer-Hartl, M.K., and Hartl, F.U. (2000). Hsp70 and hsp40 chaperones can inhibit self-assembly of polyglutamine proteins into amyloid-like fibrils. PNAS *97*, 7841-7846. 10.1073/pnas.140202897.

Mumberg, D., Müller, R., and Funk, M. (1994). Regulatable promoters of Saccharomyces cerevisiae: comparison of transcriptional activity and their use for heterologous expression. Nucleic Acids Res *22*, 5767-5768. 10.1093/nar/22.25.5767.

Mumberg, D., Müller, R., and Funk, M. (1995). Yeast vectors for the controlled expression of heterologous proteins in different genetic backgrounds. Gene *156*, 119-122. 10.1016/0378-1119(95)00037-7.

Neef, D.W., Jaeger, A.M., and Thiele, D.J. (2011). Heat shock transcription factor 1 as a therapeutic target in neurodegenerative diseases. Nat Rev Drug Discov *10*, 930-944. 10.1038/nrd3453.

Nihongaki, Y., Furuhata, Y., Otabe, T., Hasegawa, S., Yoshimoto, K., and Sato, M. (2017). CRISPR-Cas9-based photoactivatable transcription systems to induce neuronal differentiation. Nat Methods *14*, 963-966. 10.1038/nmeth.4430.

Nillegoda, N.B., Kirstein, J., Szlachcic, A., Berynskyy, M., Stank, A., Stengel, F., Arnsburg, K., Gao, X., Scior, A., Aebersold, R., et al. (2015). Crucial HSP70 co-chaperone complex unlocks metazoan protein disaggregation. Nature *524*, 247-251. 10.1038/nature14884.

Nillegoda, N.B., Wentink, A.S., and Bukau, B. (2018). Protein disaggregation in multicellular organisms. Trends Biochem Sci *43*, 285-300. 10.1016/j.tibs.2018.02.003.

Olzscha, H., Schermann, S.M., Woerner, A.C., Pinkert, S., Hecht, M.H., Tartaglia, G.G., Vendruscolo, M., Hayer-Hartl, M., Hartl, F.U., and Vabulas, R.M. (2011). Amyloid-like aggregates sequester numerous metastable proteins with essential cellular functions. Cell *144*, 67-78. 10.1016/j.cell.2010.11.050.

Osherovich, L.Z., and Weissman, J.S. (2001). Multiple Gln/Asn-rich prion domains confer susceptibility to induction of the yeast [PSI+] prion. Cell *106*, 183-194. 10.1016/S0092-8674(01)00440-8.

Osherovich, L.Z., and Weissman, J.S. (2002). The utility of prions. Dev Cell *2*, 143-151. 10.1016/s1534-5807(02)00118-1.

Ossato, G., Digman, M.A., Aiken, C., Lukacsovich, T., Marsh, J.L., and Gratton, E. (2010). A two-step path to inclusion formation of Huntingtin peptides revealed by number and brightness analysis. Biophys J *98*, 3078-3085. 10.1016/j.bpj.2010.02.058.

Palayam, M., Ganapathy, J., Guercio, A.M., Tal, L., Deck, S.L., and Shabek, N. (2021). Structural insights into photoactivation of plant Cryptochrome-2. Commun Biol *4*, 28. 10.1038/s42003-020-01531-x.

Park, S.H., Kukushkin, Y., Gupta, R., Chen, T., Konagai, A., Hipp, M.S., Hayer-Hartl, M., and Hartl, F.U. (2013). PolyQ proteins interfere with nuclear degradation of cytosolic proteins by sequestering the Sis1p chaperone. Cell *154*, 134-145. 10.1016/j.cell.2013.06.003.

Parsell, D.A., Kowal, A.S., Singer, M.A., and Lindquist, S. (1994). Protein disaggregation mediated by heat-shock protein Hsp104. Nature *372*, 475-478. 10.1038/372475a0.

Pathak, G.P., Spiltoir, J.I., Hoglund, C., Polstein, L.R., Heine-Koskinen, S., Gersbach, C.A., Rossi, J., and Tucker, C.L. (2017). Bidirectional approaches for optogenetic regulation of gene expression in mammalian cells using Arabidopsis Cryptochrome 2. Nucleic Acids Res *45*, e167. 10.1093/nar/gkx260.

Paushkin, S.V., Kushnirov, V.V., Smirnov, V., and Ter-Avenesyan, M.D. (1996). Propagation of the yeast prion-like [psi+] determinant is mediated by oligomerization of the SUP35-encoded polypeptide chain release factor. EMBO J *15*, 3127-3134. 10.1002/j.1460-2075.1996.tb00675.x.

Pelham, H.R.B. (1986). Speculations on the functions of the major heat shock and glucose-regulated proteins. Cell *46*, 959-961. 10.1016/0092-8674(86)90693-8

Peskett, T.R., Rau, F., O'Driscoll, J., Patani, R., Lowe, A.R., and Saibil, H.R. (2018). A liquid to solid phase transition underlying pathological Huntingtin exon1 aggregation. Mol Cell *70*, 588-601. 10.1016/j.molcel.2018.04.007.

Pincus, D. (2020). Regulation of Hsf1 and the heat shock response. In HSF1 and Molecular Chaperones in Biology and Cancer, M.L. Mendillo, D. Pincus, and R. Scherz-Shouval, eds. (Springer, Cham), pp. 41-50. 10.1007/978-3-030-40204-4_3.

Polesskaya, O., Baranova, A., Bui, S., Kondratev, N., Kananykhina, E., Nazarenko, O., Shapiro, T., Nardia, F.B., Kornienko, V., Chandhoke, V., et al. (2018). Optogenetic regulation of transcription. BMC Neurosci *19*, 12. 10.1186/s12868-018-0411-6.

Powers, E.T., and Balch, W.E. (2013). Diversity in the origins of proteostasis networks - a driver for protein function in evolution. Nat Rev Mol Cell Biol *14*, 237-248. 10.1038/nrm3542.

Powers, E.T., Morimoto, R.I., Dillin, A., Kelly, J.W., and Balch, W.E. (2009). Biological and chemical approaches to diseases of proteostasis deficiency. Annu Rev Biochem *78*, 959-991. 10.1146/annurev.biochem.052308.114844.

Prodromou, C., Panaretou, B., Chohan, S., Siligardi, G., O'Brien, R., Ladbury, J.E., Roe, S.M., Piper, P.W., and Pearl, L.H. (2000). The ATPase cycle of Hsp90 drives a molecular 'clamp' via transient dimerization of the N-terminal domains. EMBO J *19*, 4383-4392. 10.1093/emboj/19.16.4383.

Prusiner, S.B. (1982). Novel proteinaceous infectious particles cause scrapie. Science *216*, 136-144. 10.1126/science.6801762

Prusiner, S.B. (1997). Prion disease and the BSE crisis. Science *278*, 245-251. 10.1126/science.278.5336.245

Qian, X., Hou, W., Zhengang, L., and Sha, B. (2002). Direct interactions between molecular chaperones heat-shock protein (Hsp) 70 and Hsp40: yeast Hsp70 Ssa1 binds the extreme C-terminal region of yeast Hsp40 Sis1. Biochem J *361*, 27-34. 10.1042/0264-6021:3610027.

Qiu, X.B., Shao, Y.M., Miao, S., and Wang, L. (2006). The diversity of the DnaJ/Hsp40 family, the crucial partners for Hsp70 chaperones. Cell Mol Life Sci *63*, 2560-2570. 10.1007/s00018-006-6192-6.

Radford, S.E. (2000). Protein folding: progress made and promises ahead. Trends Biochem Sci *25*, 611-618. 10.1016/s0968-0004(00)01707-2

Radons, J. (2016). The human HSP70 family of chaperones: where do we stand? Cell Stress Chaperones *21*, 379-404. 10.1007/s12192-016-0676-6.

Rajagopal, P., Tse, E., Borst, A.J., Delbecq, S.P., Shi, L., Southworth, D.R., and Klevit, R.E. (2015). A conserved histidine modulates HSPB5 structure to trigger chaperone activity in response to stress-related acidosis. Elife *4*, e07304. 10.7554/eLife.07304.

Rappsilber, J., Mann, M., and Ishihama, Y. (2007). Protocol for micro-purification, enrichment, pre-fractionation and storage of peptides for proteomics using StageTips. Nat Protoc *2*, 1896-1906. 10.1038/nprot.2007.261.

Ripaud, L., Chumakova, V., Antonin, M., Hastie, A.R., Pinkert, S., Korner, R., Ruff, K.M., Pappu, R.V., Hornburg, D., Mann, M., et al. (2014). Overexpression of Q-rich prion-like proteins suppresses polyQ cytotoxicity and alters the polyQ interactome. PNAS *111*, 18219-18224. 10.1073/pnas.1421313111.

Rivenzon-Segal, D., Wolf, S.G., Shimon, L., Willison, K.R., and Horovitz, A. (2005). Sequential ATP-induced allosteric transitions of the cytoplasmic chaperonin containing TCP-1 revealed by EM analysis. Nat Struct Mol Biol *12*, 233-237. 10.1038/nsmb901.

Roberts, C.J. (2007). Non-native protein aggregation kinetics. Biotechnol Bioeng *98*, 927-938. 10.1002/bit.21627.

Rosenzweig, R., Nillegoda, N.B., Mayer, M.P., and Bukau, B. (2019). The Hsp70 chaperone network. Nat Rev Mol Cell Biol *20*, 665-680. 10.1038/s41580-019-0133-3.

Ross, C.A., and Poirier, M.A. (2004). Protein aggregation and neurodegenerative disease. Nat Med *10 Suppl*, S10-17. 10.1038/nm1066.

Ross, C.A., and Poirier, M.A. (2005). Opinion: What is the role of protein aggregation in neurodegeneration? Nat Rev Mol Cell Biol *11*, 891-898. 10.1038/nrm1742

Ross, C.A., and Tabrizi, S.J. (2011). Huntington's disease: from molecular pathogenesis to clinical treatment. The Lancet Neurology *10*, 83-98. 10.1016/s1474-4422(10)70245-3.

Rüdiger, S., Germeroth, L., Schneider-Mergener, J., and Bukau, B. (1997). Substrate specificity of the DnaK chaperone determined by screening cellulose-bound peptide libraries. EMBO J *16*, 1501-1507. 10.1093/emboj/16.7.1501.

Rupp, S. (2002). LacZ assays in yeast. Methods Enzymol *350*, 112-131. 10.1016/S0076-6879(02)50959-9.

Rutherford, S.L., and Lindquist, S. (1998). Hsp90 as a capacitator for morphological evolution. Nature *396*, 336-342. 10.1038/24550

Sahni, N., Yi, S., Taipale, M., Fuxman Bass, J.I., Coulombe-Huntington, J., Yang, F., Peng, J., Weile, J., Karras, G.I., Wang, Y., et al. (2015). Widespread macromolecular interaction perturbations in human genetic disorders. Cell *161*, 647-660. 10.1016/j.cell.2015.04.013.

Saibil, H. (2013). Chaperone machines for protein folding, unfolding and disaggregation. Nat Rev Mol Cell Biol *14*, 630-642. 10.1038/nrm3658.

Saibil, H.R., Fenton, W.A., Clare, D.K., and Horwich, A.L. (2013). Structure and allostery of the chaperonin GroEL. J Mol Biol *425*, 1476-1487. 10.1016/j.jmb.2012.11.028.

San Gil, R., Cox, D., McAlary, L., Berg, T., Walker, A.K., Yerbury, J.J., Ooi, L., and Ecroyd, H. (2020). Neurodegenerative disease-associated protein aggregates are poor inducers of the heat shock response in neuronal cells. J Cell Sci *133*, jcs243709. 10.1242/jcs.243709.

Sathasivam, K., Neueder, A., Gipson, T.A., Landles, C., Benjamin, A.C., Bondulich, M.K., Smith, D.L., Faull, R.L.M., Roos, R.A.C., Howland, D., et al. (2013). Aberrant splicing of HTT generates the pathogenic exon 1 protein in Huntington disease. PNAS *110*, 2366-2370. 10.1073/pnas.1221891110.

Satpute-Krishnan, P., and Serio, T.R. (2005). Prion protein remodelling confers an immediate phenotypic switch. Nature *437*, 262-265. 10.1038/nature03981.

Saudou, F., and Humbert, S. (2016). The biology of Huntingtin. Neuron *89*, 910-926. 10.1016/j.neuron.2016.02.003.

Sauer, R.T., and Baker, T.A. (2011). AAA+ proteases: ATP-fueled machines of protein destruction. Annu Rev Biochem *80*, 587-612. 10.1146/annurev-biochem-060408-172623.

Schaffar, G., Breuer, P., Boteva, R., Behrends, C., Tzvetkov, N., Strippel, N., Sakahira, H., Siegers, K., Hayer-Hartl, M., and Hartl, F.U. (2004). Cellular toxicity of polyglutamine expansion proteins: mechanism of transcription factor deactivation. Mol Cell *15*, 95-105. 10.1016/j.molcel.2004.06.029.

Scherzinger, E., Lurz, R., Turmaine, M., Mangiarini, L., Hollenbach, B., Hasenbank, R., Bates, G.P., Davies, S.W., Lehrach, H., and Wanker, E.E. (1997). Huntingtin-encoded polyglutamine expansions form amyloid-like protein aggregates in vitro and in vivo. Cell *90*, 549-558. 10.1016/S0092-8674(00)80514-0.

Scherzinger, E., Sittler, A., Schweiger, K., Heiser, V., Lurz, R., Hasenbank, R., Bates, G.P., Lehrach, H., and Wanker, E.E. (1999). Self-assembly of polyglutamine-containing Huntingtin fragments into amyloid-like fibrils: Implications for Huntington's disease pathology. PNAS *96*, 4604-4609. 10.1073/pnas.96.8.4604.

Schiestl, R.H., and Gietz, R.D. (1989). High efficiency transformation of intact yeast cells using single stranded nucleic acids as a carrier. Current Genetcis *16*, 339-346. 10.1007/BF00340712.

Schindelin, J., Arganda-Carreras, I., Frise, E., Kaynig, V., Longair, M., Pietzsch, T., Preibisch, S., Rueden, C., Saalfeld, S., Schmid, B., et al. (2012). Fiji: an open-source platform for biological-image analysis. Nat Methods *9*, 676-682. 10.1038/nmeth.2019.

Schopf, F.H., Biebl, M.M., and Buchner, J. (2017). The HSP90 chaperone machinery. Nat Rev Mol Cell Biol *18*, 345-360. 10.1038/nrm.2017.20.

Schulte, J., and Littleton, J.T. (2011). The biological function of the Huntingtin protein and its relevance to Huntington's Disease phology. Curr Trends Neurol *5*, 65-78.

Seong, J., and Lin, M.Z. (2021). Optobiochemistry: genetically encoded control of protein activity by light. Annu Rev Biochem *90*, 475-501. 10.1146/annurev-biochem-072420-112431.

Serio, T.R. (2018). [PIN+]ing down the mechanism of prion appearance. FEMS Yeast Res *18*, foy026. 10.1093/femsyr/foy026.

Serio, T.R., Cashikar, A.G., Kowal, A.S., Sawicki, G.J., Moslehi, J.J., Serpell, L., Arnsdorf, M.F., and Lindquist, S.L. (2000). Nucleated conformational conversion and the replication of conformational information by a prion determinant. Science *289*, 1317-1321. 10.1126/science.289.5483.1317

Sha, B., Lee, S., and Cyr, D.M. (2000). The crystal structure of the peptide-binding fragment from the yeast Hsp40 protein Sis1. Structure *8*, 799-807. 10.1016/s0969-2126(00)00170-2

Sharma, K., Schmitt, S., Bergner, C.G., Tyanova, S., Kannaiyan, N., Manrique-Hoyos, N., Kongi, K., Cantuti, L., Hanisch, U.K., Philips, M.A., et al. (2015). Cell type- and brain region-resolved mouse brain proteome. Nat Neurosci *18*, 1819-1831. 10.1038/nn.4160.

Sharma, S., Chakraborty, K., Muller, B.K., Astola, N., Tang, Y.C., Lamb, D.C., Hayer-Hartl, M., and Hartl, F.U. (2008). Monitoring protein conformation along the pathway of chaperonin-assisted folding. Cell *133*, 142-153. 10.1016/j.cell.2008.01.048.

Sharma, S.K., De los Rios, P., Christen, P., Lustig, A., and Goloubinoff, P. (2010). The kinetic parameters and energy cost of the Hsp70 chaperone as a polypeptide unfoldase. Nat Chem Biol *6*, 914-920. 10.1038/nchembio.455.

Shen, K., Calamini, B., Fauerbach, J.A., Ma, B., Shahmoradian, S.H., Serrano Lachapel, I.L., Chiu, W., Lo, D.C., and Frydman, J. (2016). Control of the structural landscape and neuronal proteotoxicity of mutant Huntingtin by domains flanking the polyQ tract. Elife *5*. 10.7554/eLife.18065.

Shiau, A.K., Harris, S.F., Southworth, D.R., and Agard, D.A. (2006). Structural Analysis of E. coli hsp90 reveals dramatic nucleotide-dependent conformational rearrangements. Cell *127*, 329-340. 10.1016/j.cell.2006.09.027.

Shih, Y.H., Tu, L.H., Chang, T.Y., Ganesan, K., Chang, W.W., Chang, P.S., Fang, Y.S., Lin, Y.T., Jin, L.W., and Chen, Y.R. (2020). TDP-43 interacts with Amyloid-beta, inhibits fibrillization, and worsens pathology in a model of Alzheimer's disease. Nat Commun *11*, 5950. 10.1038/s41467-020-19786-7.

Shin, Y., Berry, J., Pannucci, N., Haataja, M.P., Toettcher, J.E., and Brangwynne, C.P. (2017). Spatiotemporal control of intracellular phase transitions using light-activated optoDroplets. Cell *168*, 159-171. 10.1016/j.cell.2016.11.054.

Shorter, J., and Lindquist, S. (2004). Hsp104 catalyzes fortmation and elimination of self-replicating Sup35 prion conformers. Science *304*, 1793-1797. 10.1126/science.1098007.

Shorter, J., and Lindquist, S. (2005). Prions as adaptive conduits of memory and inheritance. Nat Rev Genet *6*, 435-450. 10.1038/nrg1616.

Shpilka, T., and Haynes, C.M. (2018). The mitochondrial UPR: mechanisms, physiological functions and implications in ageing. Nat Rev Mol Cell Biol *19*, 109-120. 10.1038/nrm.2017.110.

Sikorski, R.S., and Hieter, P. (1989). A system of shuttle vectors and yeast host strains designed for efficient manipulation of DNA in Saccharomyces cerevisiae. Genetics *122*, 19-27. 10.1093/genetics/122.1.19.

Singh, A.K., Balchin, D., Imamoglu, R., Hayer-Hartl, M., and Hartl, F.U. (2020). Efficient catalysis of protein folding by GroEL/ES of the obligate chaperonin substrate MetF. J Mol Biol *432*, 2304-2318. 10.1016/j.jmb.2020.02.031.

Sinnige, T., Meisl, G., Michaels, T.C.T., Vendruscolo, M., Knowles, T.P.J., and Morimoto, R.I. (2021). Kinetic analysis reveals that independent nucleation events determine the progression of polyglutamine aggregation in C. elegans. PNAS *118*, e2021888118. 10.1073/pnas.2021888118.

Sittler, A., Lurz, R., Lueder, G., Priller, J., Hayer-Hartl, M., Hartl, F.U., Lehrach, H., and Wanker, E.E. (2001). Geldanamycin activates a heat shock response and inhibits Huntingtin aggreagation in a cell culture model of Huntington's disease. Hum Mol Genet *10*, 1307-1315. 10.1093/hmg/10.12.1307.

Smith, C., and D'Mello, S.R. (2016). Cell and context-dependent effects of the heat shock protein DNAJB6 on neuronal survival. Mol Neurobiol *53*, 5628-5639. 10.1007/s12035-015-9452-3.

Sondheimer, N., and Lindquist, S. (2000). Rnq1: an epigenetic modifier of protein function in yeast. Mol Cell *5*, 163-172. 10.1016/s1097-2765(00)80412-8.

Sondheimer, N., Lopez, N., Craig, E.A., and Lindquist, S. (2001). The role of Sis1 in the maintenance of the [RNQ+] prion. EMBO J *20*, 2435-2442. 10.1093/emboj/20.10.2435.

Sorger, P.K., and Nelson, C.M. (1989). Trimerization of a yeast transcriptional activator via a coiled-coil motif. Cell *59*, 807-813. 10.1016/0092-8674(89)90604-1

Soto, C., and Pritzkow, S. (2018). Protein misfolding, aggregation, and conformational strains in neurodegenerative diseases. Nat Neurosci *21*, 1332-1340. 10.1038/s41593-018-0235-9.

Specht, S., Miller, S.B., Mogk, A., and Bukau, B. (2011). Hsp42 is required for sequestration of protein aggregates into deposition sites in Saccharomyces cerevisiae. J Cell Biol *195*, 617-629. 10.1083/jcb.201106037.

Sprunger, M.L., and Jackrel, M.E. (2021). Prion-like proteins in phase separation and their link to disease. Biomolecules *11*, 1014. 10.3390/biom11071014.

Stefani, M., and Dobson, C.M. (2003). Protein aggregation and aggregate toxicity: new insights into protein folding, misfolding diseases and biological evolution. J Mol Med *81*, 678-699. 10.1007/s00109-003-0464-5.

Street, T.O., Zeng, X., Pellarin, R., Bonomi, M., Sali, A., Kelly, M.J., Chu, F., and Agard, D.A. (2014). Elucidating the mechanism of substrate recognition by the bacterial Hsp90 molecular chaperone. J Mol Biol *426*, 2393-2404. 10.1016/j.jmb.2014.04.001.

Summers, D.W., Wolfe, K.J., Ren, H.Y., and Cyr, D.M. (2013). The Type II Hsp40 Sis1 cooperates with Hsp70 and the E3 ligase Ubr1 to promote degradation of terminally misfolded cytosolic protein. PLoS One *8*, e52099. 10.1371/journal.pone.0052099.

Sun, Y., and MacRae, T.H. (2005). The small heat shock proteins and their role in human disease. FEBS J *272*, 2613-2627. 10.1111/j.1742-4658.2005.04708.x.

Sunde, M., Serpell, L.C., Bartlam, M., Fraser, P.E., Pepys, M.B., and Blake, C.C. (1997). Common core structure of amyloid fibrils by synchrotron X-ray diffraction. J Mol Biol *273*, 729-739. 10.1006/jmbi.1997.1348.

Taipale, M., Jarosz, D.F., and Lindquist, S. (2010). HSP90 at the hub of protein homeostasis: emerging mechanistic insights. Nat Rev Mol Cell Biol *11*, 515-528. 10.1038/nrm2918.

Takahashi, S., Andreoletti, G., Chen, R., Munehira, Y., Batra, A., Afzal, N.A., Beattie, R.M., Bernstein, J.A., Ennis, S., and Snyder, M. (2017). De novo and rare mutations in the HSPA1L heat shock gene associated with inflammatory bowel disease. Genome Med *9*, 8. 10.1186/s13073-016-0394-9.

Takahashi, T., Kikuchi, S., Katada, S., Nagai, Y., Nishizawa, M., and Onodera, O. (2008). Soluble polyglutamine oligomers formed prior to inclusion body formation are cytotoxic. Hum Mol Genet *17*, 345-356. 10.1093/hmg/ddm311.

Tartaglia, G.G., Dobson, C.M., Hartl, F.U., and Vendruscolo, M. (2010). Physicochemical determinants of chaperone requirements. J Mol Biol *400*, 579-588. 10.1016/j.jmb.2010.03.066.

Tartari, M., Gissi, C., Lo Sardo, V., Zuccato, C., Picardi, E., Pesole, G., and Cattaneo, E. (2008). Phylogenetic comparison of Huntingtin homologues reveals the appearance of a primitive polyQ in sea urchin. Mol Biol Evol *25*, 330-338. 10.1093/molbev/msm258.

Taslimi, A., Vrana, J.D., Chen, D., Borinskaya, S., Mayer, B.J., Kennedy, M.J., and Tucker, C.L. (2014). An optimized optogenetic clustering tool for probing protein interaction and function. Nat Commun *5*, 4925. 10.1038/ncomms5925.

Taylor, R.C., Berendzen, K.M., and Dillin, A. (2014). Systemic stress signalling: understanding the cell non-autonomous control of proteostasis. Nat Rev Mol Cell Biol *15*, 211-217. 10.1038/nrm3752.

Thakur, A.K., Jayaraman, M., Mishra, R., Thakur, M., Chellgren, V.M., Byeon, I.J., Anjum, D.H., Kodali, R., Creamer, T.P., Conway, J.F., et al. (2009). Polyglutamine disruption of the Huntingtin exon 1 N terminus triggers a complex aggregation mechanism. Nat Struct Mol Biol *16*, 380-389. 10.1038/nsmb.1570.

Thal, D.R., Rüb, U., Orantes, M., and Braak, H. (2002). Phases of Abeta-deposition in the human brain and its relevance for the development of AD Neurology *58*, 1791-1800. 10.1212/wnl.58.12.1791

Thal, D.R., Rüb, U., Schultz, C., Sassin, I., Ghebremedhin, E., Del Tredici, K., Braak, E., and Braak, H. (2000). Sequence of Abeta-protein deposition in the human medial temporal lobe. J Neuropathol Exp Neurol *2000*, 8. 10.1093/jnen/59.8.733

Triandafillou, C.G., Katanski, C.D., Dinner, A.R., and Drummond, D.A. (2020). Transient intracellular acidification regulates the core transcriptional heat shock response. Elife *9*. 10.7554/eLife.54880.

Tuite, M.F., and Cox, B.S. (2003). Propagation of yeast prions. Nat Rev Mol Cell Biol *4*, 878-890. 10.1038/nrm1247.

Tuite, M.F., Mundy, C.R., and Cox, B.S. (1981). Agents that cause a high frequency of genetic change from [PSI+] to [psi-] in Saccharomyces cerevisiae. Genetics *98*, 691-711. 10.1093/genetics/98.4.691

Tyanova, S., Temu, T., Sinitcyn, P., Carlson, A., Hein, M.Y., Geiger, T., Mann, M., and Cox, J. (2016). The Perseus computational platform for comprehensive analysis of (prote)omics data. Nat Methods *13*, 731-740. 10.1038/nmeth.3901.

Tyedmers, J., Mogk, A., and Bukau, B. (2010). Cellular strategies for controlling protein aggregation. Nat Rev Mol Cell Biol *11*, 777-788. 10.1038/nrm2993.

Uhlen, M., Fagerberg, L., Hallstrom, B.M., Lindskog, C., Oksvold, P., Mardinoglu, A., Sivertsson, A., Kampf, C., Sjostedt, E., Asplund, A., et al. (2015). Proteomics. Tissue-based map of the human proteome. Science *347*, 1260419 proteinatlas.org. 10.1126/science.1260419.

Ungelenk, S., Moayed, F., Ho, C.T., Grousl, T., Scharf, A., Mashaghi, A., Tans, S., Mayer, M.P., Mogk, A., and Bukau, B. (2016). Small heat shock proteins sequester misfolding proteins in near-native conformation for cellular protection and efficient refolding. Nat Commun *7*, 13673. 10.1038/ncomms13673.

Urbanek, A., Popovic, M., Morató, A., Estaña, A., Elena-Real, C.A., Mier, P., Fournet, A., Allemand, F., Delbecq, S., Andrade-Navarro, M.A., et al. (2020). Flanking Regions Determine the Structure of the Poly-Glutamine in Huntingtin through Mechanisms Common among Glutamine-Rich Human Proteins. Structure *28*, 733-746.e735. 10.1016/j.str.2020.04.008.

Valastyan, J.S., and Lindquist, S. (2014). Mechanisms of protein-folding diseases at a glance. Dis Model Mech *7*, 9-14. 10.1242/dmm.013474.

Vasconcelos, B., Stancu, I.C., Buist, A., Bird, M., Wang, P., Vanoosthuyse, A., Van Kolen, K., Verheyen, A., Kienlen-Campard, P., Octave, J.N., et al. (2016). Heterotypic seeding of Tau fibrillization by pre-aggregated Abeta provides potent seeds for prion-like seeding and propagation of Tau-pathology in vivo. Acta Neuropathol *131*, 549-569. 10.1007/s00401-015-1525-x.

Vashist, S., Cushman, M., and Shorter, J. (2010). Applying Hsp104 to protein-misfolding disorders. Biochem Cell Biol *88*, 1-13. 10.1139/o09-121.

Vecchi, G., Sormanni, P., Mannini, B., Vandelli, A., Tartaglia, G.G., Dobson, C.M., Hartl, F.U., and Vendruscolo, M. (2020). Proteome-wide observation of the phenomenon of life on the edge of solubility. PNAS *117*, 1015-1020. 10.1073/pnas.1910444117.

Verghese, J., Abrams, J., Wang, Y., and Morano, K.A. (2012). Biology of the heat shock response and protein chaperones: budding yeast (Saccharomyces cerevisiae) as a model system. Microbiol Mol Biol Rev *76*, 115-158. 10.1128/MMBR.05018-11.

Vicart, P., Caron, A., Guicheney, P., Li, Z., Prevost, M.-C., Faure, A., Chateau, D., Chapon, F., Tome, F., Dupret, J.-M., et al. (1998). A missense mutation in the αB-crystallin chaperone gene causes a desmin-related myopathy. Nature Genetics *20*, 92-95. 10.1038/1765

Vitalis, A., and Pappu, R.V. (2011). Assessing the contribution of heterogeneous distributions of oligomers to aggregation mechanisms of polyglutamine peptides. Biophys Chem *159*, 14-23. 10.1016/j.bpc.2011.04.006.

Vitrenko, Y.A., Gracheva, E.O., Richmond, J.E., and Liebman, S.W. (2007). Visualization of aggregation of the Rnq1 prion domain and cross-seeding interactions with Sup35NM. J Biol Chem *282*, 1779-1787. 10.1074/jbc.M609269200.

Wach, A., Brachat, A., Pöhlmann, R., and Philippsen, P. (1994). New heterologous modules for classical or PCR-based gene disruptions in Saccharomyces cerevisiae. Yeast *10*, 1793-1808. 10.1002/yea.320101310.

Walker, F.O. (2007). Huntington's disease. Lancet *369*, 218-228. 10.1016/s0140-6736(07)60111-1.

Walter, G.M., Smith, M.C., Wisen, S., Basrur, V., Elenitoba-Johnson, K.S., Duennwald, M.L., Kumar, A., and Gestwicki, J.E. (2011). Ordered assembly of heat shock proteins, Hsp26, Hsp70, Hsp90, and Hsp104, on expanded polyglutamine fragments revealed by chemical probes. J Biol Chem *286*, 40486-40493. 10.1074/jbc.M111.284448.

Walter, P., and Ron, D. (2011). The unfolded protein response: from stress pathway to homeostatic regulation. Science *334*, 1081-1086. 10.1126/science.1209038

Walters, R.H., and Murphy, R.M. (2011). Aggregation kinetics of interrupted polyglutamine peptides. J Mol Biol *412*, 505-519. 10.1016/j.jmb.2011.07.003.

Walther, D.M., Kasturi, P., Zheng, M., Pinkert, S., Vecchi, G., Ciryam, P., Morimoto, R.I., Dobson, C.M., Vendruscolo, M., Mann, M., and Hartl, F.U. (2015). Widespread proteome remodeling and aggregation in aging C. elegans. Cell *161*, 919-932. 10.1016/j.cell.2015.03.032.

Wang, Q., and Lin, C. (2020). Mechanisms of cryptochrome-mediated photoresponses in plants. Annu Rev Plant Biol *71*, 103-129. 10.1146/annurev-arplant-050718-100300.

Wang, Y., Meriin, A.B., Zaarur, N., Romanova, N.V., Chernoff, Y.O., Costello, C.E., and Sherman, M.Y. (2009). Abnormal proteins can form aggresome in yeast: aggresome-targeting signals and components of the machinery. FASEB J *23*, 451-463. 10.1096/fj.08-117614.

Ward, H.J., Everington, D., Cousens, S.N., Smith-Bathgate, B., Leitch, M., Cooper, S., Heath, C., Knight, R.S., Smith, P.G., and Will, R.G. (2006). Risk factors for variant Creutzfeldt-Jakob disease: a case-control study. Ann Neurol *59*, 111-120. 10.1002/ana.20708.

Wayne, N., and Bolon, D.N. (2007). Dimerization of Hsp90 is required for in vivo function. Design and analysis of monomers and dimers. J Biol Chem *282*, 35386-35395. 10.1074/jbc.M703844200.

Wegele, H., Wandinger, S.K., Schmid, A.B., Reinstein, J., and Buchner, J. (2006). Substrate transfer from the chaperone Hsp70 to Hsp90. J Mol Biol *356*, 802-811. 10.1016/j.jmb.2005.12.008.

Wegrzyn, R.D., Bapat, K., Newnam, G.P., Zink, A.D., and Chernoff, Y.O. (2001). Mechanism of prion loss after Hsp104 inactivation in yeast. Mol Cell Biol *21*, 4656-4669. 10.1128/MCB.21.14.4656-4669.2001.

Whetten-Goldstein, K., Sloan, F., Kulas, E., Cutson, T., and Schenkman, M. (2015). The burden of Parkinson's disease on society, family, and the individual. J Am Geriatr Soc *45*, 844-849. 10.1111/j.1532-5415.1997.tb01512.x.

Wickner, R.B., Shewmaker, F.P., Bateman, D.A., Edskes, H.K., Gorkovskiy, A., Dayani, Y., and Bezsonov, E.E. (2015). Yeast prions: structure, biology, and prion-handling systems. Microbiol Mol Biol Rev *79*, 1-17. 10.1128/MMBR.00041-14.

Will, R.G., Ironside, J.W., Zeidler, M., Cousens, S.N., Estibeiro, K., Alperovitch, A., Poser, S., Pocchiari, M., Hofman, A., and Smith, P.G. (1996). A new variant of Creutzfeld-Jakob disease in the UK. Lancet *347*, 921-925. 10.1016/s0140-6736(96)91412-9

Winderickx, J., Delay, C., De Vos, A., Klinger, H., Pellens, K., Vanhelmont, T., Van Leuven, F., and Zabrocki, P. (2008). Protein folding diseases and neurodegeneration: lessons learned from yeast. Biochim Biophys Acta *1783*, 1381-1395. 10.1016/j.bbamcr.2008.01.020.

Wolfe, K.J., Ren, H.Y., Trepte, P., and Cyr, D.M. (2014). Polyglutamine-rich suppressors of Huntingtin toxicity act upstream of Hsp70 and Sti1 in spatial quality control of amyloid-like proteins. PLoS One *9*, e95914. 10.1371/journal.pone.0095914.

Wu, Y., Li, J., Jin, Z., Fu, Z., and Sha, B. (2005). The crystal structure of the C-terminal fragment of yeast Hsp40 Ydj1 reveals novel dimerization motif for Hsp40. J Mol Biol *346*, 1005-1011. 10.1016/j.jmb.2004.12.040.

Xiao, W. (2014). Yeast protocols, 3 Edition (Humana Press, New York, NY). 10.1007/978-1-4939-0799-1.

Xu, Z., Horwich, A.L., and Sigler, P.B. (1997). The crystal structure of the asymmetric GroEL-GroES-(ADP)7 chaperonin complex. Nature *388*, 741-750. 10.1038/41944

Yam, A.Y., Xia, Y., Lin, H.T., Burlingame, A., Gerstein, M., and Frydman, J. (2008). Defining the TRiC/CCT interactome links chaperonin function to stabilization of newly made proteins with complex topologies. Nat Struct Mol Biol *15*, 1255-1262. 10.1038/nsmb.1515.

Yan, W., and Craig, E.A. (1999). The glycine-phenylalanine-rich region determines the specificity of the yeast Hsp40 Sis1. Mol Cell Biol *19*, 7751-7758. 10.1128/MCB.19.11.7751

Yan, X., Shi, Q., Bracher, A., Milicic, G., Singh, A.K., Hartl, F.U., and Hayer-Hartl, M. (2018). GroEL ring separation and exchange in the chaperonin reaction. Cell *172*, 605-617. 10.1016/j.cell.2017.12.010.

Yang, W., Hamilton, J.L., Kopil, C., Beck, J.C., Tanner, C.M., Albin, R.L., Ray Dorsey, E., Dahodwala, N., Cintina, I., Hogan, P., and Thompson, T. (2020). Current and projected future economic burden of Parkinson's disease in the U.S. NPJ Parkinsons Dis *6*, 15. 10.1038/s41531-020-0117-1.

Yu, X., Liu, H., Klejnot, J., and Lin, C. (2010). The cryptochrome blue light receptors. In Arabidopsis Book, (American Society of Plant Biologists), pp. e0135. 10.1199/tab.0135.

Yushchenko, T., Deuerling, E., and Hauser, K. (2018). Insights into the aggregation mechanism of polyQ proteins with different glutamine repeat lengths. Biophys J *114*, 1847-1857. 10.1016/j.bpj.2018.02.037.

Zaarur, N., Xu, X., Lestienne, P., Meriin, A.B., McComb, M., Costello, C.E., Newnam, G.P., Ganti, R., Romanova, N.V., Shanmugasundaram, M., et al. (2015). RuvbL1 and RuvbL2 enhance aggresome formation and disaggregate amyloid fibrils. EMBO J *34*, 2363-2382. 10.15252/embj.201591245.

Zbinden, A., Perez-Berlanga, M., De Rossi, P., and Polymenidou, M. (2020). Phase separation and neurodegenerative diseases: a disturbance in the force. Dev Cell *55*, 45-68. 10.1016/j.devcel.2020.09.014.

Zhang, J., Baker, M.L., Schroder, G.F., Douglas, N.R., Reissmann, S., Jakana, J., Dougherty, M., Fu, C.J., Levitt, M., Ludtke, S.J., et al. (2010). Mechanism of folding chamber closure in a group II chaperonin. Nature *463*, 379-383. 10.1038/nature08701.

Zheng, X., Krakowiak, J., Patel, N., Beyzavi, A., Ezike, J., Khalil, A.S., and Pincus, D. (2016). Dynamic control of Hsf1 during heat shock by a chaperone switch and phosphorylation. Elife *5*, e18638. 10.7554/eLife.18638.

Appendix

Table X1: List of all vectors used in Chapter I of this work. Indicated are name of the vector, its source as well as its unique identifier (either internal reference or catalogue number for commercially available vectors).

Name	Source	Identifier
mCherry-N1	Clontech	Cat#632523
pCIneo-FlucDM	Gupta et al., 2011	N/A
pESCLeu	Agilent	Cat#217452
pFA6a-GFP(S65T)-KanMX6	Bähler et al., 1998	N/A
pGEX-2T	GE Lifesciences	Cat#28-9546-53
pRS306pGPD	Mumberg et al., 1995	N/A
pRS313	Sikorski & Hieter, 1989	N/A
pRS405pADH	Mumberg et al., 1995	N/A
pRS413pGPD	Mumberg et al., 1995	N/A
pRS414	Sikorski and Hieter, 1989	N/A
pRS414 GPD Sis1	Douglas et al., 2008	Addgene Cat#18687
pRS414pGPD	Mumberg et al., 1995	N/A
pRS415pGAL-HA-Sis1	Park et al., 2013	N/A
pRS415pGAL-HA-Sis1(AAA)	Park et al., 2013	N/A
pRS415pGAL-HA-Sis1ΔG/F	Park et al., 2013	N/A
pRS426	Christianson et al., 1992	N/A
pRS426Hsf1	Holmes et al., 2014	N/A
pRS426pGALSsa1	Muchowski et al., 2000	N/A
pYES2	Invitrogen	Cat#V82520
pYES2-myc-20QmCh	Park et al., 2013	N/A
pYES2-myc-97QmCh	Park et al., 2013	N/A
Ssa3-LacZ-Leu	Liu et al., 1997	N/A
Yeast ORF Collection	Dharmacon	Cat#YSC3868
pRS306pGPD GST-mCh-NLS	This study	pCLK181
pRS306pGPD GST-GFP-NLS	This study	pCLK207
pRS413pGPD Ssa1	This study	pCLK242
pESCLeu-20QmCh	This study	pCLK253
pESCLeu-97QmCh	This study	pCLK254
pRS414pGPD Hsf1	This study	pCLK263
pRS313pHSELacZ	This study	pCLK270
pRS405pADH Ssa1GFP	This study	pCLK295
pRS414pGALHASis1	This study	pCLK301
pRS414pGALHASis1AAA	This study	pCLK302
pRS414pGALHASis1DG/F	This study	pCLK304
pRS414pGALHASis1DC	This study	pCLK313
pRS414pGALHASis1DDD	This study	pCLK315
pRS414PGPD Ydj1	This study	pCLK323
pYES2-FlucDM-mCh	This study	pCLK332

Table X2: List of all primer oligos used in Chapter I of this work. Indicated are the DNA sequence (5'-3'), its source as well as its internal reference identifier.

DNA Sequence	Source	Identifier
AAAATCTAGAATGTCCCCTATACTAGG	This study	oCLK1
AAAAGGATCCGGTTCTGGTTCTGGTTCTTTTTGGAGGATGGTCGC	This study	oCLK2
AAAAGGATCCATGAGTAAAGGAGAAGAACTTTTC	This study	oCLK3
AAAAGTCGACTTAAACCTTTCTCTTCTTCTTTGGTTTGTATAGTTC ATCCATG	This study	oCLK4
AAAAGGATCCATGGTGAGCAAGGGCG	This study	oCLK5
AAAAGTCGACTTAAACCTTTCTCTTCTTCTTTGGCTTGTACAGCTC GTCC	This study	oCLK6
AAAAGAATTCATGAATAATGCTGCAAATAC	This study	oCLK7
AAAACTCGAGCTATTTCTTAGCTCGTTTG	This study	oCLK8
AGCCAGATCTTTTAGGCTCGAAGATCC	This study	oCLK9
AAAAGTCGACTTATTTTTGACACCAGACC	This study	oCLK10
AAAAACTAGTATGGTTAAAGAAACTAAGTTT	This study	oCLK11
AAAAGGATCCTCATTGAGATGCACATTG	This study	oCLK12
AAAAACTAGTATGTCCTACCCAT	This study	oCLK13
AAAAGGATCCTTAAAAATTTTCATCTATAGC	This study	oCLK14
AAAAGGATCCTTAGCCGCCAAAGAATTGTG	This study	oCLK15
AAAAGGATCCTTATATTGGATAGTCCACTTTA	This study	oCLK16
TAGAACTAGTGGATCCCCCGGGCTGCAGGAATGTCAAAAGCTGT CGGTATTG	This study	oCLK17
TTCTCCTTTACTGGAGCCACTACCGGAACCATCAACTTCTTCAACG GTTGG	This study	oCLK18
GGTTCCGGTAGTGGCTCCAGTAAAGGAGAAGAACTTTTCACTG	This study	oCLK19
TCGACGGTATCGATAAGCTTGATATCGAATCTATTTGTATAGTTC ATCCATGCCATG	This study	oCLK20
ATTCGATATCAAGCTTATCGATACCGTC	This study	oCLK21
TCCTGCAGCCCGGGGG	This study	oCLK22
ACTAAACGACGCTCAAAAACGTGCTATAGATGAAAATTTTGGTTC TGGTTCTGGTTCTCGGATCCCCGGGTTAATTAA	This study	oCLK23
ATTTATTTGAGTTTATAATTATATTTGCTTAGGATTACTAGAATTC GAGCTCGTTTAAAC	This study	oCLK24
AAAAGGATCCATGGTCAAGGAGACAAAAC	This study	oCLK25

Table X3: List of all yeast strains used in Chapter I of this work. Listed are the genotypes for all strains, their source as well as internal reference identifier.

Strain genotype	Source	Identifier
YPH499 MATa ura3-52 lys2-801_amber ade2-101_ochre trp1-Δ63 his3-Δ200 leu2-Δ1	Sikorski and Hieter, 1989	N/A
YPH499 MATa ura3-52 lys2-801_amber ade2-101_ochre trp1-Δ63 his3-Δ200 leu2-Δ1 SIS1GFP::KANMX6	This study	yCLK207
YPH499 MATa lys2-801_amber ade2-101_ochre trp1-Δ63 his3-Δ200 leu2-Δ1 ura3-52::URA::P_{GPD}-GST-GFP-NLS	This study	yCLK225

Strain genotype	Source	Identifier
YPH499 MATa ura3-52 lys2-801_amber ade2-101_ochre trp1-Δ63 his3-Δ200 leu2-Δ1::LEU::P_{ADH}-SSA1-GFP	This study	yCLK250
YPH499 MATa lys2-801_amber ade2-101_ochre trp1-Δ63 his3-Δ200 leu2-Δ1::LEU::P_{ADH}-SSA1-GFP ura3-52::URA::P_{GPD}-GST-mCh-NLS	This study	yCLK255
YPH499 MATa lys2-801_amber ade2-101_ochre trp1-Δ63 his3-Δ200 leu2-Δ1 SIS1GFP::KANMX6 ura3-52::URA::P_{GPD}-GST-mCh-NLS	This study	yCLK256

Table X4: List of all vectors used in Chapter II of this work. Indicated are name of the vector, its source as well as its unique identifier (either internal reference or catalogue number for commercially available vectors).

Name	Source	Identifier
pBacMam2-DiEx-LIC-C-flag_huntingtin_full-length_Q36	Harding et al., 2019	Addgene Cat#111745
pBacMam2-DiEx-LIC-C-flag_huntingtin_full-length_Q48	Harding et al., 2019	Addgene Cat#111747
pBacMam2-DiEx-LIC-C-flag_huntingtin_full-length_Q54	Harding et al., 2019	Addgene Cat#111727
pBacMam2-DiEx-LIC-C-flag_huntingtin_full-length_Q60	Harding et al., 2019	Addgene Cat#111749
pBacMam2-DiEx-LIC-C-flag_huntingtin_full-length_Q73	Harding et al., 2019	Addgene Cat#111728
pESC-URA-Rnq1-GFP	Kaganovich et al., 2008	Addgene Cat#21051
pFA6aGFP(S65T)kanMX6	Bahler et al., 1998	Addgene Cat#39292
pFA6-kanMX4	Wach et al., 1994	N/A
pGAL-CG*	Park et al., 2013	N/A
pGEX-Htt53Q	Schaffar et al., 2004	N/A
pHR-mCh-Cry2olig	Shin et al. 2017	Kind gift of C. Brangwynne; Addgene Cat#101222
pRS304	Sikorski & Hieter, 1989	N/A
pRS305	Sikorski & Hieter, 1989	N/A
pRS314	Sikorski & Hieter, 1989	N/A
pRS316	Sikorski & Hieter, 1989	N/A
pRS426	Christianson et al., 1992	N/A
pRS416pGAL	Mumberg et al., 1994	N/A
pRS416pGPD	Mumberg et al., 1995	N/A
pRS306pADH	Mumberg et al., 1995	N/A
pRS414pGPD-Sis1	Douglas et al., 2008	Addgene Cat#18687
pYES2-Htt97Q-GFP	Ripaud et al. 2014	N/A
pYES2-Htt25Q-GFP	Ripaud et al. 2014	N/A
pYES2-myc-20QmCh	Park et al., 2013	N/A
pYES2-myc-97QmCh	Park et al., 2013	N/A
Ssa3-LacZ-Leu	Liu et al., 1997	N/A
pRS316pGPD	This study	pMG6
pRS316pGAL	This study	pMG7
pRS316pGPD_mCherry-CRY2olig	This study	pMG18
pRS305pGPD_mCherry-CRY2olig	This study	pMG60
pRS316pGAL_mCherry-CRY2olig	This study	pMG88
pRS305pGAL_mCherry-CRY2olig	This study	pMG90
pRS305pGPD _97Q-mCherry-CRY2olig	This study	pMG148

Name	Source	Identifier
pRS305pGPD _97Q-mCherry	This study	pMG150
pRS305pGPD _20Q-mCherry-CRY2olig	This study	pMG154
pRS305pGPD _20Q-mCherry	This study	pMG155
pRS305pGPD _97Q-GFP	This study	pMG158
pRS305pGPD _20Q-GFP	This study	pMG159
pRS304pGPD _97Q-GFP	This study	pMG160
pRS304pGPD _20Q-GFP	This study	pMG161
pRS305pGPD _36Q-mCherry	This study	pMG185
pRS305pGPD _48Q-mCherry	This study	pMG186
pRS305pGPD _54Q-mCherry	This study	pMG187
pRS305pGPD _60Q-mCherry	This study	pMG188
pRS305pGPD _73Q-mCherry	This study	pMG189
pRS305pGPD _36Q-mCherry-CRY2olig	This study	pMG190
pRS305pGPD _48Q-mCherry-CRY2olig	This study	pMG191
pRS305pGPD _60Q-mCherry-CRY2olig	This study	pMG193
pRS305pGPD _73Q-mCherry-CRY2olig	This study	pMG194
pGEX-Htt20Q	This study	pMG202
pGEX-Htt54Q	This study	pMG205
pRS426pGAL_tox66Q-mCherry-CRY2olig	This study	pMG210
pRS426pGAL_mCherry-CRY2olig	This study	pMG245
pRS426pGAL_20Q-mCherry-CRY2olig	This study	pMG246
pRS426pGAL_36Q-mCherry-CRY2olig	This study	pMG247
pRS426pGAL_48Q-mCherry-CRY2olig	This study	pMG248
pRS426pGAL_60Q-mCherry-CRY2olig	This study	pMG250
pRS426pGAL_73Q-mCherry-CRY2olig	This study	pMG251
pRS426pGAL_97Q-mCherry-CRY2olig	This study	pMG252
pRS426pGAL_tox25Q-mCherry-CRY2olig	This study	pMG267
pRS426pGAL_tox97Q-mCherry-CRY2olig	This study	pMG268
pRS306pADH-Rnq1GFP	This study	pMG269
pESC-URA-Rnq1-GFP_noMyc	This study	pMG271

Table X5: List of all primer oligos used in Chapter II of this work. Indicated are the DNA sequence (5'-3'), its source as well as its internal reference identifier.

DNA Sequence	Source	Identifier
AAGTTTTCGTATCCGCTCGTTCGAAAGACTTTAGACAAAACAGCTGAAGCTTCGTACGC	This study	oMG1
TCTTGGTAAGTTTCTTTTCTTAACCAAATTCAAAATTCTAGCATAGGCCACTAGTGGATCTG	This study	oMG2
CGTGATCACGATTCAG	This study	oMG3
CATGTAGACCAATCTTCG	This study	oMG4
AGGAATTCGATATCAAGCTTATCGATACCGTCGACATGGTGTCTAAAGGCGAGGAG	This study	oMG22
GACATAACTAATTACATGACTCGAGGTCGACTCAGTCACGCATGTTGCAG	This study	oMG23
CCTTTAGTGAGGGTTAATTCCGAG	This study	oMG42
CCCTATAGTGAGTCGTATTACAATTC	This study	oMG43

DNA Sequence	Source	Identifier
CGCCAAGCTCGGAATTAACCCTCACTAAAG	This study	oMG44
CGACGGCCAGTGAATTGTAATACGACTCACTATAG	This study	oMG45
TGAGTCGACCTCGAGTCA	This study	oMG88
ATGGTGTCTAAAGGCGAGGAG	This study	oMG111
GTCGACGGTATCGATAAGCTTG	This study	oMG112
TTCGATATCAAGCTTATCGATACCGTCGACATGTGTGAACAAAAG CTTATTTCTGAAG	This study	oMG113
CATGTTATCCTCCTCGCCTTTAGACACCATGAATTCCGGTCGGTG CAG	This study	oMG114
ATTCGATATCAAGCTTATCGATACCGTC	This study	oMG137
TCCTGCAGCCCGGGGG	This study	oMG138
TCGACGGTATCGATAAGCTTGATATCGAATCTATTTGTATAGTTC ATCCATGCCATG	This study	oMG142
TAACTAATTACATGACTCGAGGTCGACTCACTTGTACAATTCATCC ATGCCCC	This study	oMG143
GGCCCAGCTGTGGCTGAGGAG	This study	oMG146
CTTTTGAGGGACTCGAAGGCCTTCATC	This study	oMG147
GAATTCCGGTCGGTGCAGAG	This study	oMG148
CCAGCTGTGGCTGAGGAGCCTCTGCACCGACCGGAATTCATGGT GAGTAAAGGAGAAGAACTTTTCACTG	This study	oMG149
TAACTAATTACATGACTCGAGGTCGACTCATTTGTATAGTTCATCC ATGCCATG	This study	oMG150
TTCGATATCAAGCTTATCGATACCGTCGACATGGACTACAAGGAC GACGATGACAAG	This study	oMG151
CATGTTATCCTCCTCGCCTTTAGACACCATCAGGGATCCCCCGGG CTG	This study	oMG152
CTGTGGCTGAGGAGCCGCTG	This study	oMG169
GAAGGCCTTCATCAGCTTTTCCAG	This study	oMG170
TAGAACTAGTGGATCCCCCGGGCTGCAGGAATGGATACGGATAA GTTAATCTCAG	This study	oMG199
ATGGATACGGATAAGTTAATCTCAGAGGCTG	This study	oMG207
ACCCTCGGAGCCACTACCGGAACCGTAGCGGTTCTGGTTGCCGT TATTG	This study	oMG208
CGCTACGGTTCCGGTAGTGGCTCCGAGGGTGGTCCGCTCGAG	This study	oMG209
CAGCCTCTGAGATTAACTTATCCGTATC	This study	oMG210

Table X6: List of all yeast strains used in Chapter II of this work. Listed are the genotypes for all strains, their source as well as internal reference identifier. It is also described how any strain was generated.

Strain genotype	Source	Identifier
74-D694 MATa [*PIN*$^+$] ade1-14 his3-11,-15 trp1-1 ura3-1 leu2-3, 112 can1-100	SY197 in Klaips et al., 2014	yMG31
74-D694 MATa [*PIN*$^+$] ade1-14 his3-11,-15 trp1-1 ura3-1 leu2-3,112 can1-100 pdr5Δ::kanMX	This study	yMG33
74-D694 MATa [*PIN*$^+$] ade1-14 his3-11,-15 trp1-1 ura3-1 can1-100 pdr5Δ::kanMX leu2-3,112::LEU::P_{GPD}mCherry-CRY2olig	This study	yMG49 (yMG33+pMG60)

Strain genotype	Source	Identifier
74-D694 MATa [*PIN*$^+$] ade1-14 his3-11,-15 trp1-1 ura3-1 can1-100 pdr5Δ::kanMX leu2-3,112::LEU::P_{GPD}Htt97Q-mCherry-CRY2olig	This study	yMG78 (yMG33+148)
74-D694 MATa [*PIN*$^+$] ade1-14 his3-11,-15 trp1-1 ura3-1 can1-100 pdr5Δ::kanMX leu2-3,112::LEU::P_{GPD}Htt20Q-mCherry-CRY2olig	This study	yMG88 (yMG33+pMG154)
74-D694 MATa [*pin*$^-$] ade1-14 his3-11,-15 trp1-1 ura3-1 can1-100 pdr5Δ::kanMX leu2-3,112::LEU::P_{GPD}mCherry-CRY2olig	This study	yMG91 (yMG49 cured)
74-D694 MATa [*pin*$^-$] ade1-14 his3-11,-15 trp1-1 ura3-1 can1-100 pdr5Δ::kanMX leu2-3,112::LEU::P_{GPD}Htt97Q-mCherry-CRY2olig	This study	yMG92 (yMG78 cured)
74-D694 MATa [*pin*$^-$] ade1-14 his3-11,-15 trp1-1 ura3-1 can1-100 pdr5Δ::kanMX leu2-3,112::LEU::P_{GPD}Htt20Q-mCherry-CRY2olig	This study	yMG94 (yMG88 cured)
74-D694 MATa [*pin*$^-$] ade1-14 his3-11,-15 ura3-1 can1-100 pdr5Δ::kanMX leu2-3,112::LEU::P_{GPD}mCherry-CRY2olig trp1-1::TRP::P_{GPD}Htt97Q-GFP	This study	yMG103 (yMG91+pMG160)
74-D694 MATa [*pin*$^-$] ade1-14 his3-11,-15 ura3-1 can1-100 pdr5Δ::kanMX leu2-3,112::LEU::P_{GPD}Htt97Q-mCherry-CRY2olig trp1-1::TRP::P_{GPD}Htt97Q-GFP	This study	yMG104 (yMG92+pMG160)
74-D694 MATa [*pin*$^-$] ade1-14 his3-11,-15 ura3-1 can1-100 pdr5Δ::kanMX leu2-3,112::LEU::P_{GPD}Htt20Q-mCherry-CRY2olig trp1-1::TRP::P_{GPD}Htt20Q-GFP	This study	yMG106 (yMG94+pMG161)
74-D694 MATa [*pin*$^-$] ade1-14 his3-11,-15 ura3-1 can1-100 pdr5Δ::kanMX leu2-3,112::LEU::P_{GPD}mCherry-CRY2olig trp1-1::TRP::P_{GPD}Htt20Q-GFP	This study	yMG120 (yMG91+pMG161)
74-D694 MATa [*pin*$^-$] ade1-14 his3-11,-15 ura3-1 can1-100 pdr5Δ::kanMX leu2-3,112::LEU::P_{GPD}Htt97Q-mCherry-CRY2olig trp1-1::TRP::P_{GPD}Htt20Q-GFP	This study	yMG121 (yMG92+pMG161)
74-D694 MATa [*pin*$^-$] ade1-14 his3-11,-15 ura3-1 can1-100 pdr5Δ::kanMX leu2-3,112::LEU::P_{GPD}Htt20Q-mCherry-CRY2olig trp1-1::TRP::P_{GPD}Htt97Q-GFP	This study	yMG122 (yMG94+pMG160)
74-D694 MATa [*PIN*$^+$] ade1-14 his3-11,-15 trp1-1 ura3-1 can1-100 pdr5Δ::kanMX leu2-3,112::LEU::P_{GPD}Htt36Q-mCherry-CRY2olig	This study	yMG186 (yMG33+pMG190)
74-D694 MATa [*PIN*$^+$] ade1-14 his3-11,-15 trp1-1 ura3-1 can1-100 pdr5Δ::kanMX leu2-3,112::LEU::P_{GPD}Htt48Q-mCherry-CRY2olig	This study	yMG187 (yMG33+pMG191)
74-D694 MATa [*PIN*$^+$] ade1-14 his3-11,-15 trp1-1 ura3-1 can1-100 pdr5Δ::kanMX leu2-3,112::LEU::P_{GPD}Htt60Q-mCherry-CRY2olig	This study	yMG189 (yMG33+pMG193)
74-D694 MATa [*PIN*$^+$] ade1-14 his3-11,-15 trp1-1 ura3-1 can1-100 pdr5Δ::kanMX leu2-3,112::LEU::P_{GPD}Htt73Q-mCherry-CRY2olig	This study	yMG190 (yMG33+pMG194)
74-D694 MATa [*pin*$^-$] ade1-14 his3-11,-15 trp1-1 ura3-1 can1-100 pdr5Δ::kanMX leu2-3,112::LEU::P_{GPD}Htt36Q-mCherry-CRY2olig	This study	yMG198 (yMG186 cured)

Strain genotype	Source	Identifier
74-D694 MATa [*pin*$^-$] ade1-14 his3-11,-15 trp1-1 ura3-1 can1-100 pdr5Δ::kanMX leu2-3,112::LEU::P_{GPD}Htt48Q-mCherry-CRY2olig	This study	yMG199 (yMG187 cured)
74-D694 MATa [*pin*$^-$] ade1-14 his3-11,-15 trp1-1 ura3-1 can1-100 pdr5Δ::kanMX leu2-3,112::LEU::P_{GPD}Htt60Q-mCherry-CRY2olig	This study	yMG201 (yMG189 cured)
74-D694 MATa [*pin*$^-$] ade1-14 his3-11,-15 trp1-1 ura3-1 can1-100 pdr5Δ::kanMX leu2-3,112::LEU::P_{GPD}Htt73Q-mCherry-CRY2olig	This study	yMG202 (yMG190 cured)
YPH499 MATa [*pin*$^-$] ura3-52 lys2-801 ade2-101 trp1-Δ63 his3-Δ200 leu2-Δ1	This study	yMG206 (yMG207 cured)
YPH499 MATa [*PIN*$^+$] ura3-52 lys2-801 ade2-101 trp1-Δ63 his3-Δ200 leu2-Δ1	Sikorski & Hieter, 1989	yMG207
74-D694 MATa [*PIN*$^+$] ade1-14 his3-11,-15 trp1-1 leu2-3,112 can1-100 pdr5Δ::kanMX ura3-1::URA::P_{ADH}RNQ1-GFP	This study	yMG258 (yMG33+pMG269)
74-D694 MATa [*PIN*$^+$] ade1-14 his3-11,-15 trp1-1 can1-100 pdr5Δ::kanMX leu2-3,112::LEU::P_{GPD}mCherry-CRY2olig ura3-1::URA::P_{ADH}RNQ1-GFP	This study	yMG259 (yMG49+pMG269)
74-D694 MATa [*PIN*$^+$] ade1-14 his3-11,-15 trp1-1 can1-100 pdr5Δ::kanMX leu2-3,112::LEU::P_{GPD}Htt97Q-mCherry-CRY2olig ura3-1::URA::P_{ADH}RNQ1-GFP	This study	yMG260 (yMG78+pMG269)
74-D694 MATa [*PIN*$^+$] ade1-14 his3-11,-15 trp1-1 can1-100 pdr5Δ::kanMX leu2-3,112::LEU::P_{GPD}Htt20Q-mCherry-CRY2olig ura3-1::URA::P_{ADH}RNQ1-GFP	This study	yMG262 (yMG88+pMG269)
74-D694 MATa [*pin*$^-$] ade1-14 his3-11,-15 trp1-1 leu2-3,112 can1-100 pdr5Δ::kanMX ura3-1::URA::P_{ADH}RNQ1-GFP	This study	yMG265 (yMG258 cured)
74-D694 MATa [*pin*$^-$] ade1-14 his3-11,-15 trp1-1 can1-100 pdr5Δ::kanMX leu2-3,112::LEU::P_{GPD}mCherry-CRY2olig ura3-1::URA::P_{ADH}RNQ1-GFP	This study	yMG266 (yMG259 cured)
74-D694 MATa [*pin*$^-$] ade1-14 his3-11,-15 trp1-1 can1-100 pdr5Δ::kanMX leu2-3,112::LEU::P_{GPD}Htt97Q-mCherry-CRY2olig ura3-1::URA::P_{ADH}RNQ1-GFP	This study	yMG267 (yMG260 cured)
74-D694 MATa [*pin*$^-$] ade1-14 his3-11,-15 trp1-1 can1-100 pdr5Δ::kanMX leu2-3,112::LEU::P_{GPD}Htt20Q-mCherry-CRY2olig ura3-1::URA::P_{ADH}RNQ1-GFP	This study	yMG269 (yMG262 cured)
YPH499 MATa [*PIN*$^+$] ura3-52 lys2-801 ade2-101 trp1-Δ63::TRP:: his3-Δ200 leu2-Δ1 sis1Δ::kanMX P_{TERT}SIS1	Klaips et al., 2020	yMG276
YPH499 MATa [*pin*$^-$] ura3-52 lys2-801 ade2-101 trp1-Δ63::TRP:: his3-Δ200 leu2-Δ1 sis1Δ::kanMX P_{TERT}SIS1	This study	yMG277 (yMG276 cured)